

---

# Quantum Degeneracy in an Atomic Fermi-Fermi-Bose Mixture

Matthias Taglieber

---



München 2008



---

# Quantum Degeneracy in an Atomic Fermi-Fermi-Bose Mixture

Matthias Taglieber

---

Dissertation  
an der Fakultät für Physik  
der Ludwig-Maximilians-Universität  
München

vorgelegt von  
Matthias Taglieber  
aus Mannheim

München, März 2008

Erstgutachter: Prof. Dr. Theodor W. Hänsch  
Zweitgutachter: Prof. Dr. Gerhard Rempe  
Tag der mündlichen Prüfung: 15. April 2008

## Abstract

This thesis deals with dilute fermionic and bosonic quantum gases in the nK temperature regime. In the work presented here, the first quantum-degenerate mixture of two *different* fermionic atomic species and the first triple-degenerate Fermi-Fermi-Bose mixture were produced. The quantum-degenerate mixtures were realized using sympathetic cooling of the fermionic species  ${}^6\text{Li}$  and  ${}^{40}\text{K}$  by an evaporatively cooled gas of bosonic  ${}^{87}\text{Rb}$  atoms in a magnetic trap. The apparatus, which was designed and built from scratch in this thesis work, provides a very versatile platform for a broad range of experiments.

As the first important step in the production of the quantum-degenerate three-species mixture, simultaneous magneto-optical trapping of  ${}^6\text{Li}$ ,  ${}^{40}\text{K}$ , and  ${}^{87}\text{Rb}$  was achieved, thereby demonstrating the first three-species magneto-optical trap (“triple MOT”) and the first two-fermion MOT. The triple MOT is loaded with lithium from a Zeeman slower and with potassium and rubidium from the background vapor that is maintained by atomic vapor dispensers. For this purpose, dispensers for potassium enriched in the isotope  ${}^{40}\text{K}$  were produced. The triple MOT was characterized and studied with respect to light-assisted interspecies losses. Furthermore, a sequence combining a compressed MOT and a temporal dark MOT is presented that, in spite of the differing requirements of the three species, allows us to achieve favorable starting conditions for further cooling in the QUIC-type magnetic trap. A magnetic transport system is used to transfer the precooled atomic clouds from the MOT position into the QUIC trap. The transport scheme was adapted to the specific requirements of the three-species mixture, in particular to the temperature of laser-cooled lithium, which is high in comparison to other species.

The quantum-degenerate regime is reached by evaporative and sympathetic cooling in the QUIC trap. Species-selective evaporation of rubidium is achieved by driving a  ${}^{87}\text{Rb}$  hyperfine transition to an untrapped state. In order to avoid undesired atom losses and heating due to spin-exchange collisions, the atoms are prepared in the maximally polarized internal ground states. Careful state cleaning during the cooling process was found crucial to attain quantum degeneracy. Since evaporative and sympathetic cooling both rely on energy transfer by elastic collisions between atoms, the efficiency of the cooling process depends on the relevant elastic scattering cross sections. The  ${}^{87}\text{Rb}$ - ${}^{87}\text{Rb}$  and  ${}^{40}\text{K}$ - ${}^{87}\text{Rb}$  scattering cross sections are quite favorable for this purpose. The  ${}^6\text{Li}$ - ${}^{87}\text{Rb}$  scattering cross section, however, was unknown at the beginning of the project and was later found to be comparatively small, making sympathetic cooling of  ${}^6\text{Li}$  by  ${}^{87}\text{Rb}$  rather challenging. In this thesis work, an experimental sequence was developed that nevertheless allows the production of a quantum-degenerate  ${}^6\text{Li}$  gas with large atom number in this mixture. Furthermore, it is shown that in the three-species mixture, the efficiency of the cooling process for  ${}^6\text{Li}$  is significantly increased by the presence of  ${}^{40}\text{K}$  through *catalytic cooling*. The quantum-degenerate Fermi-Fermi and Fermi-Fermi-Bose mixtures realized in this thesis work serve as a starting point for a broad range of possible future experiments, including the creation of heteronuclear Fermi-Fermi dimers and the investigation of the BEC-BCS cross-over regime. In this context, the possibilities opened by the mass difference and the differing internal structures of the two fermionic species are of particular interest.

## Zusammenfassung

Die vorliegende Arbeit befaßt sich mit verdünnten fermionischen und bosonischen Quantengasen im nK-Temperaturbereich. Im Rahmen der Arbeit wurden sowohl die erste quantenentartete Mischung zweier *verschiedener* fermionischer Atomspezies als auch die erste dreifach entartete Fermi-Fermi-Bose-Mischung erzeugt. Die quantenentarteten Mischungen wurden durch sympathetisches Kühlen der fermionischen Spezies  ${}^6\text{Li}$  und  ${}^{40}\text{K}$  mit einem mittels Verdampfungskühlung aktiv gekühlten Gas bosonischer  ${}^{87}\text{Rb}$ -Atome in einer Magnetfalle realisiert. Die Apparatur, die hierfür in dieser Arbeit entworfen und von Grund auf aufgebaut wurde, bietet eine äußerst vielseitige Plattform für ein breites Spektrum an Experimenten.

Als erster wichtiger Schritt für die Produktion der quantenentarteten Drei-Spezies-Mischung konnten  ${}^6\text{Li}$ ,  ${}^{40}\text{K}$  und  ${}^{87}\text{Rb}$  simultan magneto-optisch gefangen werden. Dies stellt die erste Realisierung einer magneto-optischen Falle für drei Spezies ("Dreifach-MOT") und einer MOT für zwei fermionische Spezies dar. Die Dreifach-MOT wird mit Lithium aus einem Zeeman-Abbremsler und mit Rubidium und Kalium aus dem Hintergrund-Gas geladen, das durch Atomgas-Dispenser aufrechterhalten wird. Zu diesem Zweck wurden Dispenser mit im Isotop  ${}^{40}\text{K}$  angereichertem Kalium hergestellt. Die Dreifach-MOT wurde charakterisiert und bezüglich lichtunterstützter Interspezies-Verluste studiert. Desweiteren wird eine aus einer komprimierten MOT und einer zeitlichen Dunkel-MOT kombinierte Sequenz vorgestellt, die es ermöglicht, trotz der sich unterscheidenden Anforderungen der drei Atomsorten günstige Ausgangsbedingungen für das folgende Kühlen in der QUIC-Magnetfalle zu erzielen. Für den Transfer der vorgekühlten Atome von der MOT-Position in die QUIC-Falle wird ein magnetisches Transport-System verwendet. Das Transport-Schema wurde an die besonderen Anforderungen der Drei-Spezies-Mischung angepaßt, insbesondere auch an die im Vergleich zu anderen Spezies hohe Temperatur von lasergekühltem Lithium.

Das quantenentartete Regime wird durch Verdampfungskühlung und sympathetisches Kühlen in der QUIC-Falle erreicht. Speziesselektive Verdampfungskühlung von Rubidium wird durch Treiben eines  ${}^{87}\text{Rb}$ -Hyperfein-Übergangs in einen ungefangenen Zustand erzielt. Um unerwünschte Atomzahlverluste und Heizen durch Spinaustausch-Stöße zu verhindern, sind die Atome in den maximal polarisierten Grundzuständen präpariert. Eine sorgfältige Zustandsreinigung während des Kühlprozesses hat sich als entscheidend zum Erreichen der Quantenentartung erwiesen. Da sowohl Verdampfungskühlung als auch sympathetisches Kühlen auf Energieübertragung durch elastische Stöße zwischen den Atomen beruhen, hängt die Effizienz des Kühlprozesses von den relevanten elastischen Streuquerschnitten ab. Die Streuquerschnitte für  ${}^{87}\text{Rb}$ - ${}^{87}\text{Rb}$ - und  ${}^{40}\text{K}$ - ${}^{87}\text{Rb}$ -Stöße sind hierfür recht günstig. Der  ${}^6\text{Li}$ - ${}^{87}\text{Rb}$ -Streuquerschnitt hingegen war zu Beginn des Projektes noch unbekannt und stellte sich später als vergleichsweise klein heraus, so dass sympathetisches Kühlen von  ${}^6\text{Li}$  durch  ${}^{87}\text{Rb}$  erheblich erschwert ist. In dieser Arbeit konnte jedoch eine experimentelle Sequenz entwickelt werden, die in dieser Mischung trotzdem die Erzeugung eines quantenentarteten  ${}^6\text{Li}$ -Gases mit großer Atomzahl gestattet. Desweiteren wird gezeigt, dass die Kühleffizienz für  ${}^6\text{Li}$  in der Drei-Spezies-Mischung durch die Anwesenheit von  ${}^{40}\text{K}$  aufgrund von *katalytischem Kühlen* signifikant erhöht ist. Die im Rahmen dieser Arbeit erzeugten quantenentarteten Fermi-Fermi- und Fermi-Fermi-Bose-Mischungen dienen als Startpunkt für ein breites Spektrum möglicher zukünftiger Experimente, wie beispielsweise der Erzeugung heteronuklearer Fermi-Fermi-Dimere oder der Erforschung des BEC-BCS-Übergangs. Besonders interessant sind dabei die Möglichkeiten, die sich durch die Massendifferenz und die unterschiedlichen internen Strukturen der zwei fermionischen Spezies ergeben.

# Contents

<b>Abstract</b>	<b>v</b>
<b>1. Introduction</b>	<b>1</b>
1.1. Bose-Einstein condensation . . . . .	1
1.2. Quantum-degenerate Fermi gases . . . . .	2
1.3. Ultracold molecules and the BEC-BCS transition . . . . .	4
1.4. This thesis . . . . .	6
<b>2. Theory</b>	<b>9</b>
2.1. Ultracold gases . . . . .	9
2.1.1. Quantum statistics . . . . .	9
2.1.2. Fermionic quantum gases . . . . .	13
2.1.3. Bosonic quantum gases . . . . .	16
2.1.4. The classical, ideal gas . . . . .	20
2.2. Evaporative and sympathetic cooling . . . . .	20
2.2.1. Collisions . . . . .	20
2.2.2. Evaporative cooling . . . . .	25
2.2.3. Sympathetic cooling . . . . .	28
<b>3. Experimental Setup</b>	<b>33</b>
3.1. Concept and overview . . . . .	33
3.2. Vacuum system . . . . .	34
3.2.1. Setup . . . . .	34
3.2.2. Installation, pump down, and baking . . . . .	36
3.2.3. Failure protection . . . . .	37
3.3. Atom sources . . . . .	37
3.3.1. Atomic vapor dispensers for $^{40}\text{K}$ and $^{87}\text{Rb}$ . . . . .	38
3.3.2. Zeeman slower for $^6\text{Li}$ . . . . .	39
3.4. Laser systems and optics . . . . .	43
3.4.1. Energy levels and transitions employed . . . . .	43
3.4.2. Rubidium laser system . . . . .	45
3.4.3. Potassium laser system . . . . .	46
3.4.4. Lithium laser system . . . . .	47
3.4.5. Combining the systems . . . . .	48
3.5. Absorption imaging . . . . .	50
3.5.1. Principle . . . . .	51
3.5.2. Optical setup . . . . .	52
3.5.3. Practical aspects . . . . .	53

3.6. Magnetic trapping . . . . .	54
3.6.1. Principle of magnetic trapping . . . . .	54
3.6.2. Magnetic transport . . . . .	56
3.6.3. QUIC trap . . . . .	60
3.6.4. Further magnetic fields . . . . .	64
3.7. Radio frequency and microwave sources . . . . .	64
3.8. Experiment control . . . . .	65
<b>4. Simultaneous magneto-optical trapping of three atomic species</b>	<b>67</b>
4.1. Introduction . . . . .	67
4.2. Experimental setup . . . . .	68
4.3. Optimization . . . . .	69
4.3.1. Single-species MOTs . . . . .	69
4.3.2. Optimization and realization of the Triple MOT . . . . .	71
4.3.3. Dispenser currents . . . . .	72
4.4. Optical molasses . . . . .	74
4.4.1. Compensation of magnetic stray fields . . . . .	74
4.4.2. Optimization of molasses parameters . . . . .	74
4.5. Light-assisted collisions . . . . .	76
4.6. Conclusions . . . . .	77
<b>5. On the road to evaporative cooling</b>	<b>79</b>
5.1. MOT . . . . .	79
5.2. Compressed MOT and temporal dark MOT . . . . .	80
5.3. State preparation . . . . .	82
5.3.1. Choice of the atomic states . . . . .	82
5.3.2. Sequence for optical pumping . . . . .	84
5.4. Magnetic transport into the UHV chamber . . . . .	86
5.5. The QUIC trap . . . . .	87
5.5.1. Loading of the QUIC trap . . . . .	87
5.5.2. Characterization of the QUIC trap . . . . .	90
<b>6. Cooling into quantum degeneracy</b>	<b>93</b>
6.1. Bose-Einstein condensation of $^{87}\text{Rb}$ . . . . .	93
6.1.1. Rf evaporation . . . . .	93
6.1.2. Optimization and efficiency of rf evaporation . . . . .	95
6.1.3. Signatures of Bose-Einstein condensation . . . . .	97
6.1.4. Limitations of rf evaporation for multi-species mixtures . . . . .	100
6.1.5. MW evaporation . . . . .	101
6.2. Quantum-degenerate Bose-Fermi mixture of $^{87}\text{Rb}$ and $^{40}\text{K}$ . . . . .	103
6.3. Simultaneous quantum degeneracy in the $^6\text{Li}$ - $^{40}\text{K}$ - $^{87}\text{Rb}$ mixture . . . . .	105
6.3.1. Sympathetic cooling of $^6\text{Li}$ . . . . .	105
6.3.2. Quantum-degenerate Fermi-Fermi mixture of $^6\text{Li}$ and $^{40}\text{K}$ . . . . .	108
6.3.3. Quantum-degenerate Fermi-Fermi-Bose mixture of $^6\text{Li}$ , $^{40}\text{K}$ , and $^{87}\text{Rb}$ . . . . .	109
6.3.4. Study of the last part of the cooling process . . . . .	110

<b>7. Conclusions and Outlook</b>	<b>115</b>
<b>A. Natural constants and atomic properties</b>	<b>117</b>
Natural constants . . . . .	117
Atomic properties . . . . .	118
<b>Bibliography</b>	<b>119</b>
<b>Danksagung</b>	<b>139</b>



# 1. Introduction

The field of ultracold quantum gases has seen a spectacular development in the last two decades. Trapping of neutral atoms was first demonstrated in 1985 in a magnetic trap [1] and in 1987 in a magneto-optical trap (MOT) [2]. After combining advanced versions of these techniques with evaporative cooling [3–5], three groups reported in 1995 on the observation of Bose-Einstein condensation (BEC) in dilute atomic gases [6–9]. Only a few years later, quantum degeneracy was also achieved in dilute fermionic gases [10–15]. This thesis reports on the realization of the first quantum-degenerate mixture of two *different* fermionic species [16]. In addition, the first quantum-degenerate three-species Fermi-Fermi-Bose mixture was produced. In the following, a brief overview over the field of dilute atomic quantum gases is given. Special emphasis is put on the concepts that are directly relevant for the present work. The last section gives an outline of the thesis.

## 1.1. Bose-Einstein condensation

The phenomenon of Bose-Einstein condensation was predicted for an ideal gas in 1925 by A. Einstein [17] based on related work by S.N. Bose [18]. BEC occurs in a gas of identical bosonic particles when the thermal de-Broglie wave length of the particles becomes comparable to the inter-particle distance. In this “quantum-degenerate” regime, the particles’ wave functions overlap and a macroscopic fraction of the particles populates the single-particle ground state of the system.

The phase transition to BEC is of purely quantum-statistical nature and does not rely on interactions between the particles. In most real systems, however, interactions play an important role. In a gas, interparticle interactions are mediated by collisions between the particles. Since the thermal de-Broglie wave length increases with decreasing temperature, BEC can in principle be achieved simply by cooling a gas to sufficiently low temperature. In most gases, however, molecules and clusters would form in this case due to many-body collisions, and liquefaction or solidification would occur before the quantum-degenerate regime was reached. Fortunately, dilute alkali gases allow one to postpone this problem and to achieve BEC in a metastable gaseous phase. This is possible because at ultralow densities (typically  $\sim 10^{14} \text{ cm}^{-3}$ ), the timescale for liquefaction or solidification, which are both initially dominated by inelastic three-body collisions, is typically much longer than the duration needed for equilibration of the translational degrees of freedom by elastic two-body collisions. Dilute gases offer the additional advantage over other systems that interparticle interactions are usually very weak because of the low particle number density. This allows the quantitative description of the static and dynamic properties of the gas from first principles. A drawback of the low density, however, is that extremely low temperatures on the order of a few hundred nK are needed to reach the quantum-degenerate regime.

This makes the production of a quantum-degenerate gas rather challenging and requires the combination of several cooling and trapping techniques.

The first cooling step from room temperature or above towards the required ultralow temperatures is achieved by laser cooling. Laser cooling of neutral atomic gases was first proposed in Ref. [19] and was extensively studied in the 1980s (for a review on laser cooling and its historical development, see Refs. [20–22]). Alkali atoms are especially well suited for laser cooling because of their favorable energy-level structure and due to the availability of convenient laser sources for the corresponding wavelengths. Nevertheless, the temperatures and densities achieved in a MOT and by further laser-cooling methods do not suffice to cross the phase transition to BEC. In all BEC experiments so far, the atoms are therefore subsequently captured in a magnetic trap or in an optical dipole trap [23, 24] and evaporative cooling is applied to increase the phase-space density by several orders of magnitude until the quantum-degenerate regime is reached. Evaporative cooling relies on selective removal of particles with above-average energy and subsequent thermalization of the remaining particles at a lower temperature by elastic collisions.

Since the first realization of BEC in 1995, the field of dilute atomic quantum gases has seen an enormous boom. An overview over the numerous exciting experiments conducted with BECs during the first following years can be found in Refs. [25, 26]. Corresponding theoretical concepts and developments are reviewed in Refs. [27, 28]. The field is still advancing at a high pace and, to this day, BEC was reached for a total of 13 different atomic species [6–8, 29–38] in almost a hundred experiments worldwide [39, 40]. A particular strength of the systems is their versatility and the extraordinary experimental control over key properties of the dilute gas. Optical light fields can be used to trap the atoms [23, 24] and to create complex and highly controllable potentials. For instance, interference patterns of far-detuned laser beams were used to generate experimental situations with effectively reduced dimensionality, which allowed the observation of new types of quantum matter [41–44]. A particularly intriguing aspect of ultracold dilute gases is the fact that the interatomic interactions can be experimentally controlled by exploiting a Feshbach resonance. A Feshbach resonance is a scattering resonance that occurs if two colliding atoms couple resonantly to a bound molecular state. The theory of Feshbach resonances was originally developed in the context of nuclear physics [45, 46]. In atomic physics, the relative energy of the colliding atoms and of the bound state can be tuned, e.g. by applying an external magnetic field [47]. The first experimental observations of Feshbach resonances in ultracold gases were reported for bosonic species [48–51] and confirmed the expected effect on the interparticle interaction due to elastic scattering. The simultaneous enhancement of inelastic losses [48, 51–53], however, seemed to be a severe limitation for future experiments. The assessment changed, though, when Feshbach resonances were successfully exploited to circumvent unfavorable scattering properties for the generation of BEC [34, 54, 55] and to associate ultracold molecules as will be discussed in Sec. 1.3.

### 1.2. Quantum-degenerate Fermi gases

A few years after the first quantum-degenerate Bose gases had been produced, the cooling and trapping schemes developed there were adapted and applied to fermionic gases. Quan-

tum degeneracy for fermions was first reached in 1999 in a gas of  $^{40}\text{K}$  atoms [10]. In the following years quantum-degenerate gases of  $^6\text{Li}$  [11–16],  $^{40}\text{K}$  [16, 56–59], metastable  $^3\text{He}^*$  [60], and of the species  $^{171}\text{Yb}$  [38] and  $^{173}\text{Yb}$  [61] have successfully been produced. A gas of indistinguishable fermionic atoms is called “quantum degenerate” if it has a temperature well below its Fermi temperature  $T_F = E_F/k_B$ . The Fermi energy  $E_F$  is defined as the zero-temperature limit of the chemical potential of the gas. As a consequence of Pauli’s exclusion principle, the energy distribution of the sample in this limit differs significantly from the classical expectation: All energy states with single-particle energy  $\epsilon \leq E_F$  are occupied by exactly one atom and all energy states with  $\epsilon > E_F$  are empty. This situation was first described in 1926 by E. Fermi [62] and is today referred to as a “Fermi sea”. It is important to note that in an *ideal* Fermi gas no phase transition occurs, in contrast to the bosonic case. When an ideal Fermi gas is cooled into the quantum-degenerate regime, its properties change smoothly from classical to non-classical behavior.

The generation of a quantum-degenerate Fermi gas is somewhat more challenging than the production of a BEC, mainly because evaporative cooling cannot be successfully applied to an ultracold single-component Fermi gas. As discussed above, evaporative cooling relies on rethermalization by elastic collisions. Collisions are conveniently described in a partial wave basis. In the relevant temperature range, all partial waves except for the lowest one (s-wave) are frozen out. In a gas of indistinguishable fermions, however, collisions in the s-wave channel are forbidden. Therefore, such a one-component Fermi gas cannot rethermalize at low temperature and evaporative cooling becomes inefficient. This difficulty was overcome in Ref. [10] by employing an incoherent mixture of two different atomic states in a magnetic trap and applying evaporation to both components. Since the two components are distinguishable, interspecies collisions are not Pauli suppressed in this case and efficient thermalization can be achieved. Spin-mixtures of different atomic states are also used in experiments that apply an all-optical strategy to produce quantum-degenerate gases of  $^6\text{Li}$  [13, 15] or  $^{173}\text{Yb}$  [61]. In the all-optical approach, the atoms are directly loaded from the MOT into an optical dipole trap. A second way to circumvent the difficulty of suppressed collisions between identical fermions at low temperature consists in sympathetic cooling [63] of a spin-polarized fermionic gas by an actively cooled bosonic gas [12]. This approach, which has the advantage that the atom number of the fermionic species is in principle not reduced by the cooling process, is pursued in most experiments today, including the one presented in this thesis. So far, fermionic quantum gases have been realized by this approach in the following mixtures:  $^6\text{Li}$ - $^7\text{Li}$  [11, 12],  $^6\text{Li}$ - $^{23}\text{Na}$  [14],  $^6\text{Li}$ - $^{87}\text{Rb}$  [64],  $^3\text{He}^*$ - $^4\text{He}^*$  [60],  $^{171}\text{Yb}$ - $^{174}\text{Yb}$  [38], and most often  $^{40}\text{K}$ - $^{87}\text{Rb}$  [57–59]. In the present experiment, a  $^6\text{Li}$ - $^{40}\text{K}$ - $^{87}\text{Rb}$  three-species mixture is used.

After the realization of the first quantum-degenerate Fermi gases in 1999, early experiments investigated basic properties of these gases like the Fermi pressure [11], the deviation of the total energy and of the momentum distributions of the Fermi gas from those of a classical gas [10], and Pauli blocking of collisions [65, 66]. In 2002, Feshbach resonances were observed in the fermionic species  $^6\text{Li}$  [67–69] and  $^{40}\text{K}$  [70]. These resonances are s-wave resonances, which for fermions can obviously only occur between distinguishable atoms. Thus, incoherent mixtures of two different hyperfine states of the respective species are used to observe and exploit the Feshbach resonances. It is important to note that for Fermi gases maximal inelastic decay loss in the vicinity of a Feshbach resonance does not

occur at the resonance point, but somewhere in the region of positive scattering length [68, 71, 72] (the exact value depends on the particular experimental conditions). This is in strong contrast to the situation in bosonic quantum gases. The strong interaction and long lifetime of Fermi gases close to a Feshbach resonance intensified the hope that these well-controlled systems could be used to study Cooper pairing and Bardeen-Cooper-Schrieffer (BCS) superfluidity [73] since the expected critical temperature in this case [74, 75] seemed to be sufficiently high to be within experimental reach, in contrast to weakly interacting gases where the predicted critical temperature is extremely low.

### 1.3. Ultracold molecules and the BEC-BCS transition

During the recent years, one major focus of research in dilute quantum gases lay on the creation of ultracold diatomic molecules (dimers). Compared to atoms, homonuclear and heteronuclear dimers possess the additional degrees of freedom of rotation and vibration making their experimental investigation more challenging. At the same time, however, molecules also offer richer physics than atoms, which justifies the increased effort required for their creation and study. For instance, heteronuclear dimers can have a large permanent electric dipole moment [76]. Applications of such dipolar molecules have been proposed with respect to quantum computation [77] and for fundamental tests like the measurement of the electron dipole moment [78, 79]. The anisotropic and long-range character of the dipole-dipole interaction bears the prospect to explore new physical regimes in ultracold quantum gases, see e.g. Refs. [80–86].

The creation of a quantum-degenerate gas of molecules is a formidable task, which can be approached by direct or indirect techniques (see e.g. Ref. [87]). Direct methods are based on cooling of preexisting molecules. Although significant progress has been achieved with techniques like buffer gas cooling [88], the Stark decelerator [89] and other more recent methods, this approach still seems to be far from reaching the quantum-degenerate regime. A main difficulty of this approach lies in the fact that laser cooling, which proved so successful for alkali atoms, cannot be easily applied to molecules due to their complex internal energy level structure. Indirect methods, in contrast, are based on the formation of molecules from precooled atoms. Dimers with temperatures on the order of  $100 \mu\text{K}$  have been produced for many different species by photoassociation of laser-cooled atoms [87, 90]. A drawback of such photoassociation schemes, however, is that they typically involve spontaneous scattering of photons, which leads to heating of the sample.

A method that allows one to generate samples of molecules with very low temperatures and high particle number densities was proposed in Ref. [91]: Starting from a quantum-degenerate gas, a slow magnetic field ramp across a Feshbach resonance in the right direction transfers the atomic population in the entrance channel into the bound molecular state that is responsible for the resonance. The molecule is created in the highest bound vibrational molecule state, which has a very small binding energy close to the resonance. The conversion process is fully reversible and under complete experimental control. In 2003, several groups employed this ramping technique to associate ultracold, homonuclear molecules from the bosonic species  $^{23}\text{Na}$  [92],  $^{87}\text{Rb}$  [93], and  $^{133}\text{Cs}$  [94], and from the fermionic species  $^6\text{Li}$  [95, 96] and  $^{40}\text{K}$  [97]. In an alternative approach, ultracold  $^6\text{Li}_2$  molecules were created

by three-body recombination [98, 99] close to a Feshbach-resonance. More recently, the association of heteronuclear dimers from a fermionic and a bosonic species [100] or from two different bosonic species [101] was demonstrated.

Soon after the first homonuclear Feshbach molecules had been created, it became clear that the lifetime of Feshbach molecules is very different in bosonic and fermionic systems: For dimers constituted of two bosonic atoms, fast loss by relaxation to deeply bound molecular states (“vibrational quenching”) was observed [102–104]. This difficulty has prohibited so far to reach the quantum-degenerate regime in a gas of Bose-Bose molecules. Experiments with bosonic systems therefore focused on the atom-molecule conversion process [102, 105–108] and on decay studies [102–104, 109]. More recently, it was shown that the lifetime of Bose-Bose Feshbach molecules can be significantly increased by confinement in an optical lattice [110, 111]. For dimers consisting of two fermionic atoms of the same species, however, it was found that vibrational quenching in the vicinity of the Feshbach resonance is suppressed even in the bulk gas by several orders of magnitude [15, 96, 112], resulting in a long trap lifetime. This suppression of vibrational relaxation is a consequence of the Pauli principle as discussed in Ref. [113]. Therefore, long lifetimes close to a Feshbach resonance are also expected for dimers composed of two atoms of *different* fermionic species.

The long lifetime of fermionic gases in the strongly interacting regime near a Feshbach resonance allowed the exploration of the so-called BEC-BCS cross-over between the region of repulsive interaction on one side (“BEC-side”) of the Feshbach resonance and the region of attractive interaction on the other side of the Feshbach resonance (“BCS-side”). The physics of this cross-over regime is best understood by considering the two limiting cases, which can be described by well-established theories: At moderate positive values of the atom-atom scattering length, the fermions form molecules. These molecules are composite bosons and their ground state at  $T = 0$  is a Bose-Einstein condensate of molecules, a molecular BEC (mBEC). For moderate negative values of the scattering length, the ground state in the zero-temperature limit is the Bardeen-Cooper-Schrieffer (BCS) state [73] of Cooper pairs. The two limiting cases are connected by the strongly interacting regime where both theories break down.

The observation of a molecular BEC (mBEC) was reported by several groups working with single-species fermionic systems [15, 99, 114] in November of 2003. Only a few weeks later, first evidence for condensation of fermion pairs on the BCS-side of the resonance was found [115, 116]. These results initiated a series of experiments investigating the BEC-BCS cross-over: The measurements reported in Ref. [117] showed that the cross-over proceeds smoothly and can be realized in an adiabatic and reversible way. The study of collective excitations in the trapped gas [118, 119] and radio-frequency spectroscopy [120] provided indication for superfluidity. The measurement of the heat capacity of the gas showed a transition at a temperature where superfluidity was expected [121]. The unambiguous proof of superfluidity over the whole BEC-BCS cross-over was finally provided by an experiment showing that quantized vortices in form of vortex arrays could be created for a wide range of magnetic field values on both sides of the resonance [122].

All these experiments were carried out with Fermi gas mixtures of two spin components with equal atom numbers. In this case, the chemical potentials of the two spin states are equal. In the BCS-limit, each atom can thus find a corresponding partner to form a Cooper

pair and the entire system can become superfluid. When the chemical potentials of the two components are different, however, pairing is qualitatively altered. Different exotic phases have been proposed for such a system [123–129]. Quantum-degenerate atomic Fermi gases are very well suited for the experimental exploration of these phases: The interaction can be tuned using a Feshbach resonance and the Fermi surface can be adjusted by choice of the atom numbers in the two components of the gas. In experiments using two spin states of one single fermionic species, it was found that above a critical population imbalance phase separation into a core of paired fermions and a shell with unpaired fermions occurs [130]. In a complementary experiment, vortices were used to map out the parameter space of interaction strength and imbalance between the Fermi surfaces where superfluidity occurs [131]. Furthermore, imbalanced spin-mixtures allowed the observation of the superfluid phase transition directly in the spatial profiles of the atomic clouds [132]. More recently, it was demonstrated that in the strongly interacting regime pairing can occur without superfluidity even on the BCS-side of the Feshbach resonance [133].

### 1.4. This thesis

The quantum-degenerate mixture of two *different* fermionic atomic species created in this thesis work will allow us to even go one step further. In this system, unmatched Fermi surfaces can be obtained even in the case of equal atom numbers in the two components. This can be exploited to study a variety of analogies to other many-body systems, in particular to a spatially inhomogeneous superfluid phase predicted to occur in certain types of high temperature superconductors [134–137]. Further, a transition to a crystalline phase in the bulk gas [138] and the possibility to simulate baryonic phases of quantum chromodynamics [139, 140] have been theoretically proposed. Moreover, the mixture bears the prospect to create heteronuclear ground state molecules [87, 141], in this way realizing a quantum gas with a particularly large dipolar interaction [76]. Finally, a two-species mixture offers the additional possibility to conveniently apply component-selective methods.

The concept of our system for the production of the quantum-degenerate two-species Fermi-Fermi mixture is based on sympathetic cooling of fermionic  ${}^6\text{Li}$  and  ${}^{40}\text{K}$  by an evaporatively cooled bosonic  ${}^{87}\text{Rb}$  gas in a magnetic trap. A three-species MOT is used as a source of precooled atoms. The laser-cooled atomic clouds are transferred from the MOT position into the final magnetic trap by a magnetic transport mechanism [142].

This thesis is organized as follows. **Chapter 2** gives an introduction into theoretical concepts that are essential for the experiments described in this thesis. Thermodynamics of ultracold (quantum) gases are reviewed and equations required for the analysis of experimental results are provided. In addition, the principles of evaporative and sympathetic cooling are discussed, techniques that are indispensable for the production of quantum-degenerate atomic gases.

**Chapter 3** describes the experimental platform for the generation of a quantum-degenerate Fermi-Fermi-Bose mixture. The basic physical principles underlying the main components of the apparatus are discussed along with their technical realization. The experimental platform has been developed from scratch during this thesis work. There-

fore, the development, the design and the construction of the very complex triple-species apparatus constitute a significant part of the work presented here.

The first step in the creation of a quantum-degenerate mixture of dilute atomic gases is to capture the relevant atomic species in a magneto-optical trap. **Chapter 4** reports on the simultaneous trapping of two fermionic species,  ${}^6\text{Li}$  and  ${}^{40}\text{K}$ , and a bosonic species,  ${}^{87}\text{Rb}$ , demonstrating the first three-species MOT (“triple MOT”). Our way to optimize the triple MOT and turn it into a suitable source for the goal to achieve quantum degeneracy by evaporative and sympathetic cooling is described. The single-species MOTs and the triple MOT are characterized. Trap loss due to interspecies collisions is briefly studied. Parts of this chapter were published in Ref. [143].

After the successful realization of the triple MOT and some extensions to the experimental apparatus, an experimental sequence that leads to a quantum-degenerate mixture of  ${}^6\text{Li}$ ,  ${}^{40}\text{K}$ , and  ${}^{87}\text{Rb}$  was developed. The first half of the sequence is described in **Chapter 5**. This includes capture and confinement in a magneto-optical trap, further increase of phase space density by laser-cooling methods, state preparation of the three species, trapping in a magnetic quadrupole trap, and transfer into the quadrupole-Ioffe configuration (QUIC) trap [144] located at the glass cell in the ultra-high vacuum (UHV) section of the apparatus. The challenge in the development of a suitable sequence is to combine the different, and in some cases opposing, constraints that the individual atomic species impose on it. The final experimental sequence is described in detail and critical points are discussed. Moreover, exemplary experimental measurements conducted for the development of the optimized sequence are presented. In addition, the final magnetic QUIC trap is characterized.

**Chapter 6** describes the second half of the experimental sequence and the achievement of simultaneous quantum degeneracy in the three-species mixture of bosonic  ${}^{87}\text{Rb}$  and fermionic  ${}^6\text{Li}$  and  ${}^{40}\text{K}$ . Rubidium is cooled by forced evaporation under “runaway” conditions. In single-species operation, radio frequency radiation is used to drive the evaporation process. The efficiency of the cooling process with respect to particle loss is evaluated and characteristic signatures of Bose-Einstein condensation are observed. In multi-species operation, the fermionic species lithium and potassium are cooled by sympathetic cooling with rubidium. In this case, evaporation of rubidium is forced by micro wave radiation allowing species- and energy-selective removal of particles from the trap. Details of the experimental sequence that proved crucial to successfully cool the mixture are described. In particular, the last part of the cooling process is studied and it is shown that the efficiency of sympathetic cooling of the  ${}^6\text{Li}$  gas by  ${}^{87}\text{Rb}$  is increased by the presence of  ${}^{40}\text{K}$  through catalytic cooling. Finally, typical quantum-degenerate samples in the  ${}^6\text{Li}$ - ${}^{40}\text{K}$  Fermi-Fermi mixture and in the  ${}^6\text{Li}$ - ${}^{40}\text{K}$ - ${}^{87}\text{Rb}$  Fermi-Fermi-Bose mixture are presented. Parts of Ch. 5 & 6 were published in Ref. [16].



## 2. Theory

This chapter presents the theoretical concepts that are essential for the experiments described in this thesis. Section 2.1 reviews thermodynamics of ultracold gases and provides equations needed for the analysis of experimental results described in a later chapter. Section 2.2 then discusses theoretical basics of evaporative and sympathetic cooling, techniques that are indispensable to produce quantum-degenerate atomic gases.

### 2.1. Ultracold gases

In the experiments presented in this thesis, atomic gases are routinely cooled to temperatures and densities at which quantum statistics must be used to correctly describe their thermodynamic properties. This section therefore introduces basic concepts of the quantum statistics of trapped atomic gases and derives intra-trap and time of flight density distributions for fermionic, bosonic and classical gases. More detailed information can be found in text books on quantum mechanics and on quantum statistics, e.g. [145–151].

#### 2.1.1. Quantum statistics

In a gas of identical particles, the total wave function must be either symmetric or antisymmetric under exchange of two particles in order to describe a physical state [152]. Particles for which the physical states are symmetric under this operation are called bosons and those for which they are antisymmetric fermions. The spin-statistics theorem [153] connects this definition to the spin of the particles and states that particles with integer spin are bosons and those with half-integer spin fermions. Starting from the thermodynamic partition function, the (anti-)symmetrization of the wave function leads to the mean occupation number  $f(\epsilon_r)$  of a single particle energy eigenstate with energy  $\epsilon_r$ . It is given by [151]

$$f(\epsilon_r) = \frac{1}{e^{\beta(\epsilon_r - \mu)} \pm 1}, \quad \begin{array}{l} + \text{ fermions} \\ - \text{ bosons} \end{array} \quad (2.1)$$

where  $\beta = (k_B T)^{-1}$  is a measure for the temperature  $T$  of the system and  $\mu$  is the chemical potential. The chemical potential is implicitly fixed by the normalization condition  $\sum_r f(\epsilon_r) = N$ , where  $N$  is the total atom number. The sum runs over all energy eigenstates of the system, counting degenerate states separately. In the denominator of Eq. (2.1) and in the following, the upper sign applies to the case of fermions (Fermi-Dirac statistics) and the lower one to the case of bosons (Bose-Einstein statistics). For fermions,  $f(\epsilon_r)$  yields only values between zero and one and the chemical potential may assume any real value. Thus, no two indistinguishable, fermionic particles may occupy the same quantum state simultaneously (Pauli exclusion principle), a property that also follows directly from the antisymmetry of the total wave function. In the case of bosons, however, for the mean

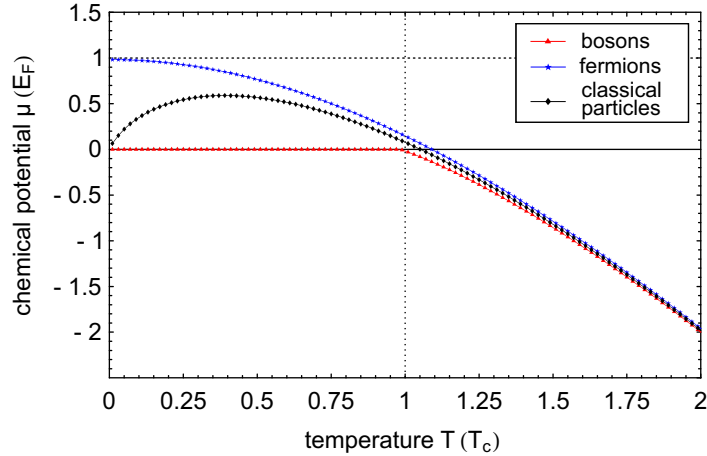


**Figure 2.1:** Chemical potential of a harmonically trapped gas. The chemical potential is plotted for different statistics (Fermi-Dirac, blue, classical Maxwell-Boltzmann, black, and Bose-Einstein, red) as a function of temperature for fixed atom number  $N = 10^5$ . The temperature is normalized to the critical temperature for Bose-Einstein condensation  $T_c$  (see Sec. 2.1.3.2) and the chemical potential is given in units of the Fermi energy  $E_F$  (see Sec. 2.1.2.1).

occupation number to be physical, the chemical potential is restricted to values  $\mu \leq \epsilon_0$ , where  $\epsilon_0$  is the energy of the ground state of the system. Furthermore, the occupation number has a singularity, which occurs when the denominator of Eq. (2.1) tends to zero. This property is closely related to Bose-Einstein condensation (BEC) as will become clear later. For the remainder of this chapter, the ground state energy  $\epsilon_0$  is set to zero without loss of generality.

We now consider an ideal, spin-polarized gas of atoms with mass  $m$  trapped in a harmonic potential

$$V_{\text{ho}}(\mathbf{r}) = \frac{m}{2} (\omega_x^2 x^2 + \omega_y^2 y^2 + \omega_z^2 z^2), \quad (2.2)$$

with angular trapping frequencies  $\omega_i$ . For any given total atom number and temperature, the chemical potential of the system can be calculated numerically using only Eq. (2.1), the energy spectrum of the harmonic oscillator, and the normalization condition for the atom number. As an example, Fig. 2.1 shows the chemical potential of a gas trapped in an isotropic harmonic oscillator potential. Once the chemical potential is known, the occupation numbers and the density and momentum distributions can be derived using Eq. (2.1) and the known eigenfunctions. The result then describes the system to any desired precision taking also finite-size effects into account (for the bosonic case see e.g. [154]). However, in typical experiments the number of trapped particles is large and the thermal energy is much bigger than the level spacing,  $k_B T \gg \hbar \omega_{x,y,z}$ . For the derivation of thermodynamic properties of the system, it is then more convenient to switch from a representation of discrete energy levels to a continuous density of states  $g(\epsilon)$ . In the semi-classical approximation, it is defined by

$$g(\epsilon) = \frac{1}{h^3} \int \delta[\epsilon - \epsilon_{\text{cl}}(\mathbf{r}, \mathbf{p})] d\mathbf{r} d\mathbf{p}, \quad (2.3)$$

where  $V(\mathbf{r})$  designates the trapping potential and where  $\epsilon_{\text{cl}}(\mathbf{r}, \mathbf{p}) = \mathbf{p}^2/2m + V(\mathbf{r})$  is the energy of a single classical particle with momentum  $\mathbf{p}$ . The integration can be carried out analytically for general power law potentials [155]. The result for the case of the harmonic potential Eq. (2.2) is given by

$$g_{\text{ho}}(\epsilon) = \frac{\epsilon^2}{2(\hbar\bar{\omega})^3}, \quad (2.4)$$

where  $\bar{\omega} = (\omega_x\omega_y\omega_z)^{1/3}$  is the geometric mean of the angular trapping frequencies. This approximation is exact in the thermodynamic limit. For the bosonic case, approximations with additional terms, which account for the finite atom number in real experimental situations, are also available [156, 157]. However, the predictions derived from Eq. (2.4) describe the results of most experiments in harmonic traps already very well.

### 2.1.1.1. Thermodynamic quantities

The density of states allows to calculate many thermodynamic quantities in a very straightforward way. Note, however, that Eq. (2.4) assigns a weight of zero to the ground state. For bosons, the ground state therefore has to be treated separately (see Sec. 2.1.3.2) due to the possible large occupation number, whereas it can safely be neglected for a large system of fermions, since the ground state is occupied by at most one identical fermion. With above definitions, the number of atoms in the excited states  $N_{\text{ex}}$  has the simple form

$$N_{\text{ex}} = \int_0^\infty f(\epsilon) g(\epsilon) d\epsilon. \quad (2.5)$$

For the harmonic potential Eq. (2.2), the integration can be carried out and yields

$$N_{\text{ex}} = \mp \left( \frac{k_{\text{B}}T}{\hbar\bar{\omega}} \right)^3 g_3(\mp\tilde{z}), \quad (2.6)$$

where I have introduced the fugacity

$$\tilde{z} = e^{\beta\mu} \quad (2.7)$$

and the polylogarithm function  $g_\alpha(s)$ , see Fig. 2.2. The polylogarithm function is defined for positive integer and half integer order  $\alpha$  by

$$g_\alpha(s) = \sum_{k=1}^{\infty} \frac{s^k}{k^\alpha} \quad (2.8)$$

and its analytic continuation. It has a branch cut discontinuity in the complex plane along the real axis for  $s > 1$ . For fast and accurate numerical calculations, adequate implementations are available in the literature [158, 159] and in mathematical function libraries [160]. The following integral representation of the polylogarithm function is often useful for calculations:

$$\int_0^\infty \frac{t^\alpha}{s^{-1}e^t \pm 1} dt = \mp \Gamma(\alpha + 1) g_{\alpha+1}(\mp s). \quad (2.9)$$

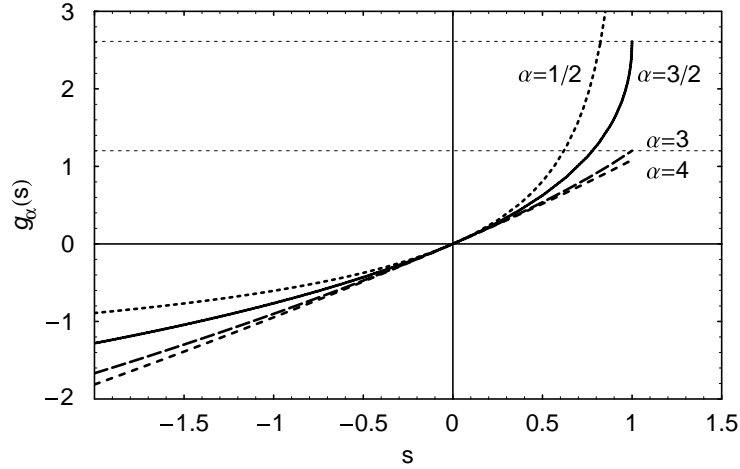


**Figure 2.2:** The polylogarithm function  $g_\alpha(s)$ , which appears in many expressions for thermodynamic quantities of a gas trapped in a harmonic potential. Shown are the cases  $\alpha = 1/2, 3/2, 3, 4$ .

It is valid for  $\text{Re}(\alpha) > 0$  and  $s \in \mathbb{C} \setminus \{s \in \mathbb{R} | s > 1\}$  and was employed to obtain Eq. (2.6). The polylogarithm function is also called the Bose-Einstein function, and  $f_\alpha(s) = -g_\alpha(-s)$  is referred to as the Fermi-Dirac function.

Similarly to the atom number, the total energy in the gas is given by the expression

$$U(T) = \int_0^\infty \epsilon f(\epsilon) g(\epsilon) d\epsilon. \quad (2.10)$$

For arbitrary given temperature, atom number, and potential, the integration can be performed numerically using the chemical potential given implicitly by Eq. (2.5). In the case of the harmonic potential Eq. (2.2), the integral can be calculated analytically and gives

$$U(T) = -3 k_B T \left( \frac{k_B T}{\hbar \bar{\omega}} \right)^3 g_4(\mp \tilde{z}). \quad (2.11)$$

This result can then be used to calculate the heat capacity  $C_{\text{heat}} = \left. \frac{\partial U}{\partial T} \right|_N$ , which is an important quantity in the sympathetic cooling process. Note, however, that the fugacity  $\tilde{z}$  is a function of the temperature.

### 2.1.1.2. The semiclassical approximation

Most data in our experiments are deduced from density distributions of clouds, either recorded intratrap or after a period of free expansion following a sudden release from the trap. These density distributions can be derived using a semiclassical approach, which is under typical experimental conditions a very good approximation for fermionic clouds and uncondensed bosonic clouds. In this approximation the particles are treated as wave packets with definite position and momentum. In order to obtain the corresponding phase

space density  $\tilde{\rho}(\mathbf{r}, \mathbf{p})$  we combine Eq. (2.3) and Eq. (2.5) with the normalization condition

$$N = \int \tilde{\rho}(\mathbf{r}, \mathbf{p}) d\mathbf{r} d\mathbf{p} \quad (2.12)$$

and use the approximation  $N \approx N_{\text{ex}}$ . This allows one to identify the phase space density

$$\tilde{\rho}(\mathbf{r}, \mathbf{p}) = \frac{1}{h^3} f[\epsilon_{\text{cl}}(\mathbf{r}, \mathbf{p})] = \frac{1}{h^3} \frac{1}{e^{\beta[p^2/2m + V(\mathbf{r}) - \mu] \pm 1}}. \quad (2.13)$$

Note that also in this semiclassical approximation the correct statistics is accounted for by the corresponding distribution function, which in the case of fermions limits the number of particles per phase space volume element  $h^3$  to one. The approach described in this paragraph corresponds to a local density approximation for the distribution function.

The distributions in position and momentum space are obtained by integrating Eq. (2.13) over the respective other space. For a cloud trapped in an arbitrary potential  $V(\mathbf{r})$ , only the integration over momentum space can be performed analytically, employing a suitable substitution and using relation 2.9. The result is

$$n(\mathbf{r}) = \mp \frac{1}{\lambda_{\text{dB}}^3} g_{3/2} \left( \mp \tilde{z} e^{-\frac{V(\mathbf{r})}{k_{\text{B}}T}} \right) \quad (2.14)$$

where

$$\lambda_{\text{dB}} = \sqrt{\frac{2\pi\hbar^2}{mk_{\text{B}}T}} \quad (2.15)$$

designates the thermal de Broglie wavelength. In the case of the harmonic potential 2.2, also the momentum distribution can be calculated analytically. In order to carry out the integration over position space one switches to the generalized coordinate  $\tilde{\mathbf{r}} = (\omega_x x, \omega_y y, \omega_z z)$ . This makes the integrand isotropic and allows one to again use Eq. (2.9), which gives

$$n(\mathbf{p}) = \mp \frac{1}{(m\bar{\omega})^3} \frac{1}{\lambda_{\text{dB}}^3} g_{3/2} \left( \mp \tilde{z} e^{\frac{-p^2}{2mk_{\text{B}}T}} \right). \quad (2.16)$$

Obviously, the momentum distribution is isotropic, whereas the symmetry of the intratrap density distribution depends on the actual trapping potential.

### 2.1.2. Fermionic quantum gases

In this section, I will briefly summarize some important aspects of the theory of fermionic quantum gases and provide equations that will be used in later chapters. More extensive discussions of the physics of Fermi gases can be found in a number of review articles, e.g. [161–164].

#### 2.1.2.1. The Fermi energy

In a system of identical fermions, any state can be occupied by at most one particle, as already explained above, and for large atom number  $N$ , the approximation  $N \approx N_{\text{ex}}$  can

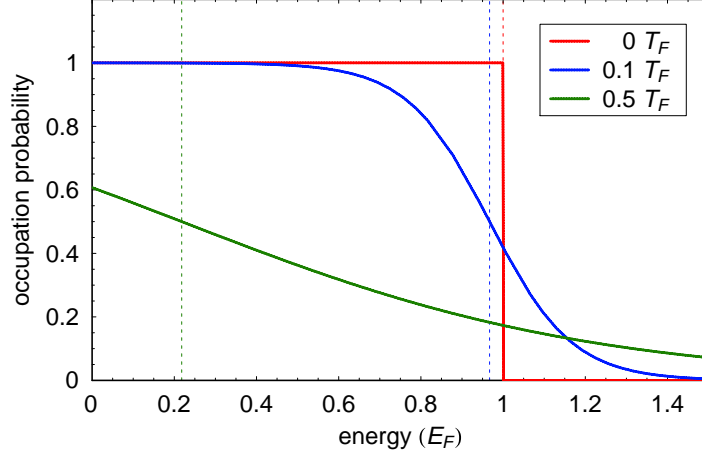


**Figure 2.3:** Fermi-Dirac statistics. The occupation probability is shown as a function of the single-particle energy for a fixed atom number at three different temperatures,  $T = 0$ ,  $T = 0.1 T_F$ , and  $T = 0.5 T_F$  (thick lines). The dashed vertical lines indicate the corresponding chemical potentials.

be used. In the limit  $T \rightarrow 0$ , the absolute value of the exponential in the Fermi-Dirac distribution function

$$f_{\text{FD}}(\epsilon) = \frac{1}{e^{\beta(\epsilon-\mu)} + 1} \quad (2.17)$$

is very large and positive for  $\epsilon > \mu(T \rightarrow 0)$  and close to zero for  $\epsilon < \mu(T \rightarrow 0)$ . At zero temperature, the energy distribution  $f_{\text{FD}}(\epsilon)$  is therefore 1 for energies  $\epsilon$  below the Fermi energy  $E_F = \mu(T \rightarrow 0, N)$  and 0 above. The temperature  $T_F = E_F/k_B$  corresponding to the Fermi energy is called the Fermi temperature. For increasing temperature, the step in  $f_{\text{FD}}(\epsilon)$  is gradually smeared out with a width on the order of  $E_F \cdot T/T_F$  as shown in Fig. 2.3. For  $T \gg T_F$ , the occupation probability  $f_{\text{FD}}(\epsilon) \ll 1$  for all energy levels so that the indistinguishability of the particles is unimportant and the gas behaves like a classical Maxwell-Boltzmann gas. The Fermi temperature therefore sets the scale for the onset of quantum behavior in a fermionic gas. However, it should be stressed that there is no phase transition in a non-interacting Fermi gas.

A particularly simple and useful expression for the Fermi energy in a harmonic potential is obtained by evaluating Eq. (2.5) for  $T = 0$ . Using  $f_{\text{FD}}(\epsilon, T=0) = \Theta(E_F - \epsilon)$  (where  $\Theta$  is the Heaviside step function) in Eq. (2.4) we obtain

$$N = \int_0^\infty f(\epsilon) g(\epsilon) d\epsilon = \int_0^{E_F} g(\epsilon) d\epsilon = \frac{E_F^3}{6(\hbar\bar{\omega})^3} \quad (2.18)$$

and thus

$$E_F = \hbar\bar{\omega} (6N)^{1/3}. \quad (2.19)$$

The combination of this equation with Eq. (2.6) then gives the universal relation

$$\frac{T}{T_F} = \left[ \frac{-1}{6 g_3(-\tilde{z})} \right]^{1/3}, \quad (2.20)$$

which is very useful for thermometry of fermionic gases.

### 2.1.2.2. Intratrap density distribution

The density distribution of an ideal spin-polarized fermionic gas in an arbitrary potential  $V(\mathbf{r})$  at finite temperature was already given in Eq. (2.14). The assumption of an *ideal* gas is a very good approximation for most experimental situations treated in this work because interactions between identical fermionic atoms are strongly suppressed at low temperatures. This is a consequence of the fermionic quantum statistics and will be discussed in more detail in Sec. 2.2.1.1.

In addition to the general case treated above, it is instructive to briefly consider the Fermi gas at  $T = 0$ . In this case, all energy states up to the Fermi energy are filled and the phase space density is  $\tilde{\rho}(\mathbf{r}, \mathbf{p}) = \frac{1}{h^3}$  for  $p^2/2m + V(\mathbf{r}) \leq E_F$  and zero otherwise. Integration over momentum space is trivial and gives the density distribution

$$n_{\text{FD}}(\mathbf{r}, T = 0) = \frac{(2m)^{3/2}}{6\pi^2\hbar^3} [E_F - V(\mathbf{r})]^{3/2} \quad (2.21)$$

$$= \frac{8N}{\pi^2 R_x R_y R_z} \left[ 1 - \left( \frac{x^2}{R_x^2} + \frac{y^2}{R_y^2} + \frac{z^2}{R_z^2} \right) \right]^{3/2}, \quad (2.22)$$

for positions  $\mathbf{r}$  where  $E_F > V(\mathbf{r})$  and 0 otherwise. The second line of the equation is valid for the harmonic potential. The Fermi radius

$$R_i = \sqrt{\frac{2E_F}{m\omega_i^2}} \quad (2.23)$$

corresponds to the size of the fermionic cloud in the direction  $i \in x, y, z$ . The non-zero size of the fermionic cloud at  $T = 0$  is a result of the Fermi pressure, which itself is a direct consequence of the Pauli exclusion principle. Figure 2.4 shows the density distribution of a fermionic gas for the  $T = 0$  limit and for two different finite temperatures.

### 2.1.2.3. Free expansion of the ideal Fermi gas

In the experiment, atomic clouds are often detected after ballistic expansion following a sudden switch-off of the trap. In the limit of long expansion time, this allows one in principle to directly measure the initial momentum distribution since it is converted into a spatial density distribution by the ballistic expansion. For intermediate expansion times, however, the initial density distribution has to be taken into account. In the semiclassical approximation, the density distribution after an arbitrary time of flight is given by

$$n_{\text{FD,tof}}(\mathbf{r}, t) = \int \int \tilde{\rho}(\mathbf{r}_0, \mathbf{p}) \delta^3\left(\mathbf{r} - \mathbf{r}_0 - \frac{\mathbf{p}t}{m}\right) d^3\mathbf{r}_0 d^3\mathbf{p}. \quad (2.24)$$

This integral can be analytically solved for the harmonic potential 2.2 using suitable substitutions and relation (2.9):

$$n_{\text{FD,tof}}(\mathbf{r}, t) = -\frac{\prod_i \eta_i(t)}{\lambda_{\text{dB}}^3} g_{3/2}\left(-\tilde{z} e^{-\frac{m}{2k_B T} \sum_i [\omega_i r_i \eta_i(t)]^2}\right) \quad (2.25)$$

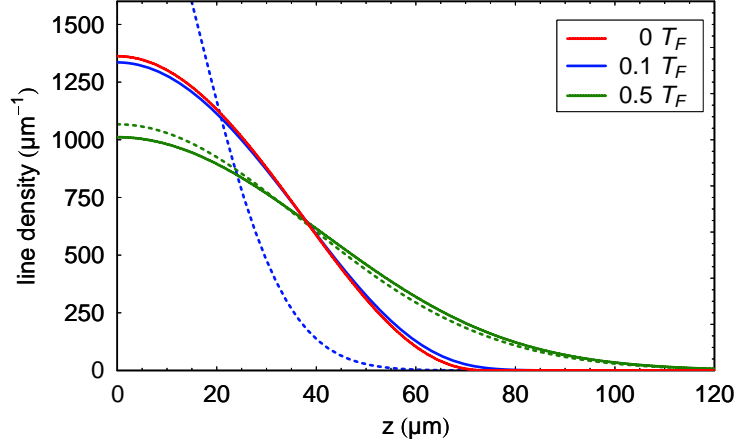


**Figure 2.4:** Density distribution of a harmonically trapped Fermi gas. The density distribution was integrated along the  $x$ - and  $y$ -axes to obtain the line densities depicted in the graph. The solid lines show Fermi-Dirac density distributions for  $T = 0$ ,  $T = 0.1 T_F$ , and  $T = 0.5 T_F$ . The dashed lines represent corresponding classical density distributions.

where

$$\eta_i(t) = [1 + \omega_i^2 t^2]^{-1/2}. \quad (2.26)$$

Thus, the effect of the free expansion from a harmonic trap is simply a rescaling of the coordinates. This remarkable result has also been derived in a fully quantum-mechanical treatment [165].

### 2.1.3. Bosonic quantum gases

In this section, I describe the properties of bosonic quantum gases that are most relevant for the work presented in this thesis. More detailed information can be found in numerous review articles, see e.g. [27, 28, 166].

#### 2.1.3.1. Density distribution of an uncondensed gas

The intratrap density and momentum distributions of an ideal Bose gas are given in Eq.(2.14) and Eq.(2.16), respectively. In contrast to Fermi gases, spin-polarized Bose gases *do* interact also at very low temperatures since the total wave function is symmetric and therefore s-wave scattering is allowed. However, above the phase transition to BEC, the density of the gas for typical experimental conditions is comparably low so that effects of the interaction can usually be neglected. Similarly to Eq. (2.25), the density distribution after release from the harmonic potential Eq. (2.2) and a subsequent time of flight  $t$  is then given by

$$n_{\text{FD,tof}}(\mathbf{r}, t) = + \frac{\prod_i \eta_i(t)}{\lambda_{\text{dB}}^3} g_{3/2} \left( + \tilde{z} e^{-\frac{m}{2k_B T} \sum_i [\omega_i r_i \eta_i(t)]^2} \right). \quad (2.27)$$

This density distribution is also a good approximation for the thermal component in a partially condensed cloud, except in the overlap region with the condensate since the density

in the BEC can be so high that the interaction can significantly distort the thermal density distribution.

### 2.1.3.2. Bose-Einstein condensation

For a system of bosons, the fugacity is limited to values smaller or equal to 1. This follows directly from its definition (Eq. (2.7)), from the requirement that the occupation number  $f(\epsilon_r)$  is non-negative, and from the choice  $\epsilon_0 = 0$ . Consequently, the total number of atoms in the excited states of a harmonic potential (Eq. (2.6)) is limited by

$$N_{\text{ex}}^{(\text{max})} = \left( \frac{k_{\text{B}}T}{\hbar\bar{\omega}} \right)^3 g_3(\tilde{z} = 1). \quad (2.28)$$

Thus, if the total number of atoms  $N$  exceeds  $N_{\text{ex}}^{(\text{max})}$ , the remaining

$$N_0 = N - N_{\text{ex}}^{(\text{max})} \quad (2.29)$$

atoms must occupy the ground state. This macroscopic occupation of the ground state is known as Bose-Einstein condensation. The atoms in the ground state are referred to as the Bose-Einstein condensate and the remaining atoms belong to the so-called thermal cloud.

The critical temperature for Bose-Einstein condensation of  $N$  identical, non-interacting bosons trapped in a harmonic potential follows from Eq. (2.28):

$$T_{\text{c}} = \frac{\hbar\bar{\omega}}{k_{\text{B}}} \left[ \frac{N}{g_3(1)} \right]^{1/3}. \quad (2.30)$$

It corresponds to a peak phase space density of

$$n_0 \lambda_{\text{dB}}^3 = g_{3/2}(1) \approx 2.612, \quad (2.31)$$

which is also the critical phase space density for BEC in a homogeneous gas. The fraction of particles in the ground state increases with decreasing temperature. For  $T < T_{\text{c}}$  it is given by

$$\frac{N_0}{N} = 1 - \left( \frac{T}{T_{\text{c}}} \right)^3. \quad (2.32)$$

The wave function of the non-interacting condensate is a product of  $N_0$  identical single particle ground state wave functions.

The formulae above are strictly true only for an ideal Bose gas in the thermodynamic limit, which is never reached exactly in real experiments. However, corrections due to the effects of interaction, the finite atom number, and the discreteness of the energy levels are small for typical experimental conditions (see Sec. II.C in [27], Sec. 5.2.1 in [166], and references therein). Finally, note that for temperatures below the temperature corresponding to the energy level splitting  $T_{\bar{\omega}} = \hbar\bar{\omega}/k_{\text{B}}$ , the ground state would be macroscopically occupied even in a classical gas. However, the critical temperature  $T_{\text{c}}$  for Bose-Einstein condensation can be much higher than  $T_{\bar{\omega}}$ , which shows that BEC is a non-classical phenomenon.

### 2.1.3.3. The weakly interacting Bose gas

Although Bose-Einstein condensates produced in cold atom experiments are dilute gases, the density in the condensate is typically sufficiently high that the elastic interaction between the atoms plays a role and strongly influences the static and dynamic properties of the condensate. However, these properties are very well described in a mean-field approach by the Gross-Pitaevskii equation (GPE) for the expectation value  $\Psi(\mathbf{r}, t) = \langle \hat{\Psi}(\mathbf{r}, t) \rangle$  of the field operator  $\hat{\Psi}(\mathbf{r}, t)$  that annihilates a boson at position  $\mathbf{r}$  at time  $t$ . This approach is discussed in detail e.g. in Ref. [27].  $\Psi(\mathbf{r}, t)$  has the meaning of an order parameter and is also called the “macroscopic condensate wave function”, since the density of the condensate is fixed by  $n_c(\mathbf{r}, t) = |\Psi(\mathbf{r}, t)|^2$ .

In a dilute gas at low temperature, only binary collisions are relevant and interactions can be described by a single parameter, the s-wave scattering length  $a$ . The interatomic interaction potential  $V(\mathbf{r}_1 - \mathbf{r}_2)$  can then be replaced by a pseudo potential  $V(\mathbf{r})\Psi(\mathbf{r}) = g \delta^{(3)}(\mathbf{r}) \frac{\partial}{\partial r}(r\Psi(\mathbf{r}))$  [146, 167] with the coupling constant

$$g = \frac{4\pi\hbar^2 a}{m}. \quad (2.33)$$

The interaction is attractive for negative values of the scattering length and repulsive for positive ones. It can be experimentally controlled in value and in sign with a static external magnetic field by making use of Feshbach resonances [47, 48, 168]. At the small values of the bias field used in this work, however, the scattering length for  $^{87}\text{Rb}$  is always positive so that we will restrict ourselves to this case in the following.

With the definitions made above and with the approximations mentioned, the Gross-Pitaevskii equation for a BEC in an external potential  $V(\mathbf{r}, t)$  reads:

$$i\hbar\partial_t\Psi(\mathbf{r}, t) = \left( -\frac{\hbar^2\nabla^2}{2m} + V(\mathbf{r}, t) + g|\Psi(\mathbf{r}, t)|^2 \right) \Psi(\mathbf{r}, t), \quad (2.34)$$

where the wave function is normalized by the atom number,  $\int |\Psi|^2 d\mathbf{r} = N_0$ . The GPE is based on a number of approximations but can safely be used for large, weakly interacting condensates ( $N_0 \gg 1$  and  $n_c|a|^3 \ll 1$ ) at small temperatures ( $T \ll T_c$ ).

**Stationary ground state** The stationary ground state wave function of a weakly interacting condensate is no longer given by the product of  $N_0$  identical single particle ground state wave functions but contains contributions from excited states. For a time-independent potential, it can be calculated by solving the stationary GPE

$$\mu\Psi(\mathbf{r}) = \left( -\frac{\hbar^2\nabla^2}{2m} + V(\mathbf{r}) + g|\Psi(\mathbf{r})|^2 \right) \Psi(\mathbf{r}), \quad (2.35)$$

which is obtained from Eq. (2.34) using the ansatz  $\Psi(\mathbf{r}, t) = \Psi(\mathbf{r}) e^{-\frac{i}{\hbar}\mu t}$ . The parameter  $\mu$  is identified as the chemical potential [28]. In the case that  $n_c g \gg \hbar\omega_{x,y,z}$ , the term for the kinetic energy in Eq. (2.35) can be neglected. In this so-called Thomas-Fermi approximation, the density is given by

$$n_c(\mathbf{r}) = \max \left[ \frac{\mu - V(\mathbf{r})}{g}, 0 \right]. \quad (2.36)$$

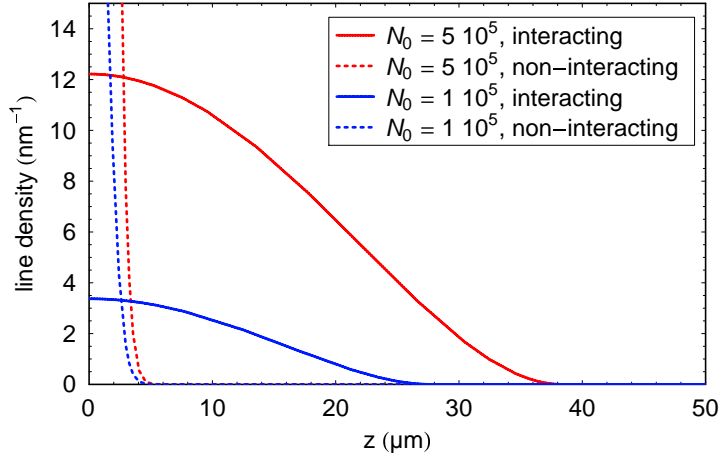


**Figure 2.5:** Line density distribution of a harmonically trapped Bose-Einstein condensate. The solid lines show the calculated density distributions of  $^{87}\text{Rb}$  BECs with  $5 \times 10^5$  (red) and  $1 \times 10^5$  (blue) atoms, respectively, in our magnetic trap, taking the effects of interaction into account. The dashed lines represent the corresponding distributions for the non-interacting case.

Hence, in a harmonic potential, the condensate has a parabolic density distribution with the Thomas-Fermi radii

$$R_i^{(\text{TF})} = \sqrt{\frac{2\mu}{m\omega_i^2}}, \quad (2.37)$$

where  $i = (x, y, z)$ . From the normalization condition, the chemical potential in this case is calculated to be

$$\mu = \frac{1}{2} (15^2 m a^2 \hbar^4 \bar{\omega}^6)^{1/5} N_0^{2/5}. \quad (2.38)$$

This equation can be plugged into Eq. (2.37) to find the relation

$$N_0 = \frac{m^2}{15 a \hbar^2 \bar{\omega}^3} (\omega_i R_{\text{TF},i})^5 \quad (2.39)$$

between the atom number in the condensate and the Thomas-Fermi radius. The density distribution of a weakly interacting BEC in the Thomas-Fermi approximation is plotted in Fig. 2.5 for two different atom numbers. For comparison, the figure also shows the corresponding density distributions for the case of vanishing interaction.

The ground state wave function of Eq. (2.35) can be calculated exactly by numerically minimizing the energy functional corresponding to Eq. (2.35), e.g. with a steepest descent method [169].

**Free expansion** It has been shown that when such a condensate is released from a cylinder-symmetrical, cigar-shaped harmonic trap, its density distribution evolves according to a

rescaling of its parabolic shape [170–172]:

$$R_\rho^{(\text{TF})}(t) = R_\rho^{(\text{TF})}(0)\sqrt{1 + \tau^2} \quad (2.40)$$

$$R_z^{(\text{TF})}(t) = \lambda R_\rho^{(\text{TF})}(0) \left[ 1 + \lambda^{-2} \left( \tau \arctan \tau - \ln \sqrt{1 + \tau^2} \right) \right], \quad (2.41)$$

where  $\lambda = \omega_\rho/\omega_z$  is the ratio of the radial and longitudinal trapping frequencies and  $\tau = \omega_\rho t$  the scaled time of flight. The expansion of the condensate is anisotropic in contrast to a thermal cloud. First, the cloud expands mainly in the radial direction as the interaction energy is converted to kinetic energy. After a subsequent intermediate expansion stage, the aspect ratio finally approaches the constant value  $R_\rho^{(\text{TF})}/R_z^{(\text{TF})} = 2\lambda^2/\pi$ . This expansion from a cigar-shaped cloud to a pancake-shaped cloud is one characteristic signature of a Bose-Einstein condensate.

#### 2.1.4. The classical, ideal gas

In the classical limit,  $\tilde{z} \rightarrow 0$ , the density and momentum distributions derived from Eq. (2.13) are those of a Maxwell-Boltzmann gas. In the case of a harmonic potential, Eqs. (2.14), (2.16) then reduce to the following Gaussian density and momentum distributions:

$$n(\mathbf{r}) = \left( \frac{2}{\pi} \right)^{3/2} \frac{N}{\sigma_x \sigma_y \sigma_z} e^{-\sum_i \frac{2x_i^2}{\sigma_i^2}} \quad (2.42)$$

$$n(\mathbf{p}) = \left( \frac{2}{\pi} \right)^{3/2} \frac{N}{\kappa^3} e^{-\sum_i \frac{2p_i^2}{\kappa^2}} \quad (2.43)$$

where  $\sigma_i = [4k_B T/m\omega_i^2]^{1/2}$  and  $\kappa = [4k_B T m]^{1/2}$  are the respective  $1/e^2$  waists of the distributions. In order to obtain this result, the property  $\lim_{s \rightarrow 0} g_n(s) = s$  was used in Eqs. (2.6), (2.14), and (2.16). In a ballistic expansion, the momentum distribution stays unaffected and the evolution of the spatial density distribution is given by a rescaling of the waists according to  $\sigma_i(t) = \sigma_i \eta_i(t)$  with  $\eta_i(t)$  defined in Eq. (2.26).

## 2.2. Evaporative and sympathetic cooling

Evaporative cooling is one of the key experimental techniques for achieving ultralow temperatures in dilute atomic gases. So far, only evaporative cooling of precooled atomic clouds has allowed to reach the quantum-degenerate regime in these systems. Evaporative and sympathetic cooling rely on redistribution of energy between different atoms by elastic collisions. This section therefore starts with a brief review of collision physics in ultracold gases. The subsequent main parts will then treat the principles and limitations of evaporative and sympathetic cooling.

### 2.2.1. Collisions

Collisions between particles can be either elastic or inelastic. Elastic collisions play a crucial role for the cooling process and for the static and dynamic properties of ultracold gases.

In the following, the concept of partial waves, which provides an elegant and very useful way to treat elastic collisions in the low-temperature limit, will be introduced. Inelastic collision processes, on the other hand, are usually unwanted since they lead to heating and particle loss in trapped atomic samples. The physical origin of inelastic collisions and the corresponding selection rules will be briefly reviewed. The selection rules have important consequences for the choice of atomic states in multi-species mixtures as will be discussed in Sec. 5.3. The reader interested in more details of scattering theory is referred to the literature [145, 149, 167, 173].

### 2.2.1.1. Elastic collisions

The problem of elastic scattering between two distinguishable particles of masses  $m_1$  and  $m_2$  can be separated into center-of-mass and relative coordinates. The center-of-mass motion is conserved. The relative motion of the two particles is equivalent to the scattering of one particle with reduced mass  $m_{\text{red}} = m_1 m_2 / (m_1 + m_2)$  off the interatomic interaction potential  $V_{\text{sc}}(\mathbf{r})$ .

In an elastic collision the energy is conserved and the scattering problem is usually formulated in a time-independent form by considering the energy eigenstates of the corresponding stationary Schrödinger equation

$$\left[ -\frac{\hbar^2 \nabla^2}{2m_{\text{red}}} + V_{\text{sc}}(\mathbf{r}) \right] \Psi_{\mathbf{k}}(\mathbf{r}) = E \Psi_{\mathbf{k}}(\mathbf{r}). \quad (2.44)$$

One is interested in solutions of Eq. (2.44) with the asymptotic form

$$\Psi_{\mathbf{k}}(\mathbf{r}) = C \left( e^{i\mathbf{k}\mathbf{r}} + f(k, \theta, \phi) \frac{e^{ikr}}{r} \right) \quad \text{for } r \rightarrow \infty \quad (2.45)$$

for distances  $|\mathbf{r}|$  much larger than the range of the interaction potential. Here,  $r$ ,  $\theta$ ,  $\phi$  are spherical coordinates and  $C$  is a normalization constant. The first part of the asymptotic wave function corresponds to an incoming plane wave with wave vector  $\mathbf{k}$  and energy  $E = \hbar^2 k^2 / (2m_{\text{red}})$ . The second part is generated by the scattering process and falls off radially like a spherical wave. The factor  $f(k, \theta, \phi)$  is called the scattering amplitude and connects the wave function with the measurable quantities, the differential and total scattering cross sections,

$$\frac{d\sigma}{d\Omega} = |f(k, \theta, \phi)|^2 \quad \text{and} \quad \sigma(k) = \int_{\Omega} |f(k, \theta, \phi)|^2 d\Omega \quad (2.46)$$

where  $d\Omega = \sin(\theta) d\theta d\phi$  denotes the differential solid angle. It should be noted that for most potentials the scattering problem cannot be solved analytically.

In the case of a spherically symmetric scattering potential  $V_{\text{sc}}(r)$ , however, the problem can be simplified by switching to an angular momentum basis, i.e. by expanding  $\Psi_{\mathbf{k}}(r, \theta, \phi)$  in terms of spherical harmonics  $Y_{l,m_l}(\theta, \phi)$  where  $l$  labels the angular momentum and  $m_l$  its projection onto the  $z$ -axis:

$$\Psi_{\mathbf{k}}(r, \theta, \phi) = \sum_{l,m_l} \frac{u_{k,l,m_l}(r)}{r} Y_{l,m_l}(\theta, \phi) \quad (2.47)$$

The contributions with angular momentum quantum numbers  $l = 0, 1, 2$  are named  $s$ -,  $p$ -, and  $d$ -waves, respectively. If the  $z$ -axis is chosen collinear with  $\mathbf{k}$ , then the problem is independent of the azimuthal angle  $\phi$  and only terms with  $m_l = 0$  contribute to Eq. (2.47). With this expansion, the scattering problem reduces to the solution of the corresponding radial Schrödinger equation

$$\left[ -\frac{\hbar^2}{2m_{\text{red}}} \frac{d^2}{dr^2} + \frac{\hbar^2 l(l+1)}{2m_{\text{red}} r^2} + V_{\text{sc}}(r) \right] u_{k,l}(r) = E u_{k,l}(r) \quad (2.48)$$

where the centrifugal potential appears in addition to the scattering potential  $V_{\text{sc}}(r)$ . The Schrödinger equation can be solved numerically, if  $V_{\text{sc}}(r)$  is known. Using standard angular momentum algebra and Eq. (2.45), the asymptotic radial wave function can be written in the form

$$u_{k,l}(r) \propto \left( (-1)^{l+1} e^{-ikr} + e^{2i\delta_l} e^{ikr} \right) \quad (2.49)$$

where the phase shifts  $\delta_l$  (defined modulo  $\pi$ ) are introduced. The effect of the potential thus simply consists in a dephasing between incoming and outgoing partial waves. Finally, once the scattering phases are calculated, the scattering amplitude is obtained from the relation [167]

$$f(k, \theta) = \frac{1}{2ik} \sum_{l=0}^{\infty} (2l+1) P_l(\cos \theta) \left( e^{2i\delta_l(k)} - 1 \right) \quad (2.50)$$

where  $P_l$  are Legendre polynomials. The total scattering cross section is obtained by inserting Eq. (2.50) into Eq. (2.46). Using the orthogonality relation of the Legendre polynomials one finds that the total scattering cross section is given as a sum over the partial wave contributions [149]

$$\sigma(k) = \sum_{l=0}^{\infty} \sigma_l(k) = \frac{4\pi}{k^2} \sum_{l=0}^{\infty} (2l+1) \sin^2(\delta_l). \quad (2.51)$$

Note that the contribution of each partial cross section to the total scattering cross section has a maximum of  $\sigma_{l,\text{max}} = 4\pi(2l+1)/k^2$ , which is called the unitarity limit.

### 2.2.1.2. Low-energy, elastic collisions

The centrifugal barrier that appears in Eq. (2.48) has a very important consequence: If the collision energy is much lower than the height of the barrier, the scattering partial wave function only probes the slowly varying and weak outer part of the scattering potential and therefore experiences no significant phase shift. Scattering of partial waves with  $l \geq 1$  is therefore suppressed for sufficiently low energies. More precisely, one finds for the scattering phase  $\delta_l$  (modulo  $\pi$ ) that [152]

$$\delta_l \propto k^{2l+1} \quad \text{for } k \rightarrow 0. \quad (2.52)$$

The contribution to the total scattering cross section thus scales as

$$\sigma_l = \frac{4\pi}{k^2} (2l+1) \sin^2(\delta_l) \propto k^{4l} \propto E^{2l} \quad \text{for } k \rightarrow 0. \quad (2.53)$$

This result is known as the Wigner threshold law [174].

For collision energies much smaller than the height of the p-wave centrifugal barrier, only s-waves contribute to the scattering process. The effect of the scattering potential can then be described by one single parameter, the s-wave scattering length  $a$ , which is defined by

$$a = - \lim_{k \rightarrow 0} \frac{\tan \delta_0(k)}{k}. \quad (2.54)$$

For distinguishable particles, the total scattering cross section is connected to the scattering length by

$$\lim_{k \rightarrow 0} \sigma_{l=0}(k) = 4\pi a^2 \quad (\text{distinguishable particles}) \quad (2.55)$$

For identical particles, the two scattering processes corresponding to  $f(k, \theta)$  and  $f(k, \pi - \theta)$  are indistinguishable. Therefore, the scattering state must be properly (anti-) symmetrized. For bosons, the interference between the two terms doubles the contribution of partial waves with even  $l$  to the total scattering cross section and cancels it for odd  $l$ . For fermions, contributions cancel for even  $l$  and double for odd  $l$ . The total scattering cross sections in the s-wave limit are therefore

$$\lim_{k \rightarrow 0} \sigma_{l=0}(k) = 8\pi a^2 \quad (\text{identical bosons}) \quad (2.56)$$

$$\lim_{k \rightarrow 0} \sigma_{l=0}(k) = 0 \quad (\text{identical fermions}) \quad (2.57)$$

for scattering between two identical bosons or between two identical fermions. A very important consequence of this result is that, at low temperature, a polarized, one-component gas of fermionic atoms is well described as an ideal quantum gas since s-wave interactions are absent and contributions from higher order partial waves ( $l = 1, 3, \dots$ ) are strongly suppressed. This makes evaporative cooling for such a fermionic gas inefficient, a difficulty that is overcome in our experiment by using sympathetic cooling for the fermionic species.

In order to estimate the height of the centrifugal barrier for neutral atoms interacting via a realistic potential, we consider the long-range part of the interaction potential, which is typically well approximated by the van der Waals interaction  $V_{\text{vdW}} = -C_6/r^6$ . The coefficient  $C_6$  describes the strength of interaction and can be found in the literature (see e.g. [175, 176] and references therein) for many species of interest. An estimate for the height  $E_{\text{th}}(l)$  of the centrifugal barrier is then obtained by evaluating the effective potential in Eq. (2.48) consisting of the sum of the centrifugal term and of the interaction potential at its local maximum at  $r > 0$ . This yields:

$$E_{\text{th}}(l) = 2 \left[ \frac{\hbar^2 l(l+1)}{6 m_{\text{red}}} \right]^{3/2} C_6^{-1/2}. \quad (2.58)$$

For the fermionic species used in our experiment, we obtain threshold energies  $E_{\text{th,p}}^{\text{Li,Li}} = 8 \text{mK} \times k_{\text{B}}$  for  ${}^6\text{Li}$ - ${}^6\text{Li}$  p-wave collisions and  $E_{\text{th,p}}^{\text{K,K}} = 280 \mu\text{K} \times k_{\text{B}}$  for  ${}^{40}\text{K}$ - ${}^{40}\text{K}$  p-wave collisions. In a gas of identical  ${}^{87}\text{Rb}$  atoms, p-wave collisions are forbidden and the estimate for the threshold energy for d-wave collisions yields  $E_{\text{th,d}}^{\text{Rb,Rb}} = 430 \mu\text{K} \times k_{\text{B}}$ .

### 2.2.1.3. Inelastic collisions

In the discussion of atomic scattering so far, we have neglected the internal degrees of freedom of the atoms. However, the internal states of two colliding atoms may be changed in the scattering process by the interatomic interaction. These collisions can result in atom loss from the trap and in heating of the trapped sample due to internal energy of the atoms being converted into external energy. This section introduces the different interaction mechanisms between two ground-state alkali atoms and gives the corresponding selection rules for state-changing collisions. More extensive discussions on this subject can be found in the literature, e.g. in [177, 178].

The interaction Hamiltonian of two ground-state alkali atoms can be written to good approximation as [179]

$$V = V_{\text{ex}} + V_{\text{disp}} + V_{\text{hf}} + V_{\text{Zeeman}} + V_{\text{dipole}}, \quad (2.59)$$

where  $V_{\text{ex}}$  denotes the electronic exchange interaction,  $V_{\text{disp}}$  is the dispersion interaction,  $V_{\text{hf}}$  is the hyperfine interaction of each atom, and  $V_{\text{Zeeman}}$  denotes the interaction of the two atoms with an external magnetic field.  $V_{\text{dipole}}$  is a dipole-dipole interaction term describing the magnetic dipole interaction of the atoms and a second order effect in the electronic spin-orbit coupling [180]. At large interatomic distance  $r$ , the atomic states are specified by the hyperfine quantum numbers  $|f_1, m_{f_1}\rangle$  and  $|f_2, m_{f_2}\rangle$  of the two colliding ground-state alkali atoms. Together with  $l, m_l, E$  they represent a complete set of quantum numbers. The total molecular spin is defined by  $\mathbf{F} = \mathbf{f}_1 + \mathbf{f}_2$  with corresponding quantum numbers  $F, M_F$ . At small interatomic distance, however, the exchange interaction dominates the interaction Hamiltonian. The electron spins  $\mathbf{s}_i$  are coupled to the total electron spin  $\mathbf{S} = \mathbf{s}_1 + \mathbf{s}_2$  with the corresponding quantum number  $S = 0, 1$  so that  $f_i, m_{f_i}$  are not good quantum numbers at this short distance.

The interaction Hamiltonian Eq. (2.59) is typically dominated by the first four terms. The state-changing collisions resulting from this part of the Hamiltonian are called spin-exchange collisions. They are typically the fastest state-changing collisions, unless they are forbidden or energetically suppressed. In order to discuss this process, let's consider two atoms entering the collision in pure hyperfine states  $|f_1, m_{f_1}\rangle$  and  $|f_2, m_{f_2}\rangle$  (entrance channel). These states are in general linear combinations of singlet ( $S = 0$ ) and triplet ( $S = 1$ ) states. Since the phase shifts that these two components accumulate during the scattering process in the corresponding singlet and triplet potentials are generally different, they do not reconstruct the original hyperfine states after the collision but usually result in changed superpositions of hyperfine states (exit channel). The scattering process thus leads to a mixing of different atomic states. The selection rules for these spin-exchange collisions are [47]

$$\Delta l = 0 \quad (2.60)$$

$$\Delta m_l = 0 \quad (2.61)$$

$$\Delta M_F = 0 \quad (2.62)$$

where  $m_l$  denotes the projection quantum number of the relative angular momentum  $\mathbf{l}$  of the two atoms. In the case of zero magnetic field even  $\mathbf{l}$  and  $\mathbf{F}$  are conserved so that much

less collision channels couple. In addition to these selection rules, transitions only occur if they are energetically allowed, i.e. if they are exothermal or if the thermal energy of the atoms is sufficiently high to overcome the energy difference in an endothermal transition. We will come back to this point, when discussing the actual three-species state mixture used in our experiment.

In the preceding discussion of spin-exchange collisions, we have neglected the dipole-dipole interaction term  $V_{\text{dipole}}$  in Eq. (2.59). For most experimental situations, this is a good approximation. In the case, however, that spin-exchange collisions are forbidden or suppressed, also this usually much weaker coupling can become important. Due to its nature, the dipole-dipole interaction can convert spin angular momentum into orbital angular momentum (and vice versa), a process called dipolar relaxation [180–182]. The selection rules for dipolar relaxation are the following [47]:

$$\Delta l = 0, \pm 2 \quad (\text{not } l=0 \rightarrow l=0) \quad (2.63)$$

$$\Delta(m_l + M_F) = 0 \quad (2.64)$$

$$0 < |\Delta M_F| \leq 2. \quad (2.65)$$

In the absence of a magnetic field, also the total angular momentum  $\mathbf{l} + \mathbf{F}$  is conserved since the Hamiltonian Eq. (2.59) only creates internal forces in this case.

So far, we have only considered binary collisions. At high atomic densities or for strong interaction, however, also inelastic losses due to three-body recombination may become important (see [53, 182–185]). In such a collision event of three atoms, two of the atoms form a molecule; the third one is necessary for conservation of momentum and energy. The binding energy of the molecule is transformed into relative kinetic energy of the collision partners. This process usually leads to loss of the molecule as well as of the third atom from the trap. An exception is three-body recombination in a two-component gas of fermionic atoms on the BEC-side close to the pole of a Feshbach resonance: In this case, very weakly bound molecules are formed. Since relaxation to deeply bound molecular states is suppressed due to the Pauli principle [113], only a very small energy is released in the process so that the molecule and the atom usually stay in the trap.

## 2.2.2. Evaporative cooling

Evaporative cooling is a very powerful technique to cool a dilute atomic gas to sub  $\mu\text{K}$  temperatures and high phase-space density. In 1995, roughly a decade after its first proposal [3, 186], evaporative cooling, combined with laser cooling, was the key to achieve Bose-Einstein condensation in atomic gases [6–8]. Reviews on evaporative cooling are available in [5, 187]. Details on the experimental realization of evaporative cooling will be given in Ch. 6.

### 2.2.2.1. Principle

Evaporative cooling of a trapped thermal cloud is based on selective removal of atoms from the trap with an energy above the mean energy per atom and subsequent thermalization of the cloud to a lower temperature by elastic collisions. In practice, all atoms

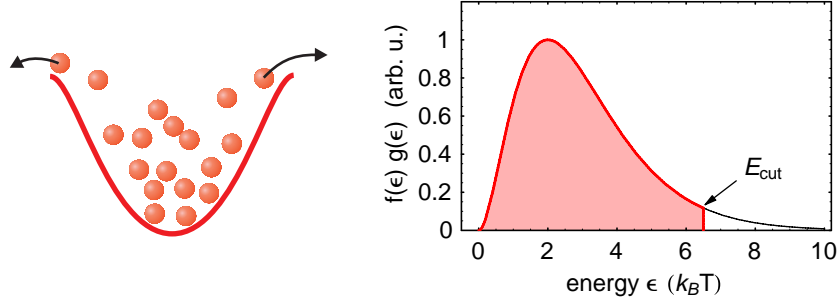


**Figure 2.6:** Principle of evaporative cooling. Atoms are confined in a conservative trap. Atoms in the high-energy tail of the energy distribution are removed from the trap by limiting the trap depth to the truncation energy  $E_{\text{cut}} = \eta k_B T$ . The remaining atoms rethermalize to a reduced temperature by elastic collisions. In the classical regime, the energy distribution of the ensemble is well approximated by a truncated Maxwell-Boltzmann distribution.

above a truncation energy  $\epsilon_t$  are removed, as illustrated in Fig. 2.6. In this case, a natural approach to describe the energy distribution of a non-degenerate gas is the truncated Maxwell-Boltzmann distribution

$$f(\epsilon) = \tilde{z} e^{-\frac{\epsilon}{k_B T}} \Theta(\epsilon_t - \epsilon) \quad (2.66)$$

with the quasi-fugacity  $\tilde{z}$  and the quasi-temperature  $T$ . Several descriptions of evaporative cooling have used Eq. (2.66) as a starting point [188–191]. This approach was later justified by a numerical solution of the Boltzmann equation [192] showing that the evaporation process rather accurately conserves a quasi-equilibrium energy distribution of this form. The following discussion is based on the corresponding model introduced by Walraven and co-workers in the same publication [187, 192] and discussed for alkali atoms by Ketterle and van Druten [5]. This model allows the description of evaporative cooling by scaling laws.

For constant truncation energy  $\epsilon_t$  (plain evaporation), elastic collisions between trapped atoms produce atoms with energy above  $\epsilon_t$ , which are evaporated from the trap. In this way, the mean energy per trapped particle is reduced and the gas cools. The characteristic evaporational decay time  $\tau_{\text{ev}}$  is given by [187]

$$\tau_{\text{ev}}^{-1} = -\frac{\dot{N}_{\text{ev}}}{N} = n_0 \bar{v} \sigma e^{-\eta} \frac{V_{\text{ev}}}{V_e} \quad (2.67)$$

with  $\bar{v} = (8k_B T / \pi m)^{1/2}$ , the truncation parameter  $\eta = \frac{\epsilon_t}{k_B T}$ , and a pseudo-density defined by  $n_0 = \tilde{z} / \lambda_{\text{dB}}^3$ . For identical bosons in the s-wave limit the scattering cross section is  $\sigma = 8\pi a^2$ . For a given potential, the volume factor  $V_{\text{ev}}/V_e$  depends on  $\eta$  and may be calculated exactly [187] but has values between 2 and 5 for typical experimental conditions. In a plain evaporation process, the truncation parameter  $\eta$  increases as the temperature of the gas decreases and evaporation is more than exponentially suppressed according to Eq. (2.67). The evaporation process can be sustained, however, by constantly decreasing the truncation energy (forced evaporation), e.g. in a way to keep  $\eta$  constant.

### 2.2.2.2. Scaling laws

Since evaporative cooling happens on an exponential scale [5], it is typically described in terms of slowly varying logarithmic derivatives. A key parameter of the cooling process is given by [5]

$$\alpha_{\text{ev}} = \frac{d(\ln T)}{d(\ln N)} = \frac{\dot{T}/T}{\dot{N}/N} \quad (2.68)$$

which expresses by how many orders of magnitude the temperature decreases per order of magnitude decrease in atom number. In a power law potential,  $V(\mathbf{r}) = \sum_{i=1}^3 b_i |x_i|^{1/\delta_i}$  (for details, see [155]), all relevant thermodynamic quantities scale as  $[N(t + \Delta t)/N(t)]^x$  during evaporative cooling, where  $x$  depends only on  $\delta = \sum \delta_i$  and the slowly varying parameter  $\alpha_{\text{ev}}(t)$  (see table I in [5]). An important quantity is the elastic collision rate  $\sigma n \bar{v} \propto n T^{1/2}$  which scales as [5]

$$\frac{d(\ln n \bar{v} \sigma)}{d(\ln N)} = 1 - \alpha_{\text{ev}} \left( \delta - \frac{1}{2} \right). \quad (2.69)$$

If  $\alpha_{\text{ev}} > \alpha_{\text{ev,crit}} = 1/(\delta - 1/2)$  in a trapping potential with  $\delta > 1/2$ , the elastic collision rate increases with decreasing atom number during the evaporation process (run-away evaporation), thus accelerating the evaporation. In a Ioffe-type trap,  $\alpha_{\text{ev,crit}}$  depends on temperature with values between 1/2 at high  $T$  and 1 at low temperature.

The efficiency of evaporative cooling is defined as the relative increase in phase-space density  $D = n \lambda_{\text{dB}}^3 \propto n T^{-3/2}$  per relative loss in atom number  $N$  [5]:

$$\chi = -\frac{d(\ln D)}{d(\ln N)} = \alpha_{\text{ev}} \left( \delta + \frac{3}{2} \right) - 1. \quad (2.70)$$

Hence, in a power-law trap with  $\delta > 1/2$ , evaporation in the run-away regime implies that also the phase space density increases with decreasing atom number. It was shown that the evaporation process is optimized globally by optimizing  $\chi$  at any moment [5]. In the absence of heating mechanisms and non-evaporative loss processes, the key parameter  $\alpha_{\text{ev}}$  depends only on the trapping potential and on  $\eta$ . In this situation,  $\alpha_{\text{ev}}$  and  $\chi$  increase without a limit with increasing  $\eta$ .

### 2.2.2.3. Loss processes

In real experiments, however, the value of  $\alpha_{\text{ev}}$  and  $\chi$  that can be achieved is limited by non-evaporative loss of particles. For alkali atoms, the dominant so-called ‘‘bad collision’’ processes, which lead to non-evaporative losses, are collisions with background gas atoms, dipolar relaxation and, at high density, three-body recombination. The ratio of atoms lost due to evaporation and atoms lost due to some i-body loss process is given by [193]

$$R_i = \frac{\dot{N}_{\text{ev}}}{(\dot{N}_{\text{loss}})_i} = \frac{1}{\lambda_i} \frac{V_{\text{ev}}}{V_{\text{e}}} e^{-\eta} \quad (2.71)$$

with the corresponding ‘‘ratio of good to bad collisions’’

$$\frac{1}{\lambda_i} = \frac{\tau_{\text{el}}^{-1}}{\tau_i^{-1}} = \frac{\bar{v} \sigma}{n_0^{i-2} G_i} \frac{V_{\text{ie}}}{V_{\text{e}}}. \quad (2.72)$$

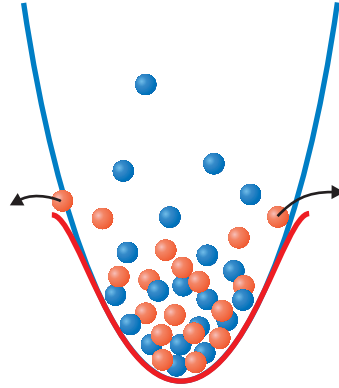


**Figure 2.7:** Principle of sympathetic cooling. Two types, A (red) and B (blue), of atoms are confined in a conservative trap. Type-A atoms are actively cooled, e.g. by evaporative cooling, whereas type-B atoms are sympathetically cooled by thermal contact with type-A atoms.

In this equation,  $V_e = N/n_0$  and  $V_{ie} = \int [n(\mathbf{r})/n_0]^i d\mathbf{r}$  with the pseudo-density  $n_0$  defined above. The rate constants  $G_i$  are defined by  $(\dot{N}_{\text{loss}})_i = -\int G_i n^i(\mathbf{r}) d\mathbf{r}$  and are the only atomic properties entering the model besides the scattering cross section  $\sigma$ . For known atomic parameters  $G_i$  (or, equivalently,  $\lambda_i$ ), the efficiency parameters  $\alpha_{\text{ev}}(\eta)$  and  $\chi(\eta)$  in the presence of loss processes can be calculated explicitly for any power-law trap (see, e.g. [194]). It is found that in typical traps the runaway regime can be achieved by optimal choice of  $\eta$  if  $1/\lambda_i$  is larger than  $\approx 10^2$ .

### 2.2.3. Sympathetic cooling

Elastic collisions are strongly suppressed in ultracold one-component fermionic quantum gases, as explained in Sec.2.2.1.1. Evaporative cooling is therefore very inefficient in a one-component Fermi gas. However, fermionic atom gases can be cooled into the quantum-degenerate regime by either direct evaporation of a two-component mixture, as first demonstrated in Boulder [10], or by sympathetic cooling with a buffer gas, a first realized in Paris [12]. In our experiment, we use sympathetic cooling of two fermionic species by a bosonic species to obtain a mixture of three quantum-degenerate gases.

#### 2.2.3.1. Principle

The idea of sympathetic cooling is to cool particles by bringing them into contact with a thermal bath that is actively cooled (see Fig.2.7). This principle was first proposed [63] and demonstrated [195, 196] for a mixture of different isotopes in an ion trap. Later it was applied to neutral atoms using cryogenically cooled helium as the thermal bath [197–199]. Sympathetic cooling in combination with evaporative cooling was first employed in [200], producing two overlapping Bose-Einstein condensates.

In trapped atomic gases, sympathetic cooling of a target gas relies on thermalization by elastic collisions with a colder buffer gas. In the following, we consider a mixture of two types of atoms, labeled 1 and 2, confined in a trap. We are interested in the average

scattering rate per type-1 atom of collisions with type-2 atoms, denoted  $\Gamma_{12}$ . In general, this quantity can only be calculated numerically. For a classical gas, i.e. at a phase space density well below the quantum-degenerate regime, however, the problem is simplified by the fact that the position and momentum distributions are uncorrelated in this case. Assuming energy-independent, isotropic collisions, the average collision rate is then given by [201]

$$\Gamma_{12} = \langle n_2 \rangle_1 \sigma_{12} \langle v_{12} \rangle_1. \quad (2.73)$$

Here,  $n_2$  is the density of type-2 atoms,  $\sigma_{12}$  is the elastic scattering cross section between type-1 and type-2 atoms, and  $v_{12} = |\mathbf{v}_1 - \mathbf{v}_2|$  is the relative collision speed. The brackets denote averaging over the distribution of type-1 atoms in position space

$$\langle n_2 \rangle_1 = \frac{1}{N_1} \int n_1(\mathbf{r}) n_2(\mathbf{r}) d\mathbf{r} \quad (2.74)$$

and in momentum space [202]

$$\langle v_{12} \rangle_1 = \left[ \frac{8k_B}{\pi} \left( \frac{T_1}{m_1} + \frac{T_2}{m_2} \right) \right]^{1/2}, \quad (2.75)$$

respectively, using the classical Maxwell-Boltzmann velocity distribution. In the case of sympathetic cooling, the two types of atoms are distinguishable and  $\sigma_{12} = 4\pi a_{12}^2$ , where  $a_{12}$  is the s-wave scattering length between type-1 and type-2 atoms.

The mean energy transfer per collision is given by [202]

$$\Delta E_{\text{coll}} = k_B \Delta T \xi \quad \text{with } \xi = \frac{4m_1 m_2}{(m_1 + m_2)^2} \quad (2.76)$$

where  $\Delta T = T_2 - T_1$  is the temperature difference between the two gases. The parameter  $\xi$  accounts for the reduction of the energy transfer per collision due to the mass difference of the collision partners. Its values for the possible collisions in our experiment are  $\xi_{\text{Li,Rb}} = 0.24$ ,  $\xi_{\text{K,Rb}} = 0.86$ , and  $\xi_{\text{Li,K}} = 0.45$ . Starting from the interspecies energy exchange rate  $N_1 \Gamma_{12} \Delta E_{\text{coll}}$ , using energy conservation, and assuming thermal equilibrium for each species separately, evolution equations for the temperatures are readily obtained. In an isolated system, the temperature difference decreases exponentially in time with a thermalization rate

$$\tau_{\text{therm}}^{-1} = N_1 \Gamma_{12} \xi \left( \frac{k_B}{C_1} + \frac{k_B}{C_2} \right) \quad (2.77)$$

where  $C_i$  is the heat capacity of gas  $i$ . The case where the temperature  $T_2$  is held constant by external cooling can be treated by assuming an infinite heat capacity  $C_2$ . In any case, the number of collisions per type-1 atom that is needed for thermalization is given by  $\tau_{\text{therm}} \Gamma_{12}$ .

In a Ioffe-Pritchard type magnetic trap [203], the heat capacity depends on the temperature of the gas. For an infinitely deep IP-trap with a magnetic bias field  $B_0$  at the trap center, the heat capacity in the classical limit is given by [192]

$$C_{\text{IP},\infty} = \frac{12 + 6 \frac{V_0}{k_B T}}{3 + 2 \frac{V_0}{k_B T}} N k_B \quad (2.78)$$

where  $V_0 = \boldsymbol{\mu} \cdot \mathbf{B}_0$  and  $\boldsymbol{\mu}$  denotes the magnetic moment of an atom in the gas. Thus, in this idealized situation and assuming  $N_1 \ll N_2$ , it follows from Eq. (2.77) that between  $3/\xi$  and  $4/\xi$  collisions, depending on the temperature, are needed per type-1 atom for thermalization.

### 2.2.3.2. Practical aspects

The previous section describes sympathetic cooling in an idealized situation. In a real experiment, a number of additional aspects have to be taken into account. The most important ones among them are briefly discussed in this section.

**Thermal equilibrium** For the derivation of Eq. (2.77) thermal equilibrium for each species separately was assumed. This is a good assumption if the intraspecies thermalization rates are at least comparable to the interspecies thermalization rate. If the target gas is a spin-polarized one-component fermionic gas, however, elastic collisions are strongly suppressed at low temperature. Therefore, each target atom must be directly cooled by collisions with the buffer gas in order to achieve thermal equilibrium. Consequently, in this situation, the mean elastic collision rate Eq. (2.73) per target atom and the thermalization rate Eq. (2.77) should only be regarded as rough estimates that are useful in the case of sufficient spatial overlap of the two clouds. Specifically, if the cloud sizes of the fermionic target gas and of the buffer gas differ significantly, it may happen that only a part of the target gas thermalizes with the buffer gas. The remaining part is then left behind in the cooling process as a hot halo around the cooled central part of the cloud. This point will be discussed in more detail with respect to sympathetic cooling of  ${}^6\text{Li}$  in Ch. 6.

**Density overlap** The density overlap between the actively cooled gas and the sympathetically cooled gas, and thus the efficiency of sympathetic cooling, obviously depends on the total potential the atoms are subjected to. In our experiment, the three atomic species are trapped in the doubly polarized ground states, which all have a magnetic moment of one Bohr magneton  $\mu_B$ . They therefore experience the same magnetic trapping potential. Under the influence of the earth's gravitational potential, however, the centers of the clouds are shifted by different amounts along the direction of the gravitational acceleration  $\mathbf{g}$  ("gravitational sag"). For atoms with mass  $m$  confined in the harmonic region of the trapping potential, the gravitational sag is given by

$$\Delta z = -\frac{g}{\omega_z^2} \propto m \quad (2.79)$$

where  $\omega_z$  denotes the angular trapping frequency for these atoms along the direction of  $\mathbf{g}$ . The density overlap Eq. (2.74) in a harmonic trap for two non-degenerate gases with atomic masses  $m_1$  and  $m_2$  and identical temperature  $T$  is then given by [201]

$$\langle n_2 \rangle_{1,\text{ho}} = N_2 \left( \frac{\bar{\kappa}}{4\pi k_B T} \right)^{3/2} f_{\text{sag}}. \quad (2.80)$$

In this equation, the factor

$$f_{\text{sag}} = e^{-\frac{(m_1 - m_2)^2 g^2}{4\kappa_z k_B T}} \quad (2.81)$$

accounts for the difference in gravitational sag, and  $\bar{\kappa} = m_1\bar{\omega}_1^2 = m_2\bar{\omega}_2^2$  and  $\kappa_z = m_1\omega_{z,1}^2 = m_2\omega_{z,2}^2$  are the mean and vertical curvatures of the trapping potential. In addition, interactions between the target gas and the buffer gas lead to increased or decreased density overlap or even to collapse or phase separation [204, 205], depending on their strength and whether they are attractive or repulsive. If the strength and the sign of the interaction are known, a set of coupled equations containing a mean-field potential for the interspecies interaction may be used to calculate the density distributions [206, 207].

**Energy dependence of the scattering cross section** It should be noted that the scattering cross section  $\sigma_{12}$  in Eq. (2.73) is in general energy-dependent. If the scattering potential is known, this energy dependence can be determined numerically. The assumption of constant  $\sigma_{12}(E) \approx \sigma_{12}(0)$  is a good approximation in most experiments with ultracold gases. Exceptions, however, are mixtures with a low-energy shape resonance or with a large negative s-wave scattering length. The latter is the case in the  $^{40}\text{K}$ - $^{87}\text{Rb}$  mixture and  $\sigma_{l=0}(E)$  is calculated to experience a zero at a collision energy of  $630 \mu\text{K} \times k_B$  [201] due to the Ramsauer-Townsend effect. This value is consistent with recent experimental data [59] of the rethermalization rate between  $^{40}\text{K}$  and  $^{87}\text{Rb}$  at different temperatures.

**Effects of quantum statistics** Up to now, we have treated sympathetic cooling for an ultracold classical gas. However, sympathetic cooling is affected by quantum statistics, when the gases enter the respective quantum-degenerate regimes during the last stage of the cooling process. The density and momentum distributions of trapped bosonic and fermionic quantum gases in the quantum-degenerate regime differ drastically from those of a classical gas with the same temperature. Especially in a Fermi-Bose mixture, the density overlap of the two clouds may be significantly reduced as compared to the classical one since the fermionic cloud is larger due to the Fermi pressure and the bosonic cloud is much smaller due to Bose-Einstein condensation. In addition, the modified momentum distribution of the fermionic gas results in Pauli blocking [66], which reduces the number of possible scattering states and therefore the thermalization rate. Moreover, superfluidity of the BEC slows down the thermalization with the bosonic gas [208]. Finally, the heat capacities of the fermionic [209] and of the bosonic [156] gases are significantly influenced by the respective quantum statistics.



## 3. Experimental Setup

This chapter describes the experimental platform for the generation of a quantum-degenerate Fermi-Fermi-Bose mixture. The basic physical principles underlying the main components of the apparatus are discussed along with their technical realization. The experimental platform has been developed from scratch during this thesis work. Therefore, the development, design and construction of the very complex triple-species apparatus constitute a significant part of the work presented in this thesis.

### 3.1. Concept and overview

The experiment was designed with the goal to build a versatile and reliable apparatus for studies with mixtures of two *different* fermionic and one bosonic species in the quantum-degenerate regime. The first step in the construction of an experiment is the choice of species, since their atomic properties strongly influence the decision for a certain concept. From the large list of possible mixtures, we have chosen to use  ${}^6\text{Li}$ ,  ${}^{40}\text{K}$ , and  ${}^{87}\text{Rb}$  for several reasons. First, all three species are alkalis and as such have a comparatively simple energy level structure that is very well suited for laser cooling. Second,  ${}^{87}\text{Rb}$  is a bosonic species whose properties are well known and very favorable for the production of a large Bose-Einstein condensate. Third, the fermionic species  ${}^6\text{Li}$  and  ${}^{40}\text{K}$  have successfully been cooled before (although not together). In addition, the laser-cooling transitions of all three species are close together at  $\lambda_{\text{Li}} = 671 \text{ nm}$ ,  $\lambda_{\text{K}} = 767 \text{ nm}$ , and  $\lambda_{\text{Rb}} = 780 \text{ nm}$ , respectively, thus allowing us to use a common set of optics in order to keep the optical setup as simple and compact as possible. Moreover, appropriate semiconductor laser sources are available for all three species. This allowed us to build a laser system that requires a minimum of daily maintenance, an important aspect in such a large system. Finally, the  ${}^6\text{Li}$ - ${}^{87}\text{Rb}$  mixture had not been studied yet, which was at the same time a risk and a great chance.

The concept of our apparatus is sketched in Fig. 3.1. Initially, cold clouds of all three species are captured in a magneto-optical trap (MOT) at the center of a common magnetic quadrupole field in a first chamber, called the “MOT chamber”. Lithium is loaded from a spin flip-Zeeman slower. Potassium and rubidium are loaded from the background vapor produced by atomic vapor dispensers. The three atomic clouds are then transferred into a magnetic quadrupole trap in the MOT chamber. In order to attain a longer trap lifetime, the trapped clouds are subsequently moved into a second chamber, an ultra high vacuum (UHV) glass cell, with a residual pressure below  $1 \times 10^{-11} \text{ mbar}$ . This transport is realized by driving a sequence of shifted quadrupole coils (“transfer coils”). The quadrupole trap at the end of the transport is then transformed into a Ioffe-type trap in order to avoid Majorana losses at low temperatures. In this final magnetic trap, a quantum-degenerate mixture of  ${}^6\text{Li}$ ,  ${}^{40}\text{K}$ , and  ${}^{87}\text{Rb}$  is produced by evaporative cooling of rubidium and sympathetic cooling of the fermionic species.

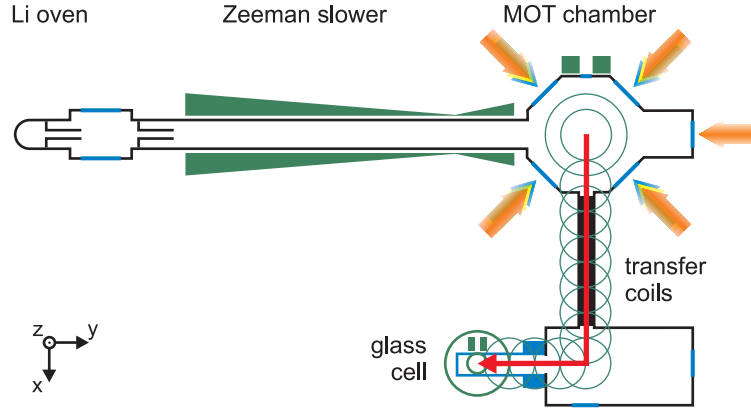


**Figure 3.1:** Concept of the apparatus. The three species  ${}^6\text{Li}$ ,  ${}^{40}\text{K}$ , and  ${}^{87}\text{Rb}$  are first captured and cooled in superimposed MOTs (triple MOT). The cold clouds are then simultaneously transferred by a series of magnetic coils into a UHV glass cell, where they are further transferred into a Ioffe-type magnetic trap. In this trap, simultaneous quantum degeneracy of all three species is achieved by means of evaporative and sympathetic cooling.

## 3.2. Vacuum system

The ultracold atomic gas is captured and trapped in an ultra-high vacuum chamber. The purpose of the vacuum chamber is to isolate the atoms from the room temperature environment. Typically, in experiments with alkali atoms in macroscopic traps, a vacuum pressure below  $1 \times 10^{-11}$  mbar is necessary for efficient production of a quantum-degenerate gas. At higher pressures, heating and loss of atoms from the trapped gas due to collisions with residual hot background atoms may be too strong to even reach the run-away regime of evaporative cooling (see Sec. 2.2.2.2). In contrast, fast loading of the MOT from the background vapor requires a significant partial pressure of the respective species. The two conflicting requirements are met by the use of multiple connected chambers and by careful design of the vacuum system.

### 3.2.1. Setup

The vacuum system is shown in Fig. 3.2. The central part consists of three chambers made of steel with a low magnetic permeability. The first chamber is used for the three-species MOT. It is connected by differential pumping tubes with the two other chambers, the oven chamber and the UHV chamber. The UHV chamber consists of two parts, a quartz cell, around which the magnetic trap is built, and a custom-designed steel chamber.

The MOT chamber has a flat octagonal shape and six indium-sealed quartz windows with a clear diameter of 40 mm allowing for large MOT beams. An additional smaller window provides access for optical pumping. Broadband antireflection (AR) coating of the windows avoids multiple reflections inside the MOT chamber. The chamber's low height of only 46 mm makes it possible to place the magnetic coils for the MOT quadrupole field and for the magnetic transfer close to the atoms for efficient operation. The rubidium and potassium vapor dispensers are placed only 4 cm away from the center of the MOT

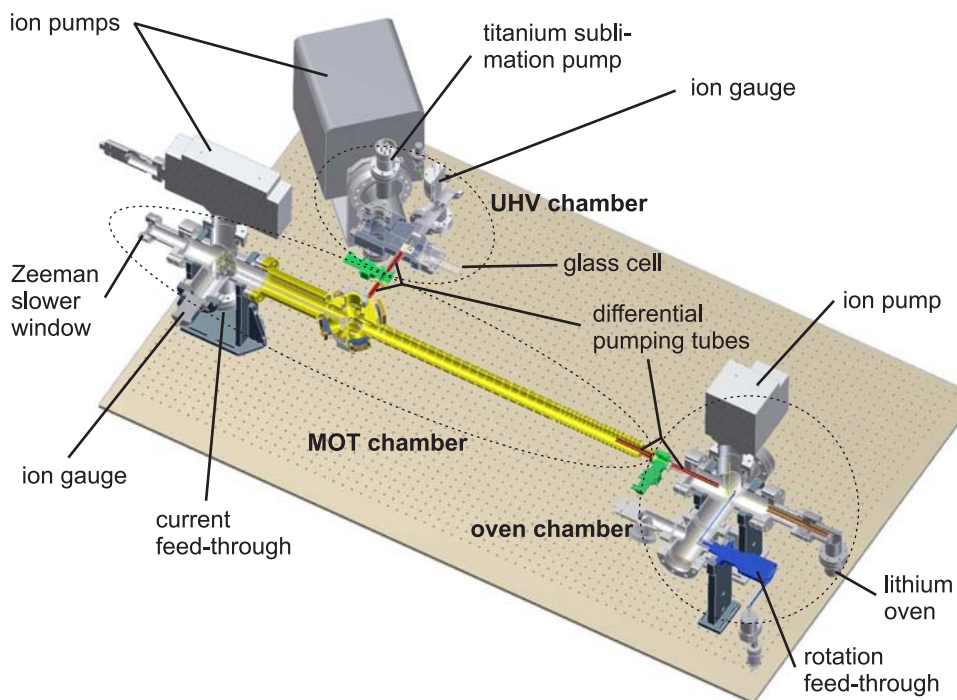


**Figure 3.2:** Vacuum system. The graph shows a 3D-CAD drawing (sectional view) of the vacuum chamber of the  ${}^6\text{Li}$ - ${}^{40}\text{K}$ - ${}^{87}\text{Rb}$  apparatus.

chamber pointing towards the capture region of the MOTs. For electrical isolation, they are mounted on supports made of Macor. The MOT chamber is pumped through a CF 63 five-way cross by a 501/s ion pump (Varian, VacIon Plus 55 StarCell). The remaining ports of the cross are used for an ion gauge (Varian, UHV-24p), a window for the laser light used for Zeeman slowing, and a six-channel electrical feedthrough (VTS Schwarz,  $I_{\text{max}} = 13.5 \text{ A}$ ) for the dispenser currents. The slower laser window is heated to  $165^\circ\text{C}$  to prevent permanent coating with incident lithium atoms. An all metal angle valve on a side port of the ion pump allows us to connect a roughing pump for initial pump down of the MOT chamber.

The MOT chamber is connected with the oven chamber by a 77 cm long steel tube, around which the Zeeman slower coil is placed, followed by a pneumatically actuated valve. On both sides of the valve, the inner diameter of the vacuum chamber is reduced to 6 mm over a total length of 23 cm to permit differential pumping. A comparatively large inner diameter of 37 mm was chosen for the long slower tube so that it can be efficiently pumped through the MOT chamber. A second differential pumping stage (6 mm inner diameter, 16.5 cm long) reduces the atom flux from the lithium oven into the oven chamber. The oven chamber is pumped by a second 501/s ion pump of the same type as above. An all metal rotation feed-through (VTS Schwarz, TMR 40, mechanically coupled, bellow-sealed) allows us to drive a mechanical shutter for the atomic beam emitted from the lithium oven. Also in this chamber, an additional free CF 40 port that can be sealed by an all metal angle valve permits us to connect a roughing pump for initial pump down. Two CF 63 viewports

give optical access to the oven chamber for spectroscopic analysis of the lithium atom beam and for general visual inspection.

Finally, the MOT chamber and the UHV chamber are connected by a CF 16 tube. Two successive insets with an inner diameter of 8 mm and lengths of 10 cm and 7.4 cm reduce the conductance of the tube to 0.11/s (calculated for rubidium atoms). The diameter of these differential pumping tubes was numerically optimized as a compromise between maximum pressure compression ratio between the chambers and minimal loss of atoms during the magnetic transfer. The connection between the MOT chamber and the UHV chamber can be closed with a pneumatically actuated valve. This allows us to flood and open the MOT chamber without flooding the UHV chamber, should this be necessary, e.g. for exchanging the dispensers. The UHV chamber is pumped by a 1251/s ion pump (Varian, VacIon Plus 150 StarCell). A titanium sublimation pump (Thermionics, four filaments) placed in a side arm of the steel chamber enhances the pumping speed for reactive, getterable gases like hydrogen and nitrogen. The pressure can be monitored down to levels below  $10^{-11}$  mbar with a high sensitivity ion gauge (Varian, UHV-24p). A pair of AR-coated windows provides optical access to the steel chamber from top and bottom for possible future projects. The main experimental chamber consists of a glass cell connected to the steel chamber. It was produced by Helma with high quality quartz glass and has a broad-band AR-coating on the outer surfaces (reflectivity smaller 0.5% for 512–1064 nm at normal incidence). The glass cell consists of a rectangular part with outer dimensions of 26 mm  $\times$  26 mm  $\times$  70.5 mm and a wall thickness of 4 mm. The rectangular part is fused to two stacked circular quartz discs (outer diameters of 37 mm and 50 mm, length of 19 mm each) with an 18 mm wide central hole. The glass cell is attached to the steel chamber by a clamp that presses the larger glass disc onto an appropriate flange. The pressure is applied with 14 screws so that the mechanical stress on the glass can be distributed evenly. A metal ring with a soft core and two knife edges (Garlock, HNV 200 Helicoflex Delta) provides a helium leak-tight glass-metal sealing. Optical access to the glass cell is excellent along all six axes due to an additional AR-coated window opposite to the glass cell in the steel chamber.

#### 3.2.2. Installation, pump down, and baking

The present apparatus was set up in two stages. In the first stage, used for the experiments described in Ch. 4, only the MOT chamber, the oven chamber and the corresponding attached equipment were installed. The valve on the vacuum tube that connects the MOT chamber and the UHV chamber in the final apparatus was sealed with a CF 16 viewport. The lithium oven was filled and the rubidium and potassium dispensers were installed (see also Sec. 3.3.1 and Sec. 3.3.2.3). A quasi oil-free roughing vacuum system consisting of a turbo-molecular pump and a membrane pump was connected to the two all metal angle valves and the system was pumped down. The apparatus was then baked for two weeks to accelerate outgassing from the bulk material of the vacuum chambers. The use of several separately controlled heating tapes allowed us to adjust the baking temperature individually for the different parts of the apparatus, according to the respective limits. Care was also taken to keep temperature gradients in time and space within the ranges allowed for the different components. During the baking procedure, the main coil of the lithium Zeeman slower was already in its final position since it cannot be installed without breaking

the vacuum, although it is wound on an independent steel tube that slips over the vacuum tube (see Sec. 3.3.2). A heating wire that is wound directly onto the vacuum tube before installation of the Zeeman slower allows for proper bake-out of the vacuum tube inside the Zeeman slower. At the end of the bake-out procedure, the heating power was gradually reduced over a period of several hours until room temperature was reached. The two ion pumps were then switched on. A final pressure of a few times  $10^{-10}$  mbar was achieved.

In a later second stage and in preparation for the experiments presented in chapters 5 & 6, the apparatus was extended by the UHV chamber. During setup of the extension, the flange for the glass cell was first provisorily closed with a Viton-sealed window. The chamber was then pumped down by a roughing pump system and baked for five days at  $\approx 200^\circ\text{C}$ . After cool-down and a subsequent thorough leak-test, the glass cell was attached to the UHV chamber. In the meanwhile, the MOT chamber was flooded with dry argon gas and the atomic vapor dispensers for potassium were replaced by an optimized second generation. Afterwards, the whole vacuum setup was pumped by a turbo-molecular vacuum pump and baked again for several days. During the baking procedure, the atomic vapor dispensers and the filaments of the titanium sublimation pump were initialized. Finally, the system was again tested for helium leaks, the ion pumps were activated and the all metal angle valves were closed. The pressures subsequently dropped to a few times  $10^{-10}$  mbar in the MOT chamber and to below the detection limit about  $1 \times 10^{-11}$  mbar in the UHV chamber.

### 3.2.3. Failure protection

The vacuum system is protected by several measures. In the case of a mains failure, an electrical circuit triggers an alarm in an automated surveillance system (Telenot Electronic, comline 2008 FS). This system in turn informs the group members by telephone about the outage. Moreover, the ion pumps are connected to an uninterruptible power supply, which guarantees full operation of the ion pumps during the blackout for at least four hours giving us ample time to react. Finally, if a vacuum leak occurs and the pressure in one of the chambers rises, the current of the corresponding ion gauge also rises. A control system (Varian, MiniLink) then closes the pneumatically actuated valves between the different vacuum chambers, if a certain threshold current is exceeded.

## 3.3. Atom sources

This section describes the atom sources from which the three-species MOT is loaded. In the cases of rubidium and potassium, atoms are directly captured from the background gas in the MOT chamber. Atomic vapor dispensers are used to generate appropriate partial pressures of  $^{87}\text{Rb}$  and  $^{40}\text{K}$ . For lithium, in contrast, vapor loading would be inefficient because of the comparatively low saturation pressure and the small fraction of atoms at speeds below a typical capture velocity of the MOT. The lithium MOT is therefore loaded from a Zeeman-slowed atomic beam.

#### 3.3.1. Atomic vapor dispensers for $^{40}\text{K}$ and $^{87}\text{Rb}$

Atomic vapor dispensers are very convenient atom sources and are widely used in cold atom experiments. They consist of a small metal boat containing a salt compound of the desired element and a reducing agent. When the dispenser is heated by sending a current through it, the redox reaction takes place and the alkali metal is released in atomic form into the vacuum vessel. The reaction speed and consequently the alkali partial pressure in the atomic vessel are controlled by the electric current.

Atomic vapor dispensers are industrially used in large quantities (e.g. for the production of ultrapure alkali metal films on surfaces). This makes them comparatively inexpensive. However, they are only commercially available with the alkali element in its natural mixture of isotopes. In the case of  $^{87}\text{Rb}$ , which has a natural abundance of 28%, this is no severe limitation for cold atom experiments. We therefore employ commercial dispensers (SAES Getters, Rb/NF/7/25 FT10+10) as atomic sources for rubidium. In contrast, the natural abundance of  $^{40}\text{K}$  is only 0.01% making the use of enriched potassium dispensers very desirable. A procedure for the construction of very efficient  $^{40}\text{K}$  vapor dispensers was developed in the group of D.S. Jin and is outlined in Ref. [210]. These dispensers rely on the redox reaction



Potassium chloride is available at different enrichment levels of  $^{40}\text{K}$ , with prices steeply increasing with the abundance. In our experiments, we have initially used potassium with a  $^{40}\text{K}$  abundance of 3%. They were built as part of F. Henkel's diploma thesis work [211]. During the extension of the apparatus by the UHV chamber, the dispensers were replaced by a second version with an increased abundance of 6% in  $^{40}\text{K}$  (MaTeck, Jülich, 72 €/mg K). Each of the three potassium dispensers installed in the apparatus contains about 10 mg of KCl and 20 mg of pure calcium, an amount expected to last for several years.

For the production of efficient  $^{40}\text{K}$  dispensers, both reaction partners, KCl and Ca, are needed in the form of pure powders. In contrast to potassium chloride, calcium is commercially not available as a powder. A fine powder of calcium is obtained by filing dendritic pieces of the pure elementary metal (Sigma-Aldrich, pureness >99.99%) and selecting grains with diameters smaller than 200  $\mu\text{m}$  using a sieve. Since calcium powder is very reactive with the main components of air, all production processes are performed either under a dry argon protective atmosphere in a glove box or under vacuum conditions. Handling of only a few milligrams of the fine powder with bulky gloves in the dry atmosphere is very delicate and special measures are necessary to avoid loss due to electrostatic charging. After filing, the KCl powder and the calcium powder are separately baked in a vacuum setup for several days to drive out impurities. They are then mixed and filled into three metal boats made of nickel-chromium foil. The boats have first also been baked under vacuum conditions. The completed potassium dispensers are mounted onto a macor ring which is subsequently transferred under an argon protective atmosphere into the MOT chamber. Further details of the production process are described Ref. [211].

### 3.3.2. Zeeman slower for ${}^6\text{Li}$

In a Zeeman slower, atoms in an atomic beam are slowed and cooled by the light pressure of a counter-propagating laser beam. The technique of Zeeman slowing was first demonstrated experimentally in 1982 [212].

#### 3.3.2.1. Principle

Consider an atom of mass  $m$ , which moves at a velocity  $\mathbf{v}$  along the  $y$ -axis and has a closed optical transition between a ground state and an excited state. The two levels are separated by an energy difference  $\hbar\omega_{\text{atom}}$  at zero magnetic field and the transition has a linewidth  $\Gamma$ . Photons in a laser beam with frequency  $\omega_{\text{laser}}$  and wave vector  $\mathbf{k}$  impinging on the atom are spontaneously scattered off the atom at a rate [213]

$$\gamma_{\text{sc}} = \frac{\Gamma}{2} \frac{S}{1 + S + (2\delta/\Gamma)^2} \quad (3.2)$$

where the saturation parameter  $S = I/I_s$  is given by the ratio of the intensity  $I$  of the impinging laser light and the saturation intensity  $I_s = \pi\hbar c\Gamma/(3\lambda^3)$  of the closed optical transition with wavelength  $\lambda = 2\pi c/\omega_{\text{laser}}$ . An effective detuning is defined by

$$\delta = \delta_0 - \mathbf{k} \cdot \mathbf{v} - \frac{\Delta E(B)}{\hbar} \quad (3.3)$$

where  $\delta_0 = \omega_{\text{laser}} - \omega_{\text{atom}}$ . The term  $-\mathbf{k} \cdot \mathbf{v}$  accounts for the Doppler shift in the non-relativistic limit ( $v \ll c$ ). Finally,  $\Delta E(B)$  is the shift of the energy difference between the two atomic energy levels due to a magnetic field  $B$ . When the atom absorbs a photon from the laser beam, it is excited to the upper energy level and receives a momentum kick  $\hbar\mathbf{k}$ . The atom subsequently returns to its ground state level either by spontaneous or stimulated emission of a photon. Averaged over many absorption-emission cycles, the spontaneously emitted photons do not transfer a net momentum onto the atom. The atom is thus decelerated on average by a momentum  $\hbar\mathbf{k}$  for each photon absorption followed by the *spontaneous* emission of a photon. A cycle of a photon absorption followed by the *stimulated* emission of a photon, in contrast, does not contribute to slowing of the atom since the momentum kicks of the two processes cancel. Consequently, the mean deceleration is given by

$$\mathbf{a} = \gamma_{\text{sc}} \frac{\hbar\mathbf{k}}{m}. \quad (3.4)$$

The maximum absolute value of the deceleration  $a_{\text{max}} = \frac{\Gamma}{2} \frac{\hbar k}{m}$  is approached for effectively resonant light ( $\delta = 0$ ), at large laser intensity ( $I \gg I_s$ ).

As an atom for which the laser light is initially effectively resonant ( $\delta = 0$ ) slows down in a homogeneous magnetic field, it is quickly shifted out of resonance by the Doppler shift and is thus not slowed any further. A very effective way to sustain the deceleration is to compensate the Doppler shift by adjusting the energy difference between the ground and excited energy levels with a suitably tapered inhomogeneous magnetic field  $B(x)$ . In the case of alkali atoms, the only closed two-level transitions are the ones between the two stretched ground states and the corresponding stretched excited states on the  $D_2$ -line. For  ${}^6\text{Li}$ , these are the transitions  $|2S_{1/2}, F = 3/2, m_F = 3/2\rangle \rightarrow |2P_{3/2}, 5/2, 5/2\rangle$

### 3. Experimental Setup

---

and  $|2S_{1/2}, 3/2, -3/2\rangle \rightarrow |2P_{3/2}, 5/2, -5/2\rangle$ . The Zeeman-shift of the levels involved is proportional to the magnetic field. Neglecting the small magnetic moment of the nucleus, the transition energy of the  $\sigma^+$  ( $\sigma^-$ ) transition is readily found to shift in a magnetic field  $B$  by  $\Delta E(B) = (-)\mu_B B$  from its value at zero magnetic field. Here,  $\mu_B = e\hbar/2m_e$  is Bohr's magneton and  $\mathbf{B}$  is assumed to be oriented parallel to the quantization axis, with respect to which the polarization of the light is defined. The scalar value  $B$  is taken to be positive for collinear orientation and negative for anti-collinear orientation.

A suitable profile of the magnetic field in a Zeeman slower is obtained from the equations above by requiring constant effective detuning  $\delta(x) = 0$  and using simple kinematics. The result for  $\sigma^-$  light is

$$B(y) = B_0 - \frac{\hbar k}{\mu_B} \sqrt{v_{\text{cap}}^2 - 2 a_{\text{zs}} y} \quad (3.5)$$

where the capture velocity  $v_{\text{cap}}$  is the speed of the atoms at the entrance of the Zeeman slower and  $a_{\text{zs}} > 0$  is the absolute value of the deceleration. The choice of the laser detuning  $\delta_0$  fixes the value of the homogeneous magnetic bias field  $B_0 = -\hbar\delta_0/\mu_B$ . For  $\sigma^+$  light,  $B(y)$  has the same value as in Eq. (3.5) but opposite sign. Obviously, the Zeeman slower must be designed for  $a_{\text{zs}} < |\mathbf{a}_{\text{max}}|$  so that the atoms can follow the magnetic field profile for the given laser intensity. Typical values of  $a_{\text{zs}}$  lie between  $1/3 a_{\text{max}}$  and  $2/3 a_{\text{max}}$ , depending on the available laser intensity.

An important feature of a Zeeman slower is that the initial velocity distribution is narrowed in the range  $v \leq v_{\text{cap}}$  during the slowing process. All atoms with velocities between the capture velocity  $v_{\text{cap}}$  and the final velocity  $v_{\text{final}}$  at the exit of the Zeeman slower fulfill the resonance condition at some point along the Zeeman slower and are slowed for the remaining length of the slower. Finally, all atoms initially in this velocity range populate a small velocity interval around  $v_{\text{final}}$ . For this reason, Zeeman slowers are sometimes said to cool an atomic beam in addition to slowing it, although, strictly speaking, no temperature can be attributed to the final velocity distribution since it is not in thermal equilibrium.

#### 3.3.2.2. Transverse heating

A final important aspect for the design of a Zeeman slower is that the random nature of the spontaneous emission of photons during the slowing process leads to transverse heating of the atomic beam [214]. The rms-width of an initially well defined transverse velocity  $v_{\perp}$  increases with time  $t$  according to

$$(v_{\perp}^{\text{rms}})^2 = \frac{9}{10} \frac{v_{\text{rec}}^2}{3} N(t) \quad (3.6)$$

where  $v_{\text{rec}} = \hbar k/m$  is the recoil velocity.  $N(t)$  is the number of photons an atom scatters between time  $t = 0$  and  $t$ . For an atom with initial velocity  $v_{\text{cap}}$ , the value of  $N$  after passage through the Zeeman slower is connected to the design parameters by  $N = (v_{\text{cap}} - v_{\text{final}})/v_{\text{rec}}$ . The deviation of the dipolar radiation pattern on the closed optical transition from an isotropic distribution is accounted for by the factor  $9/10$  [214] and is neglected in the following. Using the fact that there is no correlation between different scattering events,

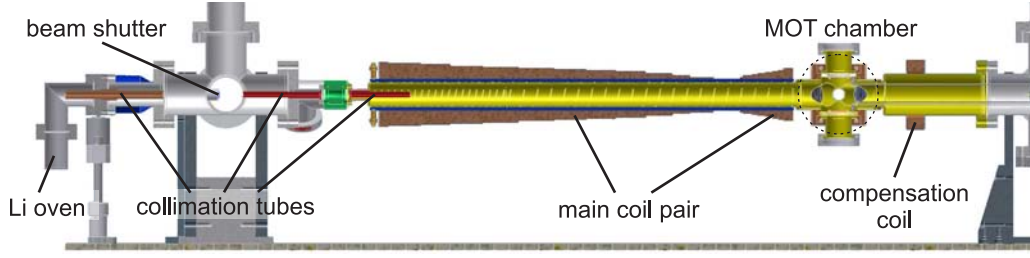


**Figure 3.3:** Zeeman slower for lithium. The overview depicts the beam source, the collimation tubes and the three coils that produce the magnetic field profile.

the rms-width at the end of the Zeeman slower of an initially narrow beam is found to be

$$(x_{\perp}^{\text{rms}})^2 = \frac{v_{\text{rec}}^2}{3} N(t) \frac{t^2}{3} = \frac{v_{\text{rec}}(v_{\text{cap}} - v_{\text{final}})^3}{9 a_{\text{zs}}}. \quad (3.7)$$

After the slowing process, the beam diverges with a constant divergence angle of  $2 v_{\perp}^{\text{rms}}/v_{\text{final}}$ . Therefore, the final velocity must not be chosen too small.

### 3.3.2.3. The lithium beam source

The experimental setup used for loading the lithium MOT is shown in Fig. 3.3. It consists of a source for the atomic beam and a Zeeman slower described in the next section. The lithium beam source was designed with the goal to produce a well-collimated atomic beam with a sufficient particle flux while not compromising vacuum quality in the MOT chamber. A few grams of pure, highly enriched lithium (Sigma-Aldrich, 95% abundance of  ${}^6\text{Li}$ ) are contained in an elbow which is heated to about  $400^\circ\text{C}$ . An atomic beam with a calculated mean velocity of roughly  $1200\text{ m/s}$  is emitted from the oven through a  $6\text{ mm}$  wide tube into the oven chamber. The tube is heated to about  $430^\circ\text{C}$  to avoid condensation of lithium and clogging of the tube. The beam can be blocked by an electrically actuated mechanical shutter in front of the tube. Two subsequent also  $6\text{ mm}$  wide tubes connect the oven chamber with the Zeeman slower vacuum tube, which is attached to the MOT chamber. The narrow tubes collimate the beam to a calculated divergence angle of less than  $0.6^\circ$  and—in combination with the ion pump in the oven chamber—limit the background gas load from the lithium oven into the MOT chamber.

### 3.3.2.4. The spin-flip Zeeman slower

In our Zeeman slower, the magnetic field profile is realized by two successive main coils both producing fields parallel to the atomic beam but with opposite directions. An additional compensation coil on the opposing side of the MOT chamber compensates the stray field of the Zeeman slower at the center position of the MOTs. This configuration, in which the sign of the magnetic field of the Zeeman slower flips, is known as a spin-flip Zeeman slower. The name is somewhat misleading since only the direction of the magnetic field switches, whereas the spins of the atoms stay spatially oriented in the same direction all along the Zeeman slower.

A spin-flip Zeeman slower has several advantages compared to other designs: First, the absolute value of the magnetic field increases at the end of the Zeeman slower, corresponding to the  $\sigma^-$  situation in Eq. (3.5). A Zeeman slower with an increasing magnetic field is more efficient and much less sensitive to variations in the laser intensity and detuning than one with a decreasing magnetic field [215]. The reason for this difference, which might be surprising at first glance, is the extraction process of slow atoms at the end of the Zeeman slower. In an increasing-field slower the extraction velocity  $v_{\text{final}}$  of the atoms is precisely determined by the maximum value of the magnetic field at the end of the Zeeman slower. Since the field decreases after the Zeeman slower, only *faster* atoms are tuned into resonance while slower atoms remain unaffected. In contrast, in a decreasing field slower, atoms *slower* than  $v_{\text{final}}$  or even with negative velocities get into resonance with the slowing light as the magnetic field decreases. The atomic beam therefore spreads significantly in the extraction region, severely limiting the efficiency of MOT loading from the Zeeman-slowed beam. Second, the difference between capture velocity and final velocity is proportional to the difference in magnetic field. By choosing a magnetic field with opposite directions at the two ends of the Zeeman slower, the absolute field strength necessary is reduced and thus the power dissipation is decreased. Third, in contrast to an increasing-field Zeeman slower with constant field direction, the coil at the end of a spin-flip Zeeman slower is much smaller and can therefore be placed closer to the MOT center thus increasing loading efficiency. Finally, the necessary detuning of the slowing laser depends on the velocity of the atoms at the spin flip point where the magnetic field vanishes. For an appropriately chosen value  $B_0$ , the slowing laser is far off-resonant for the slow atoms that are trapped in the MOT at a small magnetic field and does not affect them.

Besides compensating for the Doppler shift, the magnetic field in the slower also defines a quantization axis. In the region between the two main coils, the field is weak and its direction changes, so that different Zeeman states are mixed. However, after passage of the weak-field region, the atoms are pumped back into the correctly oriented doubly polarized state by the  $\sigma$ -polarized slowing laser beam. A repumping beam superimposed onto the slowing laser beam prevents loss of atoms that get transferred to the lower hyperfine state. In addition, the repumper beam is required for the preparation of the atoms at the beginning of the slowing process.

#### 3.3.2.5. Design and fabrication of the Zeeman slower

The Zeeman slower is designed for a deceleration  $a_{\text{zs}} = a_{\text{max}}/3 = 6.1 \times 10^5 \text{ m/s}^2$ . The winding pattern necessary to produce an appropriate magnetic field profile was determined using a numerical optimization. The final calculated and measured field profiles of the Zeeman slower are shown in Fig. 3.4 for the operation current of 10 A. The slower has an effective length of about 60 cm. The difference between the minimum and maximum magnetic field of  $-578 \text{ G}$  and  $232 \text{ G}$ , respectively, corresponds to a maximum deceleration of the atoms by  $760 \text{ m/s}$ . The detuning of  $-448 \text{ MHz}$ , for which the Zeeman slower is designed, results in a capture velocity of  $843 \text{ m/s}$  and a final velocity of  $83 \text{ m/s}$ , which is well below the capture velocity of the MOT of about  $150 \text{ m/s}$ .

The two main coils of the Zeeman slower were wound on a double-walled steel tube with outer and inner diameters of  $54 \text{ mm}$  and  $45.1 \text{ mm}$  using a lathe. The wire is electrically

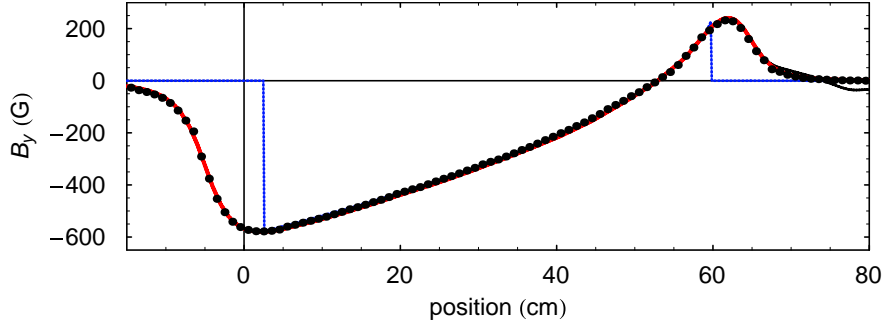


**Figure 3.4:** Magnetic field of the Zeeman slower. Shown are the calculated (red line) and measured (dots) profiles of the longitudinal magnetic field  $B(y)$  produced by the two main coils. The blue dashed line indicates the idealized magnetic field given by Eq. (3.5). The total field including the compensation coil and the MOT quadrupole field is represented by the thin black solid line.

insulated by heat resistant varnish. A comparatively large rectangular cross section of the wire (Isodraht, 4 mm  $\times$  1 mm) allows for compact construction of the coil and low power dissipation. Water flowing between the two walls of the slower tube cools the coils from inside and limits the temperature to typically below 60°C. An electrically insulating, heat-resistant and thermally conducting glue (Loctite, Hysol 9492 A&B) improves heat conductance in the coils and provides mechanical stabilization.

## 3.4. Laser systems and optics

This section describes the laser systems for the three species studied in our experiment. Near resonant laser light is needed in different phases of the experiment: For slowing, magneto-optical trapping and further cooling of the atoms, for optical pumping into the magnetically trappable states and for final detection using absorption imaging. The laser systems were designed and built with a focus on compactness, flexibility and especially reliability to keep the necessary daily maintenance at a minimum. Reliability of all components is a very important requirement in the complex and extensive apparatus necessary to work with three different species.

### 3.4.1. Energy levels and transitions employed

An overview of the atomic energy levels relevant for our experiment is given in Fig. 3.5 for all three species. Arrows indicate the optical transitions driven during the experimental cycle. The transitions have natural linewidths of about  $\Gamma/(2\pi) = 6$  MHz and the wave lengths are  $\lambda_{\text{Rb}} = 780$  nm,  $\lambda_{\text{K}} = 776$  nm, and  $\lambda_{\text{Li}} = 671$  nm, respectively. A detailed list of the atomic properties is given in App. A. In the following, the level diagrams of the three species are briefly discussed in turn, pointing out similarities and differences to an extent as they are relevant for the experiment.

Magneto-optical trapping and further laser cooling of  $^{87}\text{Rb}$  is done on the  $|5S_{1/2}, F = 2\rangle \leftrightarrow |5P_{3/2}, F' = 3\rangle$  cycling transition of the  $D_2$ -line. A repumping laser driving the

### 3. Experimental Setup

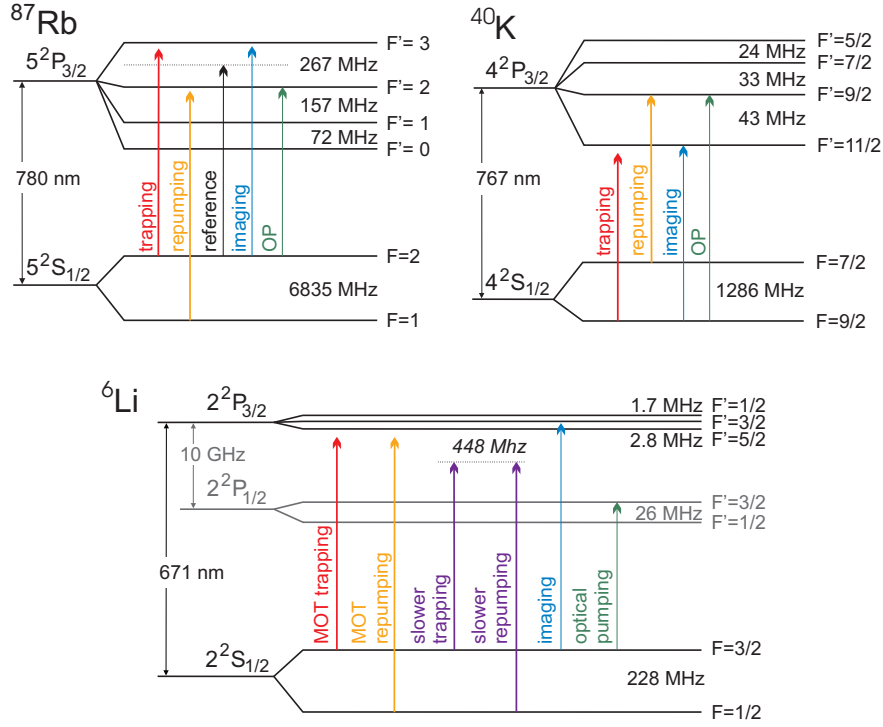


**Figure 3.5:** Energy level schemes for  $^{87}\text{Rb}$ ,  $^{40}\text{K}$  and  $^6\text{Li}$ . The arrows indicate optical transitions driven during the experimental cycle (OP=optical pumping).

$|5 S_{1/2}, F = 1\rangle \rightarrow |5 P_{3/2}, F' = 2\rangle$  transitions brings atoms ending up in the  $|5 S_{1/2}, 1\rangle$  hyperfine ground state back into the cycling transition. Optical pumping and the corresponding transitions will be discussed in Sec. 5.3.2. Laser light with a frequency close to or on the  $|5 S_{1/2}, F = 2\rangle \leftrightarrow |5 P_{3/2}, F' = 3\rangle$  cycling transition is used for detection of the atoms by absorption imaging at the end of each experimental cycle.

In contrast to rubidium, potassium has an inverted hyperfine structure in the ground and excited states because of the positive sign of the nuclear g-factor [216]. The cycling transition suitable for laser cooling therefore occurs between the two respectively lowest lying energy levels  $|4 S_{1/2}, F = 9/2\rangle$  and  $|4 P_{3/2}, F' = 11/2\rangle$ . Due to the comparatively small energy splitting between the excited states, the probability of non-resonant excitation to other excited states is larger than in the case of rubidium. Consequently, a higher intensity is necessary for the repumping light, which drives the  $|4 S_{1/2}, F = 7/2\rangle \rightarrow |4 P_{3/2}, F' = 9/2\rangle$  transition. Another beam that also drives the cycling transition is used for detection of the atoms.

In the case of lithium, the hyperfine structure of the excited  $|2 P_{3/2}\rangle$  state has an energy splitting on the order of the linewidth of the  $D_2$ -transition. This property has significant consequences: First, it makes polarization gradient cooling inefficient for lithium resulting in a considerably higher temperature of the laser-cooled atomic cloud compared to other alkali species (see Ch. 4). Second, the cycling transition  $|2 S_{1/2}, F = 3/2\rangle \leftrightarrow |2 P_{3/2}, F' = 5/2\rangle$  cannot be addressed individually. In a MOT, this results in comparable population rates of

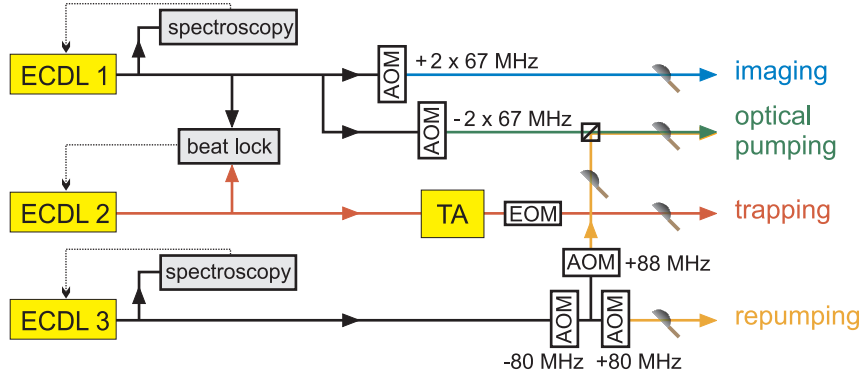


**Figure 3.6:** Schematic block diagram of the laser system for  $^{87}\text{Rb}$ . Light is emitted from three external cavity diode lasers (ECDL) and one tapered amplifier (TA). Acousto-optic modulators (AOM) are used for fast intensity modulation and shifting of the light frequencies. The intensity of the trapping light is controlled by an electro-optic modulator (EOM). Shutters allow us to block the different beams individually.

the two ground states  $|2S_{1/2}, F=1/2\rangle$  and  $|2S_{1/2}, F=3/2\rangle$ . Consequently, the ‘repumping’ light, which drives the  $|2S_{1/2}, F=1/2\rangle \rightarrow |2P_{3/2}, F'=1/2, 3/2\rangle$  transitions, may be regarded as a second trapping light. It typically has a similar detuning and intensity as the ‘official’ trapping light. The same is true for the far red-detuned pair of trapping and repumping light used in the Zeeman slower. Third, the unresolved  $|2P_{3/2}\rangle$  hyperfine structure has consequences for the optimal strategy for optical pumping (see Sec. 5.3.2). Finally,  $\sigma^+$ -polarized light on the  $|2S_{1/2}, F=3/2, m_F=3/2\rangle \leftrightarrow |2P_{3/2}, F'=5/2, m_{F'}=5/2\rangle$  cycling transition is used for absorption imaging. Repumping light, simultaneously irradiated onto the cloud from a perpendicular direction, brings atoms that accidentally end up in the lower hyperfine ground state (e.g. due to slightly imperfect polarization of the light) back into the imaging transition cycle.

### 3.4.2. Rubidium laser system

The rubidium laser system is shown in Fig. 3.6. Light is emitted from two self-built external cavity diode lasers (ECDL) [217, 218] and a commercial tapered amplifier system (Toptica, TA-780) consisting of another diode laser (ECDL 2) and a tapered amplifier chip (TA, for a review see [219]). The frequency of ECDL 1 (“reference” in Fig. 3.5) is stabilized to the cross-over signal between the  $|5S_{1/2}, F=2\rangle \rightarrow |5P_{3/2}, F'=2\rangle$  and  $|5S_{1/2}, F=2\rangle \rightarrow |5P_{3/2}, F'=3\rangle$  hyperfine transitions of the  $^{87}\text{Rb}$   $D_2$ -line using the side-band free, Doppler-free dichroic lock (DFDL) technique [220] on a rubidium vapor cell. Its output is separated into two arms and coupled into two optical fibers, providing the light for optical pumping and imaging, respectively. Acousto-optic modulators (AOM, Crystal Technologies) in double-pass configuration in the two arms shift the frequency by adjustable values and allow us to control the light intensities on a sub- $\mu\text{s}$  timescale. The frequency of the master laser ECDL 2 in the TA-system is locked relative to the frequency of ECDL 1. Light from both lasers is superimposed on a fast photodiode (Hamamatsu, 1.5 GHz) that detects the beat frequency. A beat lock technique [221] stabilizes ECDL 2

### 3. Experimental Setup

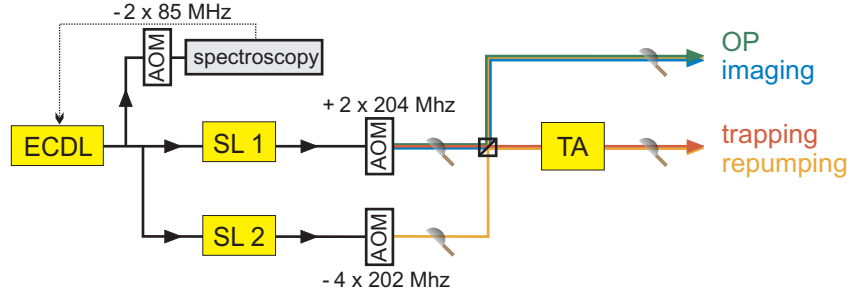


**Figure 3.7:** Laser system for  $^{40}\text{K}$ . An external cavity diode laser (ECDL), which is locked to a conveniently located spectroscopic feature of  $^{39}\text{K}$ , injection-seeds two slave lasers (SL 1 & SL 2). AOMs in the output beams shift the frequency close to the trapping and repumping transitions, respectively. A tapered amplifier boosts the output power to more than 800 mW.

at an adjustable, constant beat frequency. The output of ECDL 2 is amplified in a tapered amplifier and coupled into a single-mode, polarization-maintaining fiber, providing trapping light with a typical power of 280 mW after the fiber. The intensity can be controlled by an electro-optic modulator (Gsänger, LM 0202). The repumping laser ECDL 3 is stabilized to the  $|5 S_{1/2}, F=1\rangle \rightarrow |5 P_{3/2}, F'=2\rangle$  transition using a standard saturated absorption frequency-modulation (FM) spectroscopy setup [222, 223] on a second rubidium vapor cell. After passing through a tandem AOM setup permitting intensity control and rapid switch-off, the beam is coupled into a fiber providing the repumping light for the MOT. A tandem AOM setup consists of two consecutive AOMs shifting the light frequency by  $\nu_0 - \delta/2$  and  $-\nu_0 - \delta/2$ , respectively, where  $\nu_0 = 80$  MHz in our case. It allows a frequency tuning by typically  $\delta = -15\dots+15$  MHz with constant beam pointing. In addition, repumping light is also needed for optical pumping. Therefore, the 0<sup>th</sup> order of the second AOM in the aforementioned repumper tandem AOM setup is diverted. A third AOM is used to switch the beam intensity and to shift its frequency by a variable amount back close to the repumping transition. The beam is superimposed onto the optical pumping beam and coupled into the same optical fiber with identical linear polarization. In order to avoid heating and losses due to undesired residual light during the cooling of the gas we employ mechanical shutters between AOMs and optical fibers.

#### 3.4.3. Potassium laser system

The potassium laser system is schematically depicted in Fig. 3.7. Starting point is a self-built external cavity diode laser containing an AR-coated laser diode (Eagleyard, EYP-RWE-0790). The antireflection coating allows us to operate the laser diode at the potassium wavelength of 767 nm, although the laser diode with standard coating has a free-running center wavelength of typically 790 nm. The output power of the ECDL is typically 20 mW. The output beam of this master laser splits into three beams. The first one is frequency shifted by  $-190$  MHz and used to lock the laser frequency to the conveniently located cross-over signal between the  $|4 S_{1/2}, F=1\rangle \rightarrow |4 P_{3/2}, F'=0, 1, 2\rangle$  and  $|4 S_{1/2}, F=2\rangle \rightarrow |4 P_{3/2}, F'=1, 2, 3\rangle$  transitions of the  $D_2$ -line of  $^{39}\text{K}$  [224]. Locking to a  $^{40}\text{K}$  line is not a favorable method, as the natural abundance of  $^{40}\text{K}$  as used in the spectroscopy cell is

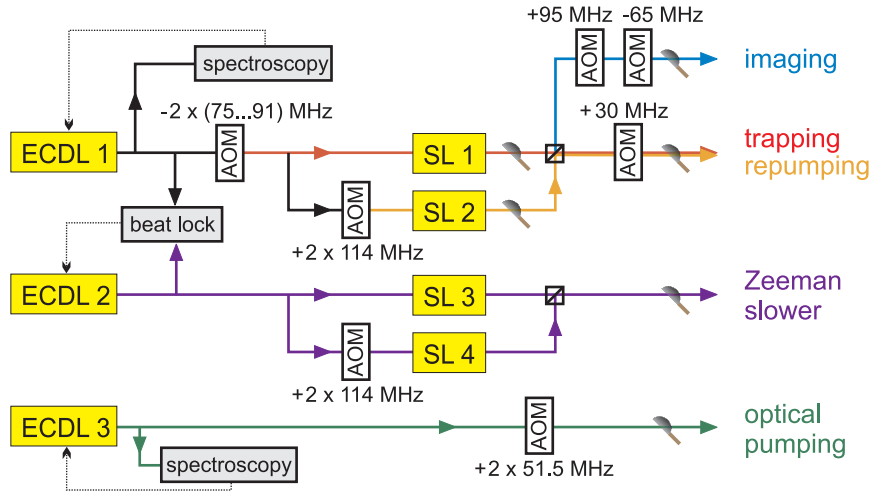


**Figure 3.8:** Laser system for  ${}^6\text{Li}$ . Light is generated by three frequency-stabilized external cavity diode lasers (ECDL 1–3). To obtain sufficient power, four injection-seeded slave lasers (SL 1–4) are used to individually amplify the frequency components that drive the trapping and repumping transitions in the MOT and in the Zeeman slower.

orders of magnitude smaller than that of  ${}^{39}\text{K}$ . Initially, the DFDL technique was also used for this lock but we were not fully satisfied with its longterm stability, in contrast to the situation with the rubidium setup. We therefore switched to a saturated absorption FM lock which is very stable with respect to temperature and slight alignment drifts. The two remaining main beams injection-seed two slave lasers (SL 1 & SL 2, same laser diodes as ECDL). The output frequency of SL 1 is shifted by a double pass AOM close to the trapping transition, whereas the output of SL 2 is shifted by a quadruple pass AOM close to the repumping transition. A quadruple pass AOM is realized with a setup similar to a double pass AOM line but extended by an additional mirror and an optical isolator. After passing individual shutters, the beams are combined on a non-polarizing beam splitter cube. One of the output beams, each of which obviously contains both frequencies, is coupled into the optical fiber connecting the laser table with the setup for optical pumping and imaging on the apparatus table. The other output beam seeds the tapered amplifier chip (Eagleyard, EYP-TPA-0765-01500-3006-CMT03). This semiconductor laser chip increases the power of the trapping and repumping beams from typically 8 mW and 2 mW to a total output power of more than 800 mW. The TA output beam, providing MOT trapping and repumping light, is transferred to the MOT optics setup on the apparatus table via an optical fiber. This single-mode fiber is important to clean the transverse spatial mode of the TA output. Typically the total power of the MOT light after the fiber is 350 mW. As in the rubidium laser system, shutters allow us to block individual laser beams.

#### 3.4.4. Lithium laser system

A schematic plot of the lithium laser system is given in Fig. 3.8. In order to minimize maintenance we chose a setup based on semiconductor laser diodes instead of a dye-laser

system. Sufficient laser power is obtained by using an injection-seeded slave laser individually for each of the four frequencies required for trapping and slowing of lithium<sup>1</sup>. The laser diodes (Mitsubishi, ML101J27) are heated to about 60°C and operated at a current above the specifications to reach the desired wavelength with sufficient power. The lithium laser system was set up largely as part of the diploma thesis of Arne-Christian Voigt [225]. The final system shown in Fig. 3.8 will be described in detail in his PhD-thesis and is only considered briefly in the following: The external cavity diode laser ECDL 1 is frequency locked to the cross-over signal between the  $|2 S_{1/2}, F = 1/2\rangle \rightarrow |2 P_{3/2}, F' = 1/2, 3/2\rangle$  and  $|2 S_{1/2}, F = 3/2\rangle \rightarrow |2 P_{3/2}, F' = 1/2 - 5/2\rangle$  transitions of the  $D_2$ -line. A part of the output beam is branched off and used to offset-lock a second master laser (ECDL 2) to the frequency of ECDL 1. The frequency of the remaining main part is shifted by a double pass AOM line and then split into two beams. One of these beams directly injection-seeds a slave laser (SL 1), the other one is first shifted by the ground state splitting of 228 MHz and then injection-seeds a second slave laser (SL 2). The output of the two slave lasers is combined on a polarizing beam splitter cube. By suitable choice of the polarizations of both beams, the main power is directed into one output port of the cube and coupled with crossed polarizations into the MOT fiber. An AOM in front of the fiber shifts the frequency of the light by a fixed value of +30 MHz and allows for rapid intensity control, a feature that is important for our laser cooling scheme (see Sec. 5.2). The second output beam of the cube passes through a tandem AOM line and provides imaging light. The laser light for Zeeman slowing is derived from ECDL 2. Its output is split into two beams. One of the beams is directly amplified in SL 3, the other one is first shifted by 228 MHz and then amplified in SL 4. The resulting beams are combined on a polarizing beam splitter cube. The frequency of the optical pump laser ECDL 3 is locked to the cross-over signal between the  $|2 S_{1/2}, F = 1/2\rangle \rightarrow |2 P_{1/2}, F' = 1/2, 3/2\rangle$  and  $|2 S_{1/2}, F = 3/2\rangle \rightarrow |2 P_{1/2}, F' = 1/2, 3/2\rangle$  transitions of the  $D_1$ -line. A double pass AOM line shifts the frequency close to the optical pump transition and provides intensity control.

#### 3.4.5. Combining the systems

Since in the magneto-optical trap and in the magnetic trap all three atomic species are usually simultaneously trapped, it is necessary to at least partially combine the optical setups for  $^{87}\text{Rb}$ ,  $^{40}\text{K}$ , and  $^6\text{Li}$ .

For the three-species MOT, we have chosen to use a configuration with three counter-propagating pairs of laser beams containing light at all three wavelengths. The principle of the optical setup is sketched in Fig. 3.9. All necessary laser beams are transferred from the laser table to the apparatus table via single-mode, polarization-maintaining optical fibers. In the case of lithium, trapping and repumping light have orthogonal linear polarizations in the optical fiber, whereas in the other three fibers the laser light is guided with only one single linear polarization. Telescopes after the optical fibers expand the individual beams to appropriate intermediate diameters.

---

<sup>1</sup>Tapered amplifiers for lithium had been available in the past (Spectra Diode Laboratories) but were discontinued a few years before the start of our project. Only recently, TA chips for this wavelength have become commercially available again (e.g. from Toptica Photonics) and might be a choice for a future simplification of the lithium laser system.

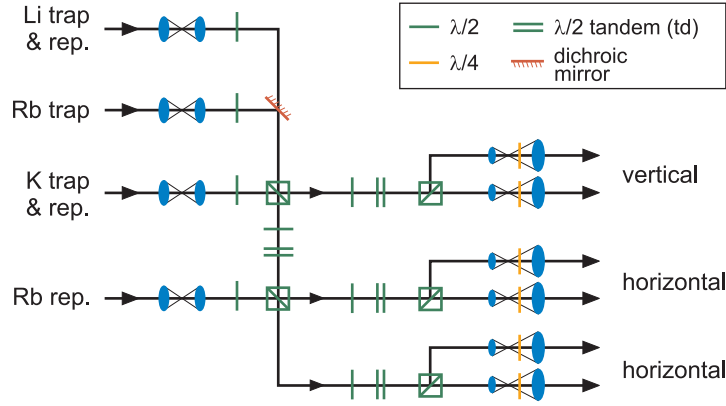


**Figure 3.9:** MOT optics. Light for operation of the three-species MOT is emitted from four single-mode, polarization-maintaining optical fibers. The four laser beams with different wavelengths are combined and redistributed into the six arms of the MOT setup by a dichroic mirror and polarization optics.

Combination of the laser beams and distribution into the six arms of the MOT works as follows. A  $\lambda/2$ -waveplate turns the polarizations of the two-frequency lithium beam to  $45^\circ$  between s- and p-polarization so that both frequencies are split individually with a splitting ratio of 50% at the first polarizing beam splitter cube (PBS). After the first cube, both frequencies have then the same polarization and the power splitting ratios at subsequent PBS can be adjusted for best MOT operation to suitable values as will be explained in the following paragraph. The rubidium trapping beam is combined with the lithium beam at a dichroic mirror that is transmittive for lithium light and reflective for rubidium light. A  $\lambda/2$ -waveplate in front of the dichroic mirror permits us to adjust the power splitting ratio of the rubidium beam at the first PBS. The remaining input port of the same PBS is used to superimpose the potassium beam onto the Li-Rb beam. The potassium power splitting ratio at the PBS can again be adjusted independently by a waveplate in the potassium beam in front of the cube. Rubidium repumping light is added to both horizontal MOT beam pairs at the free port of the corresponding PBS. Finally, a telescope in each of the six arms expands the superimposed MOT beams by a factor of five to  $1/e^2$ -diameters of 15 mm for lithium, 30 mm for potassium, 26 mm for rubidium trapping light, and 33 mm for rubidium repumping light. These diameters are large enough to trap high numbers of atoms in the MOTs and sufficiently small to keep the saturation parameters high for uncritical MOT alignment and operation.

In several positions in the setup for the MOT optics described above, the polarization of the superimposed beams for all three colors has to be turned by about  $45^\circ$  to achieve appropriate power splitting ratios at the subsequent PBS. Achromatic  $\lambda/2$  waveplates, which produce an effective differential phase retardation of  $\pi$  over a broad wavelength range, have only recently become available and are still unavailable with sufficiently large clear aperture for the MOT beams. We therefore use the following solution: First, the polarization of the rubidium light is adjusted using a zero-order  $\lambda/2$  waveplate for 780 nm. This simultaneously adjusts the polarization of the potassium light sufficiently well due to the similarity

### 3. Experimental Setup

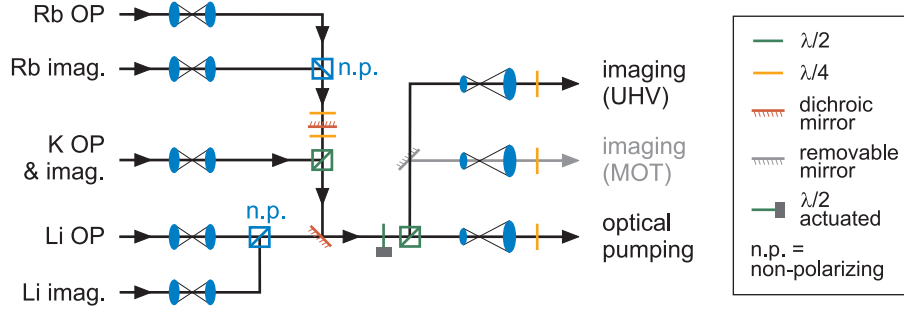


**Figure 3.10:** Optics for detection and optical pumping. The individual beams emitted from single-mode optical fibers are combined using dichroic mirrors and polarization optics. An actuated waveplate and a removable mirror permit us to use the combined beam either for optical pumping or for imaging in any of the two vacuum chambers.

of the wavelengths. A subsequent stack of two additional  $\lambda/2$  waveplates for the 780 nm wavelength mounted together in one rotatable mount with their fast axes aligned (“tandem waveplate”) has no effect on the polarization of the rubidium light. Also the effect on the potassium light is appropriately small. However, the tandem waveplates do have a significant effect on the polarization of the lithium light. By careful selection of the waveplates used in the stacks, we were able to obtain an adjustment range for the polarization of the lithium light that includes the desired power splitting ratio of 50% at the subsequent polarizing beam splitter cube.

The optical setup that provides the beams for optical pumping and imaging of the three species is sketched in Fig. 3.10. All necessary beams are transferred from the laser table to the apparatus table by five different single-mode, polarization-maintaining optical fibers. The fibers are aligned in the azimuthal direction so that all beams have linear p-polarization, except for the potassium beam that has s-polarization. The two rubidium beams are combined on a non-polarizing beam splitter cube. A dichroic mirror that is transmissive for rubidium and reflective for potassium at normal incidence is used in combination with a PBS and two properly aligned  $\lambda/4$  waveplates to add also the originally s-polarized potassium beam with p-polarization. Finally, the two lithium beams are merged on a second non-polarizing beam splitter cube and superimposed to the main beam by means of a dichroic mirror that is transmissive for Li and reflective for K and Rb at about  $45^\circ$  angle of incidence. The resulting linearly polarized beam can be directed into either of the two output ports of a subsequent PBS by a computer controlled removable  $\lambda/2$  waveplate (for details on the actuator and its driver, see Ref. [226]). In addition, a removable mirror allows to switch between imaging in the MOT chamber and imaging in the UHV chamber.

### 3.5. Absorption imaging

Absorption imaging has become a standard technique for the detection of ultracold atomic clouds and is discussed in introductory textbooks and articles, e.g. in Ref. [166]. To obtain the absorption image of an atomic cloud, the sample is illuminated by near-resonant laser light. The atoms partially absorb this light by scattering photons into a solid angle of  $4\pi$

and cast a shadow on the light beam. The shadow is imaged onto a charge-coupled device (CCD) camera. Absorption imaging is a destructive detection method since the atomic ensemble is heated by the incoherent scattering of photons. Alternative non-destructive phase contrast imaging techniques are discussed in Refs. [166, 227] but were not used in this thesis.

### 3.5.1. Principle

In the following brief explanation of absorption imaging we consider, without loss of generality, detection along the  $z$ -axis for ease of notation. Since the intensity distribution of the imaging beam is inhomogeneous, the following imaging procedure is applied for normalization: First, an absorption image  $I_{\text{abs}}(x, y)$  of the atomic cloud is recorded, then a reference image of the intensity distribution  $I_{\text{flat}}(x, y)$  ('flat field') of an identical imaging light pulse but after the cloud has left the field of view, and finally, a background image  $I_{\text{bg}}(x, y)$  (also called 'dark frame') without detection light. The transmitted relative intensity distribution  $T(x, y)$  and the optical density  $OD(x, y)$  can be determined from the three recorded images:

$$OD(x, y) = -\ln T(x, y) \quad \text{with} \quad T(x, y) = \frac{I_{\text{abs}}(x, y) - I_{\text{bg}}(x, y)}{I_{\text{flat}}(x, y) - I_{\text{bg}}(x, y)}. \quad (3.8)$$

This procedure also greatly reduces the influence of residual stray light and stationary interference fringes, which are caused e.g. by multiple reflections in the optical imaging path and appear in  $I_{\text{abs}}$  and  $I_{\text{flat}}$  at the same position. The subtraction of  $I_{\text{bg}}$  further accounts for the dark count rate of the CCD-pixels, which is always present and may vary with temperature and between different pixels. Time-dependent interference fringes, however, e.g. caused by mechanical oscillation of optical components in the imaging path, are obviously not properly canceled and limit the quality of the optical density data. Mechanical stability was therefore an important aspect in the design of the imaging setup.

The optical density and the spatial density distribution of the cloud are connected as follows: When the beam passes through the atomic cloud, photons are spontaneously scattered at a rate per atom given by Eq. (3.2) with a position-dependent saturation parameter  $S_{x,y}(z)$ , if rescattering of scattered photons can be neglected. The relative decrease of the intensity per length unit  $dz$  is then given by

$$\frac{d I_{x,y}(z)}{I_{x,y}(z)} = -n_{x,y}(z) \sigma_{\text{ph}}(z) dz \quad (3.9)$$

where  $n_{x,y}(z) = n(x, y, z)$  is the density distribution of the atomic cloud and

$$\sigma_{\text{ph}}(z) = \gamma_{\text{sc}}[S(z), \delta] \frac{\hbar\omega}{S_{x,y}(z) I_s} = \frac{\Gamma\hbar\omega}{2I_s} \frac{1}{1 + S_{x,y}(z) + (2\delta/\Gamma)^2} \quad (3.10)$$

is the scattering cross section for laser light with frequency  $\omega$  and detuning  $\delta = \omega - \omega_0$  with respect to the atomic resonance frequency  $\omega_0$ . Here, we have assumed that circularly polarized light on the closed imaging transition (see Sec. 3.4.1) is employed. The quantization axis is defined by a homogeneous magnetic field along the imaging axis with a strength of typically about 1 G.

### 3. Experimental Setup

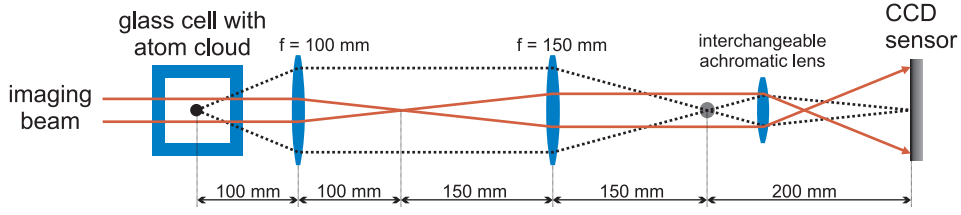


**Figure 3.11:** Setup for absorption imaging at the final trap position. The atomic cloud casts a shadow onto the collimated incident imaging beam. A confocal relay telescope produces an intermediate image outside the glass cell. This intermediate image is further imaged onto a charge-coupled device (CCD) sensor by an achromatic lens. The achromatic lens can be interchanged to realize different magnifications.

If the initial intensity and the detuning of the imaging light fulfill the condition  $S \ll [1 + (2\delta/\Gamma)^2]$ , the scattering cross section simplifies to

$$\sigma_{\text{ph}} = \frac{3\lambda_0^2}{2\pi} \frac{1}{1 + (2\delta/\Gamma)^2} \quad (3.11)$$

where the definition of  $I_s$  was used and where  $\lambda_0 = 2\pi c/\omega_0$  is the wavelength at resonance. Equation (3.9) reduces then to Lambert-Beer's absorption law and the optical density is proportional to the column density  $\tilde{n}(x, y)$ , which is the spatial density of the atomic cloud integrated along the imaging direction:

$$OD(x, y) = \sigma_{\text{ph}} \tilde{n}(x, y) \quad \text{where} \quad \tilde{n}(x, y) = \int n(x, y, z) dz. \quad (3.12)$$

If more than one transition between different Zeeman levels is involved in the imaging process (e.g. detection with  $\pi$  polarized light and more than one photon scattered per atom), an appropriately averaged scattering cross section has to be used.

#### 3.5.2. Optical setup

The optical setup used for imaging atomic clouds in the UHV chamber is shown schematically in Fig. 3.11. A Rayleigh telescope with a magnification factor of 1.5 is used to produce an intermediate image of the cloud outside the glass cell. A third lens images the intermediate image onto the CCD-sensor. The CCD-sensor (Kodak, KAF-0401E) consists of  $768 \times 512$  pixels with a size of  $9 \mu\text{m} \times 9 \mu\text{m}$ . It is part of a commercial camera developed for scientific applications (Apogee, AP1E). An electrically actuated mechanical shutter in the camera housing permits one to block incident light. The magnification of the imaging system can be adjusted by appropriate choice of the focal length and of the position of the third lens. The fine-adjustment of the focus of the detection system is done by imaging a BEC held in the magnetic trap and correcting the longitudinal position of the CCD-camera using a micrometer screw. When we image a cloud along the vertical direction ( $z$ -axis) after sudden release from the trap and subsequent time of flight (TOF), we adjust the longitudinal position of the camera correspondingly so that the imaging system stays focused onto the cloud, which is freely falling in the gravitational field. The magnification was calibrated

with a high-precision test target (Edmund Optics, USAF res target, NT 38-257)<sup>2</sup>. In the experiments, we have used overall magnifications ranging from  $M = 0.3$  to  $M = 7$ . For the  $M = 4.57(6)$  magnification, with which quantum-degenerate atomic clouds were usually imaged, we achieved a resolution of about  $7 \mu\text{m}$ .

With a removable mirror not shown in Fig. 3.11, the line of sight for detection can be chosen either along the symmetry axis of the QUIC trapping potential (x-axis) or perpendicular to it (i.e. along the z-axis). A similar setup for the MOT chamber permits detection of atomic clouds in earlier stages of the experimental sequence with  $M = 0.57$ .

### 3.5.3. Practical aspects

The intensity, detuning and duration of the imaging light pulses have to be chosen appropriately in order to allow a quantitative evaluation of the images. First, if  $S \ll [1 + (2\delta/\Gamma)^2]$ , the column density is proportional to the measured optical density, as discussed above<sup>3</sup>. Second, for dense clouds a non-zero detuning has to be used in order to keep the peak optical density well below the maximum detectable value of typically 4. For small, dense samples, however, non-zero detunings result in a degradation of the image quality by false absorptive signals due to refraction of the detection light [166]. Therefore, such samples, e.g. quantum-degenerate atomic clouds, are usually imaged after an appropriate TOF, during which the gas freely expands. Third, the duration of the imaging light pulse is limited by blurring of the recorded image due to recoil-induced motion of the atoms [166]. If a dilute atomic cloud that is initially at rest scatters  $N$  photons per atom during the duration  $\Delta t$  of the imaging pulse, each atom gains on average a velocity  $Nv_{\text{rec}}$  along the direction of the imaging beam due to absorption of the photons; in addition, the atoms gain a mean velocity  $\sqrt{N}v_{\text{rec}}$  along the other directions due to spontaneous emission of the same number of photons<sup>4</sup>. This corresponds to a longitudinal displacement by  $\Delta z = Nv_{\text{rec}}\Delta t/2$  and an additional random displacement by  $\Delta r_{\text{rms}} = \sqrt{N}/3v_{\text{rec}}\Delta t$ . A proper choice of the pulse duration keeps the longitudinal velocity sufficiently low that the resulting Doppler shift may be neglected and that the longitudinal displacement is much smaller than the depth of field of the imaging system. In addition, it assures that the random displacement is negligible compared to the optical resolution of the imaging system. For example, a typical appropriate light pulse for resonant imaging of an expanded rubidium cloud has a duration of  $100 \mu\text{s}$  and a saturation parameter of 0.1, which corresponds to a number of 172 scattered photons, a longitudinal displacement by  $100 \mu\text{m}$ , a maximal Doppler shift of  $0.2\Gamma$ , and a random displacement by about  $6 \mu\text{m}$ .

In order to be able to accurately detect also atomic clouds with very small optical density, we actually do not fix the *duration* of the imaging pulses but their *energy*. The reason is that

<sup>2</sup>Since the test target can obviously not be placed inside the vacuum chamber, a mirror is placed between the last lens and the glass cell in order to bring the focus position outside of the cell and the test target is positioned at the focus position. For imaging along the horizontal directions, the magnification can alternatively be calibrated by observing the position of an atomic cloud accelerated by gravity after release from the trap.

<sup>3</sup>For a larger saturation parameter quantitative evaluation of the data is more complicated and requires exact knowledge of the *absolute* intensity of the imaging beam.

<sup>4</sup>Note that photon absorption followed by *stimulated* emission can be neglected for low saturation parameter.

the actually measured physical quantity on the CCD-sensor is not the intensity  $I(x, y, t)$  at a certain time  $t$  but rather the energy density<sup>5</sup>  $e(x, y) = \int_0^{t_{\text{exp}}} I(x, y, t') dt'$  of the light accumulated over the camera's minimum exposure duration of 20 ms. It is obvious from Eq. (3.8) that a reliable determination of the line density  $\tilde{n}(x, y)$  is only possible, if the energy density  $e(x, y)$  in the incident beam is identical for the light pulses in the absorption image and in the reference image. Stabilization of the pulse energy is achieved by recording the power of the incident imaging beam on a photodiode and switching off the light pulse when a preset integrated energy is reached (for details, see the diploma thesis of Wolfgang Wieser [226]). This approach greatly improved imaging for very dilute atomic clouds [226].

## 3.6. Magnetic trapping

Magnetic trapping is one of the key components of our experimental concept as already mentioned in Sec. 3.1. This section introduces the basic principle of magnetic trapping. It further explains the application of this technique for transfer of the atomic clouds from the MOT vacuum chamber to the glass cell and for confinement of the atoms in the QUIC trap.

### 3.6.1. Principle of magnetic trapping

The principle of magnetic trapping of atoms is based on the interaction of the magnetic moment  $\boldsymbol{\mu}$  of an atom with an external magnetic field  $\mathbf{B}(\mathbf{r})$ . The interaction energy

$$E(\mathbf{r}) = -\boldsymbol{\mu} \cdot \mathbf{B}(\mathbf{r}) \quad (3.13)$$

results in a force that drives the atom towards a minimum or a maximum of the magnetic field depending on the orientation of  $\boldsymbol{\mu}$  with respect to the field direction. The magnetic moment  $\boldsymbol{\mu}$  of the atom moving at a velocity  $\mathbf{v}$  follows the local direction of the magnetic field  $\mathbf{B}$  adiabatically (i.e. it maintains the relative orientation), if the field direction changes with a rate much smaller than the Larmor frequency  $\omega_L = \mu B / \hbar$ :

$$\left| \frac{d \mathbf{B}}{dt} \frac{\mathbf{B}}{B} \right| = \left| (\mathbf{v} \cdot \nabla) \frac{\mathbf{B}}{B} \right| \ll \omega_L. \quad (3.14)$$

If this adiabaticity condition is violated, spin flips occur resulting in atom loss from the trap ("Majorana losses") [228].

For weak magnetic field, the interaction energy from Eq. (3.13) for an alkali atom in the hyperfine ground state  $|F, m_F\rangle$  is well described by the linear Zeeman effect

$$E = m_F g_F \mu_B |\mathbf{B}(\mathbf{r})|, \quad (3.15)$$

where  $g_F$  is the Landé g-factor of the hyperfine state. Atoms in states with  $m_F g_F > 0$  ("low field seekers") are driven towards minima of the magnetic field and can be trapped. Atoms in states with  $m_F g_F < 0$  ("high field seekers"), however, cannot be magnetically trapped since Maxwell's equations do not allow a magnetic field maximum in free space [229]. At higher magnetic field, where the Zeeman energy becomes of the order of the hyperfine

---

<sup>5</sup>multiplying by the quantum efficiency of the CCD-sensor at the respective wavelength

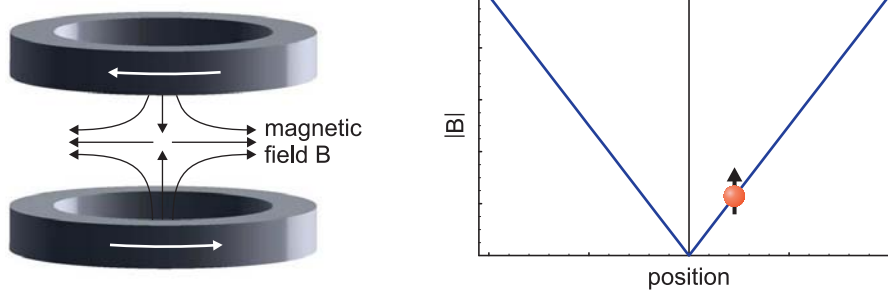


**Figure 3.12:** Magnetic quadrupole trap. Two coils with aligned axes carry opposite currents and create a magnetic field that vanishes at the center and whose absolute value increases linearly in all directions.

energy, the interaction energy  $E = E_{F,m_F}(B) - E_{F,m_F}(0)$  for ground state atoms with vanishing orbital angular momentum can be expressed in terms of the total internal and potential energy  $E_{F,m_F}(B)$  given by the Breit-Rabi formula [230]. In our experiment, we trap  $^{87}\text{Rb}$ ,  $^{40}\text{K}$ , and  $^6\text{Li}$  atoms in their respective magnetically trappable, doubly polarized ground state. In this state, all spins are aligned so that the quadratic Zeeman shift is absent and the validity of Eq. (3.15) extends to large magnetic fields.

### 3.6.1.1. Magnetic quadrupole trap

The simplest magnetic trap is realized by a pair of coils separated by a distance  $d > 0$  with aligned symmetry axes and opposing currents (see Fig. 3.12). The magnetic fields of the two coils cancel at the center of the trap and the leading contribution in a multipole expansion of the total field  $\mathbf{B}(\mathbf{r})$  is the linear term. The absolute value of the field in first order is thus given by

$$B(\mathbf{r}) = \sqrt{\left(\frac{\partial B_x}{\partial x} x\right)^2 + \left(\frac{\partial B_y}{\partial y} y\right)^2 + \left(\frac{\partial B_z}{\partial z} z\right)^2} \quad (3.16)$$

and increases in all directions linearly with the distance from the trap center. The solenoidality of the magnetic field, required by Maxwell's equations, demands  $\text{div } \mathbf{B} = \frac{\partial B_x}{\partial x} + \frac{\partial B_y}{\partial y} + \frac{\partial B_z}{\partial z} = 0$ . Any quadrupole field is therefore fully described by the field steepness  $B'_z = \frac{\partial B_z}{\partial z}$ , the aspect ratio  $A = \frac{\partial B_y}{\partial y} / \frac{\partial B_x}{\partial x}$ , and the position of its center. In the special case of two circular coils oriented along the  $z$ -axis, the rotational symmetry results in  $A = 1$  and  $\partial B_z / \partial z = 2 \partial B_y / \partial y$ .

Since at the center of a quadrupole trap the magnetic field vanishes and switches direction, atoms passing too close to the trap center do not fulfill the adiabaticity criterion Eq. (3.14) and are lost due to Majorana spin flips. For an atom moving at a velocity  $v$ , the effective size of this loss region is  $r_{\text{flip}} = \sqrt{\hbar v / \pi \mu B'_z}$  [166]. The loss rate is small as long as the cloud radius is much larger than  $r_{\text{flip}}$ . The temperature dependence of the cloud size and of the thermal velocity of the atoms results in a  $B_z'^2 / mT^2$ -dependence of the loss rate [231]. For  $^{87}\text{Rb}$  atoms confined in a quadrupole trap with a typical gradient of 140 G/cm,

Majorana losses are negligible for temperatures above  $50 \mu\text{K}$ ; the safe temperatures for  $^{40}\text{K}$  and  $^6\text{Li}$  are correspondingly higher due to the lower masses.

#### 3.6.2. Magnetic transport

The spatial separation between the MOT and the final magnetic trap is bridged by a magnetic transport mechanism, which is based on the concept first demonstrated in Ref. [142]. The magnetic transport avoids the need for a second MOT with the corresponding optics at the position of the final trap and therefore contributes to the excellent optical access to the quantum-degenerate clouds. This section briefly discusses the principle and presents key aspects of the experimental realization.

##### 3.6.2.1. Principle of the magnetic transport

The basic idea of the magnetic transport mechanism consists in trapping an atomic cloud in a quadrupole potential and shifting the potential together with the confined atomic cloud. This can be achieved either by mechanically shifting the coil pair that generates the trapping potential [201, 232, 233] or by regulating the currents in a chain of partially overlapping coil pairs that are mounted at fixed positions [142]. The latter approach, which is used in our experiments, avoids mechanically moving parts, is very reproducible and permits excellent optical and mechanical access to the glass cell.

The principle of this method is based on the fact that two partially overlapping quadrupole coil pairs generate a quadrupole potential again, if they carry currents with the same direction. When the current is decreased in the first coil pair and increased in the second one, the center of the trap moves in the corresponding direction. Consequently, a chain of quadrupole coil pairs that partially overlap the respective neighboring coil pairs can be used to transport atoms over a macroscopic distance. A disadvantage of this simple scheme is that the aspect ratio  $A$  varies significantly during the transport process. As the atoms are transported from one circular coil pair to the following one, it changes from  $A = 1$  at the initial position to a value  $A > 1$  (elongated cloud) in the region between the two coil pairs and back to  $A = 1$  at the final position. Such a modulation of the geometry of the trapping potential can lead to severe heating of the atomic cloud (see measurement in Ref. [142]).

The trapping geometry can be maintained by controlling all three characteristic quantities of a quadrupole potential: the field steepness  $B'_z(t)$ , the aspect ratio  $A(t)$ , and the position  $x(t)$  of its center along the direction of transfer. This is achieved by simultaneously regulating the currents in three consecutive quadrupole coil pairs. The exact required time dependence of the currents depends on the geometry of the chain of coils.

##### 3.6.2.2. Design and simulation

In our setup, the magnetic transport of the atoms over a distance of 39 cm is realized with the coil configuration shown in Fig. 3.13. After preparation in a suitable hyperfine state, the atoms are captured in a magnetic quadrupole field generated by the coil pair that is also used for the MOT (“MOT coils”). By means of a series of 11 transport coil pairs, the atomic cloud is subsequently transported to a quadrupole trap centered at the

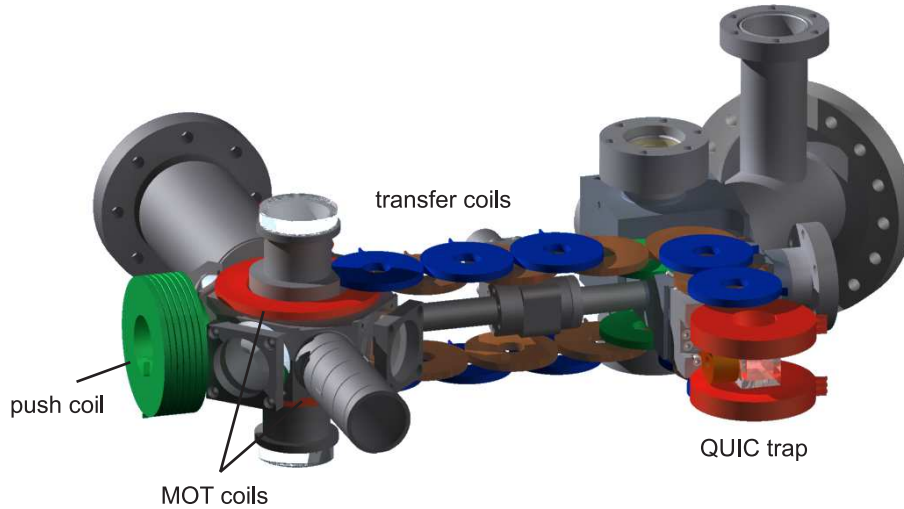


**Figure 3.13:** Magnetic transport. Atomic clouds are transferred with minimal excess heating from the MOT-position into the glass cell by driving a chain of 13 quadrupole coil pairs and an additional push coil with suitable current waveforms.

glass cell. The corresponding coil pair together with a third coil (and a pair of additional compensation coils) forms the final Quadrupole-Ioffe-configuration trap [144] (QUIC trap, see Sec. 3.6.3), which we use to produce the quantum-degenerate gases. A  $90^\circ$  corner in the transport track after 26 cm permits unperturbed optical access from six perpendicular directions to the final trapping position.

Due to the larger diameter of the MOT coils this setup of 13 quadrupole coil pairs would result in a large aspect ratio of the atomic cloud on the section between the MOT coils and the first transport coils (or require large and negative currents to keep the aspect ratio low). This difficulty is overcome by using an additional coil (“push coil”, left green coil in Fig. 3.13). It is mounted opposite to the transfer coils with its axis oriented along the transfer direction and permits us to shift the center of the first quadrupole trap towards the first transfer coil pair at the beginning of the magnetic transport sequence.

In order to keep the electrical power dissipated in the transport coils low, the distance between the two coils of each coil pair should be small. The magnetic field gradient produced by two circular coils with radius  $a$  and separated by a distance  $2d$  scales as  $a^2d/(a^2 + d^2)^{5/2}$  [234]. Thus, if a quadrupole coil pair is scaled in size, the necessary current for a given gradient scales quadratically with the scaling factor and the dissipated electrical power even with the fourth power of the scaling factor (if the thickness of each coil is kept fixed). With this in mind, the vacuum chamber was designed with a flat shape to allow small MOT and transfer coil distances. The transfer coils are circular and have a pancake-like shape with a very small thickness (see Tab. 3.1) so that for overlapping coil pairs also the coil distance of the outer lying pair can be kept small. They are arranged in two layers above and below the vacuum chambers. The inner coils are separated by a distance of 53.2 mm. Only the last transfer coil pair before the  $90^\circ$  corner (right green coil in Fig. 3.13) is an exception; since it can not be placed in any of the two layers due to geometric constraints resulting from

### 3. Experimental Setup

coil	$a_{\text{inner}}$ (mm)	$a_{\text{outer}}$ (mm)	$tn$ (mm)	$N$	wire (mm <sup>2</sup> )
MOT coils	33.7	51.1	5.5	28	$1.2 \times 2.6$
transfer coils	9.3	30.3	5.4	32	$1.2 \times 2.6$
push coil	20	28.7–43.9	28.1–37.5	140	$1.0 \times 4.0$
QUIC quadrupole	15.3	40.3	9.2	92	$1.0 \times 2.1$
loffe coil	5.15	13.1	18.9	56	$1.0 \times 2.1$
QUIC compensation	5	7.1	5.4	30/31	$0.95 \times 2.6$
Feshbach	64	70.5/93	4.3/8.5	3/14	$4.0 \times 4.0 \times 2.6$

**Table 3.1:** Characteristic parameters of different circular coils. Given are the values of the inner radius  $a_{\text{inner}}$ , the outer radius  $a_{\text{outer}}$ , the thickness  $tn$ , the number of windings  $N$  and the dimensions of the wire used. The push coil has a conical shape and the Feshbach coils have two sections.

the corner, it is mounted inside the inner coil layer. The MOT coils and the transfer coils are made from varnished copper wire with a  $1.2\text{ mm} \times 2.6\text{ mm}$  rectangular cross section. The coils were wound at our institute using custom-built guidings for small production tolerances. The windings are glued with a special epoxy (Polytec GmbH, Duralco 128) that has a high heat conductance of  $5.7\text{ Wm}^{-1}\text{K}^{-1}$ . All transfer coils and the two MOT coils are mounted into two L-shaped holders made of copper. Water from a cooling system flowing through the holders carries away the heat produced due to the Ohmic resistance of the coils. Eddy currents are suppressed by numerous slits in the holders.

The current waveforms for the different coils of the magnetic transport system are calculated in three steps using Mathematica. First, for each position  $x$  of the field minimum along the transfer track the currents in the three respectively closest coil pairs required to obtain a vertical gradient  $B'_z(x) = 1\text{ G/cm}$  and an aspect ratio  $A(x)$  are determined. Starting from the MOT quadrupole coils with  $A = 1$ , the aspect ratio is chosen to increase continuously with  $x$  until it reaches a steady state value of  $A = 1.662$  at  $x = 41\text{ mm}$ . The steady state aspect ratio is fixed by requiring a constant aspect ratio on the transport track to be achieved by positive currents in a maximum number of three coils at any time. This allows us to use a unipolar, three-channel current source (see next paragraph) for driving the magnetic transport. Close to the  $90^\circ$  corner, where the cloud is brought to a halt, the aspect ratio is continuously reduced to  $A = 1$  at the corner and then reincreased to the steady state value. Close to the end of the transport sequence, the different geometry of the QUIC quadrupole coil pair requires a temporary increase of  $A$  to a maximum value of 2.19 before the final relaxation to  $A = 1$  at the end. An additional coil at this position, in analogy to the push coil at the MOT position, would permit one to avoid this temporary change in the aspect ratio but would also reduce the optical access to the final trapping position and is therefore not used. In the second step, the obtained ‘native’ currents waveforms are multiplied by the desired gradient function  $B'_z(x)$  that connects the capture gradient of the initial quadrupole trap with the chosen transfer gradient. The resulting current waveforms for a capture gradient of  $140\text{ G/cm}$  and an identical constant transfer gradient is shown in Fig. 3.14a. In the third step, the final current waveforms  $I_A(t)$ ,  $I_B(t)$ , and  $I_C(t)$  are determined for the chosen position function  $x(t)$  of the trap minimum, which is depicted in Fig. 3.14c and corresponds to a continuous acceleration function  $a(t)$ . The durations of

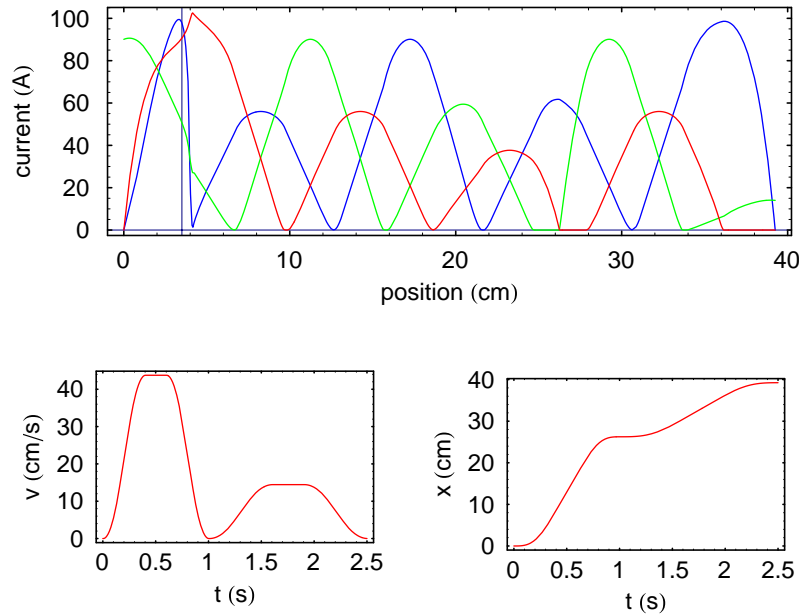


**Figure 3.14:** Magnetic transport sequence. The top graph shows the currents in the three control channels necessary to produce a quadrupole field with given aspect ratio  $A$  and steepness  $B'_z$  at the position  $x$ . At each time, the currents in a set of three neighboring coil pairs are controlled, while the currents in the remaining coil pairs are kept switched off. When the current in one of the coil pairs has vanished, the regulation of this channel is switched to the next coil in the transport chain not yet regulated before. The lower graphs give the time dependence of the velocity  $v(t)$  and of the position  $x(t)$  of the field minimum and correspond to a continuous and smooth acceleration.

the two transfer sections, from the MOT position to the corner and from the corner to the final position, were optimized experimentally by stretching the transfer sequence in time (see Sec. 5.4).

### 3.6.2.3. Current control

A diagrammatic plan of the setup that controls the currents in the coils of the magnetic transport system is shown in Fig. 3.15. The power supply (Lambda, ESS 30-500) is operated in constant voltage (CV) mode and the currents through the individual coils are controlled by several water-cooled MOSFET banks. At any time, the currents through three coils may be regulated to values  $I_A(t)$ ,  $I_B(t)$ , and  $I_C(t)$  set by corresponding analog voltages provided from the experiment control (see Sec. 3.8); the remaining currents are switched off. During the transport, a control logic switches the regulation to the appropriate set of three coils. In order to keep the power dissipation at the MOSFETs below the absolute limit of 1.4 kW, the voltage provided by the power supply has to be dynamically adjusted during the transport sequence. Additional resistors ('matching resistors') of 100 m $\Omega$ , 60 m $\Omega$ , and 40 m $\Omega$  in series with the MOT coil pair, as well as with the first and the second transfer coil pairs, respectively, help to match and smoothly connect the voltage drops in

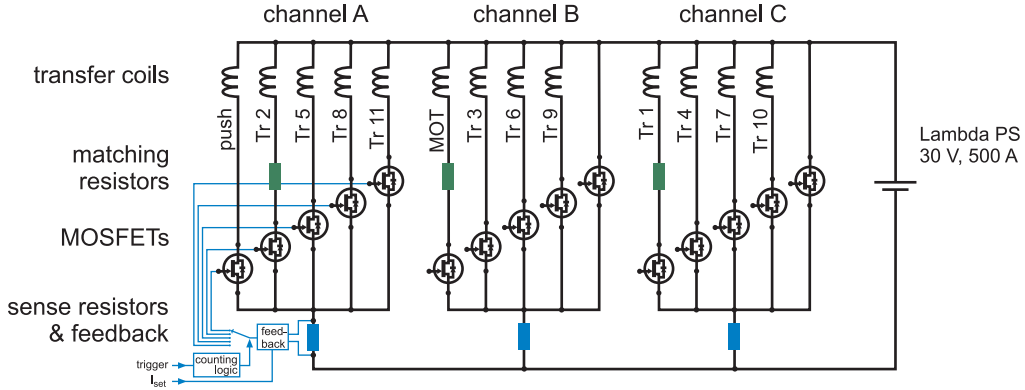


**Figure 3.15:** Diagrammatic plan of the control circuit for the magnetic transport.

the three regulation channels. This avoids destructive peaks in the power dissipation of the MOSFETs during the first part of the transfer.

### 3.6.3. QUIC trap

At low temperatures, atomic samples confined in a pure magnetic quadrupole trap suffer from severe trap loss due to Majorana spin flips, as explained in Sec. 3.6.1.1. Different trapping geometries have been developed in order to circumvent this problem. The TOP-trap [231] employs a time varying magnetic field to create a time-averaged potential with a non-zero magnetic field at the trap center and was used to produce the first Bose-Einstein condensate [6]. In contrast, the “optically plugged trap” [8] uses a static magnetic quadrupole field for confinement and the dipole forces of a tightly focused blue-detuned laser beam to repel atoms from the center of the trap. Finally, in Ioffe-type magnetic traps [203] a magneto-static field with a non-zero minimum is utilized to confine atoms and avoid Majorana losses. In this thesis, a QUIC trap [144] is used, which is a particularly simple and efficient realization of a Ioffe-type trap and can conveniently be combined with the magnetic transport mechanism described above.

#### 3.6.3.1. Trapping potential

The setup of the QUIC trap used for this thesis is shown in Fig. 3.16 a. It consists of a quadrupole coil pair, a Ioffe coil, and a compensation coil pair. At the end of the magnetic transport sequence, the atoms are confined in the magnetic quadrupole field  $B^q$  produced by the current  $I_q$  through the quadrupole coils. In order to transform the quadrupole trap into a Ioffe-type trap, the currents  $I_{\text{Ioffe}}$  and  $I_{\text{comp}}$  through the Ioffe and the compensation coils are increased to the same value as  $I_q$ ; the corresponding magnetic fields are denoted  $B^{\text{Ioffe}}$  and  $B^{\text{comp}}$ . The nearly homogeneous field  $B^{\text{comp}}$  allows us to fine-tune the value  $B_0$  of the magnetic field at the trap center (also called the “trap bottom”). An additional homogeneous field can be created with the Feshbach coil pair. This is used for an improved version of the trap transformation process, which will be discussed in Sec. 5.5.

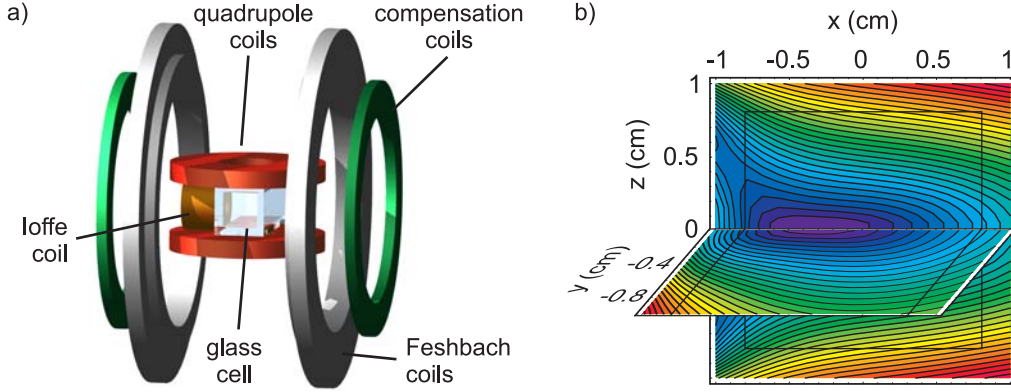


**Figure 3.16:** The QUIC magnetic trap. a) Schematics of the setup with glass cell and quadrupole coils (red), Ioffe coil (orange), compensation coils (green), and Feshbach coils. b) Field distributions in the  $xy$ - and  $xz$ -planes. Isofield lines are separated by 10 G. Thin black lines indicate the walls of the glass cell.

The calculated magnetic field distribution of the final magnetic trap for  $I_q = 30$  A is plotted in Fig. 3.16 b.

Close to the trap center  $\mathbf{r}_0 = (x_0, 0, 0)$ , the field has cylindrical symmetry around the axis of the Ioffe coil ( $x$ -axis) and is well described by

$$\mathbf{B}(x, y, z) = B_0 \begin{pmatrix} 1 \\ 0 \\ 0 \end{pmatrix} + \frac{3}{2}\alpha \begin{pmatrix} 0 \\ y \\ -z \end{pmatrix} + \frac{\beta}{2} \begin{pmatrix} (x - x_0)^2 - \frac{1}{2}(y^2 + z^2) \\ -y(x - x_0) \\ -z(x - x_0) \end{pmatrix}. \quad (3.17)$$

Here,  $2\alpha$  is the axial gradient of the pure quadrupole field and  $\beta = \frac{\partial^2}{\partial x^2} B_x^{\text{Ioffe}}(\mathbf{r}_0)$  is the curvature of  $B_x^{\text{Ioffe}}$  along the trap axis at the trap center. Equation (3.17) describes the magnetic field of the QUIC trap using only three parameters besides the position of the trap minimum. For energies smaller than  $150 \mu\text{K} \times k_B$ , the relative error of this approximation is below 5% at any classically allowed position in the trap. The characteristic parameters of the QUIC trap were measured (see Sec. 5.5.2) to be:  $B_0 = 3.16(3)$  G,  $\alpha = 146.1(7)$  G/cm, and  $\beta = 254.0(5)$  G/cm<sup>2</sup>. For calculation of the field plot Fig. 3.16 b and for simulation of the transformation of the quadrupole trap into the QUIC trap, numerical calculations are used that take into account the exact positions and dimensions of the coils.

**Origin of the potential terms** The origin of the terms in Eq. (3.17) can be easily understood. For symmetry reasons, the radial components of the magnetic field vanish on the  $x$ -axis. Therefore,  $B_x$  has a local minimum at the position  $x_0$  along the  $x$ -axis where the slopes of  $B_x^{\text{Ioffe}}$  and  $B_x^q$  cancel (the slope of the compensation field can be neglected). In the vicinity of the trap minimum, the  $x$ -component of the magnetic field of the Ioffe coil is thus well approximated by  $B_x^{\text{Ioffe}}(x, 0, 0) \approx B_0^{\text{Ioffe}} - \alpha(x - x_0) + \frac{1}{2}\beta(x - x_0)^2$  with  $B_0^{\text{Ioffe}} = B_x^{\text{Ioffe}}(\mathbf{r}_0)$ . In the first term of Eq. (3.17), all homogeneous magnetic fields are combined, and the trap bottom is given by  $B_0 = B_0^{\text{comp}} + B_0^{\text{Ioffe}} - \alpha x_0$ , where  $B_0^{\text{comp}} = B_x^{\text{comp}}(\mathbf{r}_0)$ . The second term in Eq. (3.17) accounts for the field of the quadrupole coils and a contribution from

### 3. Experimental Setup

---

the field of the Ioffe coil, whereas the last term contains only contributions from  $B^{\text{Ioffe}}$ . All these contributions from the field of the Ioffe coil can be obtained from the approximated axial field  $B_x^{\text{Ioffe}}(x, 0, 0)$  by taking into account the cylindrical symmetry and the vanishing divergence and rotation of the Ioffe field.

**Harmonic approximation** A Taylor expansion of the absolute value of the total magnetic field given by Eq. (3.17) up to quadratic order in the distance from the trap center yields

$$B(\rho, z) = B_0 + \frac{1}{4} \left( \frac{9\alpha^2}{2B_0} - \beta \right) \rho^2 + \frac{1}{2} \beta (x - x_0)^2 \quad (3.18)$$

where  $\rho = \sqrt{y^2 + z^2}$  is the radial distance from the trap axis. For a spin-polarized ensemble of atoms in the state  $|F, m_F\rangle$  with temperature  $T$ , the harmonic approximation Eq. (3.18) may be used in Eq. (3.13) to describe the trapping potential, if  $k_B T \ll \mu_B g_F m_F B_0$ . The corresponding harmonic trapping frequencies are

$$\omega_x = \sqrt{\frac{\mu_B g_F m_F}{m} \beta}, \quad \omega_\rho = \sqrt{\frac{\mu_B g_F m_F}{m} \left( \frac{9\alpha^2}{4B_0} - \frac{\beta}{2} \right)}. \quad (3.19)$$

For the typical case of strong radial confinement the radial trapping frequency is dominated by the term  $\alpha^2/B_0$  and can hence be adjusted by changing the trap bottom  $B_0$  via the compensation coils.

#### 3.6.3.2. Trap design

The dimensions of the QUIC trap and of its individual coils were designed using a numerical simulation. The final parameters of the coils are summarized in Tab. 3.1. The coils were produced at our institute in the same way as the MOT and transfer coils. They are mounted into water-cooled metal holders which are installed on a small bread-board. The coil holders and the bread-board are slit to suppress eddy currents and to allow fast switch-off of the magnetic trap. The solid setup of the QUIC trap and its mechanical separation from the transfer setup ensure a stable position of the center of the magnetic trap. This will be important for reproducible and efficient transfer of atomic clouds from the magnetic trap into an optical trap in future experiments. The fields of the individual coils and of the complete QUIC setup were measured with a calibrated Hall probe and show excellent agreement [235] with the calculations.

The total power dissipation of our QUIC trap is only 510 W at the typical current of 30 A. In combination with the water-cooling system, this permits long trapping times without overheating of the trap coils. This turned out to be an important technical feature for the success of our experiment since the small  ${}^6\text{Li}$ - ${}^{87}\text{Rb}$  interspecies scattering cross section requires long trapping durations for sympathetic cooling of  ${}^6\text{Li}$  (see Ch. 6).

#### 3.6.3.3. Trap control

The magnetic trap is controlled by the electronic setup outlined in Fig. 3.17. A commercial power supply (Delta Elektronika, SM45-70D, max. 53 V/70 A) delivers and stabilizes the

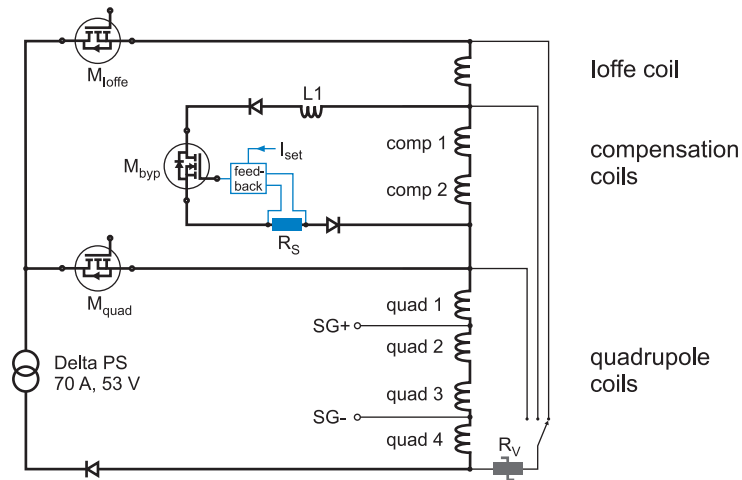


**Figure 3.17:** Control circuit of the magnetic trap. The seven coils of the QUIC trap carry currents of up to 30 A. The currents are controlled by a programmable power supply and three MOSFETs. One of the MOSFETs is part of a feedback loop that permits us to precisely adjust the small current that bypasses the compensation coils in order to set the magnetic field  $B_0$  at the trap bottom. A varistor installed in parallel to the respective current carrying coils allows rapid switch-off of the magnetic trap.

overall current. All coils are driven in series to minimize the fluctuations of the magnetic bias field  $B_0$  at the trap center due to current noise of the power supply. Two MOSFETs ( $M_{Ioffe}$  and  $M_{byp}$ ) permit us to switch the overall current and to direct the current either through the quadrupole coils only (path 1) or through all seven coils (path 2). The gate-source voltages  $U_{gs}$  of the two MOSFETs are each set by an analog channel of the experiment control. The characteristic curve of current versus  $U_{gs}$  was measured. Arbitrary waveform control allows us to control the distribution of the total current into the two paths and to smoothly divert it from one path to the other during transformation of the quadrupole trap into the QUIC trap. In addition, any of the two MOSFETs may be rapidly switched off by a transistor that shortens gate and source and that is controlled by a fast digital channel of the experiment control. During switch-off of the coils, a varistor (Epcos, S20K25), which is installed in parallel to the current carrying coils, clamps the induction voltage to an approximately constant value so that the current decreases nearly linearly in time. The switch-off time of the QUIC trap with an initial current of 30 A is 400  $\mu$ s.

The bias field  $B_0$  at the trap bottom may be adjusted by partially bypassing the compensation coils. This is implemented by the bypass circuit sketched in Fig.3.17. The current through the bypass path is measured using a shunt resistor  $R_S$  and compared to a computer-controlled set point. The difference is fed back to a MOSFET  $M_{byp}$  to regulate the bypass current. The value of the inductance  $L1$  in the circuit was fine-tuned to ensure synchronous progression of the currents through the compensation coils and through the bypass path during switch-off of the magnetic trap.

#### 3.6.4. Further magnetic fields

Besides the fields providing the confinement in the magnetic trap a couple of other magnetic fields are important in various stages of the experimental sequence.

##### 3.6.4.1. Offset fields

The MOT chamber and the final magnetic trap are each surrounded by a cage of Helmholtz-like coil pairs in the  $x$ -,  $y$ -, and  $z$ -directions. The individual coils consist of 20 windings. Each coil pair is driven by a separate channel of two custom-designed current sources. The current of each channel can be controlled via a TTL-input and an analog input. The TTL-input allows one to switch between two current set points that can be adjusted manually. The analog inputs permits dynamic control of an optional additional variable current. In the experiment, the two coil cages are used to compensate residual stray fields at the position of the MOT and of the final magnetic trap. In addition, they are employed during optical pumping and imaging to generate additional guiding fields defining the respective quantization axis.

##### 3.6.4.2. Feshbach field

Future experiments exploiting magnetically-tunable Feshbach resonances will require us to apply and control a homogeneous magnetic field of up to several hundred Gauss. For this purpose, a coil pair in almost exact Helmholtz configuration was set up already in the current apparatus. These Feshbach coils are arranged to generate a field that is parallel to the axis of the magnetic trap (see Fig. 3.16). The coils contain only 17 windings each in order to permit fast switching due to a low inductance. They are made of rectangular, hollow copper wire (4 mm  $\times$  4 mm, inner diameter 2.5 mm) to allow efficient cooling by water flowing inside the wire (for further dimensions see Tab. 3.1). The naked wire (Wolverine Tube Europe BV, The Netherlands) was electrically insulated by winding a layer of fiberglass filaments around it (SW Wire Co., USA). The final coils were wound at our institute and glued with epoxy. The Feshbach coils generate a magnetic field of up to 930 G, limited only by the maximum current of 500 A of the power supply. Since the Feshbach field and the magnetic transport system are never used simultaneously, it is possible to employ the same power supply (Lambda, ESS 30-500) for both purposes. Because of the efficient water-cooling, the coils can withstand the maximum current for more than 5 s without considerable heating. Besides their importance for future experiments, the Feshbach coils are already used in current experiments, both in an improved scheme for transforming the quadrupole trap into the QUIC trap (see Sec. 5.5.1) and to help to maintain spin-polarization of the atoms during switch-off of the magnetic trap.

#### 3.7. Radio frequency and microwave sources

The production of quantum-degenerate mixtures requires a number of radio-frequency (rf) and microwave (MW) signals to drive transitions between different Zeeman and hyperfine states in the three species. All these signals need to be dynamically controlled in intensity

and frequency. The technical implementation will be discussed in detail in the thesis of Arne-Christian Voigt and is only briefly described in the following.

For species-selective evaporative cooling of  $^{87}\text{Rb}$ , two different microwave frequencies close to 6.8 GHz are needed simultaneously (see Sec. 6.1.5). The two signals are obtained by splitting the output signal of a commercial MW-source (Systron Donner, 1720, 50 MHz–18 GHz) into two paths and mixing each one individually with a separate rf-signal. The resulting signals are combined and amplified to up to 12 W before being radiated onto the atoms via an appropriate MW-antenna. The MW-generator can be programmed via a GPIB-interface which allows us to preset the output power, a fixed output frequency or a single frequency ramp.

The two rf-signals are obtained from a two-channel rf-source that was built in our group based on a design developed at the AMOLF institute, Amsterdam. Each channel contains a direct digital synthesis (DDS) chip (Analog Devices, AD9854) integrated into a circuit board. The DDS-board can be programmed from within the experiment control software and permits us to generate a sequence of arbitrary linear frequency ramps with output frequencies between 0 MHz and 150 MHz. Each linear ramp is only started upon a hardware trigger which allows one to exactly synchronize the rf-ramps with the remaining components of the experimental sequence. The rf-power can be adjusted by a voltage-controlled attenuator (VCA) and cut off by a TTL-controlled switch.

In order to drive transitions between different Zeeman states (e.g. for rf-evaporation in single-species operation), low-frequency rf-signals are required. For this purpose, the output of the DDS-based rf-source can also be amplified directly to up to 10 W and coupled into an appropriate antenna.

For addressing of the ground state hyperfine transition in lithium close to 228 MHz, an additional commercial signal source (Rohde & Schwarz, SML 01, 9 kHz–1.1 GHz) is employed, which can be programmed via a GPIB-interface. The signal is amplified to up to 12 W and coupled into an appropriate rf-antenna; the final power can be controlled by a VCA. In this thesis work, this signal is used for energy-selective removal of lithium atoms from the magnetic trap (see Sec. 6.3.1.2). In future work, it will also be useful for preparation of the lithium atoms into a specific desired state.

Finally, the potassium hyperfine transition close to 1.3 GHz can be driven by a MW-signal obtained from another commercial frequency generator (Rohde & Schwarz, SML 02, 9 kHz–2.2 GHz). This signal was not utilized in the work presented in this thesis but will be employed in future experiments for state preparation.

### 3.8. Experiment control

Reproducible experiments with quantum-degenerate atomic gases require control over an experimental sequence of a few hundred operations separated by precise time intervals, which vary from  $1\ \mu\text{s}$  to several seconds. In our setup, this is achieved with a dedicated control system that includes several hardware components. Software with a graphical user-interface coordinates the different hardware components and allows for intuitive and flexible programming of the timing sequence. In addition, the software permits on-the-fly analysis of the recorded images and graphical representation of the extracted results. A

### 3. Experimental Setup

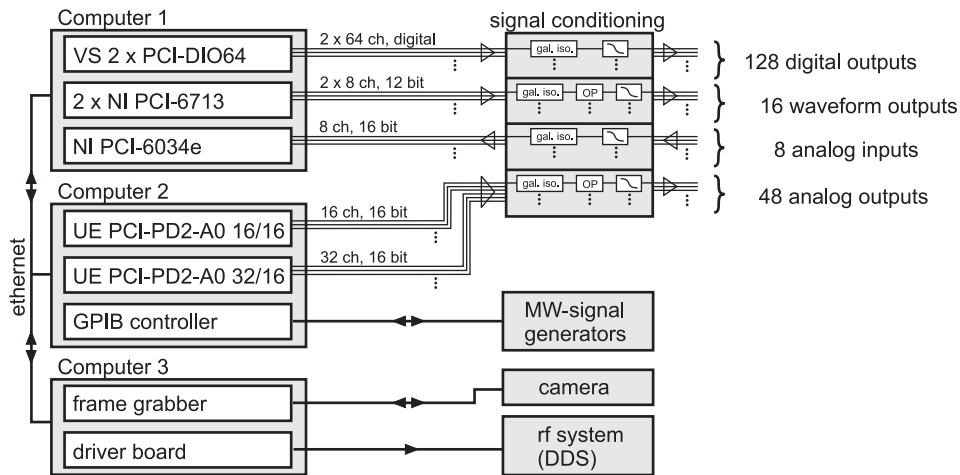


**Figure 3.18:** Schematics of the experiment control. A set of computer I/O-boards and additional signal processing circuits provide accurate, reproducible control over the different components of the experimental apparatus.

diagrammatic plan of the control system is depicted in Fig. 3.18. The hard- and software design is based on an earlier setup developed at the AMOLF institute in Amsterdam. Our hardware system consists of two digital output boards (Viewpoint Systems, PCI-DIO64) in “master-slave” configuration with a total of 128 channels, two analog waveform output boards (National Instruments, PCI-6713) with a total of 16 channels, an 8-channel analog input board (National Instruments, PCI6034e), and two analog output boards (United Electronics, PCI-PD2-A0 16/16 and PCI-PD2-A0 32/16) featuring a total of 48 channels. A GPIB controller permits remote programming of some intelligent devices, e.g. of the microwave signal generators. Images recorded by the CCD-camera (Apogee, AP1-E) are retrieved by a corresponding frame grabber board. A dedicated driver board finally permits control of a digital data synthesis (DDS) system used for the generation of more complex amplitude and frequency ramps in the radio frequency (rf) range. The ten I/O boards are distributed over three computers. Synchronized operation is assured by a common clock source and by the use of external triggering of all components by dedicated digital channels of the master digital output board. A signal-conditioning unit provides (quasi-) galvanic isolation of the digital, analog, and waveform computer boards from the input and output BNC connections. The digital signals can be switched separately to either 0/+5V standard TTL-levels or to 0/+24V (1 A maximum current) output voltage levels, allowing us to directly connect the electro-mechanical beam shutters used in the laser systems. The design of the signal conditioning units offers the option to modify each analog and waveform output signal individually by a simple operation amplifier (OP) circuit (e.g. add an offset voltage, amplify, insert a low-pass filter, and so forth). A BNC cable bus system providing connections between strategic positions in the laboratory permits us to hook up the different devices of the apparatus to the control system in a flexible and convenient way.

## 4. Simultaneous magneto-optical trapping of three atomic species

This chapter reports on the simultaneous trapping of two fermionic species,  ${}^6\text{Li}$  and  ${}^{40}\text{K}$ , and a bosonic species,  ${}^{87}\text{Rb}$ , demonstrating the first three-species magneto-optical trap (“triple MOT”). The single-species MOTs and the triple MOT are characterized. In triple-MOT operation, typical atom numbers of  $3.2 \times 10^7$  for  ${}^6\text{Li}$ ,  $1.5 \times 10^7$  for  ${}^{40}\text{K}$ , and  $5.4 \times 10^9$  for  ${}^{87}\text{Rb}$  were achieved. Trap loss due to interspecies collisions was observed. In the following, I describe our way to optimize the triple MOT and turn it into a suitable source for the goal to achieve quantum degeneracy by evaporative and sympathetic cooling.

Parts of this chapter were published in: “Simultaneous magneto-optical trapping of three atomic species”, M. Taglieber, A.-C. Voigt, F. Henkel, S. Fray, T.W. Hänsch, and K. Dieckmann, *Physical Review A* **73**, 011402(R) (2006).

### 4.1. Introduction

Following the demonstration of Bose-Einstein condensation in dilute Bose gases [6–9] and of quantum degeneracy in dilute Fermi gases [10–15], numerous recent experiments focused on the production of ultracold molecules [95–98, 236] using Feshbach resonances. Molecules consisting of two loosely bound fermionic atoms proved to be exceptionally stable against molecular decay [95, 96, 98, 112], in contrast to the bosonic case [48, 102–104]. The demonstration of Bose-Einstein condensation (BEC) of these Fermi-Fermi molecules [15, 99, 114], the observation of fermionic condensates of generalized Cooper pairs [115, 116], and their superfluidity [122] marked milestones in the physics of ultracold molecules. However, all these experiments were based on diatomic molecules composed of two fermions of the same species. Ultracold mixtures of two different fermionic atomic species are expected to provide stable systems for the investigation of long-range pairing interactions, for precision spectroscopy of molecules, or for the study of dipolar interaction between heteronuclear diatomic molecules.

The first important step in producing a quantum-degenerate gas of two different fermionic species is to load the mixture into a magneto-optical trap (MOT). Magneto-optical trapping of neutral atoms was first demonstrated in [2] following a rapid advancement in the relatively young field of laser cooling (see [19–22] and references therein). The principle of the MOT is discussed in a number of articles and textbooks (e.g. in [20, 213, 237]). The basic setup consists of a magnetic quadrupole field and six circularly polarized laser beams. Simultaneous trapping of a bosonic species in addition to the two fermionic species opens the possibility of sympathetic cooling [63, 196, 200] of the two fermionic species by the bosonic one. So far, two-species magneto-optical traps were realized only for Bose-Bose [238–245] and for Bose-Fermi [246, 247] mixtures. However, neither a two-fermion MOT nor a three-species MOT had been demonstrated yet at the time when the work presented

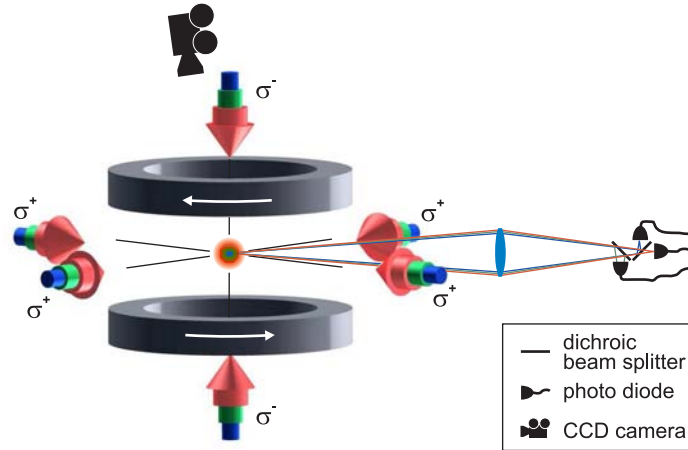


**Figure 4.1:** Setup of the magneto-optical trap (MOT) for three species. A pair of coils carrying currents in opposite directions produce a magnetic quadrupole field. Laser beams with circularly polarized light at the three wavelengths from six perpendicular directions intersect at the center of the quadrupole field; in the graph the helicity of the beams is indicated relative to the respective propagation direction. The laser light is red-detuned with respect to a closed optical transition of the respective species. It captures, traps and cools the atoms by position- and velocity-dependent light forces. A CCD camera is used for absorption imaging of the clouds. Fluorescence light from the atomic clouds is recorded on a separate photo diode for each species.

in this chapter was carried out and published [143]. In the meanwhile, two other groups have also succeeded to realize MOTs for simultaneous trapping of two different fermionic species [248, 249].

## 4.2. Experimental setup

In the experiment, the MOTs for all three species are produced in a steel vacuum chamber (“MOT chamber”) at the center of a common magnetic quadrupole field. The setup is schematically illustrated in Fig. 4.1. For loading of the rubidium and potassium MOTs we use atomic vapor dispensers. In order to make loading efficient, these dispensers are placed only 4 cm away from the center of the MOT chamber pointing towards the capture region of the MOTs. This loading configuration does not rely on a sufficient atom mobility on the chamber walls, as it would do in the case of loading from a remote reservoir. The central trapping region of the MOTs is mechanically shaded from the direct atomic flux from the dispensers. For rubidium, we use commercial dispensers (SAES Getters). For potassium, however, dispensers are commercially available with  $^{40}\text{K}$  only in the natural abundance of 0.012%. We therefore use home-built dispensers [10] with enriched potassium (3% abundance of  $^{40}\text{K}$ ). In the case of lithium, vapor loading would be inefficient due to its comparatively low saturation pressure and due to the small fraction of atoms at velocities below a typical capture velocity of the MOT. For this reason, the lithium MOT is loaded from an atomic beam out of a Zeeman slower with a maximum deceleration of the atoms

by 761 m/s as described in Sec. 3.3.2. The atomic beam is produced by an oven filled with  ${}^6\text{Li}$  at almost pure abundance. It is collimated by two tubes of 6 mm diameter and with lengths of 16.5 cm and 13 cm, both located between oven and Zeeman slower. Pumping between the two tubes limits the background gas load from the lithium oven into the MOT chamber.

The laser system used for the work reported in this chapter is not described in detail here, since it was very similar to the system delineated in Sec. 3.4. The main difference consisted in the fact that lower laser powers were available at that time. For lithium, the high-power laser diodes used in the final system were not commercially available yet and diodes with lower output power (Panasonic LNCQ05PS) were used. In the case of potassium, we utilized a tapered amplifier chip from M2K (model TA770) with a nominal optical output power of about 500 mW. The waists of the potassium and lithium MOT beams were therefore chosen accordingly smaller than in the final setup used to produce quantum-degenerate gases.

The atoms are detected with two different methods: fluorescence detection and standard absorption imaging (see Fig. 4.1). For the first method, the three superimposed MOTs are imaged onto three different photodiodes (“triple photodiode”) so that the fluorescence from the different MOTs can be monitored independently. Separation of the fluorescence light at the three wavelengths is achieved using edge filters and additionally optical band passes (see [225] for details on the photodiode setup). Cross-talk between the three channels is below the noise level of the signals. The atom numbers derived from the MOT fluorescence signals are calibrated by absorption imaging.

## 4.3. Optimization

For the realization of the triple MOT, we optimized its parameters with the goal to produce an optimally cooled rubidium sample with a large atom number. For the experiments described in the following chapters a large rubidium thermal bath for sympathetic cooling of only comparatively small lithium and potassium samples is required.

### 4.3.1. Single-species MOTs

The most obvious constraint imposed on the triple-MOT parameters is that for all three species one common magnetic field gradient has to be applied. We therefore started the optimization process by adjusting the laser detunings for maximum atom number of each single-species MOT at several magnetic field gradients. The achievable atom numbers for lithium and potassium were found to be insensitive to the magnetic field gradient over a wide range. For rubidium we found the number of trapped atoms to be highest at a magnetic field gradient of 16 G/cm (see Fig. 4.2 a). The MOT atom numbers of the three single-species MOTs at this magnetic field gradient as a function of the detuning of the respective trapping light are depicted in Fig. 4.2 b–d. The detuning of the respective repumping light was also optimized for each species.

Table 4.1 summarizes the relevant optimized parameters for the single-species MOTs at the optimized magnetic field gradient. In the case of lithium, we were able to trap  $4.2 \times 10^7$   ${}^6\text{Li}$  atoms at an initial loading rate of  $1 \times 10^8 \text{ s}^{-1}$  in the single-species MOT using a detuning

#### 4. Simultaneous magneto-optical trapping of three atomic species

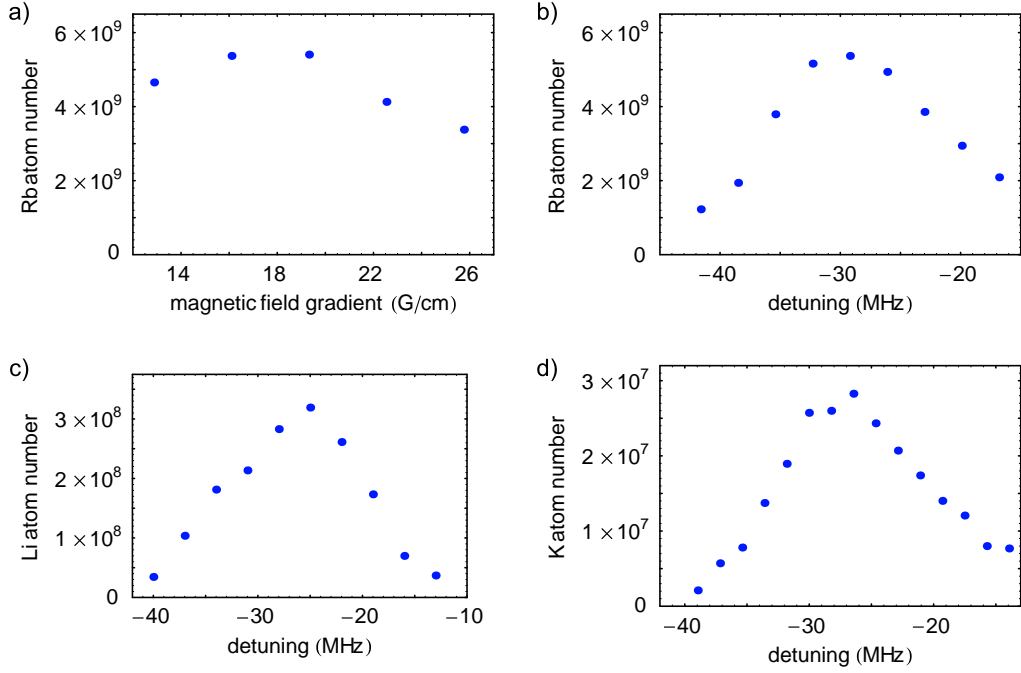


**Figure 4.2:** Optimization of the MOT parameters in single-species operation. a) Atom number in the rubidium MOT for different magnetic field gradients. b)–d) Atom numbers in the three single-species MOTs as a function of the detuning of the respective trapping laser light for a magnetic field gradient of 16 G/cm.

	${}^6\text{Li}$	${}^{40}\text{K}$	${}^{87}\text{Rb}$
$\lambda_{\text{D}_2, \text{vac}}$ (nm)	670.977	766.701	780.241
$\Gamma/2\pi$ (MHz)	5.87	6	6.07
$I_{\text{sat}}$ ( $\text{mW cm}^{-2}$ )	2.54	1.80	1.67
$I_{\text{trap}}/I_{\text{sat}}$	0.7	4	8
$I_{\text{repump}}/I_{\text{sat}}$	0.8	1.1	0.5
$\Delta\omega_{\text{trap}}$ ( $\Gamma$ )	-4.3	-4.2	-4.8
$\Delta\omega_{\text{repump}}$ ( $\Gamma$ )	-4.3	0	0
$N_{\text{single}}$	$4.2 \times 10^7$	$2.6 \times 10^7$	$5.6 \times 10^9$
$N_{\text{triple}}$	$3.2 \times 10^7$	$1.5 \times 10^7$	$5.4 \times 10^9$
$T$ ( $\mu\text{K}$ )	900	40	800 (50)

**Table 4.1:** Characteristic parameters of the three MOTs: Wavelength and width of the  $\text{D}_2$  line, saturation intensity, intensities for trapping and repumping light in each of the six MOT beams, optimized laser detunings, typical atom numbers in single- and triple-MOT operation, and typical temperature (rubidium molasses temperature in brackets).

of  $-4.3\Gamma_{\text{Li}}$  for the repumping and trapping light. The average peak intensity per beam was 0.7 and 0.8 times the saturation intensity  $I_{\text{sat}}$  of the respective transition. In the potassium MOT the peak intensities of the trapping and repumping light were  $4I_{\text{sat}}$  and  $1.1I_{\text{sat}}$ , respectively. The highest atom number of  $2.6 \times 10^7$   $^{40}\text{K}$  atoms and an initial loading rate of  $5 \times 10^7 \text{ s}^{-1}$  in single-species MOT operation were achieved at a detuning of  $-4.2\Gamma_{\text{K}}$  for the trapping light and with resonant repumping light. For the rubidium MOT we used average peak intensities of  $8I_{\text{sat}}$  for the trapping light and  $0.5I_{\text{sat}}$  for the repumping light. In the single-species case we found a maximum atom number of  $N_{\text{Rb}} = 5.6 \times 10^9$  atoms and an initial loading rate of  $8 \times 10^9 \text{ s}^{-1}$  for resonant repumping light and a detuning of  $-4.8\Gamma_{\text{Rb}}$  for the trapping light.

### 4.3.2. Optimization and realization of the Triple MOT

In order to optimize the triple MOT, we started from the optimum parameters for single-MOT operation. The atom numbers were found to be maximal in triple-MOT operation at the same detunings within measurement accuracy as in single-MOT operation. In triple-MOT operation, atom numbers of  $3.2 \times 10^7$  for  $^6\text{Li}$ ,  $1.5 \times 10^7$  for  $^{40}\text{K}$ , and  $5.4 \times 10^9$  for  $^{87}\text{Rb}$  were simultaneously trapped. In comparison to single-MOT operation, this corresponds to a reduction of the steady-state atom numbers of the lithium and potassium MOTs by 24% and 42%, respectively. These losses are attributed to light-assisted collisions (see Sec. 4.5). For the rubidium MOT, however, no significant reduction was observed.

Figure 4.3 depicts a typical time evolution of the atom numbers as inferred from the calibrated fluorescence signals for a particular sequence used to study the triple MOT. It shows the simultaneous trapping of the three species in the triple MOT and illustrates the influences between the different species. During the whole sequence, the trapping light for all three species and the comparatively strong repumping light for lithium were kept switched on. At times  $t < 0$  however, loading of the lithium MOT was avoided by a mechanical shutter blocking the lithium atom beam in front of the Zeeman slower. Loading and trapping of potassium and rubidium were suppressed by keeping the corresponding repumping light switched off. At  $t = 0$  the lithium atom beam shutter was opened and the lithium MOT loaded to its steady-state atom number for single-species MOT operation. After 5 s the potassium repumping light was switched on and the potassium MOT loaded to its steady-state atom number. We could not observe any decrease in the lithium atom number due to the presence of a potassium MOT in any of our measurements. The same holds true for the potassium MOT in the presence of a lithium MOT. However, when the rubidium MOT was loaded by switching the rubidium repumping light on at  $t = 10$  s, the lithium and potassium atom numbers decreased to the steady state values for triple-MOT operation within one second. At  $t = 15$  s, the rubidium MOT was effectively switched off again by switching off the repumping light. The lithium and the potassium MOTs then both regained their initial single-species steady-state atom numbers on a time scale typical for their loading in the single-species MOT operation. The remaining part of this particular sequence illustrates that no significant reduction of atom number in the rubidium MOT due to the presence of the potassium MOT could be observed.

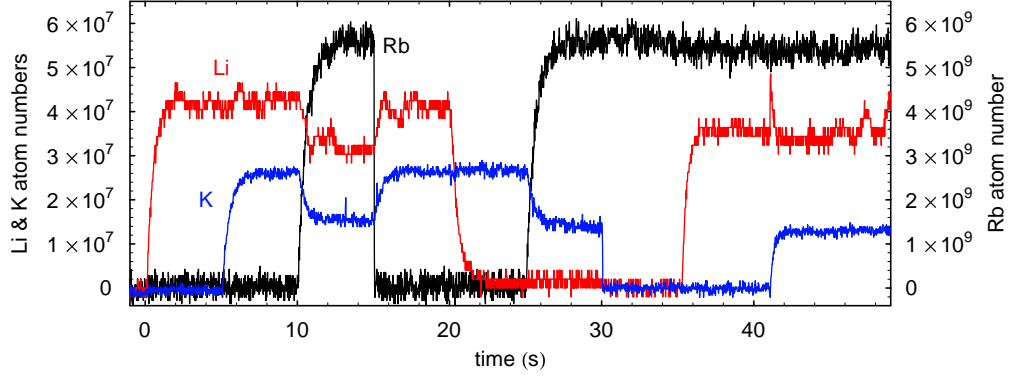


**Figure 4.3:** Typical loading sequence for studying the Li+K+Rb triple MOT. The three species are loaded in different combinations one after the other into the MOT. When the large rubidium MOT is loaded at  $t = 10$  s and again at  $t = 25$  s, the MOT atom numbers of the species already in the trap decrease due to light-assisted interspecies collisions. The atom numbers are monitored by calibrated fluorescence detection.

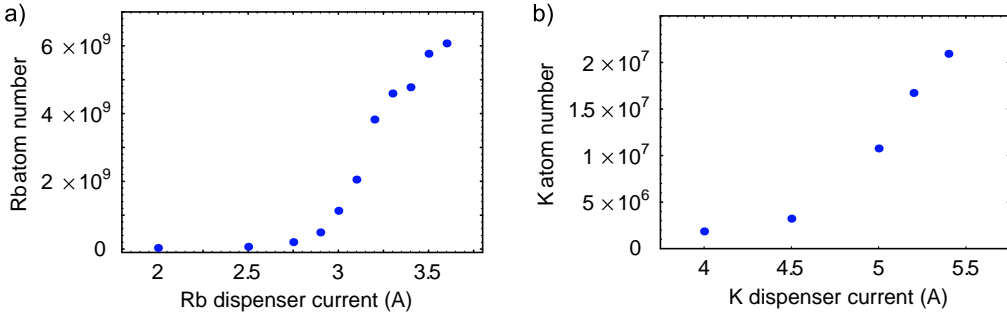


**Figure 4.4:** Steady-state atom numbers of a) rubidium and b) potassium in the MOT as a function of the respective dispenser currents.

### 4.3.3. Dispenser currents

Besides the magnetic field gradient, the three superimposed MOTs share also the same background gas. Since the potassium and rubidium MOTs are directly loaded from the background vapor, suitable partial pressures of the respective atomic species need to be maintained. The  $^{40}\text{K}$  and  $^{87}\text{Rb}$  partial pressures are set by adjusting the electrical current flowing through the corresponding atomic vapor dispenser and thus controlling the temperature of the dispenser (see Sec. 3.3.1).

Figure 4.4 shows that the steady-state atom numbers in potassium and rubidium single-species MOTs increase with increasing dispenser currents within the current ranges studied. The difference in the exact current value at which considerable atom numbers are trapped is due to the different designs and Ohmic resistances of the potassium and rubidium dispensers. In both cases, the increase in atom number with rising current is attributed to an augmented respective partial pressure and a resulting higher loading rate. However, higher partial pressures at the same time lead to faster losses due to collisions of trapped atoms

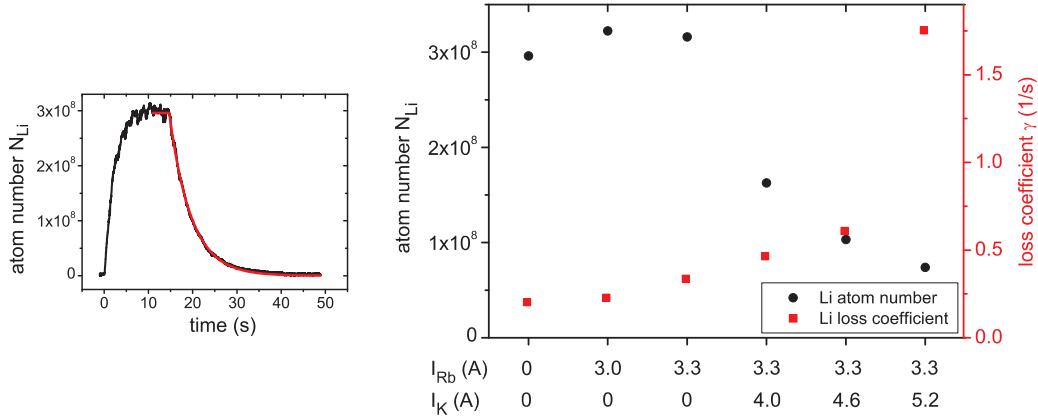


**Figure 4.5:** Influence of the Rb-dispensers and K-dispensers (first generation) on the lithium MOT for different values of the dispenser currents  $I_{\text{Rb}}$  and  $I_{\text{K}}$ . The Rb-dispensers do not significantly affect the lithium MOT. The K-dispensers, however, reduce the Li atom number and the lifetime of the Li-MOT. Therefore, an intermediate value has to be chosen for the K-dispenser current as a compromise between the requirements of the lithium and potassium MOTs. The small inset illustrates how the atom number  $N_{\text{Li}}$  and the loss coefficient  $\gamma$  are determined from the calibrated fluorescence signal of the Li-MOT.

with fast atoms of the background gas. An additional increase in the partial pressure of a species other than the one to be trapped results in a reduced steady-state MOT atom number.

In order to find a good compromise between sufficient loading rates for potassium and rubidium and vacuum requirements we have therefore studied the effects of the potassium and rubidium dispensers on a single-species lithium MOT. For different settings of the dispenser currents, the calibrated fluorescence signal of the lithium MOT was recorded during the loading phase, in steady-state operation, and during the decay of the MOT after MOT loading was suddenly stopped at a time  $t = t_0$  by mechanically blocking the lithium atomic beam. The steady-state atom number  $N_0$  and the loss coefficient  $\gamma$  were deduced from the lithium fluorescence signal by fitting the data for  $t \geq t_0$  with an exponential decay function  $N(t) = N_0 e^{-\gamma(t-t_0)}$ . This is illustrated in the inset of Fig. 4.5. The results of the series of measurements are summarized in the main part of the figure. It was found that the rubidium dispensers have only a very weak effect on the lithium MOT. The lithium atom number is almost constant and  $\gamma$  rises only slightly when the rubidium dispenser current is increased from zero to 3.3 A. The setting of the potassium dispenser current, however, shows a much more dramatic effect on the lithium MOT. The lithium atom number decreases considerably and  $\gamma$  rises steeply already at dispenser currents where the potassium atom number would still strongly benefit from a further increase of the current (compare Fig. 4.4). The first generation of potassium dispensers used for the measurements presented in this chapter was therefore replaced by an improved second generation. For this second generation of dispensers, the problem described above could be reduced considerably by utilizing potassium with a higher abundance in  $^{40}\text{K}$  of 6% and by further improving the

production process (see also Sec. 3.3.1). For the experiments described in the following chapters, the improved dispensers were used.

### 4.4. Optical molasses

Besides the number of trapped atoms, a second important characteristic of the MOT as a source of precooled atoms for further experiments is the temperature of the atomic clouds. Therefore the temperatures of the MOTs in single- and triple-MOT operation were measured. We found the temperatures in the two situations to be identical within measurement accuracy. Typical MOT temperatures were on the order of  $900 \mu\text{K}$  for lithium,  $40 \mu\text{K}$  for potassium, and  $800 \mu\text{K}$  for rubidium. The temperature of the rubidium cloud can be further reduced by applying optical molasses cooling. Optical molasses cooling was first reported in Ref. [250] and is discussed in numerous articles and textbooks, e.g. in Refs. [213, 251–253].

In our setup, a rubidium temperature of typically  $50 \mu\text{K}$  is reached after only 2 ms of polarization gradient cooling in optical molasses with beams in a  $\sigma^+-\sigma^-$  configuration. The potassium temperature could not be further lowered significantly by optical molasses. In the case of lithium, polarization gradient cooling is hindered by the unresolved hyperfine structure in the excited state of the cooling transition, and a molasses phase even led to heating. The short time needed for molasses cooling of rubidium is therefore an important result for the application of the triple MOT, since the lithium and potassium clouds will have to expand freely during the rubidium molasses before they can be recaptured in a magnetic trap. The optimization of the molasses phase leading to these results is briefly described in the following.

#### 4.4.1. Compensation of magnetic stray fields

In order for polarization-gradient cooling in optical molasses to work properly, the magnetic field at the position of the atoms must be sufficiently small. In the experiment, this is achieved by compensating any residual magnetic stray fields (e.g. the earth's magnetic field or small magnetic fields from diverse parts of the apparatus, power supplies etc.) using a cage of coils in Helmholtz-like configuration (see Sec. 3.6.4.1). For each of the three spatial directions, the optimum compensation field is determined by measuring the molasses temperature as a function of the current through the corresponding coil pair using standard time-of-flight (TOF) imaging (see Sec. 4.4.2). Figure 4.6 gives the result of such a measurement together with a parabolic fit to the data indicating an optimum compensation current of about 480 mA for this axis.

#### 4.4.2. Optimization of molasses parameters

The temperature achieved in optical molasses depends on the detuning, the laser intensity and the duration of the molasses phase. These parameters were therefore iteratively optimized. The results are summarized in Fig. 4.7. Graphs a) and b) give the temperature of the rubidium cloud as a function of the detuning and the intensity of the trapping light after 3 ms of optical molasses with the respective other parameter optimized. The final temperature decreases with increasing detuning as expected. If the laser intensity is varied

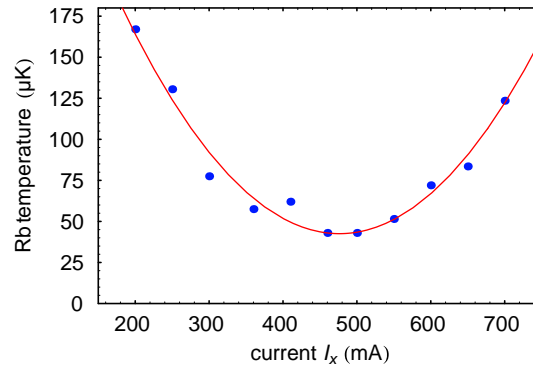


**Figure 4.6:** Compensation of residual magnetic fields at the MOT position. The molasses temperature is minimal for optimal compensation of residual magnetic fields. The field components along the remaining two axes were also compensated.

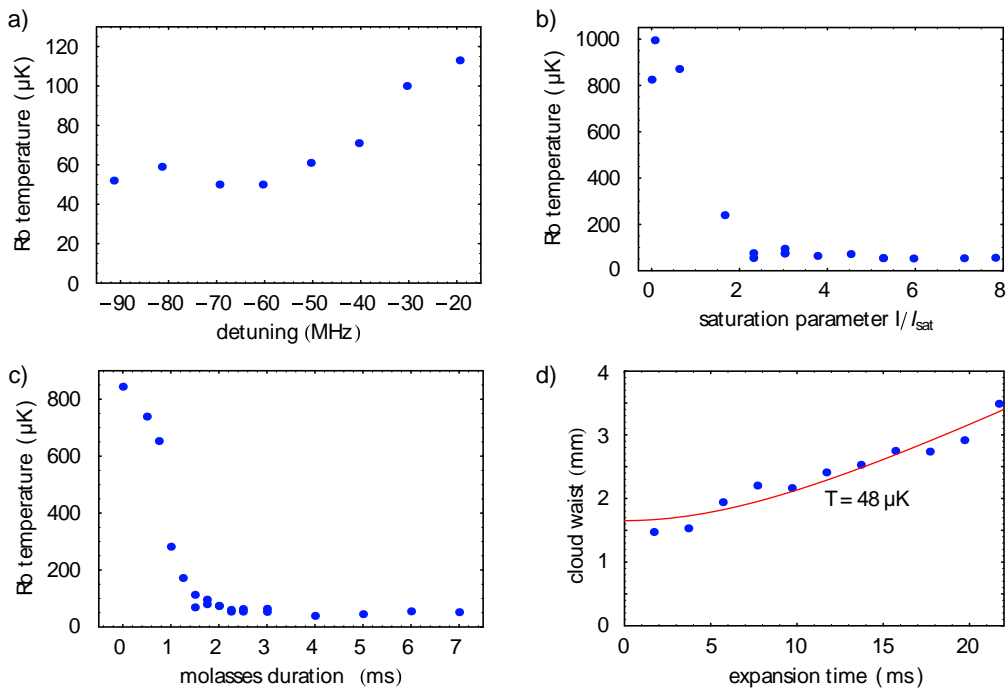


**Figure 4.7:** Optimization of the rubidium molasses. a) Dependency of the molasses temperature on the detuning of the cooling laser during the molasses phase. b) Molasses temperature for different intensities of the cooling laser. c) Molasses temperature versus duration of the molasses phase. d) The temperature of the cloud is determined from the cloud waists for different durations of free expansion after switch-off of the cooling light.

at fixed detuning, the temperature changes only slightly over a wide range of the saturation parameter. The graph shows, however, that molasses cooling breaks down for excessively small intensities. The temperature of the cloud as a function of the molasses duration is presented in graph c): During the first 2 ms it drops rapidly by more than one order of magnitude and then stays almost constant at a value of about 50  $\mu\text{K}$ . Graph d) illustrates by an example how the temperature of the laser-cooled clouds is determined: The laser fields are suddenly switched off and the cloud waist after a variable time of flight  $t_{\text{exp}}$  is measured using absorption imaging. The density distribution of the expanded cloud is a convolution of the approximately Gaussian initial spatial distribution with the Maxwell-Boltzmann velocity distribution of the atoms. For collisionless expansion the TOF density distribution is also Gaussian with a  $1/e^2$ -waist along the  $i$ -axis given by

$$W_i(t_{\text{exp}}) = \sqrt{W_i^2(t_{\text{exp}}=0) + \frac{4k_{\text{B}}T}{m} t_{\text{exp}}^2} \quad (4.1)$$

where  $m$  is the atomic mass and  $T$  is the temperature of the cloud.

## 4.5. Light-assisted collisions

We attribute the decrease of the steady-state atom numbers in triple-MOT operation compared to single-MOT operation to additional losses in the MOTs due to light-assisted collisions between trapped lithium and rubidium atoms and between trapped potassium and rubidium atoms. The main processes leading to these light-assisted losses in MOTs are radiative escape processes and fine-structure changing collisions. An extensive review on experiments and theory in cold collisions can be found in [254].

In order to assess the light-assisted interspecies losses more quantitatively for our situation we studied them in the two-species MOTs Li+Rb and K+Rb. The rate equation for the potassium atom number  $N_{\text{K}}$  in a K+Rb two-species MOT is given by:

$$\frac{dN_{\text{K}}}{dt} = L_{\text{K}} - \gamma_{\text{K}}N_{\text{K}} - \beta_{\text{K}} \int n_{\text{K}}^2 dV - \beta_{\text{K,Rb}} \int n_{\text{K}} n_{\text{Rb}} dV, \quad (4.2)$$

where  $L_{\text{K}}$  is the loading rate and  $\gamma_{\text{K}}$  is the coefficient for losses due to collisions with the background gas. The third term accounts for losses due to collisions between two different trapped potassium atoms and the last term reflects losses due to interspecies collisions of trapped atoms, where  $n_{\text{K}}$  and  $n_{\text{Rb}}$  are the atom number densities of potassium and rubidium, respectively. Because of the comparatively low potassium atom number, the losses due to intra-species collisions can be neglected when compared to the two other loss terms.

Figure 4.8 shows the time dependence of the potassium and rubidium MOT atom numbers in a typical experiment conducted to determine the inter-species loss coefficient  $\beta_{\text{K,Rb}}$ . Initially, the potassium MOT is loaded in single-species operation until the steady-state is reached. The loading rate  $L_{\text{K}}$  and the steady-state atom number  $N_{\text{K}}^{\infty}$  in single-species operation are obtained by fitting

$$N_{\text{K}}(t) = \frac{L_{\text{K}}}{\gamma_{\text{K}}} (1 - e^{-\gamma_{\text{K}} t}) \quad (4.3)$$

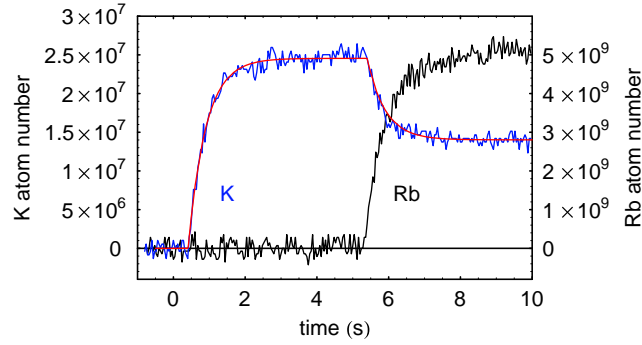


**Figure 4.8:** Measurement of the coefficient  $\beta_{\text{K,Rb}}$  characterizing inter-species losses in the two-species MOT. The graph shows the evolution of the atom numbers of  $^{40}\text{K}$  (blue) and  $^{87}\text{Rb}$  (black) trapped in the MOT as deduced from a calibrated fluorescence signal. The loss coefficient is calculated from the initial  $^{40}\text{K}$ -loading rate obtained from a fit (red), the steady-state atom numbers of potassium in single and two-species MOT operation and from the peak density of rubidium measured by a separate absorption image.

to the first part of the calibrated potassium fluorescence signal. Subsequently, the rubidium MOT is switched on and the corresponding steady-state MOT atom number  $N_{\text{K}}^{\infty'}$  for potassium in two-species MOT operation is determined. Assuming that the rubidium and potassium clouds have Gaussian shapes and that losses due collisions between trapped potassium atoms may be neglected, we obtain for  $N_{\text{K}}^{\infty'}$  the simple relation

$$N_{\text{K}}^{\infty'} = \frac{L_{\text{K}}}{\gamma_{\text{K}} + \beta_{\text{K,Rb}} n_{\text{Rb}}^{(0)} \chi}. \quad (4.4)$$

In this equation,  $\chi = [1 + W_{\text{K}}^2/W_{\text{Rb}}^2]^{-3/2}$  is a factor of order 1 that accounts for the different waists of the potassium and rubidium atom clouds. The peak density  $n_{\text{Rb}}^{(0)} = 1.4 \times 10^{11} \text{ cm}^{-3}$  of the rubidium cloud and the waists of both clouds are determined from absorption images. The coefficient  $\beta_{\text{K,Rb}}$  is then readily expressed in terms of the loading rate  $L_{\text{K}}$ , the steady-state atom numbers  $N_{\text{K}}^{\infty} = L_{\text{K}}/\gamma_{\text{K}}$  and  $N_{\text{K}}^{\infty'}$ , and the peak density  $n_{\text{Rb}}^{(0)}$  as

$$\beta_{\text{K,Rb}} = \frac{L_{\text{K}}}{n_{\text{Rb}}^{(0)} \chi} \left[ \frac{1}{N_{\text{K}}^{\infty'}} - \frac{1}{N_{\text{K}}^{\infty}} \right]. \quad (4.5)$$

Our experimental data for the K+Rb double MOT and analogous measurements for the Li+Rb double MOT yield  $\beta_{\text{K,Rb}} = 1 \times 10^{-11} \text{ cm}^3 \text{ s}^{-1}$  and  $\beta_{\text{Li,Rb}} = 8 \times 10^{-12} \text{ cm}^3 \text{ s}^{-1}$ . These results should be regarded as order-of-magnitude values. They are subject to significant uncertainties arising from the atom number calibration and from the fact that for dense atomic clouds the atom number is not exactly proportional to the fluorescence signal.

## 4.6. Conclusions

In summary, we have demonstrated simultaneous trapping of fermionic  $^6\text{Li}$  and  $^{40}\text{K}$  and bosonic  $^{87}\text{Rb}$  in a three-species MOT. We have presented the apparatus by which we were

#### 4. Simultaneous magneto-optical trapping of three atomic species

---

able to simultaneously confine  $3.2 \times 10^7$   ${}^6\text{Li}$  atoms,  $1.5 \times 10^7$   ${}^{40}\text{K}$  atoms, and  $5.4 \times 10^9$   ${}^{87}\text{Rb}$  atoms. The measured values of the coefficients  $\beta_{\text{K,Rb}}$  and  $\beta_{\text{Li,Rb}}$  associated with inter-species losses in the two-species MOTs show that these losses present no roadblock. This triple MOT is a suitable source of precooled atoms for magnetic transport [142] into an UHV chamber and subsequent evaporative and sympathetic cooling into quantum degeneracy.

## 5. On the road to evaporative cooling

This chapter treats the first half of the experimental sequence that leads to a quantum-degenerate mixture of  ${}^6\text{Li}$ ,  ${}^{40}\text{K}$ , and  ${}^{87}\text{Rb}$ . The purpose of this part of the sequence is to provide optimal starting conditions for evaporative and sympathetic cooling, which will be discussed in Ch. 6. The necessary experimental steps include capture and confinement in a magneto-optical trap, further increase of phase space density by laser-cooling methods, state preparation of the three species, trapping in a magnetic quadrupole trap, and transfer into the QUIC trap. The challenge in the development of a suitable sequence is to combine the different, and in some cases opposing, constraints that the individual atomic species impose on it. The final experimental sequence is described in detail and critical points are discussed. Moreover, exemplary experimental measurements conducted for the development of the optimized sequence are presented. In addition, the final magnetic QUIC trap is characterized. Parts of this chapter were published in Ref. [16].

### 5.1. MOT

The first step in the experimental sequence is to capture and magneto-optically trap the three different atomic species simultaneously at the center of one common magnetic quadrupole field (“triple MOT”). Details of the triple MOT setup and procedure were already discussed in the previous chapter. For the measurements presented in this chapter and the following one, however, the apparatus was extended and the laser systems were upgraded resulting in higher available laser power for lithium and potassium. Therefore, the MOT parameters were again optimized for maximum steady state atom numbers. During the collection phase of the MOT we set an axial magnetic field gradient of 15 G/cm. Rubidium is loaded with resonant repumping light and at a detuning of  $-23$  MHz for the trapping light. The corresponding peak intensities are 0.2 and 8 times the saturation intensity. In the case of lithium, we use detunings of  $-32$  MHz for trapping and repumping light and saturation parameters of 0.6 and 0.5, respectively. Potassium, finally, is captured and trapped in the MOT at detunings of  $-31$  MHz and  $-15$  MHz for trapping and repumping light and with saturation parameters of 3.3 and 0.8. Typical steady state atom numbers in triple-MOT operation are  $N_{\text{Rb}} = 3 \times 10^9$ ,  $N_{\text{Li}} = 5 \times 10^8$ , and  $N_{\text{K}} = 10^7$ .

All three species are loaded simultaneously into the MOT for typically 5–15 s. The magnetic field of the lithium Zeeman slower is switched off 50 ms before the end of the MOT loading phase. This avoids magnetic stray fields during the optical molasses phase, which follows shortly after (see below), and allows the atomic clouds to adjust to the changed magnetic field. For the realization of a triple-degenerate mixture, the number of lithium atoms trapped in the MOT has to be reduced to lower the heat load during sympathetic cooling (see Sec. 6.3). A simple method to fine-tune the lithium atom number, which proved very reproducible in our measurements, is to adjust the time when the lithium

atom beam is blocked in front of the Zeeman slower. After loading is stopped in this way the lithium atom number decays slowly due to the limited lifetime of the MOT. For the triple degeneracy measurements reported in the following chapter the atomic beam was switched off 250 ms before the end of the regular MOT loading phase.

## 5.2. Compressed MOT and temporal dark MOT

For efficient loading into the magnetic trap, it is necessary to obtain low temperatures and high densities for all three clouds simultaneously. In many laser-cooling experiments dealing with one single species, this is achieved in several steps. First, a high number of atoms is captured in the magneto-optical trap at moderate values of the magnetic field gradient and of the laser detuning. For large atom numbers, the central density of the cloud is then limited by reradiation of photons within the cloud and by attenuation of the laser beams [255]. However, the atomic cloud can be transiently compressed in a second step by increasing the magnetic field gradient and adjusting the detuning of the trapping light [256]. Finally, for some atomic species, the temperature can be significantly reduced by switching off the magnetic field and performing optical molasses cooling [250].

In a multi-species experiment compromises have to be made since some parameters, as e.g. the magnetic field, are common to all species simultaneously trapped at the same place. More specifically, polarization-gradient cooling cannot be efficiently applied to  ${}^6\text{Li}$  due to the unresolved hyperfine structure in the excited state of the laser cooling transition whereas it is very effective for rubidium. One therefore has to let the lithium cloud expand freely during a molasses phase for rubidium. A large cloud, however, gains more potential energy than a small cloud when subsequently captured in the field of the magnetic quadrupole trap. Therefore, it is highly desirable to use an experimental sequence that keeps the molasses phase as short as possible but nevertheless results in low temperatures at high atomic densities. The solution that is employed in our experiment consists of a compressed MOT (cMOT) for lithium and a temporal dark MOT (dMOT) followed by a short molasses phase for rubidium and is presented in the following. With this scheme, the phase-space density is increased by more than a factor of five for lithium and by almost two orders of magnitude for rubidium as compared to the MOT. The development of the cMOT/dMOT sequence was a crucial step for the success of the experiment: It allows magnetic transfer of the clouds with little atom loss through a narrow differential pumping tube (see Sec. 5.4) and provides high initial phase space densities for efficient evaporative and sympathetic cooling as described in Ch. 6.

The experimental sequence of the cMOT/dMOT phase is schematically illustrated in Fig. 5.1. During the first part of the cMOT/dMOT phase, the trapped clouds are compressed by linearly ramping the magnetic field gradient to 28 G/cm within 25 ms. In addition, in order to minimize the density-limiting effects of rescattered photons in the rubidium MOT, the rubidium repumper intensity is jumped down to approximately 1% of the saturation intensity at the beginning of the field ramp. The idea behind this temporal dark MOT [257, 258] is very similar to the principle of the more common dark SPOT MOT [259], except that it is applied in time rather than in space: Because of the decreased repumper intensity the rubidium atoms spend most of their time in the  $|F=1\rangle$  ground state

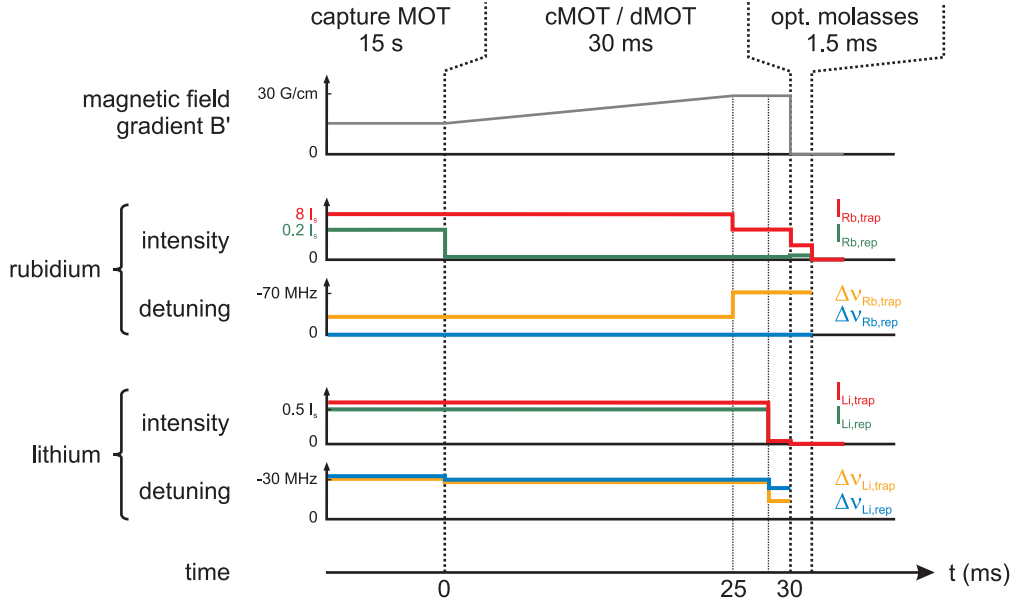


**Figure 5.1:** Experimental sequence to increase phase-space density for the lithium and rubidium clouds at the end of the MOT phase. The sequence is a combination of a compressed MOT and a temporal dark MOT followed by optical molasses for rubidium.

instead of in the  $|F=2\rangle$  ground state and interact only very weakly with the trapping laser light. This reduces the repulsive light forces between the atoms and results in an increased density.

In order to achieve high final phase space densities, this first part of the sequence is followed by further steps that decrease the temperatures of the rubidium and lithium clouds: For the next 5 ms, the detuning of the rubidium trapping light is increased to  $-72$  MHz while the intensity is slightly decreased. During the last 2 ms of this phase, the intensities of trapping and repumping light for lithium are set to approximately 3% of the saturation intensity and detunings of  $-11$  MHz and  $-21$  MHz, respectively, are employed. The detunings and intensities of the potassium light are kept at the values used for MOT loading during the whole cMOT/dMOT phase. For lithium, this scheme increases the density<sup>1</sup> to  $1.5 \times 10^{10} \text{ cm}^{-3}$  and decreases the temperature to typically  $520 \mu\text{K}$ . Both values are improved by more than a factor of two with respect to the MOT. For rubidium, typically a density of  $3 \times 10^{11} \text{ cm}^{-3}$  and a temperature of about  $200 \mu\text{K}$  are achieved at the end of the cMOT/dMOT phase.

The dMOT/cMOT phase is followed by optical molasses cooling for rubidium only. During the molasses phase, the laser parameters are the same as just before, except for the intensity of the trapping laser, which is reduced to 2.5 times the saturation intensity. Because of the comparatively low temperature after the cMOT/dMOT phase, a molasses duration of only 1.5 ms is sufficient to achieve a final rubidium temperature of typically  $45 \mu\text{K}$ , which is a factor 15 lower than the temperature in the MOT. The final density of

<sup>1</sup>The densities and temperatures listed in this section are typical for respective single-species operation. In three-species operation, the MOT atom numbers are lower by less than a factor of two.

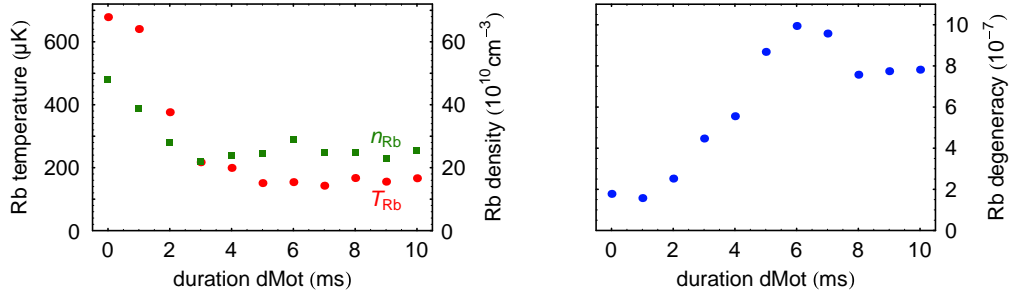


**Figure 5.2:** Example of a measurement for the optimization of the cMOT/dMOT phase. The graphs give the temperature and density of the rubidium cloud together with the corresponding phase-space density (or degeneracy parameter) for different durations of the second part of the cooling sequence described in the text.

approximately  $2 \times 10^{11} \text{ cm}^{-3}$  for rubidium corresponds to a threefold increase with respect to the MOT. We found optical molasses for lithium to lead to heating and optical molasses for potassium to be neither particularly beneficial nor detrimental. In order to keep the experimental sequence as simple and uncritical as possible for a three-species experiment, we therefore do not apply optical molasses for these two species and let the  $^6\text{Li}$  and  $^{40}\text{K}$  clouds expand freely during the rubidium molasses phase. The short duration of optical molasses required to achieve the desired ultralow temperatures in rubidium is thus an important factor contributing to the success of this cMOT/dMOT strategy. Alternative cooling schemes were evaluated but were found to be inferior to the cMOT/dMOT scheme since they resulted in lower final densities and required longer molasses durations to achieve comparable temperatures for rubidium.

The cMOT/dMOT scheme delineated above is the result of a number of optimization measurements. A typical example of such a measurement is illustrated in Fig. 5.2. In this measurement, the duration of the part of the cMOT/dMOT scheme during which the magnetic field gradient is kept constant at 28 G/cm was optimized for the phase space density of rubidium.

### 5.3. State preparation

After laser cooling, the atoms are distributed over all  $m_F$ -Zeeman levels of the ground states. Before they can be efficiently transferred into the magnetic quadrupole trap, they therefore have to be prepared into the desired, magnetically trappable states by means of optical pumping.

#### 5.3.1. Choice of the atomic states

The three species each offer several atomic states that in principle can be magnetically trapped. The energy dependence of the different ground state levels  $|F, m_F\rangle$  of  $^{87}\text{Rb}$ ,  $^{40}\text{K}$ , and  $^6\text{Li}$  as a function of the magnetic field strength  $B$  is shown in Fig. 5.3 for values up to 50 G. In the case of rubidium, the three states  $|F=1, m_F=-1\rangle$ ,  $|2, 1\rangle$ , and  $|2, 2\rangle$  are

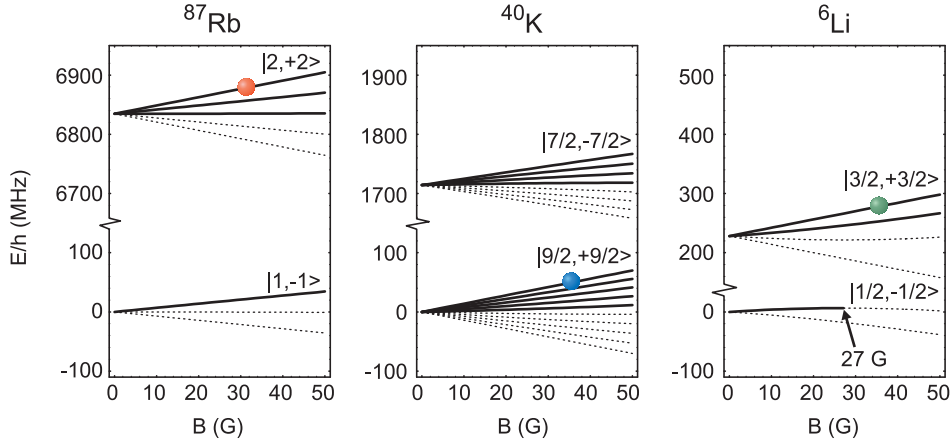


**Figure 5.3:** Choice of a stable mixture of atomic states for magnetic trapping. The graphs show the respective energy splitting of the ground state levels as a function of the magnetic field. Magnetically trappable low-field seeking states are indicated by solid lines, high-field seeking states by dashed lines. The colored balls mark the only combination of magnetically trappable states that is stable against spin-exchange collisions in the three-species mixture.

trapped due to the linear Zeeman effect. In addition, the  $|2, 0\rangle$  state is weakly trapped due to the quadratic Zeeman effect. Potassium offers a wealth of nine magnetically trappable states  $|\frac{7}{2}, -\frac{1}{2} \dots -\frac{7}{2}\rangle$  and  $|\frac{9}{2}, \frac{1}{2} \dots \frac{9}{2}\rangle$ . The trappable states for lithium are  $|\frac{3}{2}, \frac{1}{2}\rangle$  and  $|\frac{3}{2}, \frac{3}{2}\rangle$ . In addition, lithium atoms in the state  $|\frac{1}{2}, -\frac{1}{2}\rangle$  are magnetically trappable for magnetic fields below 27 G but are antitrapped for higher fields due to the quadratic Zeeman effect.

Among the magnetically trappable states, the choice is further limited by requiring stability against depolarization and decay through spin-exchange collisions. In this type of collision (see also Sec. 2.2.1.3), the states of two incoming atoms A and B can change under the conditions  $\Delta l = \Delta m_l = 0$  and

$$\Delta M_F = \Delta (m_F^A + m_F^B) = 0. \quad (5.1)$$

where  $\mathbf{l}$  is the relative angular momentum of the two atoms and  $m_l$  is its projection onto the quantization axis. Spin-exchange collisions are usually the fastest inelastic collision processes for magnetically trapped alkali atoms, unless they are forbidden by these selection rules or energetically suppressed.

Consequently, single-species experiments with  $^{87}\text{Rb}$  in a magnetic trap can be performed either in the doubly polarized state  $|2, 2\rangle$  or in the maximally stretched state  $|1, -1\rangle$ , which are both stable against decay through spin-exchange collisions. Moreover, in single-species experiments with any of the two fermionic species, spin-exchange collisions are suppressed due to the Pauli exclusion principle, as long as only one single atomic state is populated so that the atoms are indistinguishable.

In mixtures, however, the limitations are more severe. In fact, for our three-species mixture the only stable combination of magnetically trappable atomic states is

$$^{87}\text{Rb} |2, 2\rangle \ \& \ ^{40}\text{K} |\frac{9}{2}, \frac{9}{2}\rangle \ \& \ ^6\text{Li} |\frac{3}{2}, \frac{3}{2}\rangle. \quad (5.2)$$

This mixture of doubly polarized states is used in all our experiments with three species in a magnetic trap.

In a Rb-Li two-species mixture, there are two combinations of states that are stable against decay through spin-exchange collisions:

$${}^{87}\text{Rb} |2, 2\rangle \quad \& \quad {}^6\text{Li} |\frac{3}{2}, \frac{3}{2}\rangle \quad (5.3)$$

$${}^{87}\text{Rb} |1, -1\rangle \quad \& \quad {}^6\text{Li} |\frac{1}{2}, -\frac{1}{2}\rangle. \quad (5.4)$$

The first mixture is stable due to the selection rule (5.1). The stability of the second mixtures is based on the fact that all allowed state-changing spin-exchange collisions are energetically suppressed for the relevant temperature range because one of the collision partners would have to end up in the energetically higher-lying ground state manifold. The corresponding Rb-K and K-Li mixtures are not stable since the  $g_F$ -factor of the  ${}^{40}\text{K} |F = \frac{9}{2}\rangle$  manifold has opposite sign than the  $g_F$ -factor of the  ${}^{87}\text{Rb} |F = 1\rangle$  and  ${}^6\text{Li} |F = \frac{1}{2}\rangle$  manifolds. Exothermal spin-exchange collisions are therefore possible for these mixtures.

In a far off-resonant optical dipole trap (ODT) all atomic ground states can be trapped in principle and many different stable mixtures are available. Typically, a homogeneous magnetic field is applied to define a quantization axis. In this case, the selection rules discussed above apply. Here, I will not discuss all possible stable mixtures for this situation but only mention a few cases that might be important for future experiments. In the full three-species mixture, any combination with rubidium and lithium in the absolute ground states and potassium in any  $m_F$ -level of the  $F = 9/2$  manifold is energetically stabilized against depolarization by spin-exchange collision:

$${}^{87}\text{Rb} |1, 1\rangle \quad \& \quad {}^{40}\text{K} |\frac{9}{2}, m_F\rangle \quad \& \quad {}^6\text{Li} |\frac{1}{2}, \frac{1}{2}\rangle. \quad (5.5)$$

The same is of course true for the corresponding lithium-potassium mixture in the ODT. But additionally also the combinations with potassium in the absolute ground state and lithium in any of the two  $m_F$ -levels of the  $F = 1/2$  manifold is energetically stabilized:

$${}^{40}\text{K} |\frac{9}{2}, m_F\rangle \quad \& \quad {}^6\text{Li} |\frac{1}{2}, \frac{1}{2}\rangle \quad (5.6)$$

$${}^{40}\text{K} |\frac{9}{2}, -\frac{9}{2}\rangle \quad \& \quad {}^6\text{Li} |\frac{1}{2}, m_F\rangle. \quad (5.7)$$

Note, however, that although these mixtures do not decay via spin-exchange collisions they can still undergo dipolar relaxation. On the other hand, rate coefficients for dipolar relaxation in alkali gases are typically on the order of a few times  $10^{-15} \text{ cm}^3\text{s}^{-1}$  [181, 182] so that this process is comparatively slow and only becomes relevant at very high atomic densities. For the mixture of absolute ground states, dipolar relaxation is further suppressed at low temperatures due to energetic arguments.

### 5.3.2. Sequence for optical pumping

After the MOT and molasses phases, all cooling laser lights are switched off and the atoms are prepared in the target states for magnetic trapping, Rb  $|F = 2, m_F = 2\rangle$ , K  $|9/2, 9/2\rangle$ , and Li  $|3/2, 3/2\rangle$ , by means of optical pumping (OP). The principle of optical pumping for rubidium and lithium is illustrated in Fig. 5.4. A homogeneous magnetic field of about 9 G

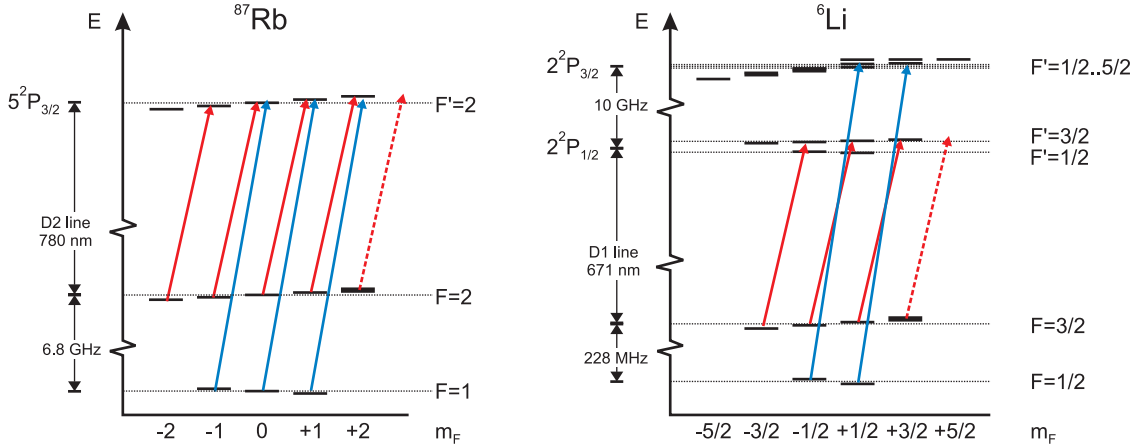


**Figure 5.4:** State preparation for  $^{87}\text{Rb}$  and  $^6\text{Li}$ . Rubidium is optically pumped into the dark state  $|F = 2, m_F = 2\rangle$  using  $\sigma^+$  polarized light on the  $D_2$  line. A similar scheme is used for optical pumping of  $^{40}\text{K}$  into the  $|9/2, 9/2\rangle$  target state. In contrast, lithium is optically pumped on the  $D_1$  line since the target state  $|3/2, 3/2\rangle$  would not be dark for pumping on the  $D_2$  line due to the unresolved hyperfine structure of the  $2^2P_{3/2}$  state.

is applied to define a quantization axis for the magnetic moments of the atoms. Rubidium is then pumped into the target state by driving the  $F = 2 \rightarrow F' = 2$  and  $F = 1 \rightarrow F' = 2$  transitions of the  $D_2$  line with  $\sigma^+$ -polarized light for  $160 \mu\text{s}$  at a typical total intensity of  $2 \text{ mW}/\text{cm}^2$ . The angular momentum of an atom along the quantization axis is increased by  $+\hbar$  for each photon the atom absorbs, whereas it changes by 0 or  $\pm\hbar$  in a subsequent spontaneous emission process. After several absorption-emission cycles the atom therefore ends up in the target state  $\text{Rb}|2, 2\rangle$ . This state is dark for  $\sigma^+$ -polarized light on the pumping transition (assuming perfect polarization), meaning that atoms do not scatter the pumping light anymore once they have reached the target state.

For lithium, however, the target state  $\text{Li}|3/2, 3/2\rangle$  is not dark for optical pumping on the  $D_2$  line. The reason for this is that the hyperfine splitting of the  $2^2P_{3/2}$  manifold is on the same order as the linewidth of the transition so that the  $F = 3/2 \rightarrow F' = 3/2$  transition cannot be addressed individually. For optical pumping of lithium we therefore apply  $\sigma^+$ -polarized light on the  $F = 3/2 \rightarrow F' = 3/2$  transition of the  $^6\text{Li}$   $D_1$  line. Atoms ending up in the lower ground state manifold are repumped into the upper ground state manifold by driving the  $F = 1/2 \rightarrow F'$  transition of the lithium  $D_2$  line. The OP pulse with the two frequency components has a duration of  $300 \mu\text{s}$  and a typical total intensity of  $1 \text{ mW}/\text{cm}^2$ . It is applied simultaneously with the OP pulse for rubidium.

The comparatively large magnetic quantization field used for optical pumping of rubidium and lithium shifts the different Zeeman levels and helps to reduce the depolarizing effect of spontaneously emitted photons. In the case of potassium, however, these Zeeman shifts would result in unacceptably large detunings for the repumping transition (for details, see [235]). After optical pumping of  $^{87}\text{Rb}$  and  $^6\text{Li}$ , the magnetic field is therefore reduced to a strength of about 1 G and  $^{40}\text{K}$  is optically pumped at this lower magnetic field. This is realized by driving the  $F = 9/2 \rightarrow F' = 9/2$  and  $F = 7/2 \rightarrow F' = 9/2$  transitions of the

potassium  $D_2$  line with  $\sigma^+$ -polarized light for  $100\ \mu\text{s}$  at a typical total intensity of about  $2\ \text{mW}/\text{cm}^2$ .

#### 5.4. Magnetic transport into the UHV chamber

After optical pumping, the atoms are captured in a magnetic quadrupole potential generated by the same coils that are also used for the MOT quadrupole field (MOT coils, see Fig. 3.13). In order to attain a longer trap lifetime for efficient evaporative and sympathetic cooling, the atoms are subsequently transferred by a magnetic transport mechanism into the second vacuum chamber, the UHV glass cell, with a residual pressure below  $1 \times 10^{-11}$  mbar. The principle of the magnetic transport mechanism and its technical realization were already discussed in Sec. 3.6.2. The experimental implementation of this sequence includes the choice of adequate magnetic field gradients for capture and transport of the atomic clouds. In addition, an appropriate function  $x_{\min}(t)$  for the time dependence of the position of the trap center during the magnetic transport has to be selected.

The value of the magnetic field gradient that maximizes the final phase space density when a laser-cooled atomic cloud is captured in a magnetic quadrupole trap depends on the initial temperature and density distribution of the sample. In multi-species experiments, the optimum can generally not be achieved for all species simultaneously and compromises have to be made. For the experiments described in the remainder of this thesis, a value of  $140\ \text{G}/\text{cm}$  was used for the capture gradient in the axial, vertical direction. This vertical gradient was maintained for the whole transport sequence; the horizontal gradients change smoothly in the way required by the transfer mechanism (see Sec. 3.6.2). The comparatively large field gradient is necessary to sufficiently compress the atomic clouds for efficient transfer through the narrow differential pumping tube that connects the two vacuum chambers (see Sec. 3.2). This is particularly important for lithium because the temperature of the cloud after laser cooling is about ten times larger than for rubidium or potassium.

The magnetic transport sequence consists of two consecutive sections, from the MOT position to the  $90^\circ$  corner and from the corner to the glass cell. For our experiments, we have chosen a function  $x_{\min}(t)$  that corresponds to continuous, linear ramps of the acceleration  $\ddot{x}_{\min}(t)$ . The function was experimentally optimized by individually stretching the two sections in time. The optimum transfer durations are compromises between heating and atom loss due to collisions of trapped atoms with atoms from the background gas on one hand and heating due to nonadiabatic acceleration and shape changes of the magnetically trapped cloud on the other hand. Typical  $1/e$ -lifetimes of magnetically trapped clouds are  $500\ \text{ms}$  in the MOT chamber and  $60\ \text{s}$  in the glass cell. The exact values vary within a factor of two, depending on the precise settings of the atomic vapor dispenser currents and on the vacuum history. The comparatively short lifetime in the MOT chamber is attributed mainly to collisions of the trapped atoms with particles evaporated from the home-made atomic vapor dispensers for potassium. Contributing factors are that the enrichment of  $^{40}\text{K}$  is limited to 6% (higher enrichments would be extremely expensive) and that the perfect conditions under which commercial dispensers are produced were not available for the production of these dispensers. We found a transfer duration of  $1.0\ \text{s}$  for the first section to be a good compromise between aforementioned requirements. The transfer duration of

the second section is less critical due to the long lifetime in the second vacuum chamber and heating is minimized for durations of 1.5 s and longer. In the experiments, we therefore use transfer durations of 1 s and 1.5 s, respectively, for the two sections.

## 5.5. The QUIC trap

Following the magnetic transport into the glass cell, the atomic clouds are transferred from the quadrupole trap into the final QUIC trap. The non-zero magnetic field at the center of this Ioffe-type magnetic trap strongly suppresses Majorana losses, which is an important precondition for efficient evaporative and sympathetic cooling into the quantum-degenerate regime. This section briefly discusses adiabatic compression of the quadrupole trap and explains the mechanism used to transfer the atoms into the QUIC trap. The section is completed by a characterization of the QUIC trap in the configuration that is used for the experiments described in the following chapter.

### 5.5.1. Loading of the QUIC trap

The transformation of the magnetic quadrupole trap at the end of the magnetic transport into the final QUIC trap consists of three main steps. First, the quadrupole trap is compressed by increasing the field gradient, then the quadrupole potential is transformed into a Ioffe-type potential, and finally the magnetic bias field at the minimum of the QUIC trap potential is ramped to an appropriate value.

#### 5.5.1.1. Adiabatic compression

Efficient evaporative cooling relies on a high elastic collision rate allowing a short thermalization time of the gas. The collision rate can be increased by adiabatic compression of the trap. In an adiabatic compression, the entropy  $S$  and atom number  $N$  are conserved per definition, whereas temperature and density change. Generally, the degeneracy parameter can be written as [260]<sup>2</sup>

$$n_0 \lambda_{\text{dB}}^3 = e^{\frac{5}{2} + \gamma - \frac{S}{Nk_{\text{B}}}} \quad (5.8)$$

where  $\gamma := \left(\frac{T}{V_e}\right) \frac{\partial V_e}{\partial T}$  with the reference volume  $V_e := N/n_0$  defined in Sec. 2.2.2. For a pure power-law trap [155] in the classical regime,  $\gamma$  is identical with the parameter  $\delta = \sum \delta_i$  [192] (as defined in Sec. 2.2.2.2) and thus independent of the temperature of the gas. An adiabatic compression therefore also conserves the degeneracy parameter in this type of trap. It is straightforward to show that the temperature during an adiabatic compression scales as

$$T_f = T_i \left[ \frac{B'_f}{B'_i} \right]^{2/3} \quad (5.9)$$

in a quadrupole trap and as  $T_f = T_i \bar{\omega}_f / \bar{\omega}_i$  in a harmonic trap. Here,  $B'_i$  and  $B'_f$  or  $\bar{\omega}_i$  and  $\bar{\omega}_f$  are the initial and final field gradients or mean trapping frequencies, respectively, and  $T_i$  and  $T_f$  are the corresponding temperatures of the cloud.

<sup>2</sup>Note that  $k_{\text{B}} \equiv 1$  is used in this publication.

In a Ioffe-quadrupole trap, however,  $\gamma$  depends on the temperature of the gas. It can be inferred from Ref. [192] and is given by

$$\gamma_{\text{IQ}} = \frac{\frac{5}{2} + \frac{V_0}{k_{\text{B}}T}}{1 + \frac{2}{3} \frac{V_0}{k_{\text{B}}T}}, \quad (5.10)$$

with  $V_0 = \boldsymbol{\mu} \cdot \mathbf{B}_0$ , where  $\boldsymbol{\mu}$  is the magnetic moment of a trapped atom and  $\mathbf{B}_0$  is the magnetic field at the trap center. Consequently, in this case the degeneracy parameter is not conserved in an adiabatic compression and has to be determined numerically using Eqs. (5.8) & (5.10). For adiabatic transformation of a quadrupole potential into a Ioffe-type potential, the degeneracy parameter decreases by a factor  $e^{-1/2}$  in the limit of high temperature  $T \gg V_0/k_{\text{B}}$ .

In our experiment, the atomic clouds in the quadrupole trap are adiabatically compressed by increasing the axial field gradient from 140 G/cm to 300 G/cm within 2.0 s. This corresponds to a calculated temperature increase by a factor of 1.7.

### 5.5.1.2. Transformation of the trapping potential

Following the compression, the quadrupole potential is smoothly converted into the QUIC potential within 3 s. In the original transformation mechanism described in Ref. [144], the transformation is achieved by continuously increasing the current  $I_{\text{Ioffe}}$  through the Ioffe coil from zero to an appropriate final value. For our specific trap design, the current through the compensation coil pair has to be ramped in parallel to  $I_{\text{Ioffe}}$  in order to obtain a QUIC trap with a bias field of a few Gauss. We could increase the calculated effective trap depth during the transformation process from  $0.9 \text{ mK} \times k_{\text{B}}$  to  $2.1 \text{ mK} \times k_{\text{B}}$  by adding a temporary over-compensation of the trap bias field to this simple scheme. The extended scheme prevents significant loss of atoms from the hot lithium cloud at the walls of the glass cell and is illustrated in Fig. 5.5. Initially, the atoms are confined in a pure quadrupole potential (graph a) with an axial gradient of 300 G/cm, which is generated by the QUIC quadrupole coils carrying a current  $I_{\text{quad}} = 30 \text{ A}$ . The actual transformation scheme consists of two parts. In the first part shown in Fig. 5.5 a)–c), the currents through the Ioffe coil  $I_{\text{Ioffe}}$  and through the compensation coil pair  $I_{\text{comp}}$  are linearly ramped up within 1 s to the same final value of 30 A (for technical details, see Sec. 3.6.3.3). In parallel, an additional homogeneous magnetic field (“over-compensation field”) is linearly increased from zero to 40 G by a corresponding ramp of the current  $I_{\text{over-comp}}$  through the Feshbach coil pair. As the currents are increased, the initially linear potential is bent and a second field minimum appears, see Fig. 5.5 b),c). In the second part of the transformation process displayed in Fig. 5.5 c)–f)  $I_{\text{over-comp}}$  is linearly decreased within 2 s to zero while the remaining currents are maintained. The two potential minima merge resulting in a QUIC trap potential with a bias field of 1.2 G as plotted in Fig. 5.5 f).

The improvement achieved by the over-compensation scheme is clearly visible by comparing graphs Fig. 5.5 d) and Fig. 5.5 g). The graphs show the field distributions for the improved and the simple transformation scheme at the respective critical moment. The critical moment occurs when the effective trap depth is minimal, i.e. when the potential barrier in between the two potential minima has the same height  $E_{\text{critical}}$  as the potential

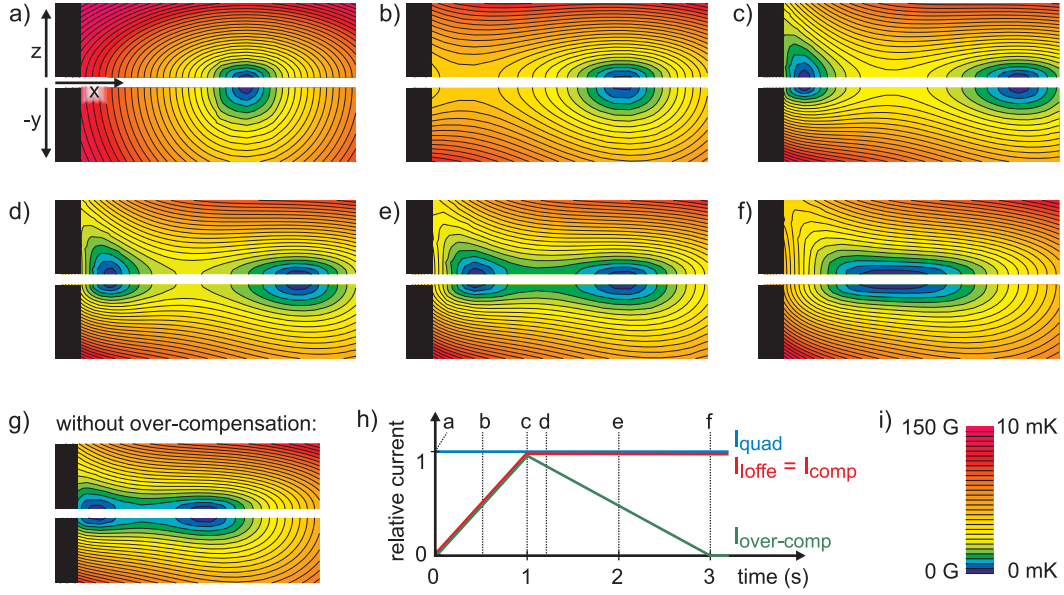


**Figure 5.5:** Transformation of the quadrupole trap potential into the QUIC trap potential with an improved scheme for larger trap depth. The sequence is illustrated in graph h) showing the currents through the different coils relative to their respective maximum value. a)–f) Field distributions at selected times of the transformation process indicated in graph h). In each graph, the upper subgraph displays the xz-half-plane and the lower one the xy-half-plane (field of view  $4\text{ mm} \times 16\text{ mm}$  each with black bar indicating the wall of the glass cell). The isofield lines are separated by 5 G. The critical time point (see text) is shown in graph d). g) Field distribution at the critical time point for the simpler transformation scheme without temporary over-compensation. The trap depth is significantly smaller than in the improved transformation scheme (compare with graph d)). i) Color legend for graphs a)–g) indicating the value of the magnetic field and the corresponding potential energy  $\mu_B B$  in units of  $k_B$ .

at the wall of the glass cell. At earlier times in the transformation process, the barrier height between the two minima is larger. Therefore, atoms with an energy below  $E_{\text{critical}}$  cannot classically move from the initial potential minimum (right minimum in Fig. 5.5) to the one closer to the glass cell wall and get lost due to collisions with the wall. At later times, the potential barrier between the two minima is lower but the potential height at the wall of the glass cell is larger than  $E_{\text{critical}}$ . Because of the over-compensation field the two minima are further separated and shifted away from the glass cell wall resulting in the increased effective trap depth.

### 5.5.1.3. Adjustment of the bias field

As the last step of the transformation process, the bias field of the QUIC trap is increased from 1.2 G to 3.2 G in 300 ms by partially bypassing the compensation coils (see also Sec. 3.6.3.3). This significantly reduces the calculated Majorana loss rate for lithium atoms at temperatures of a few ten  $\mu\text{K}$ .

## 5.5.2. Characterization of the QUIC trap

Exact knowledge of the trapping parameters is crucial for the generation of the quantum-degenerate triple mixture and for the quantitative analysis of absorption images. This section discusses measurements of the trap bottom and of the trapping frequencies of the final QUIC trap, which was used for the experiments presented in the next chapter.

### 5.5.2.1. Trap bottom

The determination of the trap bottom is initiated by producing a rubidium cloud confined in the QUIC trap with a temperature of a few  $\mu\text{K}$  using radio frequency (rf) evaporation (see Ch. 6). Subsequently, the intensity of the rf-signal is reduced to minimize errors due to dressing of the trapped states. Finally, the frequency of the rf-signal is linearly ramped to different end frequencies and held there for 1 s. The number of remaining atoms after the ramp is recorded by absorption imaging. The splitting of neighboring Zeeman levels and thus the trap bottom is readily determined from the end frequency of the rf-ramp at which all atoms are just removed from the trap. The result is  $B_0 = 1.18(1) \text{ G}$  for the QUIC trap obtained after the transformation steps explained in Sec. 5.5.1.2 and  $B_0 = 3.16(3) \text{ G}$  for the QUIC trap in the regular configuration obtained after the additional step described in Sec. 5.5.1.3.

### 5.5.2.2. Trapping frequencies

The harmonic trapping frequencies in the radial and in the longitudinal direction of the QUIC trap are measured by exciting and subsequently observing a corresponding center-of-mass dipole oscillation of the atomic clouds in the trap. Note that, in contrast to many other collective excitations, the frequency of the dipole mode in a harmonic trapping potential is independent of temperature, interactions and statistics and is always given by the respective harmonic trapping frequency [261].

The harmonic approximation of the trapping potential is only valid for sufficiently small distances from the trap center. The excursion below which the relative difference between the harmonic approximation and the numerically calculated field is below 10% is given by  $x_{\text{harm}} = 1.6 \text{ mm}$  along the longitudinal direction and  $\rho_{\text{harm}} = 99 \mu\text{m}$  in the radial direction. This corresponds to energies of  $249 \mu\text{K} \times k_{\text{B}}$  and  $45 \mu\text{K} \times k_{\text{B}}$  above the trap bottom, respectively. For the measurement of the trapping frequencies, a potassium cloud was sympathetically cooled by rubidium to a temperature below  $1 \mu\text{K}$  and rubidium was completely removed from the trap.

After preparation of the cold cloud in the trap, the dipole oscillation of the atoms was excited by sinusoidally displacing the center of the trapping potential. For the displacement a small magnetic field was applied either along the radial or the longitudinal axis by driving one of the offset coils (see Sec. 3.6.4.1) in the corresponding direction. Technical details of the driving setup are described in Ref. [235]. For excitation of the radial (longitudinal) oscillation a burst of two (ten) cycles at the respective calculated trapping frequency was used. After a variable subsequent hold time  $t$  the cloud was released from the trap and an absorption image was recorded after  $t_{\text{TOF}} = 6.7 \text{ ms}$  time of flight. Figure 5.6 shows the radial and longitudinal oscillations of the cloud center after the TOF expansion.

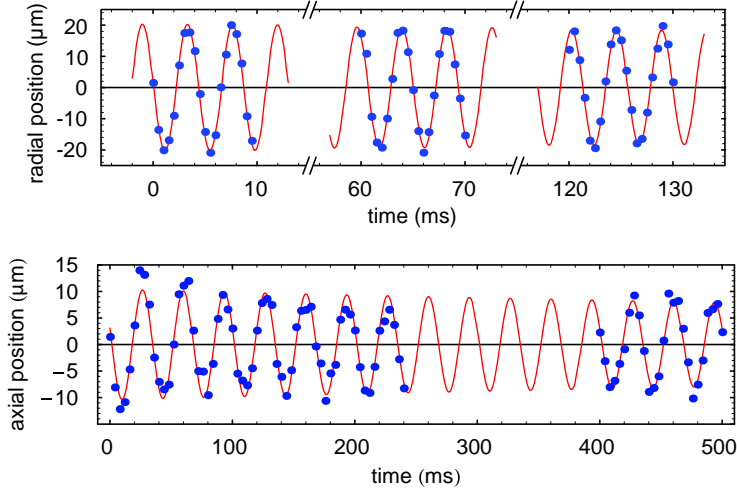


**Figure 5.6:** Measurement of the trapping frequencies in the QUIC trap. A radial (a) or a longitudinal (b) oscillation of a trapped  $^{40}\text{K}$  cloud is excited by a time-varying external magnetic field. After the excitation, the free evolution of the cloud in the trap is recorded. The fit to the position of the cloud after a variable duration of the oscillation and a fixed subsequent time of flight with a damped harmonic oscillation function yields an axial [longitudinal] frequency of  $230.88(5)$  Hz [ $29.97(3)$  Hz] for  $^{40}\text{K}$ . The corresponding values for the other two species are  $596.1(1)$  Hz [ $77.39(8)$  Hz] for  $^6\text{Li}$  and  $156.55(3)$  Hz [ $20.32(2)$  Hz] for  $^{87}\text{Rb}$ .

In order to determine the radial trapping frequency the measured positions  $\rho(t)$  of the cloud center for different holding times  $t$  are fitted with the function

$$\rho(t) = \rho_0 + A_\rho e^{-\gamma_\rho t} \cos(2\pi \nu_\rho t + \phi_\rho). \quad (5.11)$$

This function describes a damped harmonic oscillation around a central position  $\rho_0$  with amplitude  $A_\rho$ , damping rate  $\gamma_\rho$ , and phase  $\phi_\rho$ . An analogous function  $x(t)$  is used for fitting of the longitudinal oscillation. The values for the radial and longitudinal trapping frequencies determined from the fits are  $\nu_\rho^{(\text{K})} = 230.88(5)$  Hz and  $\nu_x^{(\text{K})} = 29.97(3)$  Hz for the  $^{40}\text{K}$  atoms. The resonance frequencies  $\nu_{\rho,x}^0$  of the undamped oscillation and the measured frequencies are linked by the relation  $\nu_{\rho,x}^0 = [\nu_{\rho,x}^2 + \gamma_{\rho,x}^2/(2\pi)^2]^{1/2}$ . However, for the small damping rates  $\gamma_\rho = 0.8(3) \text{ s}^{-1}$  and  $\gamma_x = 0.5(2) \text{ s}^{-1}$  obtained from the fits the damped and undamped frequencies are identical at the level of the measurement accuracy. From these trapping frequencies and the measured trap bottom of  $3.16(3)$  G the characteristic trap parameters  $\alpha$  and  $\beta$  are determined by virtue of Eqs. (3.19) to be  $\alpha = 146.1(7)$  G/cm and  $\beta = 254.0(5)$  G/cm $^2$ .

The spatial amplitude  $A^{(\text{trap})}$  of the oscillation inside the trap (i.e. before the ballistic expansion) is readily calculated from the fitting results with the relation  $A^{(\text{trap})} = A [1 + (2\pi \nu t_{\text{TOF}})^2]^{-1/2}$ . Both, the excursions in the radial direction of  $2.1 \mu\text{m}$  and in the longitudinal direction of  $6.5 \mu\text{m}$  are well in the harmonic region of the trapping potential. The assumption of a sinusoidal oscillation is therefore clearly justified.

The trapping frequencies for  ${}^6\text{Li}$  and  ${}^{87}\text{Rb}$  are related to the measured trapping frequencies for  ${}^{40}\text{K}$  by the ratios  $\sqrt{m_{\text{K}}/m_{\text{Li}}} \approx 2.58$  and  $\sqrt{m_{\text{K}}/m_{\text{Rb}}} \approx 0.678$ , respectively, since the trapped doubly polarized atomic states of the three species have the same magnetic moment. The radial and longitudinal trapping frequencies are thus given by  $\nu_{\rho}^{(\text{Li})} = 596.1(1)$  Hz and  $\nu_x^{(\text{Li})} = 77.39(8)$  Hz for lithium and by  $\nu_{\rho}^{(\text{Rb})} = 156.55(3)$  Hz and  $\nu_x^{(\text{Rb})} = 20.32(2)$  Hz for rubidium.

## 6. Cooling into quantum degeneracy

This chapter describes the achievement of simultaneous quantum degeneracy in cold gases of bosonic rubidium and fermionic lithium and potassium atoms, thereby realizing the first quantum-degenerate mixture of two different fermionic species and the first quantum-degenerate three-species mixture. Rubidium is cooled by forced evaporation under “run-away” conditions. In single-species operation, radio frequency (rf) radiation is used to drive the evaporation process. The efficiency of the cooling process with respect to particle loss is evaluated and characteristic signatures of Bose-Einstein condensation are observed. In multi-species operation, the fermionic species lithium and potassium are cooled by sympathetic cooling with rubidium and species-selective evaporation of rubidium is forced by microwave (MW) radiation. Crucial elements of the cooling sequence are described. Furthermore, it is shown that the efficiency of sympathetic cooling of the  ${}^6\text{Li}$  gas by  ${}^{87}\text{Rb}$  is increased by the presence of  ${}^{40}\text{K}$  through *catalytic* cooling. Finally, typical quantum-degenerate samples in the  ${}^6\text{Li}$ - ${}^{40}\text{K}$  Fermi-Fermi mixture and in the  ${}^6\text{Li}$ - ${}^{40}\text{K}$ - ${}^{87}\text{Rb}$  Fermi-Fermi-Bose mixture are presented.

Parts of this chapter were published in: “Quantum degenerate two-species Fermi-Fermi mixture coexisting with a Bose-Einstein condensate”, M. Taglieber, A.-C. Voigt, T. Aoki, T.W. Hänsch, and K. Dieckmann, *Physical Review Letters* **100**, 010401 (2008).

### 6.1. Bose-Einstein condensation of ${}^{87}\text{Rb}$

An important milestone for the realization of the quantum-degenerate three-species mixture was the realization of Bose-Einstein condensation in rubidium. Building on the experimental steps described in Ch. 5, BEC is achieved by forced evaporative cooling in the QUIC trap at a bias field of 3.2 G. The basic principle of evaporative cooling was introduced in Sec. 2.2.2. This section discusses two different techniques for evaporative cooling in a magnetic trap, rf evaporation and MW evaporation, and presents experimental results.

#### 6.1.1. Rf evaporation

Evaporative cooling relies on selective removal of atoms with an energy above a truncation energy  $\epsilon_t$  and subsequent rethermalization of the remaining atoms at a lower temperature by elastic collisions. In the case of rf evaporation in a magnetic trap, energy-selective removal is achieved by exploiting the spatial dependence of the confining magnetic field  $B(\mathbf{r})$ . The basic principle is illustrated in Fig. 6.1 in the diabatic and adiabatic pictures. An oscillating magnetic field (“rf knife”) of angular frequency  $\omega_{\text{rf}}$  is applied to the atomic sample. This rf field couples trapped and untrapped Zeeman-states at the positions where the resonance condition

$$\mu_B g_F |B(\mathbf{r})| = \hbar\omega_{\text{rf}} \quad (6.1)$$

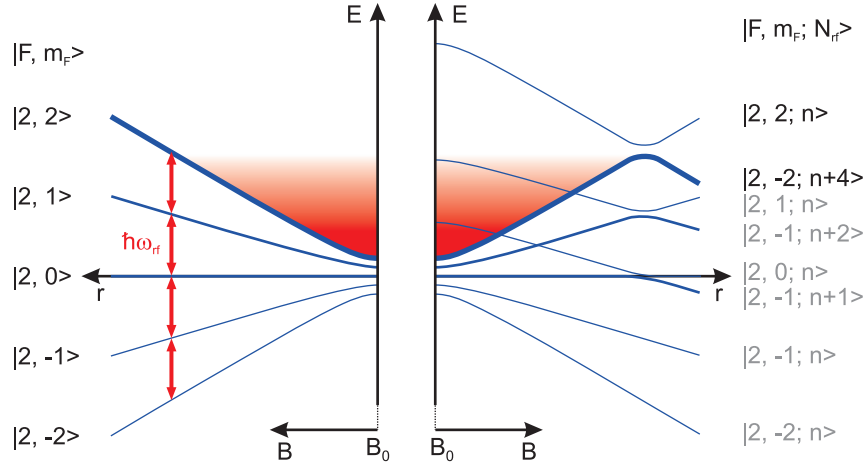


**Figure 6.1:** Principle of radio-frequency evaporation in the diabatic (left) and adiabatic (right) picture. A magnetic field oscillating at the frequency  $\omega_{\text{rf}}$  is applied to the trapped atomic sample. The field couples trapped and untrapped Zeeman states at positions where it is in resonance with the transition between two neighboring Zeeman states. Only atoms with a sufficiently high total energy reach the resonance region and are transferred into untrapped states. In the adiabatic picture the system is described by dressed states. The trapped asymptotic state  $|F, m_F; n\rangle = |2, 2; n\rangle$  (where  $n$  is the photon number of the rf field) is adiabatically connected to the untrapped asymptotic state  $|2, -2; n+4\rangle$  by an effective four photon transition.

is fulfilled. For sufficiently high rf amplitude  $B_{\text{rf}}$ , initially trapped atoms are transferred to untrapped states and removed from the trap with high probability. The truncation energy for atoms in the state  $m_F$  is thus related to the frequency of the applied rf signal by

$$\epsilon_t = m_F \hbar (\omega_{\text{rf}} - \omega_0) \quad (6.2)$$

where  $\omega_0 = \mu_B g_F B_0 / \hbar$  is the resonance frequency at the center of the trap. In the experiment, the truncation energy can easily be varied for forced evaporative cooling over a wide range by adjusting the output frequency of the computer-controlled rf source (see Sec. 3.7).

A more quantitative description of radio-frequency evaporation can be obtained in the Landau-Zener picture [262, 263] and its generalization to multi-level crossings [264]. The atoms of a trapped thermal sample pass the resonance region at different velocities due to their different thermal energies. The internal state of an atom after passage of the resonance region depends on its velocity  $\mathbf{v}$  and on the amplitude of the oscillating magnetic field. The transition probability to untrapped states is a function of the Landau-Zener parameter

$$\Gamma_{\text{LZ}} = \frac{\hbar \Omega_{\text{Rabi}}^2}{\mu_B g_F |\mathbf{v} \cdot \nabla B(\mathbf{r})|}. \quad (6.3)$$

Here,  $\Omega_{\text{Rabi}} = \mu_B g_F B_{\text{rf},\perp} / (2\hbar)$  is the Rabi frequency and  $B_{\text{rf},\perp}$  is the amplitude of the rf field component vertical to the trapping field  $\mathbf{B}(\mathbf{r})$ . The transition probability increases with increasing values of  $\Gamma_{\text{LZ}}$ . In the limit of low velocity and high rf amplitude, an initially

trapped atom undergoes a transition into an adiabatically connected untrapped state and leaves the trap (see right hand side of Fig. 6.1). In the opposite limit, it passes the resonance region unaffected and remains in the original trapped state. The transition probability in the intermediate regime between these limits can be calculated as a function of  $\Gamma_{\text{LZ}}$  for an  $N$ -level system using the relations given in Ref. [264]. In the case of rubidium atoms initially trapped in the  $|F=2, m_f=2\rangle$  state the total probability of transitions to any of the untrapped states  $|F=2, m_F=-2, -1, 0\rangle$  reaches 99% for a Landau-Zener parameter of 0.312. The corresponding minimal required amplitude of the rf field can be obtained for a known magnetic trapping potential from Eq. (6.3). However, an excessively high rf amplitude is not favorable for efficient evaporative cooling since it leads to a reduction of the effective trapping frequency and thus to a slower thermalization rate. The effective trapping frequency can be determined by calculating the energy eigenstates (“dressed states”) of the trapped atoms in the presence of the rf magnetic field [263, 265]. Hence, the optimal rf amplitude depends on the trap parameters and on the temperature of the gas. In the experiment, the amplitude is therefore gradually decreased during the evaporation process.

Finally, it should be noted that the resonance condition has the simple form of Eq. (6.1) only in the regime of the linear Zeeman effect valid for sufficiently small values of the magnetic field strength. For arbitrary magnetic field strengths, the resonance condition for any pair of Zeeman states in the ground state manifolds can be expressed in terms of the Breit-Rabi formula. For large magnetic fields, however, the equidistance of neighboring Zeeman levels is lifted. This can lead to incomplete evaporation [266] and to the formation of an Oort cloud [193].

### 6.1.2. Optimization and efficiency of rf evaporation

For the production of a Bose-Einstein condensate the principles of radio-frequency evaporation outlined above are applied to a gas of  $^{87}\text{Rb}$  atoms. It is clear from the considerations in Sec. 2.2.2 that the evaporation should ideally be performed in the runaway regime and with a time dependence of the truncation energy  $\epsilon_t(t)$  optimized for the specific experimental conditions. In order to obtain an evaporation sequence that is also a good starting point for the three-species mixture, the optimization was performed under vacuum conditions typical for three-species operation, i.e. with not only the rubidium dispensers but also the potassium dispensers and the lithium oven operating. Rubidium only was magneto-optically trapped and transferred to the QUIC trap. Under these conditions, the starting point for evaporative cooling was a sample of  $6 \times 10^8$  atoms with a temperature of about  $620 \mu\text{K}$ . This corresponds to an elastic collision rate  $\tau_{\text{el}}^{-1} = 19 \text{ s}^{-1}$  at the center of the QUIC trap. With the typical trap lifetime of  $\tau_{\text{loss}} = 60 \text{ s}$  the ratio of good to bad collisions is larger than  $10^3$  so that the preconditions (see Sec. 2.2.2.3) for achievement of runaway evaporation are well fulfilled. The frequency of the oscillating magnetic field was decreased in nine consecutive linear ramps from an initial value of 50 MHz to a final value of about 2.2 MHz close to the resonance frequency at the trap bottom. The duration of each linear ramp was experimentally optimized for evaporation efficiency resulting in a total duration of 29.3 s.

The temperature  $T$  and atom number  $N$  of the gas at different points of the optimized evaporation sequence is presented in Fig. 6.2. For each data point the evaporation was

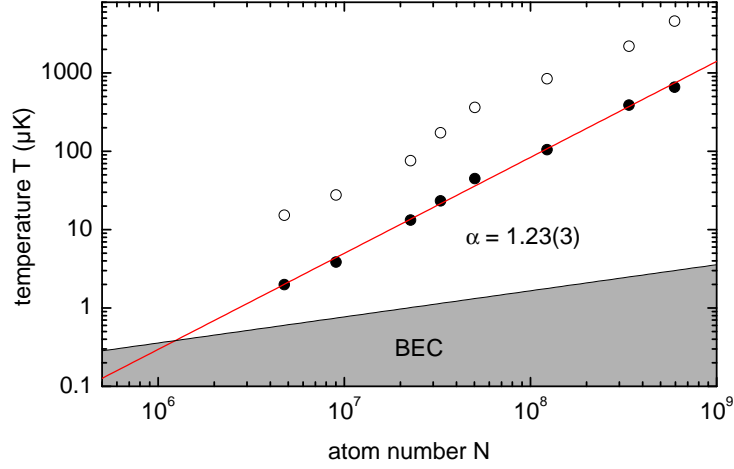


**Figure 6.2:** Evaporative cooling of  $^{87}\text{Rb}$  towards Bose-Einstein condensation by means of radio-frequency evaporation. The graph shows the measured atom numbers and temperatures (solid circles) at different final truncation energies (open circles, in units of temperature) during the cooling process. A fit of the data (solid line) yields an average efficiency parameter of  $\alpha_{\text{ev}} = 1.23(3)$ , meaning that the temperature decreases by more than one order of magnitude per order of magnitude in atom number reduction. The data show that  $\alpha_{\text{ev}}$  is almost constant over the entire evaporation.

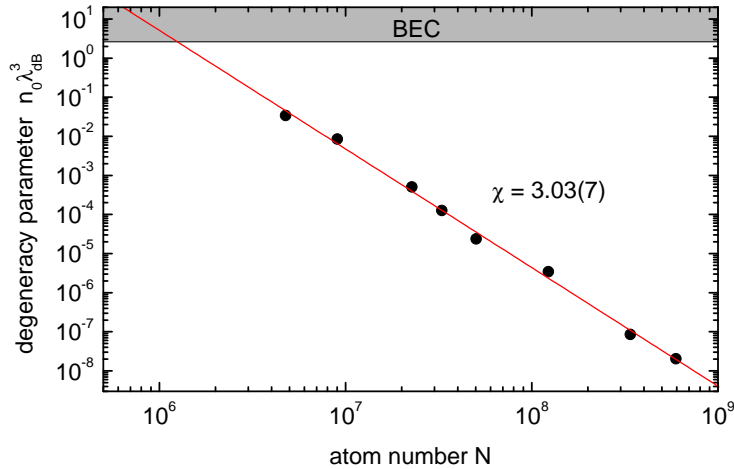
stopped at a certain truncation energy (also shown in the figure) and the trap was switched off after 30 ms equilibration time. The atom number and temperature were obtained from absorption images recorded after a duration of free expansion appropriate for the respective temperature range. A linear fit to  $\log T$  versus  $\log N$  yields  $\alpha_{\text{ev}} = 1.23(3)$  for the mean value of the efficiency parameter defined in Eq. (2.68). This means that the temperature of the gas decreases by more than one order of magnitude per order of magnitude in atom number reduction. Thus, the evaporation takes place under run-away conditions. Comparison of the data with the fit shows that  $\alpha$  is almost constant over the entire evaporation. Further evaporation leads to Bose-Einstein condensation (see Sec. 6.1.3).

Figure 6.3 shows the corresponding values of the peak phase-space density  $D = n(0)\lambda_{\text{dB}}^3$ . In the classical regime, the peak phase-space density (or “degeneracy parameter”) in a Ioffe-type trap with magnetic bias field  $B_0$  depends on the atom number  $N$  and on the temperature  $T$  as [192, 193]

$$n(0)\lambda_{\text{dB}}^3 \approx \frac{N}{6A_{\text{IQ}}(k_{\text{B}}T)^4 \left(1 + \frac{2V_0}{3k_{\text{B}}T}\right)} \quad (6.4)$$

where  $V_0 = m_F g_F \mu_B B_0$  is the potential minimum for atoms in the hyperfine state  $|F, m_F\rangle$ . The factor  $A_{\text{IQ}}$  is a constant, which depends on the strength of the potential. For the QUIC trap potential in the analytical approximation corresponding to Eq. (3.17) it is given by

$$A_{\text{IQ}} = \frac{m_{\text{Rb}}^{3/2}}{9\hbar^3 (m_F g_F \mu_B)^{5/2} \alpha^2 \beta^{1/2}}. \quad (6.5)$$



**Figure 6.3:** Evaporative cooling of  $^{87}\text{Rb}$ . For each order of magnitude in atom number reduction, the degeneracy parameter  $n(0) \lambda_{dB}^3$  increases by about three orders of magnitude. Further evaporation leads to Bose-Einstein condensation.

The parameters  $\alpha$  and  $\beta$  of our QUIC trap were determined in Sec. 5.5.2. A linear fit to  $\log D$  versus  $\log N$  yields  $\chi = 3.03(7)$  for the mean value of the efficiency parameter defined in Eq. (2.70). This corresponds to an increase of the degeneracy parameter by three orders of magnitude for each order of magnitude in atom number reduction.

### 6.1.3. Signatures of Bose-Einstein condensation

This section presents experimental data for Bose-Einstein condensates that were produced by rf evaporation and discusses characteristic signatures of Bose-Einstein condensation: the bimodal density distribution of a partially condensed cloud and the anisotropic expansion of the condensate.

#### 6.1.3.1. Bimodal density distribution

In order to observe the transition of a thermal gas to a Bose-condensed gas, ultracold clouds of  $^{87}\text{Rb}$  atoms were repeatedly produced using the evaporation scheme discussed in Sec. 6.1.2. The final frequency of the last linear frequency ramp of the rf knife was varied for the different repetitions. At the end of the evaporation sequence, the gas was allowed to thermalize for 40 ms, released from the trap and imaged with resonant light after 32 ms time of flight. Figures 6.4 a)–d) show the resulting optical column density distributions for final frequencies between 2.295 MHz and 2.225 MHz, corresponding to truncation energies between  $8 \mu\text{K} \times k_B$  and about  $1 \mu\text{K} \times k_B$ .

For the largest final truncation energy, the gas remained above the BEC phase transition and the TOF-image Fig. 6.4 a) shows an isotropically expanded thermal cloud. The temperature and atom number of the cloud are  $T = 880 \text{ nK}$  and  $N = 4 \times 10^6$ . As the truncation energy is further reduced, the phase transition is crossed and a spatially small

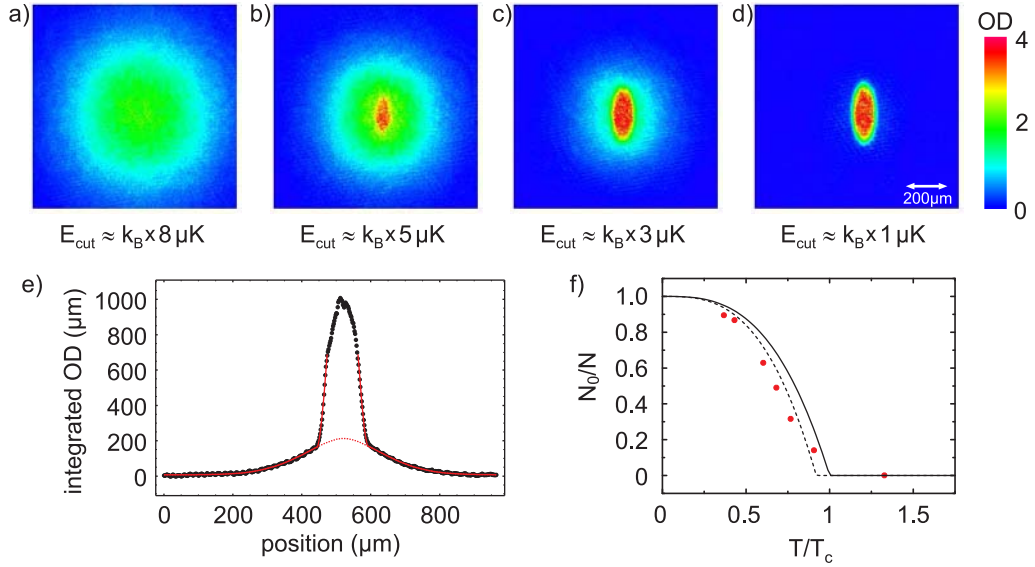


**Figure 6.4:** Bose-Einstein condensation of  $^{87}\text{Rb}$ . a)–d) Optical density distributions determined from absorption images taken after 32 ms time of flight for different final truncation energies corresponding to different final frequencies of the rf knife. With decreasing final truncation energy a spatially small peak with increasing optical density forms at the center of the thermal cloud. The field of view of each image is  $966 \times 966 \mu\text{m}^2$ . e) Characteristic bimodal density distribution of a partially condensed cloud after 20 ms time of flight. f) Condensate fraction as a function of the ratio between the measured temperature  $T$  and the calculated critical temperature  $T_c$  for an ideal gas. The solid line shows the theoretical expectation in the ideal-gas case; for the dashed line, the critical temperature was adjusted to account for finite-size and interaction effects.

peak with increasing optical density forms at the center of the thermal cloud as shown in Fig. 6.4b). This central part of the expanded cloud is the Bose-Einstein condensate. A fit of the data with an appropriate model function (see below) gives atom numbers of  $N_{\text{thermal}} = 2.2 \times 10^6$  and  $N_0 = 2.7 \times 10^5$  for the thermal cloud and the condensate, and a temperature of  $T = 404 \text{ nK}$ . The onset of Bose-Einstein condensation is thus reached with more than two million rubidium atoms. With a further reduction of the final truncation energy, the condensate fraction grows (Fig. 6.4c,d)) until an almost pure condensate is produced. If evaporation is continued to even smaller truncation energies, the condensate is spilled from the trap until no atoms are left.

Figure 6.4e) illustrates how the temperature of the gas as well as the atom numbers in the condensate and in the thermal fraction are determined from the experimental data. In order to improve the signal to noise ratio, the optical density distribution is first projected along a radial direction of the trap (y axis) yielding the “optical line density“. The thermal cloud is then analyzed by fitting its wings outside the condensate region with a model function that is derived from the Bose density distribution Eq. (2.27):

$$OD_{\text{line,thermal}} = c_0 + \frac{A}{g_{5/2}(\tilde{z})} g_{5/2} \left( \tilde{z} e^{-\frac{m}{2k_B T} \omega_x^2 \eta_x^2(t) x^2} \right), \quad (6.6)$$

where  $m$  is the atomic mass,  $\omega_x$  the longitudinal trapping frequency,  $t$  the expansion time,  $\eta_x(t) = [1 + \omega_x^2 t^2]^{-1/2}$  the scaling factor defined in Eq. (2.26),  $\sigma_{\text{ph}}$  the photon-atom scattering cross section (see Eq. (3.11)), and  $A$  the peak optical density of the cloud. The parameter  $c_0$  accounts for a possible small offset. For a purely thermal cloud, the fugacity  $\tilde{z}$  is used as a fit parameter, whereas  $\tilde{z}$  is fixed to unity for fitting of the thermal fraction of a partially condensed cloud. The number of thermal atoms is related to the fit parameters by

$$N_{\text{thermal}} = \frac{A}{\sigma_{\text{ph}}} \left( \frac{2\pi k_{\text{B}} T}{m} \right)^{1/2} \frac{g_3(\tilde{z})}{\omega_x \eta_x g_{5/2}(\tilde{z})}. \quad (6.7)$$

In order to determine the atom number in the condensate, the fitted thermal density distribution is subtracted from the optical line density and the obtained data are fitted with a Thomas-Fermi density distribution (see Sec. 2.1.3.3) that was integrated along the  $z$  and  $y$  axes and multiplied by  $\sigma_{\text{ph}}$ . The atom number in the condensed fraction is then deduced from the Thomas-Fermi radius and the known rubidium s-wave scattering length by means of Eqs. (2.39)–(2.41). For the data shown in Fig. 6.4, resonant imaging light was used in order to make the thermal cloud clearly visible also for deeply degenerate clouds. In the very dense central part of the atomic cloud containing the condensate, however, the imaging light is almost completely absorbed and the measured optical density does not allow a reliable determination of the real column density. Therefore, data points with an optical density above 3.5 are excluded from the fitting procedure. For the example of Fig. 6.4 e), one obtains  $N_0 = 8.9 \times 10^5$ ,  $N_{\text{thermal}} = 2.6 \times 10^5$  and  $T = 156$  nK with this procedure.

Figure 6.4 f) plots the condensate fraction  $N_0/N$  as a function of the ratio between the temperature  $T$  of the gas and the critical temperature  $T_c$  calculated with Eq. (2.30) from the determined total atom number. This critical temperature is only exact for an ideal Bose gas in the thermodynamic (large  $N$ ) limit. For our experimental conditions, the critical temperature is expected to be shifted by -1% due to the finite atom number [154] and by -7% due to interaction effects [267]. The expected dependence of the condensate fraction on  $T/T_c$  for an ideal Bose gas (see Eq. (2.32)) is shown in the plot. A corresponding graph where the critical temperature was reduced by 8% fits the data points in its validity range close to the critical temperature reasonably well.

### 6.1.3.2. Anisotropic expansion

The second characteristic signature of Bose-Einstein condensation is the anisotropic expansion of the condensate after sudden release from an anisotropic trap. An example is shown in Fig. 6.5. Inside the harmonic trap with cylindrical symmetry ( $\omega_x \ll \omega_y = \omega_z$ ), both the thermal fraction and the condensate have cigar-like shape. The momentum distribution of the thermal fraction is isotropic (see Eq. (2.16)) so that the thermal cloud approaches a spherically symmetric density distribution after long time of flight (see dilute part of the expanding cloud in Fig. 6.5). The condensate, however, expands more quickly along the direction that is more strongly confined inside the trap. In the non-interacting case, the ground state wave function of the condensate is proportional to the single-particle ground state wave function of the trapping potential and the anisotropic expansion is a direct consequence of Heisenberg's uncertainty relation. In the case of weak interaction, the ground

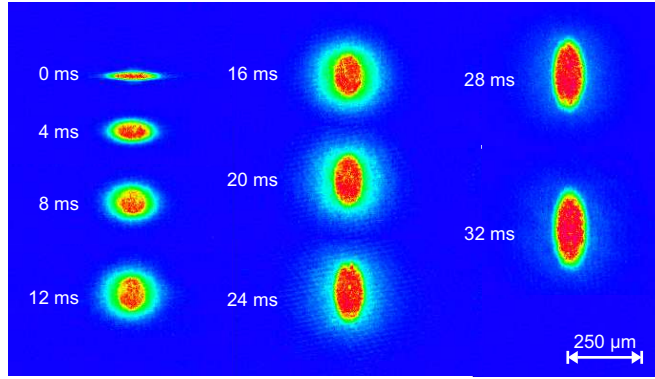


**Figure 6.5:** Anisotropic expansion of a rubidium Bose-Einstein condensate. A BEC is repeatedly produced, released from the trap and imaged after variable time of flight (TOF) using resonant light. The images are taken along the  $z$ -axis (i.e. perpendicular to the trap axis) and correspond to TOFs between 0 ms and 32 ms in steps of 4 ms as indicated. The thermal fraction of the cloud expands isotropically. The central part of the cloud is the condensate, which expands more slowly and changes shape from cigar-like inside the trap to pancake-like after long TOF, a typical signature of a BEC.

state and the dynamics of the condensate can be described by the Gross-Pitaevskii equation (GPE, see Sec. 2.1.3.3). For a trapped condensate, the kinetic energy term in the GPE can typically be neglected (Thomas-Fermi approximation) and the density distribution in a harmonic trap is well described by an inverted parabola (see Eq. (2.36)). In this limit, the anisotropy of the expansion is a result of the mean-field interaction energy that is converted into kinetic energy during the first part of the expansion. The accelerating force is proportional to the gradient of the atomic density and therefore strongest along the initially more tightly confined direction. Equations (2.40), (2.41) provide a quantitative description of the expansion within the Thomas-Fermi approximation.

#### 6.1.4. Limitations of rf evaporation for multi-species mixtures

The radio-frequency evaporation technique discussed above is conceptionally and technically quite simple. It is therefore employed for evaporative cooling in most single-species experiments that use a magnetic trap. For an experiment dealing with a mixture of several species, however, this method has the disadvantage of not being perfectly species-selective. According to Eq. (6.2), the truncation energy  $\epsilon_t$  for  ${}^6\text{Li}$ ,  ${}^{40}\text{K}$ , and  ${}^{87}\text{Rb}$  in the states  $|F=3/2, m_F=3/2\rangle$ ,  $|9/2, 9/2\rangle$ , and  $|2, 2\rangle$ , respectively, is related to the rf frequency by

$$\epsilon_{t,\text{Li}} = \frac{3}{2} \hbar\omega_{\text{rf}} - \mu_{\text{B}}B_0 \quad (6.8)$$

$$\epsilon_{t,\text{K}} = \frac{9}{2} \hbar\omega_{\text{rf}} - \mu_{\text{B}}B_0 \quad (6.9)$$

$$\epsilon_{t,\text{Rb}} = 2 \hbar\omega_{\text{rf}} - \mu_{\text{B}}B_0 \quad (6.10)$$

in the regime of the linear Zeeman effect. In these relations,  $B_0$  denotes the magnetic bias field at the trap minimum. In a  $^{40}\text{K}$ - $^{87}\text{Rb}$  mixture the lack of perfect species-selectivity of the rf evaporation method is usually acceptable since the truncation energy at any given rf frequency is significantly higher for potassium than for rubidium. As long as the two species are well thermalized, evaporation of potassium atoms is therefore strongly suppressed. Rf evaporation has been used successfully by several groups [56, 58, 268, 269] and in our experiment to cool  $^{40}\text{K}$ - $^{87}\text{Rb}$  mixtures and to produce quantum-degenerate Fermi gases of potassium. In a  $^6\text{Li}$ - $^{87}\text{Rb}$  mixture, however, the situation is different: Over a wide range of relevant truncation energies, rf evaporation of rubidium atoms results in simultaneous undesired removal of lithium atoms at a *lower* energy. The concept of our experiment, however, relies on evaporative cooling of  $^{87}\text{Rb}$  only and on sympathetic cooling of the fermionic species with minimal particle loss. Consequently, the rf evaporation technique is not the optimal choice for cooling of the *three*-species mixture.

### 6.1.5. MW evaporation

In order to avoid the problems and limitations of the rf evaporation method for cooling of multi-species mixtures discussed in Sec. 6.1.4, we evaporate  $^{87}\text{Rb}$  by driving its ground-state hyperfine transition. As the transition frequency of  $\nu_{\text{HF,Rb}} \approx 6.8$  GHz is in the microwave (MW) range, this method is called MW evaporation. The atom numbers of the fermionic species  $^6\text{Li}$  and  $^{40}\text{K}$  are not affected by the MW-evaporation signal for  $^{87}\text{Rb}$ , since the respective hyperfine transitions are at 228 MHz and at 1.3 GHz.

The principle of MW evaporation for  $^{87}\text{Rb}$  in the  $|F=2, m_F=2\rangle$  state is illustrated in Fig. 6.6 a). It requires to drive three different transitions: One signal couples the trapped Rb  $|2, 2\rangle$  state to the untrapped Rb  $|1, 1\rangle$  state (red solid line) and is used for the actual evaporation process of the Rb  $|2, 2\rangle$  atoms. Two other signals drive the Rb  $|2, 1\rangle \rightarrow \text{Rb } |1, 0\rangle$  and Rb  $|1, -1\rangle \rightarrow \text{Rb } |2, 0\rangle$  transitions (green and yellow lines). These signals are employed to remove rubidium atoms from the other two magnetically trappable, but undesired states Rb  $|2, 1\rangle$  and Rb  $|1, -1\rangle$  (“state cleaning”). Populations in these states have to be removed because they can lead to spin-exchange collisions, resulting in depolarization and heating of the bosonic as well as of the fermionic clouds. Furthermore, if atoms in these undesired states are not actively cooled or removed, they represent an additional heat load for the cooling process of the Rb  $|2, 2\rangle$  atoms. We have observed that careful state cleaning is a necessary precondition to reach BEC in the Rb  $|2, 2\rangle$  state. It was also found indispensable for successful sympathetic cooling of the fermionic species into quantum degeneracy.

For the implementation of the evaporation sequence, we have a MW carrier signal and two variable sidebands produced by frequency mixing with variable rf sources (DDS boards) at our disposal (compare Sec. 3.7). Higher-order sidebands are present but do not influence the cloud during the cooling and cleaning sequence that is described in the following. The sequence consists of four consecutive sections A–D and is shown in Fig. 6.6 b). In order to remove initial populations in the Rb  $|2, 1\rangle$  and Rb  $|1, -1\rangle$  states from the trap, we initiate the sequence by sweeping the carrier with the sidebands switched off within 1.2 s from 43 MHz below the Rb  $|1, -1\rangle \rightarrow \text{Rb } |2, 0\rangle$  transition to 2 MHz above the Rb  $|2, 1\rangle \rightarrow \text{Rb } |1, 0\rangle$  transition at the trap bottom (section A). Subsequently, the evaporation ramp is started by switching on one sideband (“knife”). In the following, the truncation energy is gradually

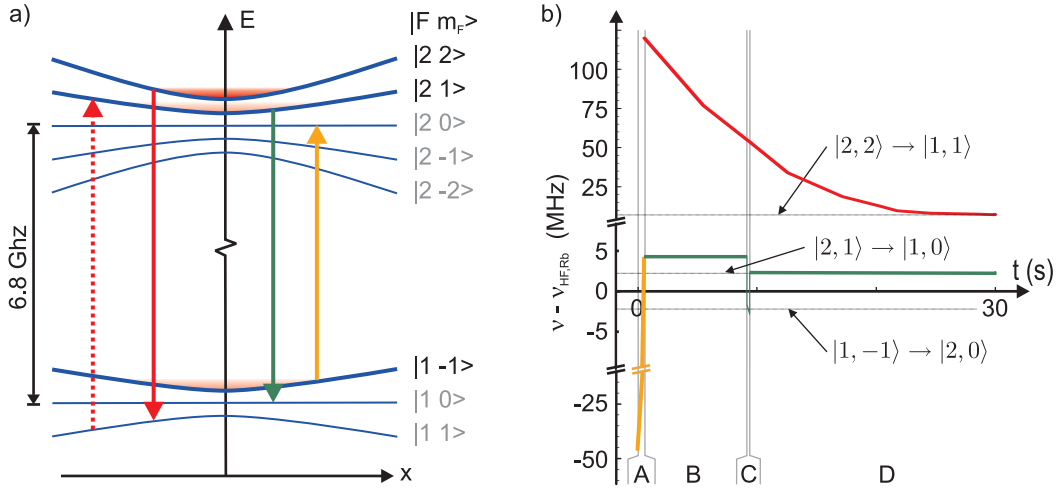


**Figure 6.6:** Species-selective evaporation of  $^{87}\text{Rb}$  using microwave radiation. a) Schematic level scheme in the magnetic trap with the relevant transitions. Rubidium atoms in the state  $|F=2, m_F=2\rangle$  with an energy larger than the truncation energy  $\epsilon_t$  (see text) are transferred into the state  $|1, 1\rangle$  by a microwave radiation signal (solid red line). Since this state is antitrapped, the atoms are accelerated away from the trap center towards regions of higher magnetic field. At a certain magnetic field, the same microwave signal becomes resonant with the  $|1, 1\rangle \rightarrow |2, 1\rangle$  transition (dashed red line) and some atoms are transferred into the trapped state  $|F=2, m_F=1\rangle$ . Populations in this state are therefore constantly removed by a second microwave signal (green line). In addition, any populations in the undesired trapped state  $|F=1, m_F=-1\rangle$  are cleaned away by two short frequency sweeps. b) Time dependence of the evaporation sequence employing two microwave signals. The thin dotted lines indicate the resonance frequencies for relevant transitions at the magnetic bias field in the trap center.

reduced by lowering the frequency of the knife from  $119 \text{ MHz} + \nu_{\text{HF,Rb}}$  (at the beginning of section B) to a value close to the resonance frequency at the trap bottom of about  $6.7 \text{ MHz} + \nu_{\text{HF,Rb}}$  (at the end of section D). The frequencies of this MW-evaporation ramp were chosen such that the optimized time evolution of the truncation energy obtained with the rf evaporation (see Sec. 6.1.2) was reproduced.

We observe that the Rb  $|2, 1\rangle$  state is continuously repopulated during the evaporation process. Therefore, this state is constantly cleaned (except during the short section C). In section B, this is realized by the carrier signal whose frequency is kept constant at the final frequency of the initial cleaning sweep. At the beginning of section C, the frequency of the carrier signal is jumped by  $-50 \text{ MHz}$  and the second sideband (“cleaner”) is switched on for state cleaning. During section C, the cleaner signal is used for a 500 ms long, 1 MHz wide sweep crossing the Rb  $|1, -1\rangle \rightarrow \text{Rb } |2, 0\rangle$  transition frequency at the trap bottom. This sweep is continuous in frequency and removes any cold Rb  $|1, -1\rangle$  atoms that may have remained in the trap after the initial cleaning sweep, which had to be performed in discrete frequency steps due to technical limitations of the MW source (Systron Donner). In contrast to the case of the Rb  $|2, 1\rangle$  state, we do not observe a repopulation of the Rb  $|1, -1\rangle$  state so that the single sweep in section C is sufficient to permanently remove these atoms. During the final section D, the cleaner signal is used for state cleaning of the

undesired Rb  $|2, 1\rangle$  atoms by a linear frequency ramp from 150 kHz above to close to the Rb  $|2, 1\rangle \rightarrow \text{Rb } |1, 0\rangle$  transition frequency at the trap bottom. This cleaning scheme for the Rb  $|2, 1\rangle$  atoms was found to give the best results compared to alternative schemes with repeated ramps. Finally, it should be noted that the use of the “cleaner” sideband signal for a similar frequency sweep also during sections A and B of the evaporation sequence is not possible with the current rf sources due to a limitation of their frequency range. A new version of rf sources with an increased frequency range is currently being developed by our group.

The repopulation of the Rb  $|2, 1\rangle$  state mentioned above is attributed mainly to an effect of the MW-evaporation process itself as illustrated in Fig. 6.6 a). For evaporation, atoms are transferred from the trapped Rb  $|2, 2\rangle$  state to the antitrapped Rb  $|1, 1\rangle$  state as explained. After the state transfer, the atoms are accelerated away from the trap center towards regions of higher magnetic field. At some point, the main MW-evaporation signal becomes resonant with the Rb  $|1, 1\rangle \rightarrow \text{Rb } |2, 1\rangle$  transition and some atoms are pumped into the Rb  $|2, 1\rangle$  state (dashed red line in the graph). Note that the polarization of the MW signal can never be perfectly circular for all atoms confined in a Ioffe-type trap since the direction of the magnetic field varies over the extension of the atomic cloud. Different antenna designs including a helix antenna were tested and yielded comparable results. In order to maintain an optimal optical access to the trapped atoms we therefore use in the present setup a simple dipole antenna placed close to the glass cell. In addition to the fast repopulation of the Rb  $|2, 1\rangle$  state induced by MW transitions, we also observed a slow repopulation of the Rb  $|2, 1\rangle$  state when a cloud with a temperature of about  $1.5 \mu\text{K}$  was held in the magnetic trap for up to 20s with all MW signals switched off. This effect is attributed to dipolar relaxation of the trapped Rb  $|2, 2\rangle$  atoms. For the development of the sequence described above and for verification of the effectiveness of state cleaning, a Stern-Gerlach method was used to detect the populations in the different atomic states. Details of the method will be discussed in Sec. 6.3.4.2.

## 6.2. Quantum-degenerate Bose-Fermi mixture of $^{87}\text{Rb}$ and $^{40}\text{K}$

After evaporative cooling of rubidium by MW evaporation was established, we focused on the realization of a quantum-degenerate Fermi gas by sympathetic cooling. The critical parameter in this case is the thermalization rate between the sympathetically cooled and the actively cooled species because it sets the timescale for the duration of the sympathetic cooling process. For the  $^{40}\text{K}$ - $^{87}\text{Rb}$  mixture, the situation is comparatively favorable making sympathetic cooling rather efficient, as will be discussed in this section. Sympathetic cooling of lithium, however, is more challenging, as we will see in Sec. 6.3.1.

The interspecies thermalization rate depends on the mass ratio of the two species, on the heat capacities (i.e. the atom numbers) of the two atomic clouds, and on the scattering rate between the two species as discussed in Sec. 2.2.3. For the  $^{40}\text{K}$ - $^{87}\text{Rb}$  mixture, the mass ratio is 2.2 so that the energy transfer per interspecies collision is only 14% smaller than in a collision between two atoms of the same species ( $\xi_{\text{K,Rb}} = 0.86$ , see Eq. (2.76)). The scattering rate between the two trapped species depends on the temperature of the two clouds and is proportional to the density-density overlap integral (2.74) and to the elastic

interspecies scattering cross section (under the conditions assumed in Sec. 2.2.3.1). In the s-wave limit, the scattering cross section is given by  $\sigma_{\text{K,Rb}} = 4\pi a_{\text{K,Rb}}^2$ . The triplet s-wave interspecies scattering length was determined in Ref. [270, 271] as  $a_{\text{K,Rb}} = (-215 \pm 10) \times a_0$ , where  $a_0$  is the Bohr radius. The comparatively large value of the scattering cross section results in a high interspecies thermalization rate and allows efficient sympathetic cooling of potassium by rubidium. The fast thermalization between the two species is further supported by the attractive interaction ( $a < 0$ ), which improves the density-density overlap. Note, however, that the  $^{40}\text{K}$ - $^{87}\text{Rb}$  scattering cross section is significantly smaller at higher temperatures, partially due to the Ramsauer-Townsend effect [59, 201].

In the experiment, we cool the  $^{40}\text{K}$ - $^{87}\text{Rb}$  mixture into quantum degeneracy using the 30 s long MW-evaporation ramp for rubidium discussed in Sec. 6.1.5. At the end of the experimental sequence, the atomic clouds are released from the trap and absorption images are taken along the z-axis after an appropriate time of flight. The properties of the clouds are extracted from these absorption images: The optical column-density distribution is deduced (see Sec. 3.5) from the data and is projected along the symmetry axis (x axis) of the trap for potassium and along the remaining radial axis of the trap (y axis) for rubidium (“optical line density”) to improve the signal to noise ratio. The optical line density is then fitted with an appropriate model function. For the fermionic species, the fit function is derived from the Fermi-Dirac density distribution Eq. (2.25) by integration along the z- and the x-axes and by multiplication with the effective photon-atom scattering cross section  $\sigma_{\text{ph}}$ . The full fit function for  $^{40}\text{K}$  then reads

$$OD_{\text{line}}(y) = c_0 + c_1 y - \sigma_{\text{ph}} \frac{\eta_y(t) \omega_y m^{1/2} (k_{\text{B}} T)^{5/2}}{(2\pi)^{1/2} (\hbar \bar{\omega})^3} g_{5/2} \left( -\tilde{z} e^{-\frac{m}{2k_{\text{B}} T} [\omega_y (y-y_0) \eta_y(t)]^2} \right). \quad (6.11)$$

In this equation,  $m$  is the atomic mass of  $^{40}\text{K}$ ,  $\omega_y$  and  $\bar{\omega}$  denote the radial and mean trapping frequencies for potassium, and  $\eta_i(t) = [1 + \omega_i^2 t^2]^{-1/2}$  is the scaling factor defined in Eq. (2.26). The physical fit parameters are the temperature  $T$ , the fugacity  $\tilde{z}$ , and the position  $y_0$  of the cloud center. The two additional fit parameters  $c_0$  and  $c_1$  are used to account for any residual offset and slope, respectively, due to possible imaging artifacts in the optical line-density distribution. The ratio  $T/T_{\text{F}}$  and the atom number  $N$  are calculated directly from the fit parameters using the relations (2.20) and (2.6). We conservatively estimate the systematic uncertainty of the atom numbers to be below 50% and of the temperatures to be lower than  $\pm 0.1 T_{\text{F}}$  in the temperature range of 0.2–0.5  $T_{\text{F}}$ . For the bosonic rubidium gas, an appropriate two-component fitting function is used as discussed in Sec. 6.1.3.1.

An example of a quantum-degenerate mixture of  $^{40}\text{K}$  and  $^{87}\text{Rb}$  produced by the 30 s long cooling sequence is shown in Fig. 6.7. The left-hand side of the figure displays the optical column densities deduced from absorption images taken after 15 ms time of flight. The right-hand side of the figure gives the corresponding optical line densities of the fermionic and the bosonic species together with the fits. The atom numbers and temperatures determined from the fit for potassium are  $N_{\text{K}} = 1.4 \times 10^5$  and  $T_{\text{K}} = 113 \text{ nK} = 0.21 T_{\text{F}}$ . For rubidium, we obtain a temperature  $T_{\text{Rb}} = 149 \text{ nK}$  and atom numbers  $N_{\text{thermal}} = 9.5 \times 10^4$  in the thermal fraction and  $N_0 = 3.5 \times 10^5$  in the condensate.

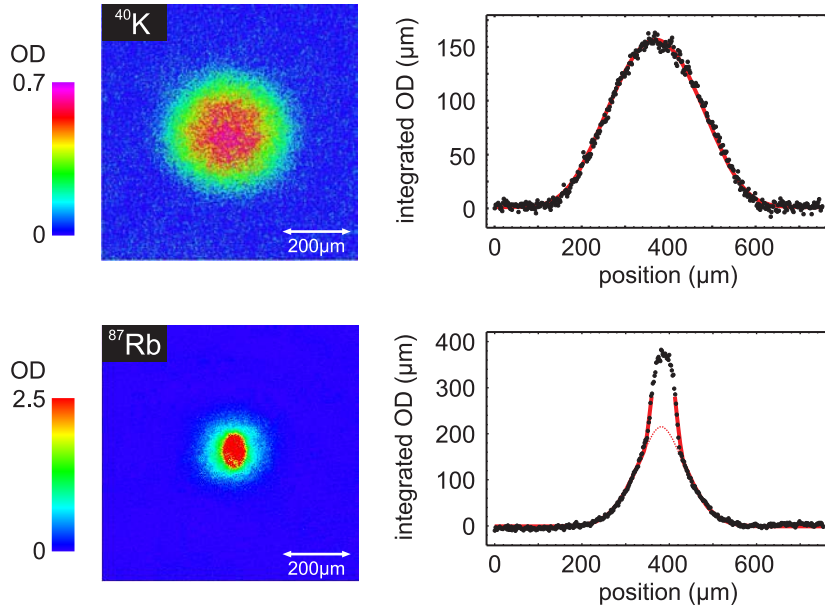


**Figure 6.7:** Absorption images of a quantum-degenerate  ${}^{40}\text{K}$ - ${}^{87}\text{Rb}$  mixture obtained after 30 s of sympathetic and evaporative cooling in the QUIC trap. Shown are the optical column densities (left) and projections of the optical column densities (right) along with corresponding fits (solid lines). For both species, the expansion time was 15 ms and the field of view is  $755 \times 755 \mu\text{m}^2$ .

### 6.3. Simultaneous quantum degeneracy in the ${}^6\text{Li}$ - ${}^{40}\text{K}$ - ${}^{87}\text{Rb}$ mixture

One of the major goals of the work presented in this thesis was the generation of a quantum-degenerate mixture of two different fermionic species. Fine-tuning of the experimental parameters allowed us to additionally produce a quantum-degenerate three-species mixture of two fermionic and one bosonic species. This section starts with a discussion of the challenges encountered in sympathetic cooling of the second fermionic species,  ${}^6\text{Li}$ , and presents our solutions. In the subsequent main part of the section, the realization of the quantum-degenerate Fermi-Fermi and Fermi-Fermi-Bose mixtures is discussed.

#### 6.3.1. Sympathetic cooling of ${}^6\text{Li}$

The starting point for sympathetic cooling of lithium by rubidium is a corresponding mixture in the QUIC trap. The rubidium cloud contains typically  $5\text{--}8 \times 10^8$  atoms at a temperature of  $0.6(1)$  mK. For the lithium cloud, we roughly estimate an atom number of  $1\text{--}2 \times 10^7$  and a temperature of  $1.5(5)$  mK from time-of-flight measurements. A more exact determination of the atom number and the temperature of the lithium sample at this point of the sequence is hindered by the low optical density of the cloud and by the extremely fast expansion after trap switch-off due to the low atomic mass. Note that intratrap imaging

cannot be readily applied in this case since the resonance frequency of the atoms varies significantly over the extension of the hot cloud due to the confining magnetic field.

### 6.3.1.1. Challenges

If we apply the cooling sequence that was successfully employed for producing a quantum-degenerate  $^{40}\text{K}$ - $^{87}\text{Rb}$  mixture (see Sec. 6.2) to a  $^6\text{Li}$ - $^{87}\text{Rb}$  mixture in our experiment, we do not observe any detectable cold lithium cloud at the end of the cooling process. This is attributed to the small  $^6\text{Li}$ - $^{87}\text{Rb}$  interspecies scattering cross section resulting in a low thermalization rate. Thermalization measurements between trapped clouds of  $^6\text{Li}$  and  $^{87}\text{Rb}$  reported in Ref. [64] are consistent with an absolute value of the s-wave triplet interspecies scattering length of  $|a_{\text{Li,Rb}}| = 20_{-6}^{+9} a_0$ . A more precise value for the scattering length and its sign could be obtained in the future from the positions of  $^6\text{Li}$ - $^{87}\text{Rb}$  interspecies Feshbach resonances; so far only two such resonances were observed [272]. The value of  $a_{\text{Li,Rb}}$  given above corresponds to a  $^6\text{Li}$ - $^{87}\text{Rb}$  scattering cross section that is roughly two orders of magnitude smaller than the  $^{40}\text{K}$ - $^{87}\text{Rb}$  scattering cross section (in the s-wave limit).

In addition, the larger mass ratio of 14.4 in the  $^6\text{Li}$ - $^{87}\text{Rb}$  mixture compared to 2.2 in the  $^{40}\text{K}$ - $^{87}\text{Rb}$  mixture results in a lower energy transfer per elastic collision ( $\xi_{\text{Li,Rb}} = 0.24$ ), which is only partially compensated by a higher mean thermal relative velocity. Furthermore, the different masses cause different gravitational sags (see Eq. (2.79)) for the two species, which reduces the density-density overlap and thus lowers the thermalization rate (see Sec. 2.2.3.2). For our magnetic trap, the difference in gravitational sag between the lithium cloud and the rubidium cloud amounts to  $\Delta z_{\text{sag}} = 9.4 \mu\text{m}$ . At high temperatures, the clouds are much larger than  $\Delta z_{\text{sag}}$  and the effect on the thermalization rate can be neglected. For temperatures below about  $1 \mu\text{K}$  and typical atom numbers, however, the radial extensions of the clouds are comparable to or smaller than  $\Delta z_{\text{sag}}$  and the density-density overlap between the two species is reduced below the value that would be reached, if the gravitational sag were absent. For example, at a temperature of  $500 \text{ nK}$ , the radial  $1/e$ -radius of a lithium cloud with  $10^5$  atoms is  $12 \mu\text{m}$ , the one of a rubidium cloud with  $10^6$  atoms is  $9 \mu\text{m}$  and the value of the density-density overlap integral Eq. (2.74) in this case is only  $2/3$  of what it would be for  $\Delta z_{\text{sag}} = 0$ . It should be noted again that a fully quantitative calculation of the thermalization rate has to take into account several quantum statistical effects as discussed in Sec. 2.2.3.2.

### 6.3.1.2. Solutions

In order to deal with the challenges discussed in the previous section, the following experimental measures are taken for sympathetic cooling of lithium:

**Duration of the cooling sequence** The evaporation sequence is stretched in time with respect to the sequence optimized for the production of rubidium BEC. Experimentally, we found gradually increased stretching towards the end of the evaporation ramp to be more beneficial than stretching at the beginning. The optimal duration of the cooling sequence is a compromise between the duration required for sufficient thermalization of the lithium sample with the rubidium gas on one hand and atom loss from both species due to collisions

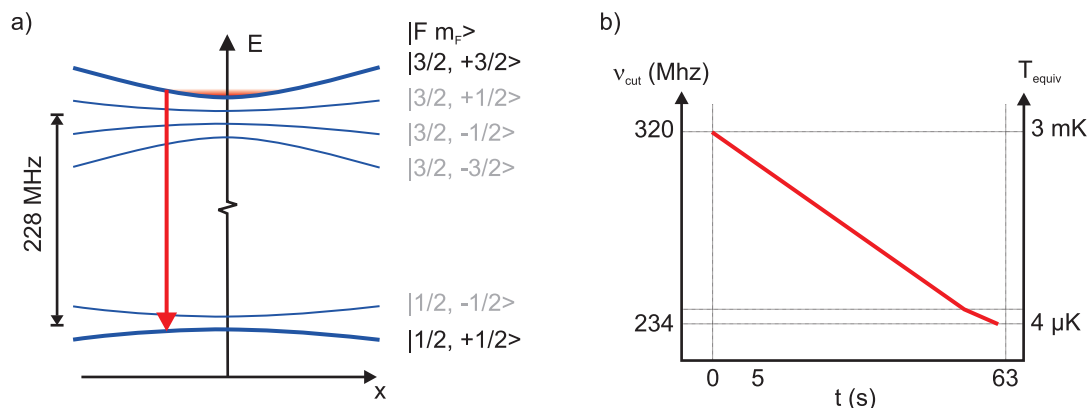


**Figure 6.8:** Selective removal of lithium atoms not sufficiently thermalized during sympathetic cooling. a) A radio-frequency signal (“Li hyperfine knife”) couples the trapped  $|F=3/2, m_F=3/2\rangle$  and the untrapped  $|1/2, 1/2\rangle$  hyperfine states of  ${}^6\text{Li}$  at a magnetic field defined by the frequency of the rf signal. Lithium atoms with an energy above the corresponding reduced trap depth are thus removed from the trap. b) During the sympathetic cooling sequence, the trap depth for lithium is gradually reduced from about  $3\text{ mK} \times k_B$  to  $4\ \mu\text{K} \times k_B$  by lowering the frequency of the rf signal. This ensures that at any time lithium atoms that are left behind in the sympathetic cooling process are removed from the trap.

with the background gas (the trap lifetime is typically 60 s in the UHV chamber) on the other hand. For the work presented here, an optimized ramp with a total duration of 63 s was used.

**Removal of high-energy  ${}^6\text{Li}$  atoms** We observed that even with the stretched cooling sequence, a significant fraction of the lithium atoms did not fully thermalize with the rubidium gas and was left behind in the sympathetic cooling process. These atoms appeared in time-of-flight images as a hot halo around a cold lithium cloud containing only a small fraction of the atoms. We found that cold lithium clouds with large atom numbers can only be achieved, if the lithium atoms that are left behind in the cooling process (i.e. lithium atoms with an energy much higher than the average energy of the rubidium atoms) are constantly removed from the trap. This energy-selective removal is realized by applying radio-frequency radiation on the hyperfine transition of the lithium ground state (“lithium hyperfine (hf) knife”, see Fig. 6.8). During the evaporation ramp for rubidium, the cut energy of the lithium hf knife is decreased in two consecutive linear sweeps with durations of 60 s and 3 s, respectively, from  $3\text{ mK} \times k_B$  to about  $20\ \mu\text{K} \times k_B$  and further to  $4\ \mu\text{K} \times k_B$ .

In order to further elucidate the function of the lithium hf knife we conducted a separate experiment illustrated in Fig. 6.9. In this experiment, the first linear sweep of the lithium cut energy was divided into two linear sweeps with durations of 5 s and 55 s, and the intermediate cut energy was varied. The atom number of the cold lithium cloud at the end of the cooling sequence is plotted in Fig. 6.9b). It clearly shows that lower final cut energies of the fast first frequency ramp result in lower final lithium atom numbers. This is a strong indication that not only atoms in the low-energy tail of the initial lithium cloud

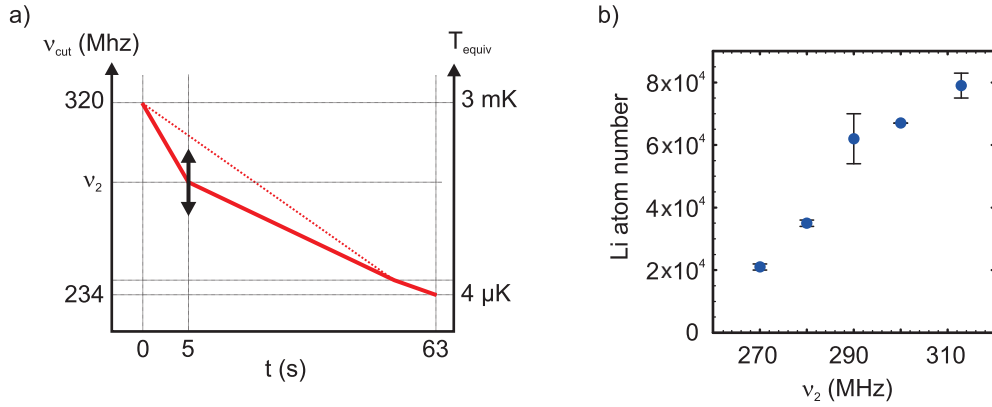


**Figure 6.9:** Capture of high-energy lithium atoms during sympathetic cooling. a) The original slow linear ramp of the lithium hyperfine cut frequency (dotted line) is replaced by a fast ramp to a variable intermediate frequency  $\nu_2$  followed by a slow ramp to the same final frequency (solid line). b) Lithium atom number at the end of the sympathetic cooling process for different intermediate frequencies  $\nu_2$ . The degeneracy parameter  $T/T_F$  was almost constant at a value of about 0.35.

are sympathetically cooled but also lithium atoms at initially high energy but with low angular momentum, which traverse through the dense central part of the rubidium cloud.

**“Catalytic” sympathetic cooling** Experimentally, we also found that sympathetic cooling of  ${}^6\text{Li}$  is more efficient in the  ${}^6\text{Li}$ - ${}^{40}\text{K}$ - ${}^{87}\text{Rb}$  three-species mixture than in a pure  ${}^6\text{Li}$ - ${}^{87}\text{Rb}$  mixture. This effect is attributed to energy transfer from the lithium gas to the actively cooled rubidium gas via the simultaneously trapped potassium gas and will be discussed more quantitatively in Sec. 6.3.4.

### 6.3.2. Quantum-degenerate Fermi-Fermi mixture of ${}^6\text{Li}$ and ${}^{40}\text{K}$

For the realization of a quantum-degenerate mixture of  ${}^6\text{Li}$  and  ${}^{40}\text{K}$ , the experimental sequences for sympathetic cooling of the two species described in Sec. 6.2 & 6.3.1 are combined: The three-species MOT for lithium, potassium and rubidium is loaded for 15 s to maximum atom numbers. The MOT capture phase is followed by the cMOT/dMOT phase, the optical molasses phase and the magnetic transfer to the QUIC trap as explained in Ch. 5. Subsequently, the evaporative and sympathetic cooling process with a total duration of 63 s is started. At the end of the cooling process, rubidium is completely removed from the trap by choosing a final cut energy of the MW knife just below the trap bottom. This procedure then results in a mixture of  $1.8 \times 10^5$  lithium atoms at a temperature ratio of  $T/T_F = 0.3$  and  $1.8 \times 10^5$  potassium atoms at  $T/T_F = 0.40$  (see Fig. 6.10). The atom numbers and temperatures were obtained from an analysis of the potassium absorption images as described in Sec. 6.2 and an analogous treatment of the lithium data. This mixture is an optimal starting point for Fermi-Fermi experiments that require two different fermionic species.

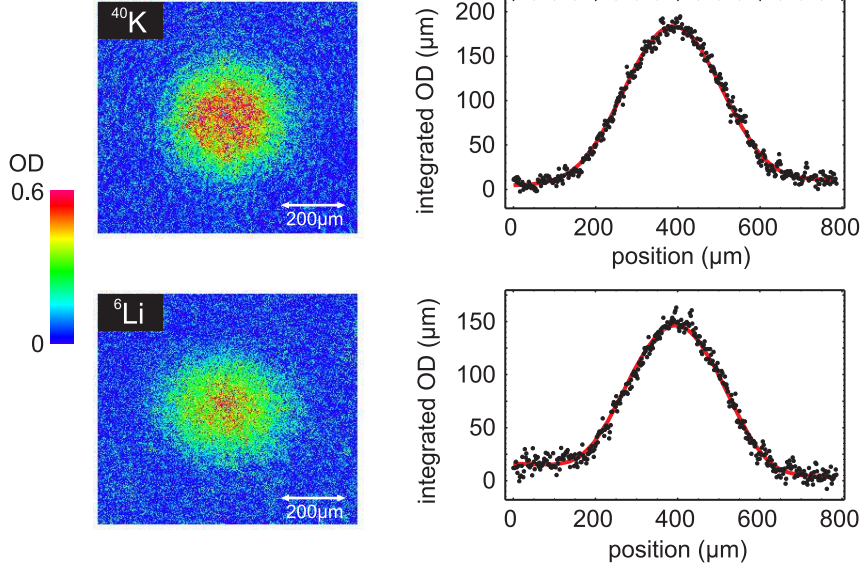


**Figure 6.10:** Time-of-flight absorption images of the quantum-degenerate two-species Fermi-Fermi mixture. Shown are the optical column densities (left) and projections of the optical column densities (right) along with corresponding fits (lines). The projections are taken along the symmetry axis of the trap ( $x$ -axis) after expansion times of 15 ms for potassium and 4 ms for lithium, respectively. The field of view is  $788 \times 886 \mu\text{m}^2$  in each image.

### 6.3.3. Quantum-degenerate Fermi-Fermi-Bose mixture of ${}^6\text{Li}$ , ${}^{40}\text{K}$ , and ${}^{87}\text{Rb}$

In order to realize a quantum-degenerate mixture of the two fermionic species  ${}^6\text{Li}$  and  ${}^{40}\text{K}$  and of the bosonic species  ${}^{87}\text{Rb}$  simultaneously, the experimental sequence described above had to be adapted and fine-tuned. For our setup, we found that if the triple MOT is loaded to maximum atom number for all three species, we are able to obtain quantum-degenerate clouds of the fermionic species and an ultracold thermal sample of rubidium but no Bose-Einstein condensate. This is attributed to the large heat load that the fermionic clouds with high initial atom numbers represent for the actively cooled rubidium gas. For the generation of the triple-degenerate mixture, the heat load on rubidium is therefore reduced by loading fewer lithium atoms into the MOT. This is realized by simply blocking the lithium atom beam at the entrance of the Zeeman slower already 200 ms before the end of the MOT capture phase. In addition, the currents of the atomic vapor dispensers for potassium and rubidium were adjusted in order to optimize the background vapor pressure and trap lifetime in the MOT chamber and, as a consequence, in the UHV chamber. With these settings, we reproducibly generate a quantum-degenerate  ${}^6\text{Li}$ - ${}^{40}\text{K}$  Fermi-Fermi mixture coexisting with a  ${}^{87}\text{Rb}$  Bose-Einstein condensate.

A typical example of the quantum-degenerate three-species mixture is shown in Fig. 6.11. For potassium, fitting with an appropriate Fermi-Dirac density distribution function yields an atom number of  $N_{\text{K}} = 1.3 \times 10^5$  and a temperature of  $T_{\text{K}} = 184 \text{ nK} = 0.35 T_{\text{F}}$ . The corresponding numbers for lithium are  $N_{\text{Li}} = 0.9 \times 10^5$  and  $T_{\text{Li}} = 313 \text{ nK} = 0.27 T_{\text{F}}$ . For rubidium, fitting with an appropriate two-component density distribution gives  $N_{\text{thermal,Rb}} =$

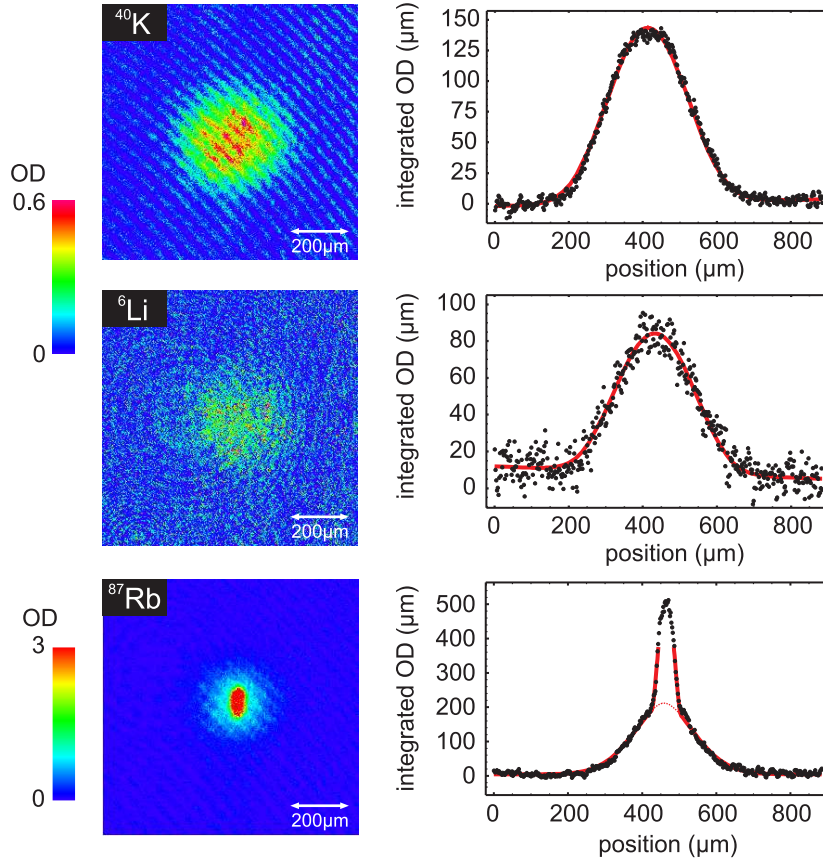


**Figure 6.11:** Time-of-flight absorption images of the quantum-degenerate Fermi-Fermi-Bose mixture. Shown are the optical column densities (left) and projections of the optical column densities (right) along with corresponding fits (lines). The projections are taken along the symmetry axis of the trap ( $x$ -axis) for the fermionic species and along the radial axis ( $y$ -axis) for rubidium. Expansion times are 15 ms, 4 ms and 20 ms for potassium, lithium and rubidium, respectively. The field of view is  $886 \times 886 \mu\text{m}^2$  in each image.

$1.5 \times 10^5$  and  $T_{\text{Rb}} = 189 \text{ nK}$  for the thermal fraction and an atom number of  $N_{0,\text{Rb}} = 1 \times 10^5$  in the condensed fraction.

### 6.3.4. Study of the last part of the cooling process

The temperatures and atom numbers during the last part of the cooling sequence are shown in Fig. 6.12. The trapped mixture has been repeatedly produced for different end frequencies of the MW-evaporation ramp and for separate imaging of the three species. As the final MW frequency is lowered, the temperature and atom number of the  $^{87}\text{Rb}$  gas decrease as expected. For partially condensed rubidium clouds the atom numbers of the thermal fraction are given. For the two very lowest evaporation end frequencies, rubidium clouds were absent or too small in atom number to be fittable. The fermionic species, however, are almost constant in atom numbers at about  $10^5$  during the observed part of

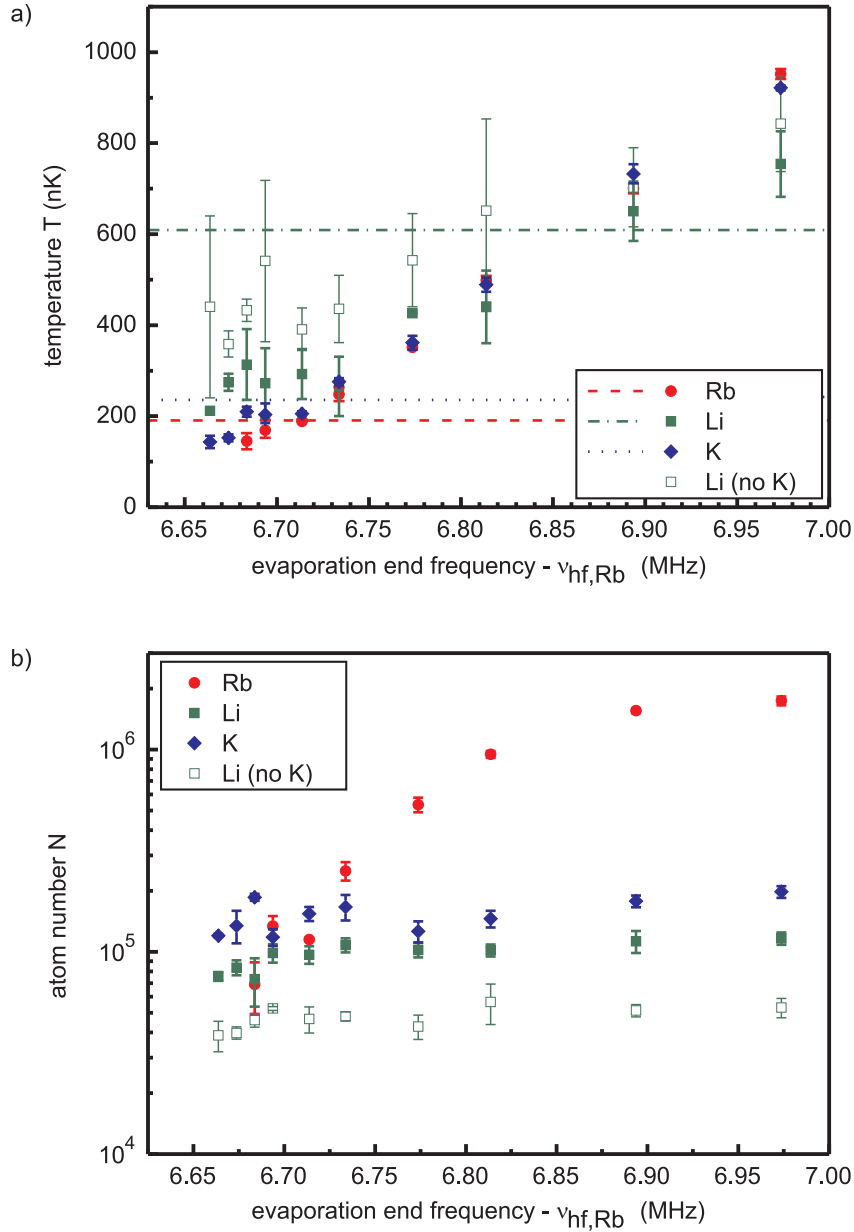


**Figure 6.12:** Temperatures (a) and atom numbers (b) during the very last part of simultaneous trapping and cooling of the three-species mixture (filled symbols).  ${}^{87}\text{Rb}$  is evaporatively cooled,  ${}^6\text{Li}$  and  ${}^{40}\text{K}$  are sympathetically cooled by thermal contact with the rubidium cloud. Corresponding data for lithium in a two-species  ${}^6\text{Li}$ - ${}^{87}\text{Rb}$ -mixture are also shown (empty rectangles). The horizontal lines in (a) indicate the critical temperature  $T_c$  for rubidium and half the Fermi temperature  $T_F$  for the fermions, respectively. For our trap parameters and typical atom numbers of  $1.5 \times 10^5$  for rubidium and  $10^5$  for the fermionic species, the critical temperature is  $T_c^{\text{Rb}} = 190$  nK and the Fermi temperatures are  $T_F^{\text{Li}} = 1.2 \mu\text{K}$  and  $T_F^{\text{K}} = 470$  nK. The error bars represent the r.m.s.-deviation for at least three consecutive repetitions.

the cooling sequence because they are not affected by the species-selective evaporation of  $^{87}\text{Rb}$ . The temperature data in Fig. 6.12 a) confirm that rubidium and potassium are very well thermalized throughout the temperature range observed. The data further show that the lithium cloud is also cooled significantly for the slow evaporation ramp in use but is not fully thermalized with the rubidium gas at the lowest observed temperatures for the reasons already discussed in Sec. 6.3.1.

#### 6.3.4.1. Catalytic cooling

We also investigated sympathetic cooling of a two-species  $^6\text{Li}$ - $^{87}\text{Rb}$  mixture by omitting loading of potassium. The comparison of the lithium temperatures in the two-species and three-species situations (see Fig. 6.12 a)) clearly shows that lithium can be cooled more efficiently if also potassium is present in the trap during the cooling process. This is further supported by the measured atom numbers shown in Fig. 6.12 b): During the observed part of the cooling process, the lithium atom number is nearly constant at approximately  $10^5$  in the  $^6\text{Li}$ - $^{40}\text{K}$ - $^{87}\text{Rb}$  three-species mixture and at about  $5 \times 10^4$  in the  $^6\text{Li}$ - $^{87}\text{Rb}$  two-species mixture. This difference in the number of successfully cooled atoms indicates that the  $^6\text{Li}$ - $^{40}\text{K}$  thermalization rate is comparable to or even larger than the  $^6\text{Li}$ - $^{87}\text{Rb}$  thermalization rate, at least at some temperature during the evaporation ramp. Since the potassium atom number is constant and the rubidium and potassium clouds are in good thermal contact, the energy of the lithium cloud is eventually transferred to the rubidium cloud. In this sense, potassium acts as a catalytic cooling agent for lithium.

Several factors contribute to this effect: First, while the  $^{40}\text{K}$ - $^{87}\text{Rb}$  scattering cross section is comparatively large (see Sec. 6.2) resulting in a fast thermalization of the two species (see Sec. 2.2.3), lithium thermalizes only very slowly by direct collisions with rubidium due to the small  $^6\text{Li}$ - $^{87}\text{Rb}$  scattering cross section (see Sec. 6.3.1.1). The value of the triplet scattering length  $a_{\text{Li,K}} = 63.5(1) a_0$  for  $^6\text{Li}$ - $^{40}\text{K}$  collisions measured very recently [248], however, corresponds to a scattering cross section  $\sigma_{\text{Li,K}} = 4\pi a_{\text{Li,K}}^2$  that is a factor 10 larger than the  $^6\text{Li}$ - $^{87}\text{Rb}$  scattering cross section (in the limit of low collision energy). Second, thermalization of  $^6\text{Li}$  with  $^{40}\text{K}$ , which is efficiently cooled by  $^{87}\text{Rb}$ , requires fewer collisions than direct thermalization of  $^6\text{Li}$  with  $^{87}\text{Rb}$ , since the mass ratio  $m_{\text{K}}/m_{\text{Li}}$  is closer to unity than  $m_{\text{Rb}}/m_{\text{Li}}$  (larger  $\xi$ , see Sec. 2.2.3). Third, the difference in the mass ratios also results in a more favorable density-density overlap Eq. (2.74) between  $^6\text{Li}$  and  $^{40}\text{K}$  than between  $^6\text{Li}$  and  $^{87}\text{Rb}$ . Taking all these factors together, the relevant energy transfer rates between the different species can be estimated based on the known interspecies s-wave scattering lengths by assuming a negligible energy-dependence of the scattering cross sections and neglecting quantum-statistical effects. With this approximation, it is found that the energy transfer rate from the lithium sample to the rubidium sample via the potassium sample is comparable to or larger than the rate for direct energy transfer from lithium to rubidium, if the rubidium atom number is less than  $20 \left( \begin{smallmatrix} +18 \\ -12 \end{smallmatrix} \right)$  times the potassium atom number, i.e. over the whole part of the cooling sequence discussed in this section.

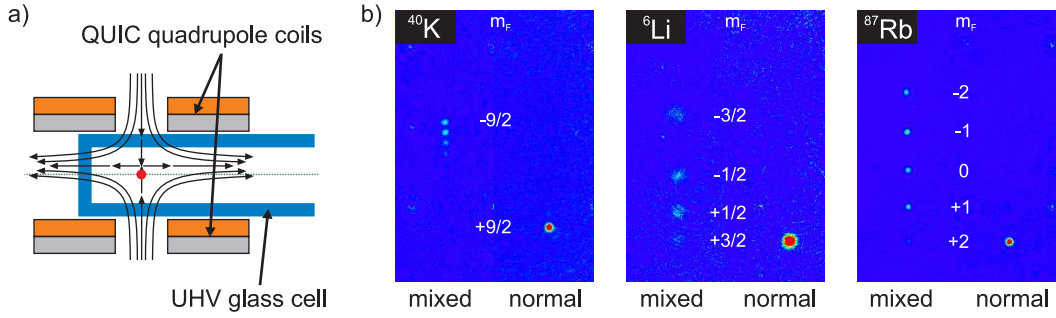


**Figure 6.13:** Verification of state pureness in the triple mixture. a) After release from the trap, the different Zeeman states are separated by applying a magnetic field gradient during the free expansion of the cloud (Stern-Gerlach method). An asymmetric pair (displayed in orange color) of the QUIC quadrupole coils is used for this purpose. b) Absorption images of  ${}^6\text{Li}$ ,  ${}^{40}\text{K}$  and  ${}^{87}\text{Rb}$  after 4 ms, 2.5 ms, and 6 ms time of flight, respectively. For each species, the right-hand side image shows that almost perfectly pure atomic samples in the desired states were produced. For the left-hand side images, the different Zeeman states were deliberately mixed to show where wrong Zeeman components appear if present. The field of view is  $4.3 \times 1.6 \text{ mm}^2$ .

#### 6.3.4.2. Verification of state pureness

Further experiments with the quantum-degenerate three-species mixture require defined starting conditions. Therefore, state pureness at the end of the evaporation process was verified for all three species, using a Stern-Gerlach method. This is illustrated in Fig. 6.13. In order to separate the different Zeeman components of the atomic cloud, we release the atoms from the trap and subsequently apply a field gradient of about  $150 \text{ G/cm}$  for a duration of a few milliseconds (depending on the species) to the atoms. The field gradient is generated by sending a current pulse through an asymmetric pair of coils in the coil stacks that are normally used to produce the quadrupole field of the QUIC trap (see Fig. 6.13 a)). This setup has the advantage that no additional coils are necessary that would potentially reduce the excellent optical and mechanical access to the glass cell. Moreover, it allows us to obtain comparatively high field gradients with low offset fields at the position of the atoms. This feature is particularly important for separation of the different Zeeman components in the lithium and potassium clouds. The current pulse is generated by temporarily switching a precharged condensator with a large capacity of  $470 \text{ mF}$  to the coil pair using computer-controlled MOSFETs. Care was taken that the whole Stern-Gerlach setup is at a floating electrical potential in order to avoid an influence on the offset magnetic field of the trap. The absorption images obtained with this method are shown in Fig. 6.13 b). For each species two images were recorded separately: one in normal configuration to verify state pureness (right half of each subfigure) and one, where the different  $m_F$ -states were deliberately mixed (left half of each subfigure) to give the positions where atoms in wrong  $m_F$ -states appear in the absorption image. Evaluation of the data yields that more than 97% of the atoms are in the correct  $m_F$ -state for any of the species.



## 7. Conclusions and Outlook

In recent years, ultracold dilute quantum gases have been used as very well controllable model systems for the study of phenomena relevant also for other physical fields, especially for condensed-matter physics. In particular, the investigation of the cross-over regime between a Bose-Einstein condensate (BEC) of molecules and a Bardeen-Cooper-Schrieffer (BCS) type superfluid of Cooper pairs using ultracold fermionic atoms was a breakthrough in the field of quantum gases. The experiments on the BEC-BCS cross-over conducted so far have employed a mixture of two different internal states of a single fermionic species. In this thesis work, the first two-species Fermi-Fermi mixture was produced and cooled into quantum-degeneracy. The use of two different fermionic species adds the mass as an additional degree of freedom to the system and will allow us to conveniently apply component-selective methods.

The experimental concept for the realization of the quantum-degenerate two-species Fermi-Fermi mixture (optionally coexisting with a BEC), which relies on sympathetic cooling of the two fermionic species  ${}^6\text{Li}$  and  ${}^{40}\text{K}$  by a large cloud of the bosonic species  ${}^{87}\text{Rb}$ , proved to be successful. A three-species magneto-optical trap was realized as a source of precooled atoms. Light-assisted interspecies losses were found to be at an acceptable level so that all three species can be loaded simultaneously into the MOT. This avoids the need of sequential loading of the species into the magnetic trap. The challenge in the development of an appropriate experimental sequence was to combine the different constraints that the individual atomic species enforce on the set of trapping and cooling parameters. Especially, the lack of sub-Doppler cooling for lithium and the small elastic scattering cross section between rubidium and lithium were demanding preconditions. Nevertheless, good starting conditions for evaporative and sympathetic cooling could be obtained for all three species simultaneously by applying a combined temporal dark MOT (dMOT) and compressed MOT (cMOT) phase at the end of the laser-cooling stage. In addition, we showed that the efficiency of sympathetic cooling can be improved by the presence of a third species through catalytic cooling. We demonstrated this by studying the final stage of sympathetic cooling of  ${}^6\text{Li}$  by  ${}^{87}\text{Rb}$  into quantum degeneracy in the presence and in the absence of  ${}^{40}\text{K}$ . The inherent complexity of the system requires an experimental apparatus that is very reliable. Care was also taken to employ components that require as little daily maintenance work as possible, e.g. a laser system based solely on semiconductor devices, so that the experiment can be run by a small team. This experimental system is a very versatile platform for a wide range of experiments. For instance, the excellent optical access to the atoms allows us to conveniently apply a variety of optical potentials.

One direction of possible research projects with the system focuses on ultracold molecules consisting of two atoms of *different fermionic* species. Such heteronuclear Fermi-Fermi dimers could be associated by exploiting an appropriate magnetically tunable interspecies Feshbach resonance, as has been demonstrated for the homonuclear case [97]. These molecules are expected to be stable in the vicinity of the relevant Feshbach resonance

due to consequences of the Pauli principle [113]. In a subsequent step, the molecules could be transferred into the ro-vibrational ground state, e.g. by schemes that rely on short laser pulses shaped by optimal control and on the dynamical evolution of the radial molecule wavefunction to overcome the challenge of small Frank-Condon overlap integrals [273, 274]. In the ro-vibrational ground state, the heteronuclear  ${}^6\text{Li}-{}^{40}\text{K}$  molecules exhibit a large permanent electrical dipole moment [76]. It has been proposed that dipolar molecules could be used to measure the permanent electric dipole moment of the electron [275, 276], for quantum computations [77, 277] or to study new quantum phases in optical lattices [85, 278, 279]. Possible more immediate projects include the characterization of  ${}^6\text{Li}-{}^{40}\text{K}$  Feshbach resonances, a study of the molecule association efficiency and a measurement of the lifetime of these molecules close to a Feshbach resonance.

Another line of research will employ the two-species Fermi-Fermi mixture to investigate the BEC-BCS cross-over, in particular the regime of strong interactions close to a Feshbach resonance. On resonance, the physics of the system does not depend on the details of the interaction but is universal [280]. The only relevant length scale in this case is the inter-particle distance, the corresponding energy scale is set by the Fermi energy. An important aspect of the two-species Fermi-Fermi mixture is now that unmatched Fermi surfaces can be obtained even in the case of equal atom numbers in the two components. This can be exploited to study a variety of analogies to other many-body systems, in particular to a spatially inhomogeneous superfluid phase predicted to occur in certain types of high temperature superconductors [134–137]. Furthermore, a transition to a crystalline phase in the bulk gas [138] and the possibility to simulate baryonic phases of quantum chromodynamics [139, 140] have been theoretically proposed for the two-species Fermi-Fermi mixture. The possibility to tune interactions and to conveniently apply component-selective methods further broadens the experimental options of the system.

## A. Natural constants and atomic properties

### Natural constants

The values of the following natural constants correspond to the recommendations of the CODATA commission and can be found at <http://physics.nist.gov/funcon.html>.

quantity	symbol	unit	value
speed of light	$c$		299 792 458 $\text{m s}^{-1}$
Planck's constant	$h$		$6.626\,069\,3(11) \times 10^{-34}$ J s
electron charge	$e$		$1.602\,176\,53(14) \times 10^{-19}$ C
Bohr magneton	$\mu_{\text{B}}$		$9.274\,009\,49(80) \times 10^{-24}$ J T $^{-1}$
nuclear magneton	$\mu_{\text{N}}$		$5.050\,783\,43(43) \times 10^{-27}$ J T $^{-1}$
Bohr radius	$a_0$		$0.529\,177\,210\,8(18) \times 10^{-10}$ m
electron mass	$m_{\text{e}}$		$9.109\,382\,6(16) \times 10^{-31}$ kg
Boltzmann constant	$k_{\text{B}}$		$1.380\,6504(24) \times 10^{-23}$ J K $^{-1}$
atomic mass unit	$u$		$1.660\,538\,782(83) \times 10^{-27}$ kg

## Atomic properties

The following table summarizes the most important atomic properties for the species used in the experiments described in this thesis:

symbol	${}^6\text{Li}$	${}^{40}\text{K}$	${}^{87}\text{Rb}$	unit	references
$\eta$	7.59 (4) %	0.0117 (1) %	27.83 (2) %		[281]
$m$	6.015 122 3 (5)	39.963 998 67 (29)	86.909 187 35 (27)	u	[282]
$T_{1/2}$	stable	$1.25 \times 10^9$	$4.81 \times 10^{10}$	years	[281]
$I$	1	4	3/2		[281]
$g_I$	-4.476 540 (3)	1.765 490 (34)	-9.951 414 (10)	$10^{-4}$	[216]
$\nu_{\text{hf}}$	228.205 28 (8)	1285.79 (1)	6834.682 6109 (3)	MHz	[216]
$a_S$	+38.75	+104.8 (4)	+90.6	$a_0$	[70, 283–285]
$a_T$	-2240	+174 (7)	+98.96	$a_0$	[70, 283–285]
$\tau$	27.102	25.7	26.24	ns	[286, 287]
$\Gamma$	5.8724	6.2	6.065	MHz	[288]
$\lambda_2$	670.977	766.7	780.246	nm	[288–290]
$I_s$	2.541	1.8	1.669	$\text{mW cm}^{-2}$	
$v_{\text{rec}}$	9.9	1.3	0.59	cm/s	
$T_{\text{rec}}$	7089	814	362	nK	
$T_D$	141	149	146	$\mu\text{K}$	

Here,  $\eta$  is the relative abundance of the isotope,  $m$  the atomic mass,  $T_{1/2}$  the nuclear half-lifetime,  $I$  the nuclear spin,  $g_I$  the nuclear g-factor,  $\nu_{\text{hf}}$  the ground state hyperfine splitting,  $a_S$  the singlet s-wave scattering length,  $a_T$  the triplet s-wave scattering length,  $\tau$  the lifetime of the excited  $P_{3/2}$  state,  $\Gamma$  the corresponding linewidth,  $\lambda_2$  the resonance wavelength of the  $D_2$  line in vacuum,  $I_s = \pi \hbar c \Gamma / (3\lambda_2^3)$  the saturation intensity,  $v_{\text{rec}} = \hbar / (m\lambda_2)$  the photon recoil velocity,  $T_{\text{rec}} = mv_{\text{rec}}^2 / k_B$  the photon recoil temperature, and  $T_D = \hbar \Gamma / (2k_B)$  the Doppler temperature.

The triplet interspecies scattering lengths of  ${}^6\text{Li}$ ,  ${}^{40}\text{K}$ , and  ${}^{87}\text{Rb}$  are given in the following table:

quantity	symbol	value	unit	reference
${}^6\text{Li}$ - ${}^{87}\text{Rb}$ triplet scattering length	$a_{T,LiRb}$	$\pm 20 \begin{smallmatrix} +9 \\ -6 \end{smallmatrix}$	$a_0$	[64]
${}^{40}\text{K}$ - ${}^{87}\text{Rb}$ triplet scattering length	$a_{T,KRb}$	-215 (10)	$a_0$	[270, 271]
${}^6\text{Li}$ - ${}^{40}\text{K}$ triplet scattering length	$a_{T,LiK}$	+63.5 (1)	$a_0$	[248]

## Bibliography

- [1] A. L. Migdall, J. V. Prodan, W. D. Phillips, T. H. Bergeman, and H. J. Metcalf. First observation of magnetically trapped neutral atoms. *Phys. Rev. Lett.* **54**, 2596 (1985).
- [2] E. L. Raab, M. Prentiss, A. Cable, S. Chu, and D. E. Pritchard. Trapping of neutral sodium atoms with radiation pressure. *Phys. Rev. Lett.* **59**, 2631 (1987).
- [3] H. F. Hess. Evaporative cooling of magnetically trapped and compressed spin-polarized hydrogen. *Phys. Rev. B* **34**, 3476 (1986).
- [4] N. Masuhara, J. M. Doyle, J. C. Sandberg, D. Kleppner, T. J. Greytak, H. F. Hess, and G. P. Kochanski. Evaporative cooling of spin-polarized atomic hydrogen. *Phys. Rev. Lett.* **61**, 935 (1988).
- [5] W. Ketterle and N. van Druten. Evaporative cooling of trapped atoms. In B. Bederson and H. Walther (eds.), *Advances in Atomic, Molecular, and Optical Physics*, vol. 37, p. 181. Academic Press, San Diego (1996).
- [6] M. Anderson and J. Ensher. Observation of Bose-Einstein condensation in a dilute atomic vapor. *Science* **269**, 198 (1995).
- [7] C. C. Bradley, C. A. Sackett, J. J. Tollett, and R. G. Hulet. Evidence of Bose-Einstein condensation in an atomic gas with attractive interactions. *Phys. Rev. Lett.* **75**, 1687 (1995).
- [8] K. B. Davis, M. O. Mewes, M. R. Andrews, N. J. van Druten, D. S. Durfee, D. M. Kurn, and W. Ketterle. Bose-Einstein condensation in a gas of sodium atoms. *Phys. Rev. Lett.* **75**, 3969 (1995).
- [9] C. C. Bradley, C. A. Sackett, and R. G. Hulet. Bose-Einstein condensation of lithium: Observation of limited condensate number. *Phys. Rev. Lett.* **78**, 985 (1997).
- [10] B. de Marco and D. Jin. Onset of Fermi degeneracy in a trapped atomic gas. *Science* **285**, 1703 (1999).
- [11] A. G. Truscott, K. E. Strecker, W. I. McAlexander, G. B. Partridge, and R. G. Hulet. Observation of Fermi pressure in a gas of trapped atoms. *Science* **291**, 2570 (2001).
- [12] F. Schreck, L. Khaykovich, K. L. Corwin, G. Ferrari, T. Bourdel, J. Cubizolles, and C. Salomon. Quasipure Bose-Einstein condensate immersed in a Fermi sea. *Phys. Rev. Lett.* **87**, 080403 (2001).

- [13] S. R. Granade, M. E. Gehm, K. M. O'Hara, and J. E. Thomas. All-optical production of a degenerate Fermi gas. *Phys. Rev. Lett.* **88**, 120405 (2002).
- [14] Z. Hadzibabic, C. A. Stan, K. Dieckmann, S. Gupta, M. W. Zwierlein, A. Görlitz, and W. Ketterle. Two-species mixture of quantum degenerate Bose and Fermi gases. *Phys. Rev. Lett.* **88**, 160401 (2002).
- [15] S. Jochim, M. Bartenstein, A. Altmeyer, G. Hendl, S. Riedl, C. Chin, J. H. Denschlag, and R. Grimm. Bose-Einstein condensation of molecules. *Science* **302**, 2101 (2003).
- [16] M. Taglieber, A.-C. Voigt, T. Aoki, T. W. Hänsch, and K. Dieckmann. Quantum degenerate two-species Fermi-Fermi mixture coexisting with a Bose-Einstein condensate. *Phys. Rev. Lett.* **100**, 010401 (2008).
- [17] A. Einstein. Quantentheorie des idealen einatomigen Gases. *Sitzungsber. Preuss. Akad. Wiss.* **3**, 18 (1925).
- [18] S. Bose. Plancks Gesetz und Lichtquantenhypothese. *Zeitschrift für Physik* **26**, 178 (1924).
- [19] T. W. Hänsch and A. L. Schawlow. Cooling of gases by laser radiation. *Opt. Commun.* **13**, 68 (1975).
- [20] S. Chu. Nobel lecture: The manipulation of neutral particles. *Rev. Mod. Phys.* **70**, 685 (1998).
- [21] C. N. Cohen-Tannoudji. Nobel lecture: Manipulating atoms with photons. *Rev. Mod. Phys.* **70**, 707 (1998).
- [22] W. D. Phillips. Nobel lecture: Laser cooling and trapping of neutral atoms. *Rev. Mod. Phys.* **70**, 721 (1998).
- [23] J. Dalibard and C. Cohen-Tannoudji. Dressed-atom approach to atomic motion in laser light: the dipole force revisited. *J. Opt. Soc. Am. B* **2**, 1707 (1985).
- [24] S. Chu, J. E. Bjorkholm, A. Ashkin, and A. Cable. Experimental observation of optically trapped atoms. *Phys. Rev. Lett.* **57**, 314 (1986).
- [25] E. A. Cornell and C. E. Wieman. Nobel lecture: Bose-Einstein condensation in a dilute gas, the first 70 years and some recent experiments. *Rev. Mod. Phys.* **74**, 875 (2002).
- [26] W. Ketterle. Nobel lecture: When atoms behave as waves: Bose-Einstein condensation and the atom laser. *Rev. Mod. Phys.* **74**, 1131 (2002).
- [27] F. Dalfovo, S. Giorgini, L. P. Pitaevskii, and S. Stringari. Theory of Bose-Einstein condensation in trapped gases. *Rev. Mod. Phys.* **71**, 463 (1999).
- [28] A. J. Leggett. Bose-Einstein condensation in the alkali gases: Some fundamental concepts. *Rev. Mod. Phys.* **73**, 307 (2001).

- 
- [29] D. G. Fried, T. C. Killian, L. Willmann, D. Landhuis, S. C. Moss, D. Kleppner, and T. J. Greytak. Bose-Einstein condensation of atomic hydrogen. *Phys. Rev. Lett.* **81**, 3811 (1998).
- [30] A. Robert, O. Sirjean, A. Browaeys, J. Poupard, S. Nowak, D. Boiron, C. I. Westbrook, and A. Aspect. A Bose-Einstein condensate of metastable atoms. *Science* **292**, 461 (2001).
- [31] F. Pereira Dos Santos, J. Léonard, J. Wang, C. J. Barrelet, F. Perales, E. Rasel, C. S. Unnikrishnan, M. Leduc, and C. Cohen-Tannoudji. Bose-Einstein condensation of metastable helium. *Phys. Rev. Lett.* **86**, 3459 (2001).
- [32] G. Modugno, G. Ferrari, G. Roati, R. J. Brecha, A. Simoni, and M. Inguscio. Bose-Einstein condensation of potassium atoms by sympathetic cooling. *Science* **294**, 1320 (2001).
- [33] A. Griesmaier, J. Werner, S. Hensler, J. Stuhler, and T. Pfau. Bose-Einstein condensation of chromium. *Phys. Rev. Lett.* **94**, 160401 (2005).
- [34] S. L. Cornish, N. R. Claussen, J. L. Roberts, E. A. Cornell, and C. E. Wieman. Stable  $^{85}\text{Rb}$  Bose-Einstein condensates with widely tunable interactions. *Phys. Rev. Lett.* **85**, 1795 (2000).
- [35] T. Weber, J. Herbig, M. Mark, H.-C. Nägerl, and R. Grimm. Bose-Einstein condensation of cesium. *Science* **299**, 232 (2002).
- [36] Y. Takasu, K. Maki, K. Komori, T. Takano, K. Honda, M. Kumakura, T. Yabuzaki, and Y. Takahashi. Spin-singlet Bose-Einstein condensation of two-electron atoms. *Phys. Rev. Lett.* **91**, 040404 (2003).
- [37] T. Fukuhara, S. Sugawa, and Y. Takahashi. Bose-Einstein condensation of an ytterbium isotope. *Physical Review A (Atomic, Molecular, and Optical Physics)* **76**, 051604 (2007).
- [38] T. Fukuhara, Y. Takasu, and S. S. und Y. Takahashi. Quantum degenerate Fermi gases of ytterbium atoms. *J. Low Temp. Phys.* **148**, 441 (2007).
- [39] Group of R. Grimm. <http://www.uibk.ac.at/exphys/ultracold/atomtraps.html>.
- [40] J. H. Thywissen and A. Danilova. <http://ucan.physics.utoronto.ca/News>.
- [41] M. Greiner, O. Mandel, T. Esslinger, T. W. Hänsch, and I. Bloch. Quantum phase transition from a superfluid to a Mott insulator in a gas of ultracold atoms. *Nature* **415**, 39 (2002).
- [42] T. Kinoshita, T. Wenger, and D. S. Weiss. Observation of a one-dimensional Tonks-Girardeau gas. *Science* **305**, 1125 (2004).
- [43] B. Paredes, A. Widera, V. Murg, O. Mandel, S. Fölling, I. Cirac, G. V. Shlyapnikov, T. W. Hänsch, and I. Bloch. Tonks-Girardeau gas of ultracold atoms in an optical lattice. *Nature* **429**, 277 (2004).

- [44] Z. Hadzibabic, P. Krüger, M. Cheneau, B. Battelier, and J. Dalibard. Berezinskii-Kosterlitz-Thouless crossover in a trapped atomic gas. *Nature* **441**, 1118 (2006).
- [45] H. Feshbach. Unified theory of nuclear reactions. *Ann. Phys. (N.Y.)* **5**, 357 (1958).
- [46] H. Feshbach. A unified theory of nuclear reactions. II. *Ann. Phys. (N.Y.)* **19**, 287 (1962).
- [47] E. Tiesinga, B. J. Verhaar, and H. T. C. Stoof. Threshold and resonance phenomena in ultracold ground-state collisions. *Phys. Rev. A* **47**, 4114 (1993).
- [48] S. Inouye, M. Andrews, J. Stenger, H.-J. Miesner, D. M. Stamper-Kurn, and W. Ketterle. Observation of Feshbach resonances in a Bose-Einstein condensate. *Nature* **392**, 151 (1998).
- [49] P. Courteille, R. S. Freeland, D. J. Heinzen, F. A. van Abeelen, and B. J. Verhaar. Observation of a Feshbach resonance in cold atom scattering. *Phys. Rev. Lett.* **81**, 69 (1998).
- [50] J. L. Roberts, N. R. Claussen, J. P. Burke, C. H. Greene, E. A. Cornell, and C. E. Wieman. Resonant magnetic field control of elastic scattering in cold  $^{85}\text{Rb}$ . *Phys. Rev. Lett.* **81**, 5109 (1998).
- [51] V. Vuletić, A. J. Kerman, C. Chin, and S. Chu. Observation of low-field Feshbach resonances in collisions of cesium atoms. *Phys. Rev. Lett.* **82**, 1406 (1999).
- [52] J. Stenger, S. Inouye, M. R. Andrews, H.-J. Miesner, D. M. Stamper-Kurn, and W. Ketterle. Strongly enhanced inelastic collisions in a Bose-Einstein condensate near Feshbach resonances. *Phys. Rev. Lett.* **82**, 2422 (1999).
- [53] J. L. Roberts, N. R. Claussen, S. L. Cornish, and C. E. Wieman. Magnetic field dependence of ultracold inelastic collisions near a Feshbach resonance. *Phys. Rev. Lett.* **85**, 728 (2000).
- [54] L. Khaykovich, F. Schreck, G. Ferrari, T. Bourdel, J. Cubizolles, L. D. Carr, Y. Castin, and C. Salomon. Formation of a matter-wave bright soliton. *Science* **296**, 1290 (2002).
- [55] K. E. Strecker, G. B. Partridge, A. G. Truscott, and R. G. Hulet. Formation and propagation of matter-wave soliton trains. *Nature* **417**, 150 (2002).
- [56] G. Roati, F. Riboli, G. Modugno, and M. Inguscio. Fermi-Bose quantum degenerate  $^{40}\text{K}$ - $^{87}\text{Rb}$  mixture with attractive interaction. *Phys. Rev. Lett.* **89**, 150403 (2002).
- [57] M. Köhl, H. Moritz, T. Stöferle, K. Günter, and T. Esslinger. Fermionic atoms in a three dimensional optical lattice: Observing Fermi surfaces, dynamics, and interactions. *Phys. Rev. Lett.* **94**, 080403 (2005).
- [58] C. Ospelkaus, S. Ospelkaus, K. Sengstock, and K. Bongs. Interaction-driven dynamics of  $^{40}\text{K}$ - $^{87}\text{Rb}$  Fermion-Boson gas mixtures in the large-particle-number limit. *Phys. Rev. Lett.* **96**, 020401 (2006).

- 
- [59] S. Aubin, S. Myrskog, M. Extavour, L. Leblanc, D. McKay, A. Stumm, and J. Thywissen. Rapid sympathetic cooling to Fermi degeneracy on a chip. *Nature Physics* **2**, 384 (2006).
- [60] J. M. McNamara, T. Jeltsov, A. S. Tychkov, W. Hogervorst, and W. Vassen. Degenerate Bose-Fermi mixture of metastable atoms. *Phys. Rev. Lett.* **97**, 080404 (2006).
- [61] T. Fukuhara, Y. Takasu, M. Kumakura, and Y. Takahashi. Degenerate Fermi gases of ytterbium. *Phys. Rev. Lett.* **98**, 030401 (2007).
- [62] E. Fermi. Zur Quantelung des idealen einatomigen Gases. *Z. Phys.* **36**, 902 (1926).
- [63] D. J. Wineland, R. E. Drullinger, and F. L. Walls. Radiation-pressure cooling of bound resonant absorbers. *Phys. Rev. Lett.* **40**, 1639 (1978).
- [64] C. Silber, S. Günther, C. Marzok, B. Deh, P. W. Courteille, and C. Zimmermann. Quantum-degenerate mixture of fermionic lithium and bosonic rubidium gases. *Phys. Rev. Lett.* **95**, 170408 (2005).
- [65] G. Ferrari. Collisional relaxation in a fermionic gas. *Phys. Rev. A* **59**, R4125 (1999).
- [66] B. de Marco, S. B. Papp, and D. S. Jin. Pauli blocking of collisions in a quantum degenerate atomic Fermi gas. *Phys. Rev. Lett.* **86**, 5409 (2001).
- [67] K. M. O'Hara, S. L. Hemmer, S. R. Granade, M. E. Gehm, J. E. Thomas, V. Venturi, E. Tiesinga, and C. J. Williams. Measurement of the zero crossing in a Feshbach resonance of fermionic  ${}^6\text{Li}$ . *Phys. Rev. A* **66**, 041401 (2002).
- [68] K. Dieckmann, C. A. Stan, S. Gupta, Z. Hadzibabic, C. H. Schunck, and W. Ketterle. Decay of an ultracold fermionic lithium gas near a Feshbach resonance. *Phys. Rev. Lett.* **89**, 203201 (2002).
- [69] S. Jochim, M. Bartenstein, G. Hendl, J. H. Denschlag, R. Grimm, A. Mosk, and M. Weidemüller. Magnetic field control of elastic scattering in a cold gas of fermionic lithium atoms. *Phys. Rev. Lett.* **89**, 273202 (2002).
- [70] T. Loftus, C. A. Regal, C. Ticknor, J. L. Bohn, and D. S. Jin. Resonant control of elastic collisions in an optically trapped Fermi gas of atoms. *Phys. Rev. Lett.* **88**, 173201 (2002).
- [71] T. Bourdel, J. Cubizolles, L. Khaykovich, K. M. F. Magalhães, S. J. J. M. F. Kokkelmans, G. V. Shlyapnikov, and C. Salomon. Measurement of the interaction energy near a Feshbach resonance in a  ${}^6\text{Li}$  Fermi gas. *Phys. Rev. Lett.* **91**, 020402 (2003).
- [72] S. Jochim. *Bose-Einstein condensation of molecules*. Ph.D. thesis, Leopold-Franzens-Universität, Innsbruck (2004).
- [73] J. Bardeen, L. N. Cooper, and J. R. Schrieffer. Theory of superconductivity. *Phys. Rev.* **108**, 1175 (1957).

- [74] M. Houbiers, R. Ferwerda, H. T. C. Stoof, W. I. McAlexander, C. A. Sackett, and R. G. Hulet. Superfluid state of atomic  ${}^6\text{Li}$  in a magnetic trap. *Phys. Rev. A* **56**, 4864 (1997).
- [75] M. Houbiers, R. Ferwerda, H. T. C. Stoof, W. I. McAlexander, C. A. Sackett, and R. G. Hulet. Erratum: Superfluid state of atomic  ${}^6\text{Li}$  in a magnetic trap [Phys. Rev. A 56, 4864 (1997)]. *Phys. Rev. A* **57**, 4065 (1998).
- [76] M. Aymar and O. Dulieu. Calculation of accurate permanent dipole moments of the lowest  ${}^1,{}^3\Sigma^+$  states of heteronuclear alkali dimers using extended basis sets. *J. Chem. Phys.* **122**, 204302 (2005).
- [77] D. de Mille. Quantum computation with trapped polar molecules. *Phys. Rev. Lett.* **88**, 067901 (2002).
- [78] M. G. Kozlov and D. de Mille. Enhancement of the electric dipole moment of the electron in PbO. *Phys. Rev. Lett.* **89**, 133001 (2002).
- [79] J. J. Hudson, B. E. Sauer, M. R. Tarbutt, and E. A. Hinds. Measurement of the electron electric dipole moment using YbF molecules. *Phys. Rev. Lett.* **89**, 023003 (2002).
- [80] L. Santos, G. V. Shlyapnikov, P. Zoller, and M. Lewenstein. Bose-Einstein condensation in trapped dipolar gases. *Phys. Rev. Lett.* **85**, 1791 (2000).
- [81] L. Santos, G. V. Shlyapnikov, P. Zoller, and M. Lewenstein. Erratum: Bose-Einstein condensation in trapped dipolar gases [Phys. Rev. Lett. **85**, 1791 (2000)]. *Phys. Rev. Lett.* **88**, 139904 (2002).
- [82] A. Griesmaier, J. Stuhler, T. Koch, M. Fattori, T. Pfau, and S. Giovanazzi. Comparing contact and dipolar interactions in a Bose-Einstein condensate. *Phys. Rev. Lett.* **97**, 250402 (2006).
- [83] K. Góral and L. Santos. Ground state and elementary excitations of single and binary Bose-Einstein condensates of trapped dipolar gases. *Phys. Rev. A* **66**, 023613 (2002).
- [84] M. A. Baranov, M. S. Mar'enko, V. S. Rychkov, and G. V. Shlyapnikov. Superfluid pairing in a polarized dipolar Fermi gas. *Phys. Rev. A* **66**, 013606 (2002).
- [85] K. Góral, L. Santos, and M. Lewenstein. Quantum phases of dipolar bosons in optical lattices. *Phys. Rev. Lett.* **88**, 170406 (2002).
- [86] B. Damski, L. Santos, E. Tiemann, M. Lewenstein, S. Kotochigova, P. Julienne, and P. Zoller. Creation of a dipolar superfluid in optical lattices. *Phys. Rev. Lett.* **90**, 110401 (2003).
- [87] J. Doyle, B. Friedrich, R. V. Krems, and F. Masnou-Seeuws. Editorial: Quo vadis, cold molecules? *Eur. Phys. J. D* **31**, 149 (2004).

- 
- [88] J. D. Weinstein, R. de Carvalho, T. Guillet, B. Friedrich, and J. M. Doyle. Magnetic trapping of calcium monohydride molecules at millikelvin temperatures. *Nature* **395**, 148 (1998).
- [89] H. L. Bethlem, G. Berden, and G. Meijer. Decelerating neutral dipolar molecules. *Phys. Rev. Lett.* **83**, 1558 (1999).
- [90] K. M. Jones, E. Tiesinga, P. D. Lett, and P. S. Julienne. Ultracold photoassociation spectroscopy: Long-range molecules and atomic scattering. *Rev. Mod. Phys.* **78**, 483 (2006).
- [91] F. H. Mies, E. Tiesinga, and P. S. Julienne. Manipulation of Feshbach resonances in ultracold atomic collisions using time-dependent magnetic fields. *Phys. Rev. A* **61**, 022721 (2000).
- [92] K. Xu, T. Mukaiyama, J. R. Abo-Shaeer, J. K. Chin, D. E. Miller, and W. Ketterle. Formation of quantum-degenerate sodium molecules. *Phys. Rev. Lett.* **91**, 210402 (2003).
- [93] S. Dürr, T. Volz, A. Marte, and G. Rempe. Observation of molecules produced from a Bose-Einstein condensate. *Phys. Rev. Lett.* **92**, 020406 (2004).
- [94] J. Herbig, T. Kraemer, M. Mark, T. Weber, C. Chin, H.-C. Nägerl, and R. Grimm. Preparation of a pure molecular quantum gas. *Science* **301**, 1510 (2003).
- [95] K. E. Strecker, G. B. Partridge, and R. G. Hulet. Conversion of an atomic Fermi gas to a long-lived molecular Bose gas. *Phys. Rev. Lett.* **91**, 080406 (2003).
- [96] J. Cubizolles, T. Bourdel, S. J. J. M. F. Kokkelmans, G. V. Shlyapnikov, and C. Salomon. Production of long-lived ultracold  $\text{Li}_2$  molecules from a Fermi gas. *Phys. Rev. Lett.* **91**, 240401 (2003).
- [97] C. Regal, C. Ticknor, J. Bohn, and D. Jin. Creation of ultracold molecules from a Fermi gas of atoms. *Nature* **424**, 47 (2003).
- [98] S. Jochim, M. Bartenstein, A. Altmeyer, G. Hendl, C. Chin, J. H. Denschlag, and R. Grimm. Pure gas of optically trapped molecules created from fermionic atoms. *Phys. Rev. Lett.* **91**, 240402 (2003).
- [99] M. W. Zwierlein, C. A. Stan, C. H. Schunck, S. M. F. Raupach, S. Gupta, Z. Hadzibabic, and W. Ketterle. Observation of Bose-Einstein condensation of molecules. *Phys. Rev. Lett.* **91**, 250401 (2003).
- [100] C. Ospelkaus, S. Ospelkaus, L. Humbert, P. Ernst, K. Sengstock, and K. Bongs. Ultracold heteronuclear molecules in a 3D optical lattice. *Phys. Rev. Lett.* **97**, 120402 (2006).
- [101] S. B. Papp and C. E. Wieman. Observation of heteronuclear Feshbach molecules from a  $^{85}\text{Rb}$ - $^{87}\text{Rb}$  gas. *Phys. Rev. Lett.* **97**, 180404 (2006).

- [102] T. Mukaiyama, J. R. Abo-Shaeer, K. Xu, J. K. Chin, and W. Ketterle. Dissociation and decay of ultracold sodium molecules. *Phys. Rev. Lett.* **92**, 180402 (2004).
- [103] C. Chin, T. Kraemer, M. Mark, J. Herbig, P. Waldburger, H.-C. Nägerl, and R. Grimm. Observation of Feshbach-like resonances in collisions between ultracold molecules. *Phys. Rev. Lett.* **94**, 123201 (2005).
- [104] N. Syassen, T. Volz, S. Teichmann, S. Dürr, and G. Rempe. Collisional decay of  $^{87}\text{Rb}$  Feshbach molecules at 1005.8 G. *Phys. Rev. A* **74**, 062706 (2006).
- [105] S. Dürr, T. Volz, and G. Rempe. Dissociation of ultracold molecules with Feshbach resonances. *Phys. Rev. A* **70**, 031601 (2004).
- [106] T. Volz, S. Dürr, N. Syassen, G. Rempe, E. van Kempen, and S. Kokkelmans. Feshbach spectroscopy of a shape resonance. *Phys. Rev. A* **72**, 010704 (2005).
- [107] M. Mark, T. Kraemer, J. Herbig, C. Chin, H.-C. Nägerl, and R. Grimm. Efficient creation of molecules from a cesium Bose-Einstein condensate. *Europhys. Lett.* **69**, 706 (2005).
- [108] E. Hodby, S. T. Thompson, C. A. Regal, M. Greiner, A. C. Wilson, D. S. Jin, E. A. Cornell, and C. E. Wieman. Production efficiency of ultracold Feshbach molecules in bosonic and fermionic systems. *Phys. Rev. Lett.* **94**, 120402 (2005).
- [109] S. T. Thompson, E. Hodby, and C. E. Wieman. Spontaneous dissociation of  $^{85}\text{Rb}$  Feshbach molecules. *Phys. Rev. Lett.* **94**, 020401 (2005).
- [110] G. Thalhammer, K. Winkler, F. Lang, S. Schmid, R. Grimm, and J. H. Denschlag. Long-lived Feshbach molecules in a three-dimensional optical lattice. *Phys. Rev. Lett.* **96**, 050402 (2006).
- [111] T. Volz, N. Syassen, D. M. Bauer, E. Hansis, S. Dürr, and G. Rempe. Preparation of a quantum state with one molecule at each site of an optical lattice. *Nature Physics* **2**, 692 (2006).
- [112] C. A. Regal, M. Greiner, and D. S. Jin. Lifetime of molecule-atom mixtures near a Feshbach resonance in  $^{40}\text{K}$ . *Phys. Rev. Lett.* **92**, 083201 (2004).
- [113] D. S. Petrov, C. Salomon, and G. V. Shlyapnikov. Weakly bound dimers of fermionic atoms. *Phys. Rev. Lett.* **93**, 090404 (2004).
- [114] M. Greiner, C. A. Regal, and D. S. Jin. Emergence of a molecular Bose-Einstein condensate from a Fermi gas. *Nature* **426**, 537 (2003).
- [115] C. A. Regal, M. Greiner, and D. S. Jin. Observation of resonance condensation of fermionic atom pairs. *Phys. Rev. Lett.* **92**, 040403 (2004).
- [116] M. W. Zwierlein, C. A. Stan, C. H. Schunck, S. M. F. Raupach, A. J. Kerman, and W. Ketterle. Condensation of pairs of fermionic atoms near a Feshbach resonance. *Phys. Rev. Lett.* **92**, 120403 (2004).

- 
- [117] M. Bartenstein, A. Altmeyer, S. Riedl, S. Jochim, C. Chin, J. H. Denschlag, and R. Grimm. Crossover from a molecular Bose-Einstein condensate to a degenerate Fermi gas. *Phys. Rev. Lett.* **92**, 120401 (2004).
- [118] J. Kinast, S. L. Hemmer, M. E. Gehm, A. Turlapov, and J. E. Thomas. Evidence for superfluidity in a resonantly interacting Fermi gas. *Phys. Rev. Lett.* **92**, 150402 (2004).
- [119] M. Bartenstein, A. Altmeyer, S. Riedl, S. Jochim, C. Chin, J. H. Denschlag, and R. Grimm. Collective excitations of a degenerate gas at the BEC-BCS crossover. *Phys. Rev. Lett.* **92**, 203201 (2004).
- [120] C. Chin, M. Bartenstein, A. Altmeyer, S. Riedl, S. Jochim, J. H. Denschlag, and R. Grimm. Observation of the pairing gap in a strongly interacting Fermi gas. *Science* **305**, 1128 (2004).
- [121] J. Kinast, A. Turlapov, J. E. Thomas, Q. Chen, J. Stajic, and K. Levin. Heat capacity of a strongly interacting Fermi gas. *Science* **307**, 1296 (2005).
- [122] M. W. Zwierlein, J. R. Abo-Shaer, A. Schirotzek, C. H. Schunck, and W. Ketterle. Vortices and superfluidity in a strongly interacting Fermi gas. *Nature* **435**, 1047 (2005).
- [123] P. Fulde and R. A. Ferrell. Superconductivity in a strong spin-exchange field. *Phys. Rev.* **135**, A550 (1964).
- [124] A. I. Larkin and Y. N. Ovchinnikov. *Sov. Phys. JETP* **20**, 762 (1965).
- [125] G. Sarma. On the influence of a uniform exchange field acting on the spins of the conduction electrons in a superconductor. *J. Phys. Chem. Solids* **24**, 1029 (1963).
- [126] W. V. Liu and F. Wilczek. Interior gap superfluidity. *Phys. Rev. Lett.* **90**, 047002 (2003).
- [127] P. F. Bedaque, H. Caldas, and G. Rupak. Phase separation in asymmetrical fermion superfluids. *Phys. Rev. Lett.* **91**, 247002 (2003).
- [128] H. Caldas. Cold asymmetrical fermion superfluids. *Phys. Rev. A* **69**, 063602 (2004).
- [129] J. Carlson and S. Reddy. Asymmetric two-component fermion systems in strong coupling. *Phys. Rev. Lett.* **95**, 060401 (2005).
- [130] G. B. Partridge, W. Li, R. I. Kamar, Y. Liao, and R. G. Hulet. Pairing and phase separation in a polarized Fermi gas. *Science* **311**, 503 (2006).
- [131] M. W. Zwierlein, A. Schirotzek, C. H. Schunck, and W. Ketterle. Fermionic superfluidity with imbalanced spin populations. *Science* **311**, 492 (2006).
- [132] M. W. Zwierlein, C. H. Schunck, A. Schirotzek, and W. Ketterle. Direct observation of the superfluid phase transition in ultracold Fermi gases. *Nature* **442**, 54 (2006).

- [133] C. H. Schunck, Y. Shin, A. Schirotzek, M. W. Zwierlein, and W. Ketterle. Pairing of strongly interacting fermions without superfluidity. arXiv:cond-mat/0702066v2 [cond-mat.str-el] (2007).
- [134] R. Casalbuoni and G. Nardulli. Inhomogeneous superconductivity in condensed matter and QCD. *Rev. Mod. Phys.* **76**, 263 (2004).
- [135] T. Mizushima, M. Ichioka, and K. Machida. Fulde-Ferrell-Larkin-Ovchinnikov states in a superfluid Fermi gas. *J. Phys. Chem. Sol.* **66**, 1359 (2005).
- [136] S.-T. Wu, C.-H. Pao, and S.-K. Yip. Resonant pairing between fermions with unequal masses. *Phys. Rev. B* **74**, 224504 (2006).
- [137] H. Hu, X.-J. Liu, and P. D. Drummond. Phase diagram of a strongly interacting polarized Fermi gas in one dimension. *Phys. Rev. Lett.* **98**, 070403 (2007).
- [138] D. S. Petrov, G. E. Astrakharchik, D. J. Papoular, C. Salomon, and G. V. Shlyapnikov. Crystalline phase of strongly interacting Fermi mixtures. *Phys. Rev. Lett.* **99**, 130407 (2007).
- [139] D. Wilczek. Quantum chromodynamics: Lifestyles of the small and simple. *Nature Physics* **3**, 375 (2007).
- [140] Á. Rapp, G. Zaránd, C. Honerkamp, and W. Hofstetter. Color superfluidity and “baryon” formation in ultracold fermions. *Phys. Rev. Lett.* **98**, 160405 (2007).
- [141] S. Azizi, M. Aymar, and O. Dulieu. Prospects for the formation of ultracold ground state polar molecules from mixed alkali atom pairs. *Eur. Phys. J. D* **31**, 195 (2004).
- [142] M. Greiner, I. Bloch, T. W. Hänsch, and T. Esslinger. Magnetic transport of trapped cold atoms over a large distance. *Phys. Rev. A* **63**, 031401 (2001).
- [143] M. Taglieber, A.-C. Voigt, F. Henkel, S. Fray, T. W. Hänsch, and K. Dieckmann. Simultaneous magneto-optical trapping of three atomic species. *Phys. Rev. A* **73**, 011402 (2006).
- [144] T. Esslinger, I. Bloch, and T. W. Hänsch. Bose-Einstein condensation in a quadrupole-Ioffe-configuration trap. *Phys. Rev. A* **58**, R2664 (1998).
- [145] J. Sakurai. *Modern quantum mechanics*. Addison-Wesley, New York, 2nd edn. (1994).
- [146] K. Huang. *Statistical Mechanics*. John Wiley, New York, 2nd edn. (1987).
- [147] C. Cohen-Tannoudji, B. Diu, and F. Laloë. *Quantum Mechanics*, vol. I. Wiley & Sons, New York (1977).
- [148] C. Cohen-Tannoudji, B. Diu, and F. Laloë. *Quantum Mechanics*, vol. II. Wiley & Sons, New York (1977).
- [149] F. Schwabl. *Quantenmechanik*. Springer, Berlin, 5th edn. (1998).

- 
- [150] F. Schwabl. *Quantenmechanik für Fortgeschrittene*. Springer, Berlin, 2nd edn. (2000).
- [151] W. Nolting. *Grundkurs Theoretische Physik - 6 Statistische Physik*. Verlag Vieweg (1998).
- [152] L. Landau and E. Lifschitz. *Quantenmechanik*, vol. III. Akademie Verlag, Berlin (1985).
- [153] W. Pauli. The connection between spin and statistics. *Phys. Rev.* **58**, 716 (1940).
- [154] W. Ketterle and N. J. van Druten. Bose-Einstein condensation of a finite number of particles trapped in one or three dimensions. *Phys. Rev. A* **54**, 656 (1996).
- [155] V. Bagnato, D. E. Pritchard, and D. Kleppner. Bose-Einstein condensation in an external potential. *Phys. Rev. A* **35**, 4354 (1987).
- [156] S. Grossmann and M. Holthaus. On Bose-Einstein condensation in harmonic traps. *Phys. Lett. A* **208**, 188 (1995).
- [157] K. Kirsten and D. J. Toms. Density of states for Bose-Einstein condensation in harmonic oscillator potentials. *Phys. Lett. A* **222**, 148 (1996).
- [158] A. MacLeod. Accurate and efficient evaluation of the Bose-Einstein functions  $g_{3/2}$  and  $g_{5/2}$ . *Comput. Phys.* **11**, 385 (1997).
- [159] A. MacLeod. Algorithm 779: Fermi-Dirac functions of order  $-1/2$ ,  $1/2$ ,  $3/2$ ,  $5/2$ . *ACM Trans. Math. Soft.* **24**, 1 (1998).
- [160] Gnu scientific library (gsl). Available at: <http://www.gnu.org/software/gsl/>.
- [161] D. A. Butts and D. S. Rokhsar. Trapped Fermi gases. *Phys. Rev. A* **55**, 4346 (1997).
- [162] S. Giorgini, L. P. Pitaevskii, and S. Stringari. Theory of ultracold Fermi gases. arXiv:0706.3360v2 [cond-mat.other] (2007).
- [163] R. Grimm. Ultracold Fermi gases in the BEC-BCS crossover: a review from the Innsbruck perspective. arXiv:cond-mat/0703091v1 [cond-mat.other] (2007). To be published in: Proceedings of the International School of Physics - Enrico Fermi - Course CLXIV.
- [164] W. Ketterle and M. W. Zwierlein. Making, probing and understanding ultracold Fermi gases. arXiv:0801.2500v1 [cond-mat.other] (2008). To be published in: Proceedings of the International School of Physics - Enrico Fermi - Course CLXIV.
- [165] G. M. Bruun and C. W. Clark. Ideal gases in time-dependent traps. *Phys. Rev. A* **61**, 061601 (2000).
- [166] W. Ketterle, D. S. Durfee, and D. M. Stamper-Kurn. Making, probing and understanding Bose-Einstein condensates. In M. Inguscio, S. Stringari, and C. E. Wieman (eds.), *Proceedings of the International School of Physics - Enrico Fermi - Course CXL*, p. 67. IOS Press (1999). Also available as: arXiv:cond-mat/9904034v2.

- [167] J. Dalibard. Collisional dynamics of ultra-cold atomic gases. In M. Inguscio, S. Stringari, and C. Wieman (eds.), *Proceedings of the International School of Physics Enrico Fermi, Course CXL*, p. 321. IOS Press, Amsterdam (1999).
- [168] E. A. Donley, N. R. Claussen, S. L. Cornish, J. L. Roberts, E. A. Cornell, and C. E. Wieman. Dynamics of collapsing and exploding Bose-Einstein condensates. *Nature* **412**, 295 (2001).
- [169] F. Dalfovo and S. Stringari. Bosons in anisotropic traps: Ground state and vortices. *Phys. Rev. A* **53**, 2477 (1996).
- [170] Y. Castin and R. Dum. Bose-Einstein condensates in time dependent traps. *Phys. Rev. Lett.* **77**, 5315 (1996).
- [171] Y. Kagan, E. Surkov, and G. Shlyapnikov. Evolution of a Bose-condensed gas under variation of the confining potential. *Phys. Rev. A* **54**, R1753 (1996).
- [172] F. Dalfovo, C. Minniti, S. Stringari, and L. Pitaevskii. Nonlinear dynamics of a Bose condensed gas. *Physics Letters A* **227**, 259 (1997).
- [173] J. Taylor. *Scattering Theory*. Wiley, New York (1972).
- [174] E. P. Wigner. On the behavior of cross sections near thresholds. *Phys. Rev.* **73**, 1002 (1948).
- [175] Z.-C. Yan, J. F. Babb, A. Dalgarno, and G. W. F. Drake. Variational calculations of dispersion coefficients for interactions among H, He, and Li atoms. *Phys. Rev. A* **54**, 2824 (1996).
- [176] A. Derevianko, W. R. Johnson, M. S. Safronova, and J. F. Babb. High-precision calculations of dispersion coefficients, static dipole polarizabilities, and atom-wall interaction constants for alkali-metal atoms. *Phys. Rev. Lett.* **82**, 3589 (1999).
- [177] D. Heinzen. Ultracold atomic interactions. In M. Inguscio, S. Stringari, and C. E. Wieman (eds.), *Proceedings of the International School of Physics Enrico Fermi, Course CXL*, pp. 351–390. IOS Press, Amsterdam (1999).
- [178] C. Pethick and H. Smith. *Bose-Einstein Condensation in Dilute Gases*. Cambridge University Press (2002).
- [179] H. T. C. Stoof, J. M. V. A. Koelman, and B. J. Verhaar. Spin-exchange and dipole relaxation rates in atomic hydrogen: Rigorous and simplified calculations. *Phys. Rev. B* **38**, 4688 (1988).
- [180] F. H. Mies, C. J. Williams, P. S. Julienne, and M. Krauss. Estimating bounds on collisional relaxation rates of spin-polarized  $^{87}\text{Rb}$  atoms at ultracold temperatures. *J. Res. Natl. Inst. Stand. Technol.* **101**, 521 (1996).
- [181] H. M. J. M. Boesten, A. J. Moerdijk, and B. J. Verhaar. Dipolar decay in two recent Bose-Einstein condensation experiments. *Phys. Rev. A* **54**, R29 (1996).

- 
- [182] A. J. Moerdijk and B. J. Verhaar. Collisional two- and three-body decay rates of dilute quantum gases at ultralow temperatures. *Phys. Rev. A* **53**, R19 (1996).
- [183] A. J. Moerdijk, H. M. J. M. Boesten, and B. J. Verhaar. Decay of trapped ultracold alkali atoms by recombination. *Phys. Rev. A* **53**, 916 (1996).
- [184] P. O. Fedichev, M. W. Reynolds, and G. V. Shlyapnikov. Three-body recombination of ultracold atoms to a weakly bound  $s$  level. *Phys. Rev. Lett.* **77**, 2921 (1996).
- [185] T. Weber, J. Herbig, M. Mark, H.-C. Nägerl, and R. Grimm. Three-body recombination at large scattering lengths in an ultracold atomic gas. *Phys. Rev. Lett.* **91**, 123201 (2003).
- [186] R. V. E. Lovelace, C. Mehanian, T. J. Tammila, and D. M. Lee. Magnetic confinement of a neutral gas. *Nature* **318**, 30 (1985).
- [187] J. Walraven. Atomic hydrogen in magnetostatic traps. In G. L. Oppo, S. M. Barnett, E. Riis, and M. Wilkinson (eds.), *Quantum Dynamics of Simple Systems*. CRC Press, London (1996).
- [188] J. M. Doyle. *Energy distribution measurements of magnetically trapped spin polarized atomic hydrogen : evaporative cooling and surface sticking*. Ph.D. thesis, Massachusetts Institute of Technology (1991).
- [189] O. J. Luiten. *Lyman- $\alpha$  spectroscopy of magnetically trapped atomic hydrogen*. Ph.D. thesis, University of Amsterdam (1993).
- [190] K. B. Davis, M.-O. Mewes, and W. Ketterle. An analytical model for evaporative cooling of atoms. *Appl. Phys. B* **60**, 155 (1995).
- [191] J. M. Doyle, J. C. Sandberg, I. A. Yu, C. L. Cesar, D. Kleppner, and T. J. Greytak. Evaporative cooling of atomic hydrogen: Theory of cooling and progress towards the Bose-Einstein transition. *Physica B* **194–196**, 13 (1994).
- [192] O. J. Luiten, M. W. Reynolds, and J. T. M. Walraven. Kinetic theory of the evaporative cooling of a trapped gas. *Phys. Rev. A* **53**, 381 (1996).
- [193] K. Dieckmann. *Bose-Einstein condensation with high atom number in a deep magnetic trap*. Ph.D. thesis, University of Amsterdam (2001).
- [194] P. Valkering. *Optimization of evaporative cooling of Rubidium atoms in a magnetic trap*. Master's thesis, FOM Institute for Atomic and Molecular Physics (1999). Unpublished.
- [195] R. Drullinger, D. Wineland, and J. Bergquist. High-resolution optical spectra of laser cooled ions. *Appl. Phys.* **22**, 365 (1980).
- [196] D. J. Larson, J. C. Bergquist, J. J. Bollinger, W. M. Itano, and D. J. Wineland. Sympathetic cooling of trapped ions: A laser-cooled two-species nonneutral ion plasma. *Phys. Rev. Lett.* **57**, 70 (1986).

- [197] J. Kim, B. Friedrich, D. P. Katz, D. Patterson, J. D. Weinstein, R. de Carvalho, and J. M. Doyle. Buffer-gas loading and magnetic trapping of atomic europium. *Phys. Rev. Lett.* **78**, 3665 (1997).
- [198] J. D. Weinstein, R. de Carvalho, J. Kim, D. Patterson, B. Friedrich, and J. M. Doyle. Magnetic trapping of atomic chromium. *Phys. Rev. A* **57**, R3173 (1998).
- [199] D. Egorov, J. D. Weinstein, D. Patterson, B. Friedrich, and J. M. Doyle. Spectroscopy of laser-ablated buffer-gas-cooled PbO at 4 K and the prospects for measuring the electric dipole moment of the electron. *Phys. Rev. A* **63**, 030501 (2001).
- [200] C. J. Myatt, E. A. Burt, R. W. Ghrist, E. A. Cornell, and C. E. Wieman. Production of two overlapping Bose-Einstein condensates by sympathetic cooling. *Phys. Rev. Lett.* **78**, 586 (1997).
- [201] J. Goldwin. *Quantum Degeneracy and Interactions in the  $^{87}\text{Rb}$ - $^{40}\text{K}$  Bose-Fermi Mixture*. Ph.D. thesis, University of Colorado (2005).
- [202] A. Mosk, S. Kraft, M. Mudrich, K. Singer, W. Wohlleben, R. Grimm, and M. Weidemüller. Mixture of ultracold lithium and cesium atoms in an optical dipole trap. *Appl. Phys. B* **73**, 791 (20010101).
- [203] D. E. Pritchard. Cooling neutral atoms in a magnetic trap for precision spectroscopy. *Phys. Rev. Lett.* **51**, 1336 (1983).
- [204] S. Ospelkaus, C. Ospelkaus, L. Humbert, K. Sengstock, and K. Bongs. Tuning of heteronuclear interactions in a degenerate Fermi-Bose mixture. *Phys. Rev. Lett.* **97**, 120403 (2006).
- [205] S. Ospelkaus-Schwarzer. *Quantum Degenerate Fermi-Bose Mixtures of  $^{40}\text{K}$  and  $^{87}\text{Rb}$  in 3D Optical Lattices*. Ph.D. thesis, Universität Hamburg (2006).
- [206] R. Roth and H. Feldmeier. Mean-field instability of trapped dilute boson-fermion mixtures. *Phys. Rev. A* **65**, 021603 (2002).
- [207] R. Roth. Structure and stability of trapped atomic boson-fermion mixtures. *Phys. Rev. A* **66**, 013614 (2002).
- [208] E. Timmermans and R. Côté. Superfluidity in sympathetic cooling with atomic Bose-Einstein condensates. *Phys. Rev. Lett.* **80**, 3419 (1998).
- [209] M. Li, Z. Yan, J. Chen, L. Chen, and C. Chen. Thermodynamic properties of an ideal Fermi gas in an external potential with  $u = br^t$  in any dimensional space. *Phys. Rev. A* **58**, 1445 (1998).
- [210] B. de Marco, H. Rohner, and D. S. Jin. An enriched  $^{40}\text{K}$  source for fermionic atom studies. *Rev. Sci. Instrum.* **70**, 1967 (1999).
- [211] F. Henkel. *Fermionisches Kalium in der dreikomponentigen magnetooptischen Falle*. Diplomarbeit, Ludwig-Maximilians University, Munich (2005). Unpublished.

- 
- [212] W. D. Phillips and H. Metcalf. Laser deceleration of an atomic beam. *Phys. Rev. Lett.* **48**, 596 (1982).
- [213] H. J. Metcalf and P. van der Straten. *Laser Cooling and Trapping*. Springer, New York (2002).
- [214] M. A. Joffe, W. Ketterle, A. Martin, and D. E. Pritchard. Transverse cooling and deflection of an atomic beam inside a Zeeman slower. *J. Opt. Soc. Am. B* **10**, 2257 (1993).
- [215] T. E. Barrett, S. W. Dapore-Schwartz, M. D. Ray, and G. P. Lafyatis. Slowing atoms with  $\sigma^-$  polarized light. *Phys. Rev. Lett.* **67**, 3483 (1991).
- [216] E. Arimondo, M. Inguscio, and P. Violino. Experimental determinations of the hyperfine structure in the alkali atoms. *Rev. Mod. Phys.* **49**, 31 (1977).
- [217] C. E. Wieman and L. Hollberg. Using diode lasers for atomic physics. *Rev. Sci. Instrum.* **62**, 1 (1991).
- [218] L. Ricci, M. Weidemüller, T. Esslinger, A. Hemmerich, C. Zimmermann, V. Vuletic, W. König, and T. W. Hänsch. A compact grating-stabilized diode laser system for atomic physics. *Optics Comm.* **117**, 541 (1995).
- [219] J. N. Walpole. Semiconductor amplifiers and lasers with tapered gain regions. *Opt. Quant. Elec.* **28**, 623 (1996).
- [220] G. Wasik, W. Gawlik, J. Zachorowski, and W. Zawadzki. Laser frequency stabilization by Doppler-free magnetic dichroism. *Appl. Phys. B* **75**, 613 (2002).
- [221] U. Schünemann, H. Engler, R. Grimm, M. Weidemüller, and M. Zielonkowski. Simple scheme for tunable frequency offset locking of two lasers. *Rev. Sci. Instrum.* **70**, 242 (1999).
- [222] G. Bjorklund, M. Levenson, W. Lenth, and C. Ortiz. Frequency modulation (FM) spectroscopy. *Appl. Phys. B* **32**, 145 (1983).
- [223] R. Drever, J. Hall, F. Kowalski, J. Hough, G. Ford, A. Munley, and H. Ward. Laser phase and frequency stabilization using an optical resonator. *Appl. Phys. B* **31**, 97 (1983).
- [224] F. S. Cataliotti, E. A. Cornell, C. Fort, M. Inguscio, F. Marin, M. Prevedelli, L. Ricci, and G. M. Tino. Magneto-optical trapping of fermionic potassium atoms. *Phys. Rev. A* **57**, 1136 (1998).
- [225] A.-C. Voigt. *Simultanes Fangen von drei Atomsorten in einer magnetooptischen Falle*. Diplomarbeit, Technische Universität München (2004). Unpublished.
- [226] W. Wieser. *An optical dipole trap for ultracold bosons and fermions*. Diplomarbeit, Ludwig-Maximilians University Munich (2006). Unpublished.

- [227] M. R. Andrews, M.-O. Mewes, N. J. van Druten, D. S. Durfee, D. M. Kurn, and W. Ketterle. Direct, nondestructive observation of a Bose condensate. *Science* **273**, 84 (1996).
- [228] E. Majorana. Atomi orientati in campo magnetico variabile. *Nuovo Cimento* **9**, 43 (1932).
- [229] W. H. Wing. On neutral particle trapping in quasistatic electromagnetic fields. *Prog. Quant. Electr.* **8**, 181 (1984).
- [230] G. Breit and I. I. Rabi. Measurement of nuclear spin. *Phys. Rev.* **38**, 2082 (1931).
- [231] W. Petrich, M. H. Anderson, J. R. Ensher, and E. A. Cornell. Stable, tightly confining magnetic trap for evaporative cooling of neutral atoms. *Phys. Rev. Lett.* **74**, 3352 (1995).
- [232] H. J. Lewandowski, D. M. Harber, D. L. Whitaker, and E. A. Cornell. Simplified system for creating a Bose-Einstein condensate. *J. Low Temp. Phys.* **132**, 309 (2003).
- [233] C. Klempt. *Wechselwirkung in Bose-Fermi-Quantengasen*. Ph.D. thesis, Gottfried Wilhelm Leibniz University, Hannover (2007).
- [234] T. Bergeman, G. Erez, and H. J. Metcalf. Magnetostatic trapping fields for neutral atoms. *Phys. Rev. A* **35**, 1535 (1987).
- [235] C. Eigenwillig. *Optimierte Herstellung einer ultrakalten Bose-Fermi-Mischung in der Magnetfalle*. Diplomarbeit, Ludwig-Maximilians University Munich (2007). Unpublished.
- [236] E. A. Donley, N. R. Claussen, S. T. Thompson, and C. E. Wieman. Atom-molecule coherence in a Bose-Einstein condensate. *Nature* **417**, 529 (2002).
- [237] C. Adams and E. Riis. Laser cooling and trapping of neutral atoms. *Prog. Quant. Electr.* **21**, 1 (1997).
- [238] W. Süptitz, G. Wokurka, F. Strauch, P. Kohns, and W. Ertmer. Simultaneous cooling and trapping of  $^{85}\text{Rb}$  and  $^{87}\text{Rb}$  in a magneto-optical trap. *Opt. Lett.* **19**, 1571 (1994).
- [239] M. S. Santos, P. Nussenzeig, L. G. Marcassa, K. Helmerson, J. Flemming, S. C. Zilio, and V. S. Bagnato. Simultaneous trapping of two different atomic species in a vapor-cell magneto-optical trap. *Phys. Rev. A* **52**, R4340 (1995).
- [240] G. D. Telles, L. G. Marcassa, S. R. Muniz, S. G. Miranda, A. Antunes, C. Westbrook, and V. S. Bagnato. Inelastic cold collisions of a Na/Rb mixture in a magneto-optical trap. *Phys. Rev. A* **59**, R23 (1999).
- [241] G. D. Telles, W. Garcia, L. G. Marcassa, V. S. Bagnato, D. Ciampini, M. Fazzi, J. H. Müller, D. Wilkowski, and E. Arimondo. Trap loss in a two-species Rb-Cs magneto-optical trap. *Phys. Rev. A* **63**, 033406 (2001).

- 
- [242] U. Schlöder, H. Engler, U. Schünemann, R. Grimm, and M. Weidemüller. Cold inelastic collisions between lithium and cesium in a two-species magneto-optical trap. *Eur. Phys. J. D* **7**, 331 (1999).
- [243] V. Wippel, C. Binder, and L. Windholz. Cross-section for collisions of ultracold  ${}^7\text{Li}$  with Na. *Eur. Phys. J. D* **21**, 101 (2002).
- [244] C. I. Sukenik and H. C. Busch. Simultaneous trapping of rubidium and metastable argon in a magneto-optical trap. *Phys. Rev. A* **66**, 051402 (2002).
- [245] S. Hensler, A. Griesmaier, J. Werner, A. Görlitz, and T. Pfau. A two species trap for chromium and rubidium atoms. *J. Mod. Opt.* **51**, 1807 (2004).
- [246] M.-O. Mewes, G. Ferrari, F. Schreck, A. Sinatra, and C. Salomon. Simultaneous magneto-optical trapping of two lithium isotopes. *Phys. Rev. A* **61**, 011403 (1999).
- [247] J. Goldwin, S. B. Papp, B. de Marco, and D. S. Jin. Two-species magneto-optical trap with  ${}^{40}\text{K}$  and  ${}^{87}\text{Rb}$ . *Phys. Rev. A* **65**, 021402 (2002).
- [248] E. Wille, F. M. Spiegelhalder, G. Kerner, D. Naik, A. Trenkwalder, G. Hendl, F. Schreck, R. Grimm, T. G. Tiecke, J. T. M. Walraven, S. J. J. M. F. Kokkelmans, E. Tiesinga, and P. S. Julienne. Exploring an ultracold Fermi-Fermi mixture: Interspecies Feshbach resonances and scattering properties of  ${}^6\text{Li}$  and  ${}^{40}\text{K}$ . *Phys. Rev. Lett.* **100**, 053201 (2008).
- [249] A. Ludewig, T. Tiecke, S. Kraft, S. Gensemer, and J. Walraven. A Fermion mixture of ultracold  ${}^6\text{Li}$  and  ${}^{40}\text{K}$ . Poster at the DPG-conference, Düsseldorf (2007).
- [250] S. Chu, L. Hollberg, J. E. Bjorkholm, A. Cable, and A. Ashkin. Three-dimensional viscous confinement and cooling of atoms by resonance radiation pressure. *Phys. Rev. Lett.* **55**, 48 (1985).
- [251] J. Dalibard and C. Cohen-Tannoudji. Laser cooling below the Doppler limit by polarization gradients: simple theoretical models. *J. Opt. Soc. Am. B* **6**, 2023 (1989).
- [252] P. J. Ungar, D. S. Weiss, E. Riis, and S. Chu. Optical molasses and multilevel atoms: theory. *J. Opt. Soc. Am. B* **6**, 2058 (1989).
- [253] S. Chu. Laser manipulation of atoms and ions. In E. Arimondo, W. Phillips, and F. Strumia (eds.), *Proceedings of the International School of Physics "Enrico Fermi", Course CXVIII*, p. 239. North-Holland, Amsterdam (1992).
- [254] J. Weiner, V. S. Bagnato, S. Zilio, and P. S. Julienne. Experiments and theory in cold and ultracold collisions. *Rev. Mod. Phys.* **71**, 1 (1999).
- [255] D. W. Sesko, T. G. Walker, and C. E. Wieman. Behavior of neutral atoms in a spontaneous force trap. *J. Opt. Soc. Am. B* **8**, 946 (1991).
- [256] W. Petrich, M. H. Anderson, J. R. Ensher, and E. A. Cornell. Behavior of atoms in a compressed magneto-optical trap. *J. Opt. Soc. Am. B* **11**, 1332 (1994).

- [257] C. S. Adams, H. J. Lee, N. Davidson, M. Kasevich, and S. Chu. Evaporative cooling in a crossed dipole trap. *Phys. Rev. Lett.* **74**, 3577 (1995).
- [258] S. Friebel, R. Scheunemann, J. Walz, T. Hänsch, and M. Weitz. Laser cooling in a CO<sub>2</sub>-laser optical lattice. *Appl. Phys. B* **67**, 699 (1998).
- [259] W. Ketterle, K. B. Davis, M. A. Joffe, A. Martin, and D. E. Pritchard. High densities of cold atoms in a dark spontaneous-force optical trap. *Phys. Rev. Lett.* **70**, 2253 (1993).
- [260] P. W. H. Pinkse, A. Mosk, M. Weidemüller, M. W. Reynolds, T. W. Hijmans, and J. T. M. Walraven. Adiabatically changing the phase-space density of a trapped Bose gas. *Phys. Rev. Lett.* **78**, 990 (1997).
- [261] L. Pitaevskii and S. Stringari. *Bose-Einstein condensation*. Oxford University Press (2003).
- [262] C. Zener. Non-adiabatic crossing of energy levels. *Proceedings of the Royal Society of London, Series A* **137**, 696 (1932).
- [263] J. R. Rubbmark, M. M. Kash, M. G. Littman, and D. Kleppner. Dynamical effects at avoided level crossings: A study of the Landau-Zener effect using Rydberg atoms. *Phys. Rev. A* **23**, 3107 (1981).
- [264] N. V. Vitanov and K.-A. Suominen. Time-dependent control of ultracold atoms in magnetic traps. *Phys. Rev. A* **56**, R4377 (1997).
- [265] C. Cohen-Tannoudji, J. Dupont-Roc, and G. Grynberg. *Atom-Photon Interactions*. Wiley & Sons, New York (1992).
- [266] B. Desruelle, V. Boyer, S. G. Murdoch, G. Delannoy, P. Bouyer, A. Aspect, and M. Lécroivain. Interrupted evaporative cooling of <sup>87</sup>Rb atoms trapped in a high magnetic field. *Phys. Rev. A* **60**, R1759 (1999).
- [267] S. Giorgini, L. P. Pitaevskii, and S. Stringari. Condensate fraction and critical temperature of a trapped interacting Bose gas. *Phys. Rev. A* **54**, R4633 (1996).
- [268] J. Goldwin, S. Inouye, M. L. Olsen, B. Newman, B. D. DePaola, and D. S. Jin. Measurement of the interaction strength in a Bose-Fermi mixture with <sup>87</sup>Rb and <sup>40</sup>K. *Phys. Rev. A* **70**, 021601 (2004).
- [269] T. Rom, T. Best, D. van Oosten, U. Schneider, S. Fölling, B. Paredes, and I. Bloch. Free fermion antibunching in a degenerate atomic Fermi gas released from an optical lattice. *Nature* **444**, 733 (2006).
- [270] F. Ferlaino, C. D’Errico, G. Roati, M. Zaccanti, M. Inguscio, G. Modugno, and A. Simoni. Feshbach spectroscopy of a K-Rb atomic mixture. *Phys. Rev. A* **73**, 040702 (2006).

- 
- [271] F. Ferlaino, C. D’Errico, G. Roati, M. Zaccanti, M. Inguscio, G. Modugno, and A. Simoni. Erratum: Feshbach spectroscopy of a K-Rb atomic mixture [*Phys. Rev. A* **73** 040702 (2006)]. *Phys. Rev. A* **74**, 039903 (2006).
- [272] B. Deh, C. Marzok, C. Zimmermann, and P. W. Courteille. Feshbach resonances in mixtures of ultracold  $^6\text{Li}$  and  $^{87}\text{Rb}$  gases. *Phys. Rev. A* **77**, 010701 (2008).
- [273] C. P. Koch, J. P. Palao, R. Kosloff, and F. Masnou-Seeuws. Stabilization of ultracold molecules using optimal control theory. *Phys. Rev. A* **70**, 013402 (2004).
- [274] B. Schäfer-Bung, R. Mitric, and V. Bonacic-Koutecky. Photostabilization of the ultracold  $\text{Rb}_2$  molecule by optimal control. *J. Phys. B* **39**, S1043 (2006).
- [275] J. J. Hudson, P. C. Condylis, H. T. Ashworth, M. R. Tarbutt, B. E. Sauer, and E. A. Hinds. Towards a new measurement of the electron’s electric dipole moment. arXiv:physics/0509169v1 (2005).
- [276] W. Bernreuther and M. Suzuki. The electric dipole moment of the electron. *Rev. Mod. Phys.* **63**, 313 (1991).
- [277] C. Lee and E. A. Ostrovskaya. Quantum computation with diatomic bits in optical lattices. *Phys. Rev. A* **72**, 062321 (2005).
- [278] A. Micheli, G. K. Brennen, and P. Zoller. A toolbox for lattice-spin models with polar molecules. *Nature Physics* **2**, 341 (2006).
- [279] R. Barnett, D. Petrov, M. Lukin, and E. Demler. Quantum magnetism with multicomponent dipolar molecules in an optical lattice. *Phys. Rev. Lett.* **96**, 190401 (2006).
- [280] T.-L. Ho. Universal thermodynamics of degenerate quantum gases in the unitarity limit. *Phys. Rev. Lett.* **92**, 090402 (2004).
- [281] Brookhaven National Laboratory. National Nuclear Data Center. <http://www.nndc.bnl.gov/nudat2/>.
- [282] J. S. Coursey, D. J. Schwab, and R. A. Dragoset. NIST standard reference database 144. <http://physics.nist.gov/PhysRefData/Compositions/>.
- [283] K. M. O’Hara. *Optical Trapping and Evaporative Cooling of Fermionic Atoms*. Ph.D. thesis, Duke University (2000).
- [284] A. Marte, T. Volz, J. Schuster, S. Dürr, G. Rempe, E. G. M. van Kempen, and B. J. Verhaar. Feshbach resonances in rubidium 87: Precision measurement and analysis. *Phys. Rev. Lett.* **89**, 283202 (2002).
- [285] E. G. M. van Kempen, S. J. J. M. F. Kokkelmans, D. J. Heinzen, and B. J. Verhaar. Interisotope determination of ultracold rubidium interactions from three high-precision experiments. *Phys. Rev. Lett.* **88**, 093201 (2002).

- [286] W. I. McAlexander, E. R. I. Abraham, and R. G. Hulet. Radiative lifetime of the 2P state of lithium. *Phys. Rev. A* **54**, R5 (1996).
- [287] U. Volz and H. Schmoranzer. Precision lifetime measurements on alkali atoms and on helium by beam-gas-laser spectroscopy. *Phys. Scr.* **T65**, 48 (1996).
- [288] G. Roati, W. Jastrzebski, A. Simoni, G. Modugno, and M. Inguscio. Optical trapping of cold fermionic potassium for collisional studies. *Phys. Rev. A* **63**, 052709 (2001).
- [289] W. Scherf, O. Khait, H. Jäger, and L. Windholz. Re-measurement of the transition frequencies, fine structure splitting and isotope shift of the resonance lines of lithium, sodium and potassium. *Z. Phys. D* **36**, 31 (1996).
- [290] J. Ye, S. Swartz, P. Jungner, and J. L. Hall. Hyperfine structure and absolute frequency of the  $^{87}\text{Rb}$   $5\text{P}_{3/2}$  state. *Opt. Lett.* **21**, 1280 (1996).

## Danksagung

Viele Menschen haben direkt und indirekt zum Gelingen dieser Arbeit beigetragen. Ihnen möchte ich an dieser Stelle meinen herzlichen Dank aussprechen.

An erster Stelle sei hier mein Doktorvater Prof. Dr. Theodor W. Hänsch genannt, der mir die Möglichkeit gegeben hat, unter hervorragenden Rahmenbedingungen an einem hochaktuellen Projekt mitzuwirken. Er hat unserem Projekt stets großes Vertrauen entgegengebracht, uns großzügig unterstützt und uns viel Freiraum für eigene Ideen gelassen. Seine eigene Begeisterung für die Physik habe ich dabei immer als sehr motivierend empfunden.

Herrn Prof. Dr. Gerhard Rempe danke ich für die freundliche Bereitschaft, diese Arbeit zu begutachten.

Meinem Gruppenleiter Dr. Kai Dieckmann bin ich dankbar für die vertrauensvolle und konstruktive Zusammenarbeit. In dieser gemeinsamen Zeit konnte ich viele Dinge lernen, die mir auch in der Zukunft noch von großem Nutzen sein werden. Im Labor hat er mich ein ordentliches Maß Pragmatismus gelehrt, hat oft fest mit angepackt und selbst in schwierigen Zeiten nie den festen Glauben an den Erfolg verloren. Die zahlreichen heißen Diskussionen mit ihm über physikalische und nicht-physikalische Themen haben die Zeit immer spannend bleiben lassen. Besonderer Dank gilt ihm auch für das kritische Korrekturlesen dieser Arbeit und die wertvollen Verbesserungsvorschläge - und natürlich dafür, dass wir ihn beim Probieren der zahlreichen indonesischen Leckereien von Yeti "unterstützen" durften.

Mit meinem Mitdokoranden Arne-Christian Voigt bin ich gemeinsam die Achterbahn der Hochs und Tiefs gefahren, die ein so ambitioniertes Projekt mit sich bringt. Unsere zahlreichen gemeinsamen Messnächte werden mir immer in Erinnerung bleiben. Bei den gelegentlichen Kickerduellen war er stets ein guter Partner und fairer Gegner — und seine Statistik-Rechnungen danach sind mittlerweile legendär.

Ebenso möchte ich den weiteren Mitstreitern am Experiment danken: Sebastian Fray, der einige Zeit als Postdoc an unserem Experiment verbracht hat, danke ich für seine Beiträge zum Projekt, für die lustigen gemeinsamen Abende und dafür, dass wir sein altes Experiment ausräubern durften. I am also grateful to our current post-doc Takatoshi Aoki for his contributions to the experiment, for his refreshing company, and for the delicious souvenirs he brought from Japan. Louis Costa, der unser Team seit einigen Monaten tatkräftig als neuer Doktorand unterstützt, hat sich durch seine ruhige, freundliche und sehr unkomplizierte Art schnell in das Projekt eingefunden. Florian Henkel, Wolfgang Wieser und Christoph Eigenwillig haben zu unterschiedlichen Zeiten als Diplomanden am Projekt mitgearbeitet und einige wertvolle Beiträge geleistet.

Für ihre äußerst wertvolle Unterstützung in elektronischen, organisatorischen und technischen Dingen bin ich Toni Scheich, Gabriele Gschwendtner, Rosemarie Lechner, Nicole

Schmidt, Wolfgang Simon, Charlie Linner, Helmut Brückner, sowie den Werkstätten des MPQ und der LMU sehr dankbar. Ebenfalls gedankt sei auch unseren Hiwis Peter Hiltz, Johannes Hofer, Johannes Thürigen und Benedikt Breitenfeld für ihre Beiträge zum Projekt.

Ganz herzlich bedanken möchte ich mich auch bei allen Mitgliedern der AG Weinfurter und des Mikrofallen-Projektes. Sie waren stets offen für Fragen und Diskussionen und haben großzügig gerade nicht gebrauchte Gerätschaften und Komponenten an uns verliehen. Ganz besonders aber haben sie alle auch ganz wesentlich zu der guten Stimmung auf dem Stockwerk beigetragen - und das bei weitem nicht nur aufgrund ihrer ausgefeilten Kuchen- und Espressokultur! Bei diversen gemeinsamen Unternehmungen sind insbesondere Florian und Daniel zu guten Freunden geworden. Auch bei allen noch nicht genannten Mitgliedern der Hänsch-Gruppe möchte ich mich für die schöne Zeit und die freundschaftliche Atmosphäre bedanken. Insbesondere auch die Gruppenseminare auf Schloß Ringberg werden mir immer in sehr positiver Erinnerung bleiben.

Ganz besonders dankbar bin ich auch all meinen Freunden, die das Leben außerhalb der Arbeit sehr bereichert haben. Niels danke ich zudem für das äußerst gründliche und konstruktive Korrekturlesen dieser Arbeit.

Ein riesiges Dankeschön geht natürlich an meine Familie und insbesondere meine Eltern, die mich bei all meinen privaten und beruflichen Interessen und Aktivitäten vorbehaltlos gefördert und immer regen Anteil an meinem Weg genommen haben.

Tini hat mit mir alle Phasen dieser Arbeit durchlebt und mich in vielerlei Hinsicht sehr unterstützt. Sie hatte nicht nur großes Verständnis für die zahllosen langen Labornächte, sondern hat auch dafür gesorgt, dass ich die Arbeit auch mal ganz vergessen konnte. Ein ganz, ganz dickes Dankeschön für alles!